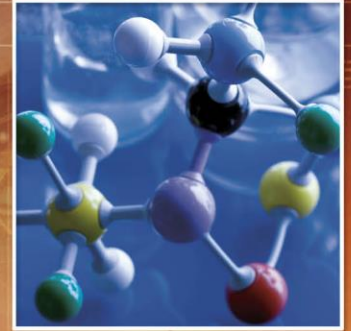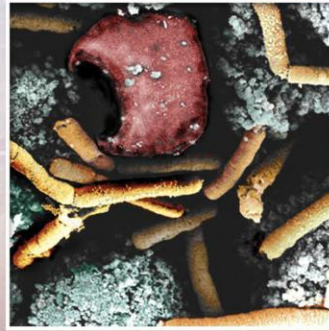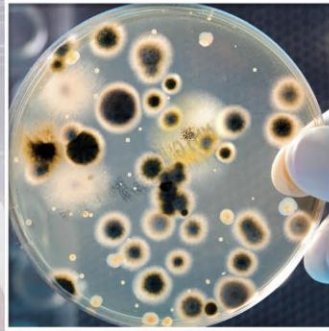*TECHNOLOGY DRIVEN. WARFIGHTER FOCUSED.*

PROCEEDINGS OF THE
EDGEWOOD CHEMICAL BIOLOGICAL CENTER

IN-HOUSE LABORATORY INDEPENDENT RESEARCH AND SURFACE SCIENCE INITIATIVE PROGRAMS

FY13

U.S. ARMY
RDECOM®
TECHNOLOGY DRIVEN.

ECBC Strategic Mission and Vision

The U.S. Army Edgewood Chemical Biological Center (ECBC) functions as the nation's principal research, development, and engineering resource for non-medical chemical and biological (CB) defense applications. ECBC's mission is *to integrate life-cycle science, engineering, and operations solutions to counter CBRNE threats to U.S. forces and the nation.* This mission recognizes that ECBC's range of influence has grown to include military and homeland defense as well as expanding research, development, and engineering needs beyond CB defense to include comparable technical solutions for radiological, nuclear, and explosives (RNE) hazards. ECBC's vision is *to be the premier resource for CBRNE solutions, uniting and informing the defense community.* As such, ECBC is charged with understanding the comprehensive threat to the warfighter and providing the scientific knowledge, technology, and materiel required to protect and enable the warfighter to effectively operate and implement strategic decisions while in the presence of CB contamination.

ECBC's mission and vision are supported by the Center's three Directorates of Research and Technology (R&T), Engineering, and Program Integration. The R&T Directorate provides integrated science and technology solutions that address CB defense knowledge gaps and vulnerabilities. The Center's R&T capability areas include BioSciences, CB Detection, CB Protection and Decontamination, Chemical Sciences, Physics and Computational Sciences, and Toxicology and Obscurants. Basic science research at ECBC contributes valuable information to the fundamental science knowledgebase, enabling the development of technologies that directly benefit the warfighter and further strengthen the Army's Science and Technology (S&T) mission. ECBC's unique set of core research and technology capabilities position it to be the Army's fundamental source of research in chemistry and biology.

APPROVED FOR PUBLIC RELEASE

ECBC ILIR Proposal Process

The purpose of the In-House Laboratory Independent Research (ILIR) program is to fund innovative basic research projects that are high risk and have high potential payoff for fulfilling Army needs. The Department of Defense (DoD) defines *basic research* as "the systematic study directed toward greater knowledge or understanding of the fundamental aspects of phenomena and of observable facts without specific applications toward processes or products in mind." The ILIR program is specifically designed to foster increased innovation within the ECBC Basic Research portfolio. ECBC views the program as a critical part of its efforts at ensuring a high level of basic science, to foster innovation in the areas of chemistry and biology, and to mentor junior investigators in the art and practice of new technological innovations and new phenomenology at the boundaries of chemistry, biology, mathematics, or physics that will gain additional insight and advances in support of CBRNE defense missions.

The ILIR program solicits innovative proposals from the center's principal investigators that correspond to ECBC's critical core capability areas: Rational Molecular and Nano-system Design, Synthetic Biology, Nano-scale CB Sensing and Signaling, Molecular Toxicoloy, Aerosol Physics, Materials Science, and Algorithm Design and Development. Proposals are first reviewed internally by the Branch and Division Chiefs for their technical innovation, alignment to Army/ECBC S&T topic areas, and programmatic completeness. The proposals are then reviewed and critiqued by a panel comprised of resident and external Department of the Army Senior Technologists (STs), Senior Scientists from other DoD organizations, and civilian and military faculty members at the U.S. Military Academy. Some of these same reviewers also serve on a Technical Advisory Board (TAB), which convenes annually in the fourth quarter of the program to assess the year-to-date performance of the basic science research projects.

The review panels evaluate each proposal on its scientific objective, the scientific methods proposed, the qualifications of the investigator, and the budget, with the scientific objective and methods weighted as the most important criteria. The proposals are then ranked according to merit. Only proposals deemed by the panel as basic research are considered for funding. Quality comments from the reviewers are compiled and used, with the numerical score, as a critical assessment of the proposal. This written feedback is essential for ECBC's mentoring of researchers and for justifying the elimination of research programs that are not competitive. Quarterly reviews of project performance and the end-of-the-year TAB review provide additional guidance to the program's participants, ensuring projects meet significant milestones, and substantive new knowledge is produced and transferred to the ECBC and broader scientific community.

This cyclical review and assessment process was used to select and monitor the progress of three new ILIR projects and two projects already in existence. Internal funds were also used to support four directed basic research projects, under the Surface Science Initiative (SSI) program, and four "Seedling" projects, which are smaller-scale projects of high risk, high reward basic research. This Proceedings Report contains the technical reports from all thirteen ECBC-produced ILIR/SSI/Seedling-funded projects.

FY13 ILIR Technical Report Executive Summary

The ECBC ILIR program funded five projects in fiscal year 2013 (FY13), the SSI Program divided funding between four projects, and internal "seedling" funding was distributed to four projects. Together, the ILIR, SSI, and Seedling projects covered multiple areas of interest across the chemical, biological, and physical sciences, including: molecular toxicology, rational molecular and nano-system design, synthetic biology, nano-scale CB sensing and signaling, aerosol physics, materials science, algorithm design and development, detection and ecotoxicity of chemicals, biosurveillance and pathogen detection, individual protection, data fusion, hazard prediction and consequence management, electromagnetic manipulation, decontamination and hazard mitigation approaches, and attribution of CB incidents to region or actor. The projects funded in FY13 are briefly summarized below:

In-House Laboratory Independent Research (ILIR) Projects

Secretome biomarkers for the identification and differentiation of enterohemorrhagic and enteropathogenic and *Escherichia coli* strains
PI: Rabih E. Jabbour

Genomic studies of enterohemorrhagic and enteropathogenic *Escherichia coli* (EHEC and EPEC, respectively) do not directly characterize the biomolecules involved in virulence activities. This effort sought to utilize metaproteomic mass spectrometry to characterize the virulence of secreted proteins from EHEC and EPEC strains. Secretome analysis, compared to whole cell processing, is useful, practical, and uses fewer and more efficient experimental procedures. This work indicated that differentiation among EHEC and EPEC strains was improved using secreted proteins as differentiation biomarkers. The secretome provided a unique source of cellular variability that was not observed when compared to whole cell lysates. Additionally, tandem-mass spectrometry (MS-MS)-based proteomics and bioinformatics were shown to have utility in the comparative proteomics study for the differentiation of EHEC and EPEC strains, indicating that this approach has potential to characterize emerging and unknown microbes and aid in genomic sequencing analyses.

Microbial wargaming: Modeling the contributions to fitness of bacteria encoding deployable genetic weaponry
PI: Henry S. Gibbons

The use of synthetic biology, namely the treatment of genes, promoters, and regulatory systems as interchangeable parts, facilitates the construction of defined bacterial strains containing cryptic antimicrobial proteins that can be deployed with a range of experimentally tunable levels. This project investigated a simple *in vitro* model system for inter-community warfare using bacterial strains equipped with antibacterial colicin-based weapons. To visualize colicin-mediated growth inhibition, this work developed a simple growth assay on low-concentration agar plates that allow greater strain mobility on the plate surface. To provide a more quantitative assessment of growth rates on plates, a custom image processing algorithm was developed to convert a sequence of images into quantitative measures of area over time for each colony. This work indicated that a synthetic approach to generate truly isogenic strains (without confounding genes and potential regulatory elements introduced by the heterogeneous plasmid backbones) is necessary to evaluate the relative efficacy of the colicin operons. However, heterogeneous colony growth phenotypes allowed the development of the computerized image processing technique for measuring the growth of colonies over time.

Role of acetylcholinesterase in the regulation of mesenchymal stem cell proliferation and differentiation
PI: James D. Wright

Mesenchymal stem cells (MSC) are derived from adult tissue and are significantly involved in tissue regeneration following injury. These cells have been shown to express active acetylcholinesterase (AChE), but the role this enzyme plays in MSC proliferation and differentiation is unknown.

Organophosphate (OP) chemicals, known to perturb MSC function and alter AChE activity, could affect MSCs' ability to proliferate and/or differentiate, thereby reducing the ability to recover from injuries. This effort examines the role of AChE in MSC proliferation and differentiation by inhibiting AChE activity through exposure to the OPs parathion and paraoxon. The results of this work indicate that parathion and paraoxon disrupt the normal pathways associated with AChE in human MSCs. These altered pathways induce cellular death as well as the normal proliferative function of MSCs. Additionally, this study demonstrated that prior treatment of MSCs with either parathion or paraoxon significantly reduced the MSCs' ability to differentiate into adipocytes, suggesting a possible role of AChE in this process.

A platform approach to produce polymer nanoparticles with modular functionality from block copolymer surfactants
PI: Kato L. Killops

This work investigated the formation of monodispersed particles with varied peripheral functionality from block copolymer (BCP) surfactants and dependence of particle properties on BCP surfactant concentration, particularly the self-assembly of particle films/structures and how functionality influences self-assembly behavior. This effort aimed to achieve control over peripheral functionality of polymer particles by using modifiable BCP surfactants, and thereby tune particle physical properties. A functional amphiphilic BCP, polystyrene-*b*-poly(ethylene oxide-*co*-allyl glycidyl ether), was successfully employed as a stabilizer in emulsion polymerization. This work demonstrated control over the size of the particles by varying the amount of BCP incorporated into the particles, to give particles with low polydispersity; however, this control was primarily exerted at a narrow molecular weight value. Smaller and larger BCPs demonstrated a loss of control, primarily due to steric stabilization factors. The inclusion of allyl groups within the hydrophilic portion of the BCP allowed for modification of a single polymer scaffold to create a library of particles with functional corona. Analysis from x-ray photoelectron spectroscopy and zeta potential measurements indicated that that the functional corona resides at the periphery of the particles, extending into solution.

On resonant Raman enhancement driven by nano-scale intermolecular interactions
PI: Jerry B. Cabalo

Resonance Raman spectroscopy (RRS) demonstrates increased Raman scattering due to resonance caused by coupling between the excitation laser and electronic absorption within the analyte molecule. With RRS, vibrational modes involving the chromophore are preferentially enhanced. Based on the theoretical understanding of the Raman response, this effort anticipated that intermode coupling, driven by intermolecular interactions, enhances modes not directly connected to the absorbing chromophore. Theoretical modeling of these interactions can be used to control the selection of modes that undergo enhancement. Model and experimental spectra differed on a number of Raman bands. Spectra calculated by this method predicted that the Raman response from Cysteine was negligible, that symmetric hydrogen motion about the amine group was a primary contributor to the Raman signature, and that the aromatic ring stretches and breathing modes were not significant contributors. These differences may be explained by the choice of water model, functional, or molecular conformation and will be explored further.

Surface Science Initiative (SSI) Projects

Layer-by-layer self-assembly of plexitonic nanoparticles
PI: Dr. Brendan DeLacy

Colloidal suspensions of multilayer nanoparticles (NP) composed of a silver core, a polyelectrolyte spacer layer (inner shell), and a J-aggregate cyanine dye (outer shell) have been prepared for the first time. This multilayer architecture served as a framework for examining the coupling of the localized surface plasmon resonance exhibited by the silver core with the molecular exciton exhibited by the J-aggregate outer shell. The polyelectrolyte spacer layer promotes the formation of an excitonic J-aggregate while

serving as a means of controlling the plasmon-exciton (i.e., plexciton) coupling strength through changing the distance between the core and the shell. An analytical expression based on Mie Theory and the Transfer Matrix Method was obtained for describing the optical response of these multilayered nanostructures. Computational and experimental results indicate that the absorption wavelength of the J-aggregate form of the dye is dependent on both the distance of the dye layer from the silver core and the degree of dye aggregation.

Highly ordered nanowire arrays based on polydiacetylene for sensing applications
PI: Dr. Kato Killops

This effort explored side-chain diacetylene (DA) structures and a post-modification strategy to functionalize BCPs with polydiacetylene (PDA) for chemical sensing. The objective of this effort was to create PDA-BCP hybrid materials displaying hierarchical self-assembly. The proposed methodology attached PDA as a side chain to the BCP and attached DA to functional BCP, with groups to react with analytes. With the aim of producing stable DA structures with hierarchical, long range order, this work synthesized semiconducting DA polymers. By using a BCP as a template to induce phase separation, thin films exhibiting hierarchical structure were produced. The PDA films showed photoluminescent behavior, as well as colorimetric transitions when exposed to a thermal stimulus.

A rational design approach to multifunctional nanostructured materials
PI: Dr. Chris Karwacki

This research pursued fundamental understanding of the structure-property-activity relationships of complexes composed of carbon-metal-oxygen, as a basis for enhancing spectral and catalytic activities. In this study, we build rationally-designed architectures based on graphene materials using alizarin and titanium isopropoxide (TIP). A hybrid form of nanostructured graphene-titanium oxide (Gr-TiO$_2$) was prepared using a bottom-up synthetic approach. The enhanced photocatalytic activity of Gr-TiO$_2$ was demonstrated through the degradation of methylene blue (MB) under ultraviolet (UV) light irradiation and carbon monoxide (CO) oxidation. These results show how properties of designed nanostructured materials can be rationally tailored by choosing the starting materials that already have the desired characteristics embedded in them. The data can be used to establish trends and design rules for design of novel functional materials.

Understanding the role of physical and chemical adsorption on the Raman enhancement from metallic nanoparticles and nanostructured surfaces
PI: Dr. Jason Guicheteau

This works explored the effects of chemical and physical adsorption on the surface-enhanced Raman intensity and provide an improved experimental and theoretical understanding of the physical phenomena that govern the adsorption and interaction of analytes with metallic nanoparticles and nanostructured metallic surfaces. To accomplish this, a series of benzene derivative chemicals was analyzed to study the effects of molecular polarity on the adsorption of molecules on the surface of metallic nanoparticles and nanostructured surfaces. Time-dependent Langmuir isotherms were used to analyze the surface-enhanced Raman spectroscopy (SERS) data for nanoparticle solutions and nanostructured surfaces as well as size, zeta potential, and UV-visible (UV-vis) measurements. This work provides insight into this fundamental phenomenon, resulting in greater knowledge and understanding of the interaction of molecules with metal nanoparticles and nanostructures and allowing customization of metallic structures for selective binding of analytes and enhanced molecular sensing. This knowledge can impact the molecular sensing fields including novel SERS sensors.

Seedling Projects

Decontamination of sulfur mustard by polymerization
PI: Dr. Patrick Riley

The improvement of decontaminant technology requires an understanding of material-contaminant interactions to produce decontaminants that can mitigate hazards and reduce material damage. For this work, a polymerization reaction was performed between sulfur mustard (HD) and bisphenol A (BPA) to yield a novel polymeric product that may explain the noted "thickening" of contaminants observed in dynamic contact angle (DCA) experiments. This work demonstrated that a condensation reaction occurs between HD and phenols, which allows for polymerization. The work highlights the importance of HD forming a more reactive intermediate in order for step-wise polymerization to proceed, thus presenting a pathway for bulk decontamination.

Raman spectroscopic analysis of whole blood acetylcholinesterase
PI: Dr. Phillip Wilcox

In this research, Raman spectra were taken of whole sheep's blood with varying levels of AChE inhibition using 229 and 532 nm laser excitation wavelengths. AChE levels were inhibited using the OPs malathion, paraoxon-ethyl, and octamethyldiphosphoramide and confirmed using the Ellman method. The confirmed AChE activity level was combined with the Raman spectra and analyzed using a partial least squares calibration and cross validation to determine if the AChE activity could be predicted from the Raman spectrum. While no spectral feature that could be correlated to AChE activity was found, it was possible to predict a trend in AChE activity using Raman spectra using 229 nm excitation. This does not show the same quality of results as a laboratory technique, but could potentially be used as a trigger for a blood draw and more precise measurement using the current methodology.

Magnetic measurement of particle adhesion forces
PI: Dr. Jerry Cabalo

This study explored the forces of adhesion between particles and a surface in air by examining the contribution of chemical interactions to the adhesion force. Using the interaction between carboxylic-acid-functionalized polystyrene latex (PSL) beads and substrates coated with functionalized self-assembled monolayers, force measurements were performed using magnetic PSL beads and a well-characterized magnet. Two technical barriers were encountered during this study of adhesion. First, the magnetic force on the beads was two to three orders of magnitude less than atomic force microscopy measurements of the chemical contribution to adhesion force. Second, difficulties in producing a distribution of single PSL particles on the substrate without any liquid or solid material between the particles and the substrate were encountered. Using larger particles with higher magnetic material content should result in sufficient magnetic force to detach particles from the surface and facilitate more efficient deposition onto the test substrates.

Raman interrogation of viable and non-viable spores for determination of biomolecular information activity
PI: Dr. Jason Guicheteau

This effort investigated the use of Raman microscopy for understanding biololecular information on spore growth and germination. Changes in the Raman spectral response of supposed dormant spores suspended in non-nutrient rich environment (deionized water) were observed, which defeats the notion that the spores are fully inactive during a dormant state. This research provides insight on spectral variations occurring with residence time under non-germination conditions and biomarkers indicating pre-germination activity. Clear spectral distinction between the viable and non-viable spores was observed, along with slight variations in residence time for the viable spores. Temporal spectral analyses showed that select wavenumbers suggest an increase in pre-germination activity that was thought not to occur.

Table of Contents

ILIR PROJECTS

Secretome biomarkers for the identification and differentiation of enterohemorrhagic and enteropathogenic *Escherichia coli* strains

Rabih E. Jabbour[a], Samir V. Deshpande[b], Patrick E. McCubbin[c], James D. Wright[a],
Mary Margaret Wade[a]

[a]U.S. Army Edgewood Chemical Biological Center, Research and Technology Directorate,
5183 Blackhawk Rd, Aberdeen Proving Ground, MD 21010
[b]Science and Technology Corporation Edgewood, MD 21040
[c]Optimetrics, Inc., Abingdon, MD 21009

ABSTRACT

The secreted proteins of enterohemorrhagic *Escherichia coli* (EHEC) can cause hemorrhagic colitis which may cause life threatening hemolytic-uremic syndrome, while that of enteropathogenic and enteroaggregative *E. coli* (EPEC & EAEC) can clump to intestinal membranes. Liquid chromatography-electrospray ionization-tandem mass spectrometry based proteomics is used to evaluate a preliminary study on the secreted and whole cell protein extracts associated with *E. coli* strain pathogenicity. Proteomics analysis, which is independent of genomic sequencing of sequenced EPEC O111:H2 and unsequenced genome of EAEC O104:H4 identified a number of secreted proteins that provided differentiation among the studied *E. coli* strains. Proteomics of EHEC O104:H4, causative agent of the Germany outbreak, showed a closest match with *E. coli* E55989, in agreement with genomic studies. Dendrogram analysis separated EHEC O157:H7 and EPEC/EAEC O111:H2 and O104:H4. Secretome analysis, compared to whole cell processing, entails fewer steps and more convenient experimental extraction procedures. Bacterial characterization results are promising in exploring the impact of environmental conditions on *E. coli* secreted biomarker proteins with a few relatively straightforward protein extraction steps.

Keywords: electrospray, liquid chromatography-tandem mass spectrometry, proteomics, enteropathogenic, enterohemorrhagic *E. coli*, enteroaggregative *E. coli*

1. INTRODUCTION

The U.S. Government has initiated efforts for the detection and identification of biological threats in the Defense Advanced Research Projects Agency programs that explore the "detect-to-protect" and "detect-to-treat" paradigms.[1,2] These initiatives cover areas of general health risk, bioterrorism utility, Homeland Security, agricultural monitoring, food safety, and biological warfare agents in battlefield situations.[2] Some of these health concerns include food contamination outbreaks that affect military and civilian populations and also the transmission from abroad to the U.S. An example of the latter is the fatal enteroaggregative *Escherichia coli* (EAEC) O104:H4 outbreak that occurred in Germany in 2011, which infected citizens from sixteen different nations including the U.S.[3-5]

The O104:H4 strain exhibits characteristics of enterohemorrhagic *E. coli* (EHEC) and EAEC. EHEC strains can cause hemorrhagic colitis (bloody diarrhea or hemolytic uremic syndrome), and EAEC produces clumping of the bacteria on intestinal membranes.

EHEC and EAEC cause diseases in humans by their presence in food and water matrices. Infection in host cells is by attaching and effacing mechanisms. These occur by the pathogen secreting various proteins that compromise the cytoskeleton of the host cell.[6] EHEC and EAEC pathogens show different responses to antibiotics, and their human pathogenicity is enhanced with an antibiotic regimen. Studies have reported the differences in the number and nature of the secreted proteins (secretome) between EHEC, enteropathogenic *E. coli* (EPEC), and EAEC.[7] Development of protein/peptide identification techniques between EHEC and EAEC is desirable to provide effective medical countermeasures.

A pilot study was initiated to characterize a few *E. coli* strains based on their documented secretomes. To achieve this goal, a proteomics analytical system was used as a means of characterizing virulence proteins and amino acid

sequences to differentiate EHEC and EAEC strains. Relatively fewer purification steps are required for secretome analysis compared to that of the intracellular proteins for proteomics utility. An advantage is that the secretome facilitates the discovery of the low amounts and numbers of proteins by liquid chromatography-electrospray ionization-tandem mass spectrometry (LC-ESI-MS-MS).

The present study sought to determine whether MS-based proteomics could be used to distinguish between EHEC and EAEC strains with respect to their secreted and whole cell protein compositions. A contrast between the two types of proteins is that there are inherently fewer protein experimental extraction and separation steps from the secretome than that of the whole cell lysate. In addition, the use of MS-based proteomics is useful in characterizing and identifying biological agents without a known genome sequence[8] as is the case with the EHEC/EAEC O104:H4 strain.

2. METHODS

2.1 EHEC, EPEC, and EAEC strain preparation

In the present study, the pathogenic *E. coli* strains were O157:H7 (EHEC), O111:H2, and O104:H4. The cultures were prepared by streaking cells from cryopreserved stocks onto tryptic soy broth (TSB) and incubated at 37°C with shaking at 180 rpm overnight until a stationary growth phase was observed. After incubation, cells were harvested and colony counts were performed using optical density measurements. Three biological replicates for each strain were cultivated as mentioned above.

2.2 Isolation of the secreted proteins

The harvested cells were pelleted by centrifugation at 2,300 revolution centrifugal force (RCF) for 30 minutes and the supernatant was immediately separated into 30 mL aliquots. The supernatants were filtered using 0.22 µm hollow fiber dialysis filters to ensure no large particulates or cellular debris were present in the samples. Pelleted and supernatant samples were frozen at -70°C until further processing.

2.3 Processing of secreted and whole cell proteins

Whole cell samples were lysed using the bead beating technique (30 seconds on, 10 seconds off for 3 minutes duration). The lysates were centrifuged at 14,100 x g for 30 minutes to remove cellular debris and large particulates. The supernatant from the whole cell lysates and the filtered secretome samples were loaded separately onto PALL MW-3 kDa filter units (Ann Arbor, MI) and centrifuged at 14,100 x g for 30 min. The effluents were discarded and the filter membranes were washed with 100 mM ammonium bicarbonate (ABC) and centrifuged for 20 minutes at 14,100 x g. Proteins from the whole cell and secretome fractions were denatured by adding 8 M urea and 30 mg/mL dithiothreitol (DTT) to the filter and incubating for an hour at 40°C. The tubes were then centrifuged at 14,100 x g for 40 minutes and washed three times using 150 mL of 100 mM ABC solution. On the last wash, ABC was allowed to sit on the membrane for 20 minutes while shaking, followed by centrifugation at 14,100 x g for 40 min. The filter units were then transferred to new receptor tubes and the proteins were digested with 5 µL trypsin in 240 µL of ABC solution + 5 µL acetonitrile (ACN). Proteins were digested overnight at 37°C on an orbital shaker set to 90 rpm. To each filter, 60 µL of 5% ACN/0.5% formic acid (FA) were added to quench the trypsin digestion followed by two minutes of vortexing. The tubes were centrifuged for 10 minutes at 14,100 x g. An additional 60 mL of 5% ACN/0.5% FA mixture was added to the filter and centrifuged. The effluents were then analyzed using LC-ESI-MS-MS.

2.4 LC-MS-MS analysis of tryptic peptides

The tryptic peptides were separated using a capillary Hypersil C18 column (300 Å, 5 µm, 0.1 mm i.d. × 100 mm) by using the Surveyor LC from ThermoFisher (San Jose, CA 95101). The elution was performed using a linear gradient from 98% A (0.1% FA in water) and 2% B (0.1% FA in ACN) to 60% B over 60 minutes at a flow rate of 200 µL/min, followed by 20 minutes of isocratic elution. The resolved peptides were electrosprayed into a linear ion trap mass spectrometer (LTQ-XL, Thermo Scientific, San Jose, CA 95101) at a flow rate of 0.8 µL/min. Product ion mass spectra were obtained in the data dependent acquisition mode that consisted of a survey scan over the m/z range of 400-2000, followed by seven scans on the most intense precursor ions activated for 30 ms by an excitation energy level of 35%. A dynamic exclusion was activated for 3 minutes after the first MS-MS spectrum acquisition for a given ion. Uninterpreted product ion mass spectra were searched against a microbial database with

2

TurboSEQUEST (Bioworks 3.1, Thermo Scientific, San Jose, CA 95101) followed by application of an in-house proteomic algorithm for bacterial identification.

2.5 Protein database and database search engine

A protein database was constructed in a FASTA format using the annotated bacterial proteome sequences derived from fully sequenced chromosomes of all available *E. coli* strains. There were 54 documented strains as of September 2012 with 13 EHEC, 7 EPEC, and 5 EAEC strains. A PERL program (http://www.activestate.com/ActivePerl; accessed September 2013) was written to download these sequences automatically from the National Institutes of Health National Center for Biotechnology (NCBI) site (http://www.ncbi.nlm.nih.gov; accessed September 2013). Of the two *E. coli* strains investigated, O104:H4 does not have its genome sequenced. Each database protein sequence was supplemented with information about a source organism and a genomic position of the respective open reading frame (ORF) embedded into a header line. The database of the *E. coli* bacterial proteome was constructed by translating putative protein-coding genes and consists of a few million amino acid sequences of potential tryptic peptides obtained by the in-silico digestion of all proteins (allowing up to two missed cleavages).

The experimental MS-MS spectral database of bacterial peptides was searched using the SEQUEST algorithm against a constructed proteome database of microorganisms. The SEQUEST thresholds for searching the product ion mass spectra of peptides were Xcorr, deltaCn, Sp, RSp, and deltaMpep. The top peptide hits generated by SEQUEST were filtered with a relative correlation score $\Delta Cn > 0.1$ and the filtered hits were accepted as peptide identifications when their correlation scores (Xcorr) were higher than the thresholds that allowed generating a desired false discovery rate (FDR) value.[9] The peptide validation was performed using the PeptideProphet algorithm[10] to provide probabilities score on the peptide assignment to the MS-MS spectra. Peptide sequences with a probability score of 95% and higher were retained in the dataset and used to generate a binary matrix of sequence-to-bacterium (STB) assignments. The binary matrix assignment was populated by matching the peptides with corresponding proteins in the database and assigning a score of 1. A score of 0 was assigned for a non-match. The column in the binary matrix represents the proteome of a given *E. coli* strain, and each row represents a tryptic peptide sequence from the LC-MS-MS analysis. A protein is identified as present when it is found in two or more of the three biological replicates that were analyzed for each *E. coli* strain. Analyzed samples were matched with the *E. coli* strains based on the number of unique peptides that remained after further filtering of degenerate peptides from the binary matrix. Verification of the classification and identification of candidate microorganisms was performed through hierarchical clustering analysis and taxonomic classification.

The in-house developed software ABOID™[11-12] transformed the results of searching the product ion mass spectra of peptide ions against a custom protein database, which was downloaded from NCBI with the commercial software SEQUEST into a taxonomically meaningful and easy to interpret output. It calculated probabilities that peptide sequence assignment to a product ion mass spectrum was correct and used accepted spectrum–to-sequence matches to generate an STB binary matrix of assignments. Validated peptide sequences, differentially present or absent in various strains (STB matrices), were visualized as assignment bitmaps and analyzed by ABOID™ that used phylogenetic relationships among *E. coli* strains as part of the decision tree process. The ABOID™ bacterial classification and identification algorithm uses assignments of organisms to taxonomic groups (phylogenetic classification) based on an organized scheme that begins at the phylum level and follows through classes, orders, families, and genus down to the strain level. ABOID™ was developed in-house using PERL, MATLAB, and Microsoft Visual Basic.

3. RESULTS AND DISCUSSION

3.1 Determination of common proteins using secretome lysates for EHEC and EAEC strains

EHEC and EAEC strains O157:H7 and O104:H4, respectively, were analyzed by MS proteomics to determine the proteins from their secretomes. Tables 1 and 2 list secretome proteins that were consistently obtained from three analyses of the O104:H4 and O157:H7 strains, respectively. These analyses originated from three separate agar plate cultures for each strain. The BLAST procedure was used for the peptides that identified the proteins in Tables 1 and 2, and it was determined that there was one protein match from one strain for the secretome proteins. Protein matching was performed using the uniprotKB database (http://www.uniprot.org/help/uniprotKB). The uniprotKB is a non-redundant database that includes all sequenced microbes and provides biological ontologies, classifications

3

and cross-references, cellular processes, and biochemical function for each protein. One or more peptides were used to identify a protein in the in-house database.[13,14] Further, one or more peptides were used to characterize one strain of *E. coli*. In Table 2, the first three of the four listed proteins have the highest hit/correlation with O157:H7 and two of the four proteins feature cellular functionality related to the flagellum filament. The dominant flagellar functions are often observed with EHEC bacteria as the responsible pathogenic factors.[6] This agreement between the genomics and proteomics studies showed that the MS-proteomics approach may be used as an effective complement to genomic-based techniques.

Table 1: *E. coli* O157:H7 Unique Secreted Proteins Identified using UniProt non-redundant protein database.

Accession #	Protein Name	Highest Hit	Process	Function	Component
AP_002538.1	Flagellar filament structural protein	EC O157:H7 / EC K12	Cilliary or flagellar motility	ND	Bacterial-type flagellum hook
AP_003849.1	DNA-binding transcriptional dual regulator	EC O157:H7	Binding	Transcription	ND
NP_288384.1	Flagellin	EC O157:H7	Cilliary or flagellar motility	Structural molecule activity	Bacterial-type flagellum filament
YP_001882351.1	Hypothetical protein SbBS512_E4084	*Shigella boydii* / EC NC101	ND	ND	ND

Table 2. *E. coli* O104:H4 Unique Secreted Proteins Identified using UniProt non-redundant protein database.

Accession #	Protein Name	Highest Hit	Process	Function	Component
YP_003223560.1	Secreted autotransporter serine protease	EC O103:H2	Proteolysis	Serine-type endopeptidase activity	Peptidase activity
YP_001463426.1	Multidrug efflux system subunit MdtA	EC O139:H28	Transport	Transporter activity	Plasma membrane
YP_002292692.1	Conserved hypothetical protein	EC SE11	ND	ND	ND
YP_003229309.1	Putative DNA primase	EC O26:H11	ND	ND	ND
YP_541664.1	DNA-binding protein	EC UTI89_C2667	Nitrogen utilization	DNA binding	ND
NP_286019.1	Hypothetical protein	EC O157:H7	Lipoprotein metabolic process	Lipase/hydrolase activities	Lipid particle

On the other hand, the data showed that the consistent proteins identified were strain-unique regardless of the database used. For example, utilization of the in-house database that includes only *E. coli* strains resulted in the same match as that found in the uniprotKB database which includes all sequenced bacteria. Figure 1 represents the output of the uniprotKB database analyses for the proteins identified in the secretome fraction of the O104:H4 strain of *E. coli*.
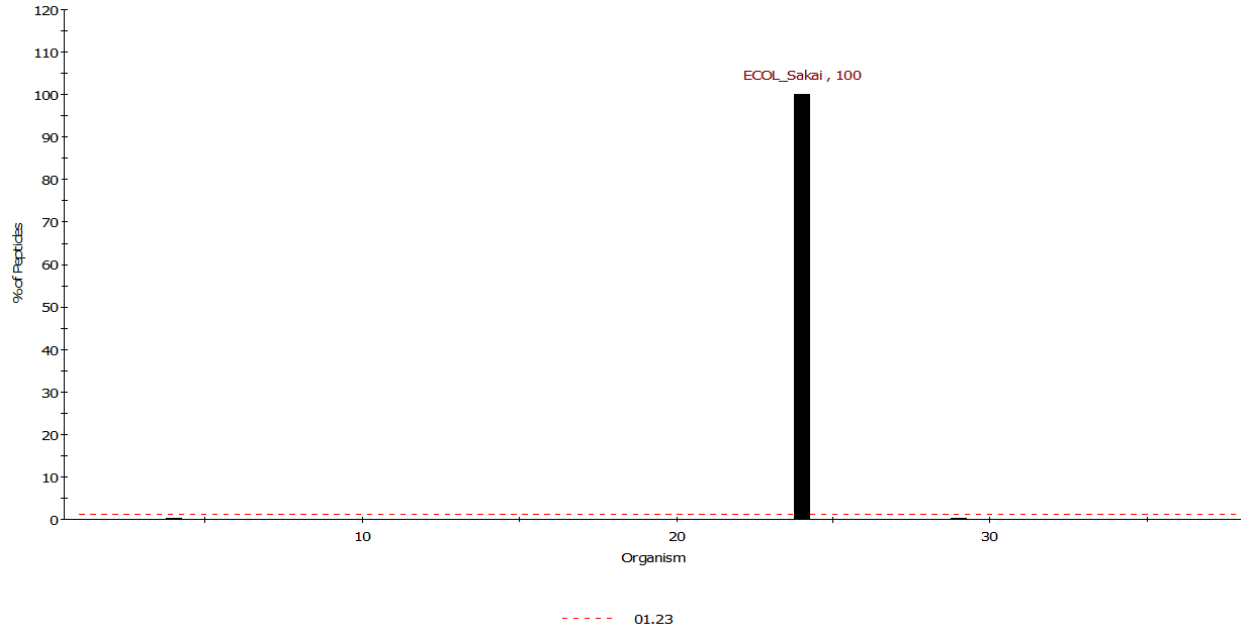

Figure 1. Histogram representing the output of the binary matrix of the unique peptides identified for *E. coli* O157:H7 from ABOID™. Peptides were extracted at a 95% confidence level.

The proteins were first identified using ABOID™, and then the uniprotKB database determined the non-redundant matching and cellular functions and processes. O104:H4 is not included in either database, because its genomic sequence has not been performed. The highest hit in Figure 1 (0103:H2) represents the closest match between the studied strain (O104:H4) and that of bacterial strains in the uniprotKB database. Most of the matches consist of EAEC and/or EAEC strains. Only one of the six matches was with the O157:H7 strain, indicating that O104:H4 is not closely related to EHEC strains. Also, the proteins consistently identified from replicate O104:H4 were diverse in cellular function compared to those of O157:H7. UniprotKB database examination of the cellular functions on the O104:H4 common proteins revealed the potential cellular functionality of the tryptic peptides. The uniprotKB cellular function tools utilize solid thick colored lines (see Figure 2) to represent the different cellular functions for each active site in a given protein. For example, the tryptic peptides that correspond to the identified secreted autotransporter serine protease were located in the region of the protein that constitutes the virulence function as shown in Figure 2. The dotted circle represents the region of the identified peptides for the serine protease for the secreted fraction of the O104:H4 strain.
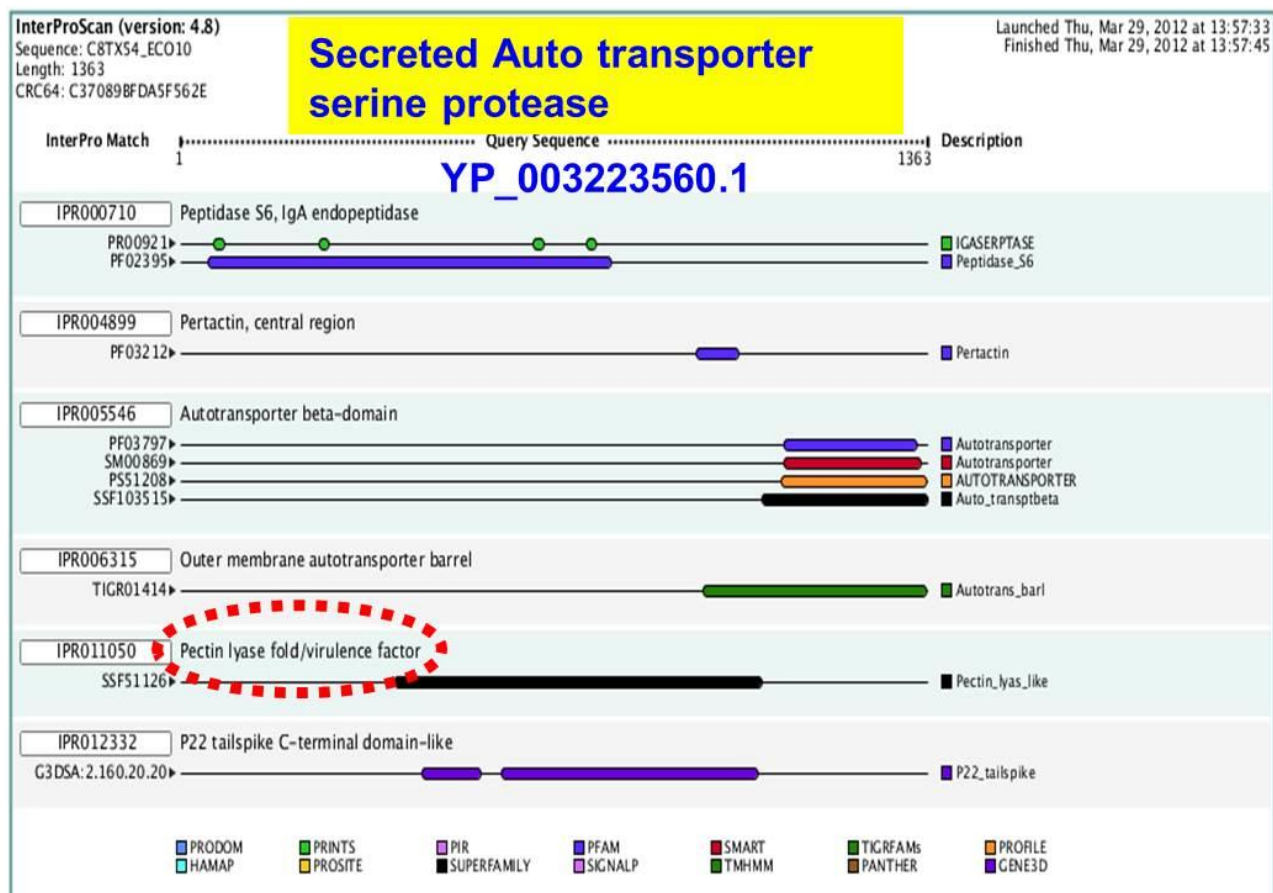
Figure 2. UniprotKB cellular functions identification tool, InterProScan, for the secreted, autotransporter serine protease consistently identified in the secreted fractions of *E. coli* O104:H4 replicate experiments. Dotted oval shape represents the cellular function of the peptides identified from LC-MS-MS analyses.

The relatively low number of genuine secretome proteins listed in Figures 1 and 2 are a portion of the 76 identified proteins in the supernatant medium. The majority of proteins were identified as intracellular vs. the few secreted proteins from the uniprotKB database. These intracellular proteins likely were in the supernatant milieu due to cell death such as from lyase autoproteolysis and cell lysis. Xia et al., 2008 however, list 83 extracellular proteins from two *E. coli* strains of which the majority are known to be of intracellular origin. The experimental method included the usual protein extraction, purification, and isolation procedures.[15]

3.2 Effect of cellular fraction on the differentiation of EHEC O157:H7

Whole cell and secreted fractions from O157:H7 were analyzed by LC-MS-MS followed by ABOID™ data processing. The samples were correctly established as the O157:H7 strain but with more ambiguity using the whole cell compared to the secreted fraction. A nearest neighbor analysis, using the Euclidean distance single linkage approach, showed 100% similarity (linkage distance) between the analyzed secretome (Figure 3a) and nearest neighbor in the database. There was approximately 92% similarity (8% dissimilarity) for O157:H7 between the whole cell fraction (Figure 3b) and database O157:H7.
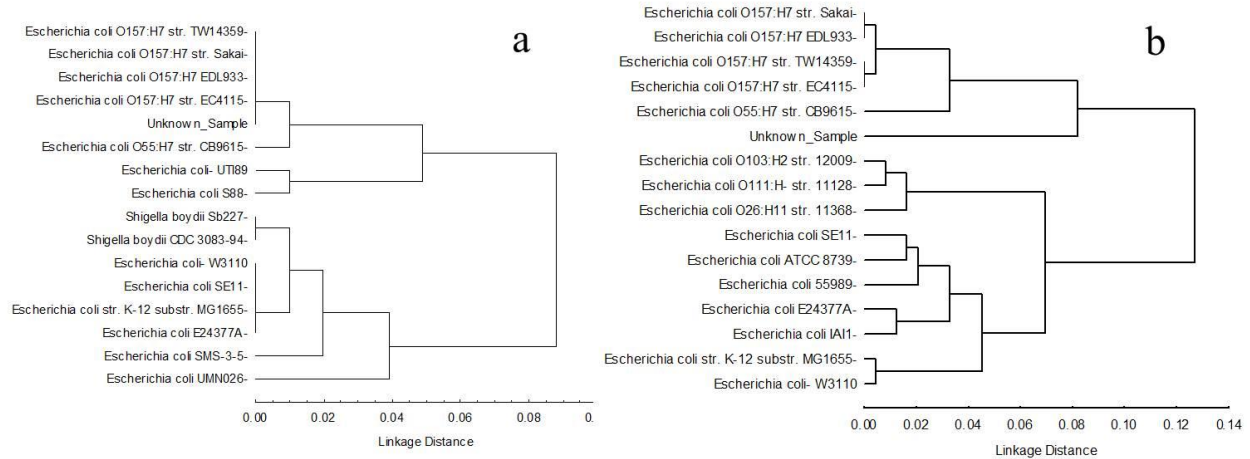
Figure 3. Euclidean distance single linkage dendrograms for the nearest neighbor classification of EHEC *E. coli* O157:H7 from the (a) secretome and (b) whole cell fractions.

This similarities and differences between whole cell and secretome fractions could be attributed to a number of factors. There is the possibility of more strain-unique proteins from the secretome fraction than that of the whole cell. Also, the sheer abundance of proteins in the whole cell extract may hinder the ability of the LC-ESI-MS-MS system to distinguish the strain-unique proteins compared to that from the significantly lower abundant secretome proteins. The proteins in the whole cell fraction constitute a large number of ribosomal proteins. Such types of proteins may result in less differentiation than that of the secretome proteins, which does not include ribosomal or other highly expressed and conserved proteins. This difference in types of proteins from the two fractions is reflected in the taxonomic classification as shown in Figure 3. Further, secretome analysis is a simple and relatively rapid experimental method that is capable of enhancing characterization information with respect to the whole cell protein extract procedure.

3.3 Effect of cellular fraction on the differentiation of EHEC/EAEC O104:H4

Whole cell and secretome protein fractions from *E. coli* O104:H4 were analyzed by MS proteomics and ABOID™. This *E. coli* strain does not have its genome sequenced; hence, it is not resident in a public repository. The characterization of the sample was correctly established. Nearest neighbor analysis, using the Euclidean distance single linkage approach, showed that the identified unique set of proteins had a closest match with the database *E. coli* 55989 for both secretome (Figure 4a, 97% similarity) and whole cell (Figure 4b, 98% similarity) fractions.
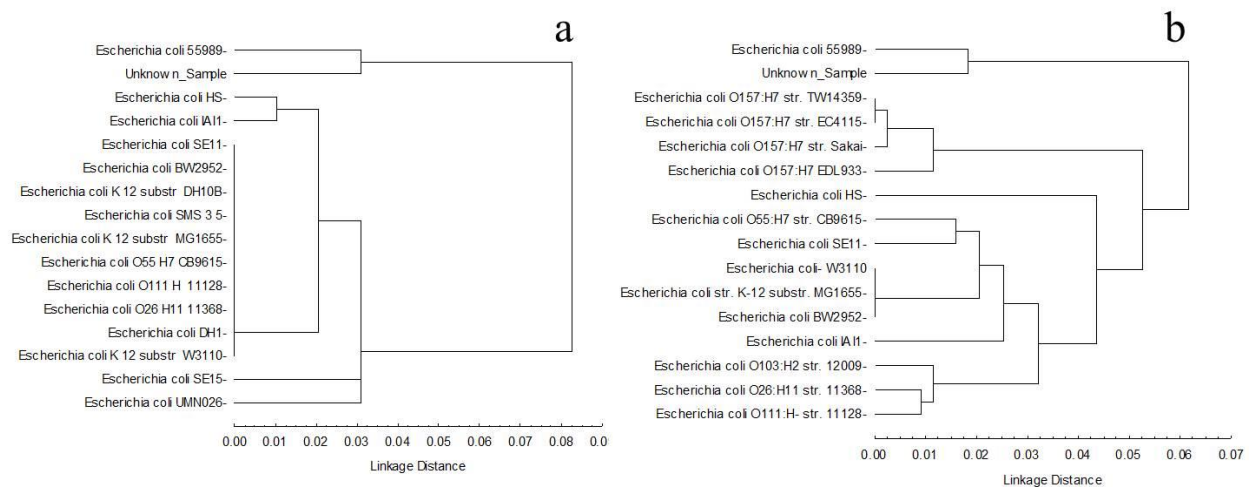

Figure 4. Euclidean distance single linkage dendrograms for the nearest neighbor classification of pathogenic *E. coli* O104:H4 from the (a) secretome and (b) whole cell fractions.

7

EAEC 55989 was originally isolated from the diarrheagenic stools of a human immunodeficiency virus (HIV)-positive adult suffering from persistent watery diarrhea in the Central African Republic in 2002. The EAEC strains form aggregates as their name suggests, and are an emerging cause of gastroenteritis (http://hamap.expasy.org/proteomes/ECO55.html). The proteomics LC-ESI-MS-MS classification of O104:H4 agrees with genomic sequencing of the *E. coli* that was the causative agent in the deadly outbreak in Germany in 2011.[16] The genomic sequencing of O104:H4 showed 93% genomic similarity[16] to EAEC 55989 and suggests that this strain is more of a hybrid clone between 55989 and ancestor O104:H4. This new strain from genomic classification showed to be distant from EHEC strains including O157:H7 which is a culprit in food contamination outbreaks.[5] The genomic studies (93% similarity) provide strong support for proteomic identification of the strains (97-98% similarity) and in the agreement of the phylogenetic classification for EAEC O104:H4.

The utilization of proteomics-based discrimination and phylogenetic classification of the *E. coli* strains from their secretome fractions showed that this approach is an effective and reliable complementary approach to whole genome sequencing and optical genetic mapping techniques. Moreover, a recent study on the pathogenicity mechanism of O104:H4 showed that this *E. coli* strain displays verotoxicity to host cells which is a characteristic of EAEC strains.[17] In addition, the *E. coli* O104:H4 whole cell protein extract analysis supports the utility of the secretome approach.

Although the proteomics classification showed strain level classification, each strain did not show close relation to the others. This observation is important to support the findings reported in genomic studies that those strains are different in their protein expression.[16,17]

3.4 Effect of growth phase on classification of *E coli* strain O111:H2

Figures 5a-c show the results obtained from the proteomic analysis of EPEC O111:H2 strain that was harvested in Luria Bertani (LB) at the lag, exponential, and stationary phases.
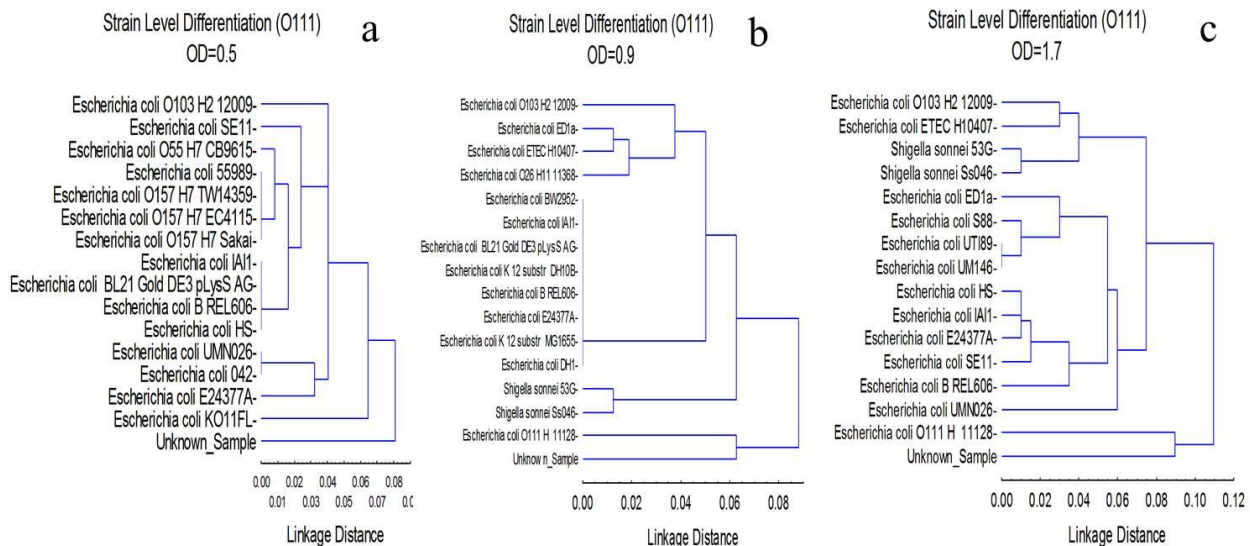
Figure 5. Effect of growth phase on the nearest neighbor classification of pathogenic *E. coli* O111:H2 from the (a) lag phase, (b) exponential phase, and (c) stationary phase.

The taxonomic classification showed a species level identification obtained at the early growth phase, as shown in Figure 5a. The search database consisted of all sequenced *E. coli*, *Salmonella*, *Shigella* spps. Figure 5b-c show the taxonomic classification at the exponential and stationary phases. In these figures, the classification of the sample matches with more than 92% similarity with O111:H2. This is noteworthy, given that identifying pathogenic bacteria in real world samples at an early infectious stage is desired for diagnostic purposes and providing effective countermeasures at an early stage of infection. The results also showed that there were 21 common proteins identified in all growth phase and the number of identified proteins reach maximum level at the exponential growth phase (i.e., 63, 112, and 97 proteins in lag, exponential, and stationary phases respectively).

4. CONCLUSIONS

The utility of secretome proteins as biomarkers for characterization of EHEC, EPEC, and EAEC *E. coli* strains is useful, practical, and uses few and efficient experimental procedures. Differentiation among EHEC, EPEC, and EAEC strains was improved using secreted proteins as differentiation biomarkers. In addition, very few experimental procedures were necessary to capture and detect secreted biomarker proteins. The secretome, thus, provides a unique source of cellular variability that was not observed when compared to whole cell lysates. The genomic studies on the studied strains showed agreement in the MS proteomics-based classification of the non-database O104:H4 strain (i.e., determined using the MS-based proteomics approach). Such agreement, however, must be further examined through a larger set of *E. coli* strains and under various environmental conditions to verify the effectiveness of the utilized approach. In addition, such studies, once validated, could increase the confidence in identifying microbes to the strain level at early stages of outbreaks using protein biomarkers to enhance medical countermeasures and diagnostics.

MS-MS-based proteomics and bioinformatics were shown to have utility in the comparative proteomics study for the differentiation of EHEC and EPEC strains. This resulted in different degrees of separation between the correctly determined database organism and the next nearest neighbor organism(s). Classification and identification of an organism that is not in the genome database and not using a genome sequencing technique is possible as with the case of O104:H4 and O111:H2 strains. Such properties will allow the utilization of this MS-based proteomics approach to infer taxonomic classification based on the depth of available genomic sequencing information. The secretome MS-proteomics approach has the potential to characterize emerging and unknown microbes and aid in genomic sequencing analyses.

REFERENCES

[1] Demirev, P.A., Feldman, A.B, Lin, J.S., "Chemical and biological weapons: current concepts for future defenses". *Johns Hopkins APL Tech. Digest* 26, p321-333, **2005a**.

[2] Demirev, P.A. and Fenselau, C., *Annual Review of Analytical Chemistry,* **2008**, 1, p71-93.

[3] European Food Safety Authority (EFSA) Joint EFSA/ECDC technical report. **2011**, Available: http://www.efsa.europa.eu/en/supporting/pub/166e.htm.

[4] Perna, N.T., et al. *Nature*, **2001**, 409, p529–533.

[5] Mellmann, A., et al. *PLoS One*, **2011**, 6(7): e22751. doi:10.1371/journal.pone.0022751.

[6] Frankel, G., et al. *Molecular Microbiology,* **1998**, 30, p911-921.

[7] Deng, W., et al. *Molecular and Cellular Proteomics*, **2012**, 11, p692-709.

[8] Jabbour, R.E., et al., *Applied Environmental Microbiology,* **2010**, 76, pp3637-3644.

[9] Peng. J., et al. *Journal of Proteome Research*, **2003**, 2, p43–50.

[10] Keller, A., et al. *Analytical Chemistry,* **2002**, 74, p5383-5392.

[11] Jabbour, R.E., et al. *Journal Proteome Research,* **2010,** 9, p3647-3655.

[12] Deshpande, S.V., et al. *Journal of Chromatography and Separation Techniques*, **2011**, S5:001. DOI:10.4172/2157-7064.

[13] Wang, N., et al. *Analytical Chemistry,* **2010**, 82, p2262-2272.

[14] Dworzanski, J.P., et al. *Journal of Proteome Research*, **2006**, 5, p76-87.

[15] Xia, X.X., et al. *Proteomics*, **2008**, 10, p2089-2013.

[16] Kupferschmidt, K., *Science*, **2011**, 332 (6035) p1249-1250.

[17] Al Safadi, R. et al. *PLoS One*, **2012**, 7(7):e41628. doi: 10.1371/journal.pone.0041628 .

Microbial wargaming: Modeling the contributions to fitness of bacteria encoding deployable genetic weaponry

Aleksandr Miklos[a,b], Matt Lux[a], Vanessa Funk[a], Steven Yee[a,c], and Henry S. Gibbons[a]

[a]U.S. Army Edgewood Chemical Biological Center, Research and Technology Directorate,
5183 Blackhawk Rd, Aberdeen Proving Ground, MD 21010
[b]Excet Inc., 8001 Braddock Road, Suite 303, Springfield, VA 22151
[c]Defense Threat Reduction Agency, Ft. Belvoir, VA

ABSTRACT

Basic biological research seeks to understand the workings of observable biological phenomena and to recapitulate those phenomena under controlled conditions in which variables can be individually tested to understand the underlying rules of behavior. While this reductionist, experimentally driven approach can easily be applied to single organisms, the application of such approaches to complex behaviors of social organisms, such as warfare or terrorism in human societies, is not possible. Recent advancements in synthetic biology tools have enabled the modeling of simple *in vitro* systems of complex community dynamics. Here, we develop a simple *in vitro* model system for inter-community warfare using bacterial strains equipped with antibacterial colicin and/or phage weapons and test carriage, to determine how weapons deployment affects strain fitness in model ecosystems. The use of the concepts of synthetic biology, namely the treatment of genes, promoters, and regulatory systems as interchangeable parts, will facilitate the construction of defined strains containing cryptic weapons systems that can be developed and employed with a range of experimentally tunable frequencies of development or deployment. We will therefore be able to test a defined hypotheses regarding the emergence of warfare in a simple and infinitely permutable model system.

Keywords: colicin, competition, evolution, synthetic biology, niche maintenance, competitive exclusion

1. BACKGROUND

To date, it has not been possible to test in a controlled manner what factors lead to the evolution of intraspecies aggression, nor have the effects of such abilities on the development or maintenance of communities been thoroughly explored. We propose a novel approach to studying the emergence of warfare in large populations – a petri-plate based wargaming system in which opposing bacterial communities are equipped with weapons existing in either a fully evolved state or in a cryptic, resting state awaiting development or deployment. Using this simple modeling system with defined and interchangeable genetic components, we hope to quantify the contribution to fitness of bacterial communities of model weapon systems.

1.1 Bacteria as models of social behavior

Recent research has revealed that bacteria, despite their relatively simple unicellular structure and small size, engage in a number of striking collective behaviors, including altruism, cooperation, restricted growth, and self-policing.[1-4] While bacterial communities can be observed to follow paths in which the whole community benefits from the actions of its individual parts, this is not always the case for individual bacterial cells. Bacteria have been observed to cheat[5-7], that is to exploit the activity of the community without contributing to a common good; pollute[7], and other individual deviant behavior. Likewise, cooperative communities have been shown to evolve strategies to suppress cheater populations.[8] Together, these represent both collective survival strategies combined with bet-hedging strategies on the level that, in spite of the divergent and antisocial behavior of a small minority, benefits the species by insuring maximal likelihood of survival, should growth conditions rapidly become unfavorable.

1.2 Bacterial communities employ offensive weaponry and defensive measures to take and hold territory

Bacteria have been engaging in competitive behaviors for billions of years, and have evolved highly diversified strategies to achieve superiority within a niche relative to their interspecies and intraspecies rivals. These include strategies that are analogous to human wartime behaviors and include offensive, defensive, counteroffensive,

APPROVED FOR PUBLIC RELEASE

intelligence, and counterintelligence strategies. Offensive strategies include the synthesis of antibacterial compounds (antibiotics, bacteriocins); defensive measures include modifications to cell walls and the acquisition of resistance cassettes or degradative enzymes; intelligence strategies include utilizing quorum-sensing signals from opposing communities to "read the enemy's mail," and so forth. The diversity of methods employed in the microbial world suggests that these simple organisms might serve as model systems for complex social human behaviors such as warfare (Table 1). Bacteriocins in particular have been shown to play roles in competitive exclusion ("taking and holding territory") against invading strains.[9]

1.3 A body of knowledge is readily exploitable to develop synthetic model systems

The signals driving communal behaviors are becoming better understood and are being employed as interchangeable tools for engineering complex social behaviors among microbial communities.[10,11] Communal behavior is driven by quorum-sensing mechanisms, which rely on secreted diffusible small molecules to monitor bacterial population density. Offensive weapons are often driven by population density, proximity (antibiotics can themselves be considered quorum sensing molecules), or contact with the enemy[9], while defensive measures can be pre-emptive (regulated based on the ambient environmental conditions rather than direct encounter), triggered by encounter with an enemy's offensive weapons, or both.[12] The effector molecules and regulatory systems are well-characterized and can serve as model systems to study the deployment of tactical and strategic weaponry including weapons of mass destruction by individuals or states (Table 1). Interestingly, as with defense budgets for human societies, deployment of colicins and defensive measures incurs a significant energetic cost that must be carefully balanced with the evolutionary gains, lest it become a fitness disadvantage.[13]

Table 1. Bacterial components as models for human weapons classes.

Class	Characteristics	Weapon	Model system	Costs to produce	Defense	Costs to defend
Strategic	Transmissible; mass casualty	Plague; smallpox	Cryptic lytic bacteriophage	Metabolic burden; host cell lysis	Target modification	Nutrient loss due to target function changes
Tactical	Non-contagious; diffusible	Anthrax; chemicals; artillery	**Bacteriocins (e.g., colicins); antibiotics**	Metabolic costs of production; efflux	Outer membrane modification; target modification; degradation; immunity	Decreased permeability to nutrients; efflux effort
Individual	Single-victim; contact	Ricin	Contact-dependent inhibition toxins[14]		Target modification	Nutrient loss due to target function changes

Colicin protein toxins offer ideal platforms for the development of simple *in vitro* competition systems for Gram-negative bacteria. Broadly, colicins belong to a wide family of bacteriocidal proteins that are produced and secreted by bacteria. Cidal activities of bacteriocins can either exhibit broad or narrow host ranges depending on the nature of the toxin and can even suppress the growth of competitive eukaryota. Specifically, colicins are secreted by Enterobacteriaceae, notably *Escherichia coli* for which they are named. Most wild-type isolates of *E. coli* and almost all pathogenic *E. coli* strains encode at least one colicin module, suggesting prominent roles for these genetic elements in establishing and maintaining the presence of a given strain within an ecological niche.

In general, colicins target a specific protein localized in the outer membrane that facilitates entry and uptake into the host cell by means of one or more adenosine triphosphate (ATP) binding cassette (ABC) transporters. Colicins are generally internalized by this process and then exhibit a toxic behavior toward the target strain.[15] Different colicins have different enzymatic or inhibitory functions, such as nuclease activity, the ability to depolarize membranes, or inhibit peptidoglycan synthesis. Colicins are typically encoded as three-gene modules containing the colicin itself, an immunity protein, and a lysis protein. The immunity protein protects the host strain from the effects of the colicin, while the lysis protein functions to break open expressing cells to discharge the colicin payload into the environment (Figure 1).
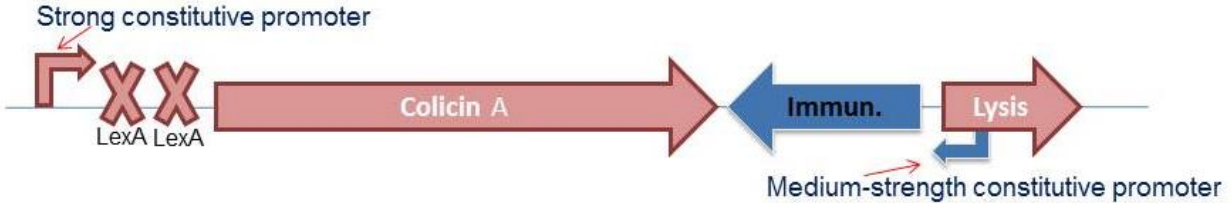
Figure 1. Colicin A locus showing colicin A, immunity, and lysis protein genes, LexA repressor binding sites, and promoters. The colicin itself is the toxic secreted product, the immunity protein protects the host population, while the lysis protein causes a subpopulation of the host strain to lyse, liberating the colicin proteins into the culture medium.

2. METHODS

2.1 Bacterial strains

E. coli W3110 (ATCC 27325), *E. coli* (ATCC 14763), *Pseudomonas aeruginosa* (ATCC 25360), and *P. aeruginosa* (ATCC 25360) were acquired from American Type Culture Collection (Manassas, VA). Colicin-producing or -susceptible *E. coli* strains BZB 1011, BZB 1030, BZB 1191, BZB 2101, BZB 2102, BZB 2103, BZB 2104, BZB 2125, BZB 2149, PAP 308, and PAP 702 (Table 2) were obtained from Institut Pasteur (Paris, France).

Table 2. Colicin-producing strains utilized in this study.

CIP idx	Strain	PRODUCES	RESISTS	Mechanism	Receptor	Translocation
105643	BZB2101	colA	colA	Pore Forming	BtuB	OmpF/TolQRAB
105642	BZB2102	colB	colB	Pore Forming	FepA	?/TonB, ExbBD
105641	BZB2103	colD	colD	tRNase	FepA	?/TonB, ExbBD
105640	BZB2104	colE1	colE1	Pore Forming	BtuB	OmpF/TolQRAB
105644	BZB2125	colE2	colE2	DNase	BtuB	OmpF/TolQRAB
105646	BZB2149	colE3	colE3	16s rRNase	BtuB	OmpF/TolQRAB
105664	BZB1011	--	--			
105637	BZB1191	--	--			
105665	BZB1030	--	(A),(E1),E2,E3			
105669	PAP308	--	A,E2-8 tol.			
105671	PAP702	--	--			

2.2 Strain fitness assay

Luria-Bertani (LB) Broth (Sigma-Aldrich, St. Louis, MO) and Tryptic Soy (TS) Broth (EMD Chemicals, Inc., Gibbstown, NJ) were prepared according to manufacturer's instructions. Non-swarming agar plates were prepared using either 1.5% bacto-agar (Sigma-Aldrich) in LB or TS broth. Swarming agar plates were prepared using 0.75% or 0.5% bacto agar, or 0.5% Eiken agar (Eiken Chemical Co., Ltd., Tokyo, Japan) in either LB or TS broth. Cultures were grown overnight from glycerol stocks in either LB or TS broth at 37°C with shaking at 180 rpm (Innova 4200 Incubator Shaker; New Brunswick Scientific, Edison, NJ). Inocula were normalized to an optical density measured at 600 nm (OD_{600}) < 0.1 (Spectronic 21 Spectrophotometer; Milton Roy Company, Ivyland, PA) and plated on (swarming or non-swarming) agar plates using a sterile toothpick in a head-to-head competition style of some combination of pyocin-susceptible or pyocin-producer *P. aeruginosa* and/or colicin-susceptible or colicin-producer *E. coli*. These competition-style plates were quartered with the upper quadrants reserved for controls and the bottom quadrants reserved for a single inocula susceptible or producer strain surrounded by three inoculums of susceptible or producer strains. Plates were incubated at 37°C in a humidified Innova 4200 for up to 21 days. Colony growth photographs were taken at various times using a Colony Q Count Automatic Colony Counter with Color Count (version 2.3) software (Spiral Biotech, Inc., Norwood, MA). Alternatively, time-lapse images were collated from plates incubated at 37°C in an Innova 4330 (New Brunswick Scientific, Edison, NJ) and scanned hourly using an Epson Perfection V600 Photo Scanner (Seiko Epson; Longbeach, CA) with Rap-ID Software (Specific Technologies).

We began development of a simple *in vitro* competition assay using a number of colicin-expressing strains obtained from the Institut Pasteur (Table 2). These strains, initially described by Pugsley and co-workers[16] express a variety of colicins and are resistant to a number of colicins produced by other strains within the collection, making these an ideal set of initial tester strains for the development of simple competition scenarios.

2.3 *In vitro* competition assay

We inoculated 0.5% agar plates with spot cultures of each strain using a toothpick or inoculation loop such that a single colony of a "target" strain would be surrounded by three colonies of the producer strain.

3. RESULTS

To demonstrate that we could visualize colicin-mediated growth inhibition, we developed a simple growth assay on low-concentration agar plates that allow greater strain mobility on the plate surface. Colicin strains were plated in a spatial scheme noted in Figure 2. In this assay system, colicin-mediated growth inhibition manifests as the formation of smaller colonies at the centers of the triangular arrangements or as distorted colony shapes in the colonies at the apices.
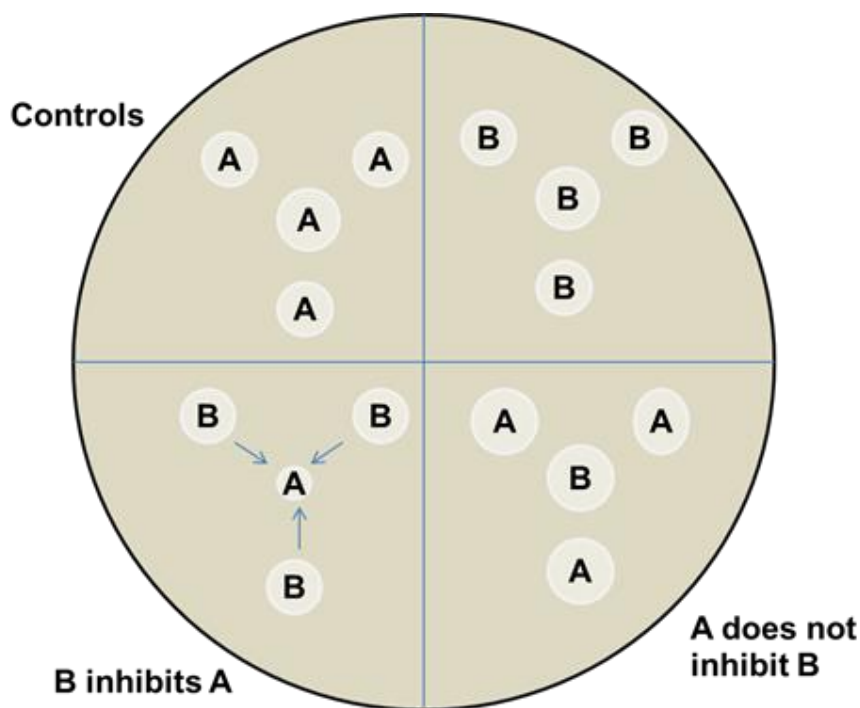

Figure 2. Colicin plate inhibition assay. Two strains A and B are plated in arrangements to allow the comparison of colony size. Growth inhibition manifests as a decrease in size of the central colony in one or both of the lower quadrants, relative to the same strain in the upper quadrants. The top quadrants represent controls to insure that colony size difference of the middle colony is not due to autoinhibition.

Differences in colony sizes were evident depending on the colicin status of strains. We demonstrated growth inhibition by producing strains (Figure 3). In particular, a ColA producing strain BZB2101 dramatically inhibited a ColB producing strain (BZB2102). However, the base strain phenotypes were inconsistent across the panel of producing strains. Notably, strain motility on the soft agar medium ranged significantly and confounded the interpretation of the initial results. The plasmids encoding the colicins in these strains are derived from wild strains[16], are poorly characterized, and likely encode elements that contribute to the diversity of phenotypes we observed in the initial studies of producing strains. In addition, while the strain backgrounds of each of these constructs is thought to be W3110, it is not clear how storage or passage at other institutions might have affected the phenotypes of the base strain. Together, these results highlighted the need to employ defined genetic backgrounds with identical genetic makeup.
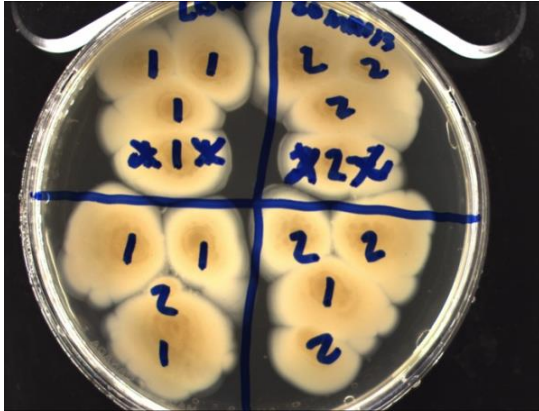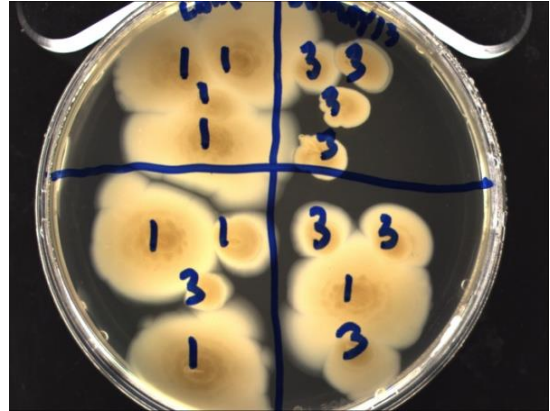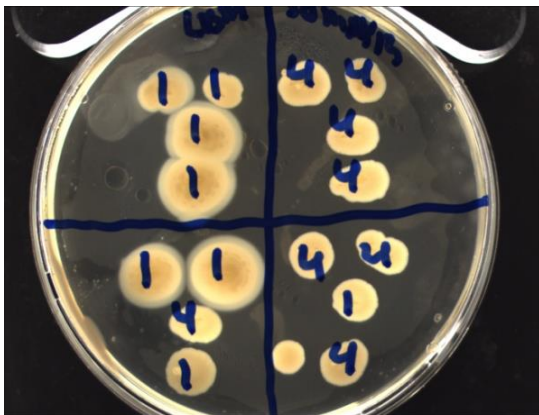
Figure 3. Inhibition of growth by colicin-producing strains.

3.1 Establishment of a quantitative plate competition evaluation method

To provide a more quantitative assessment of growth rates on plates, we developed a custom image processing algorithm to convert our sequence of images into quantitative measures of area over time for each colony. First, we determined a region of the image that contains the agar medium where colonies can grow. The first image in the series, where no colonies are present, was processed to identify this region (Figure 4a). The plate edge is bright is used to locate this region (Figure 4b). A series of erosions were performed to eliminate noise in the region of interest (Figure 4c), the corners filled, and dilations performed to buffer the edge. The result was a mask for the region of interest that can be used for subsequent images (Figure 4d). The analysis of all later time points bagan by applying this mask (Figure 4e-f). Next, automatic thresholding (Figure 4g) and a series of erosions and dilations were performed to recover colony outlines (Figure 4h).
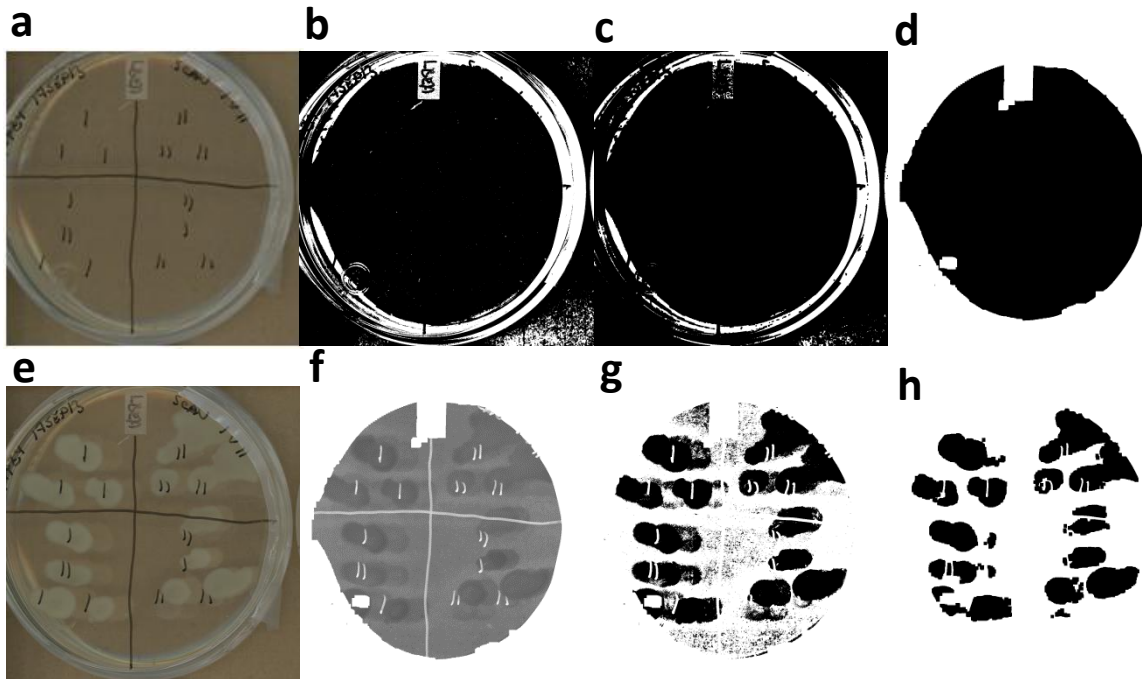
Figure 4. Image processing procedure. The first plate image, with no colonies (a), is used to create a mask for the region of potential colony growth by identifying edges (b), eroding away noise (c), and filling in corners and dilating for buffering purposes (d). Subsequent images, such as (e), are processed by applying the previously calculated mask (f),automatic thresholding (g), and eroding and dilating to clear up noise (h). The resulting image is analyzed to determine the area of each colony.

Each distinct colony was identified, and the area and center coordinates were recorded. This process was repeated for all images in a time series, and by grouping identified colonies with similar coordinates across time points, the area over time of each colony was extracted (Figure 5).
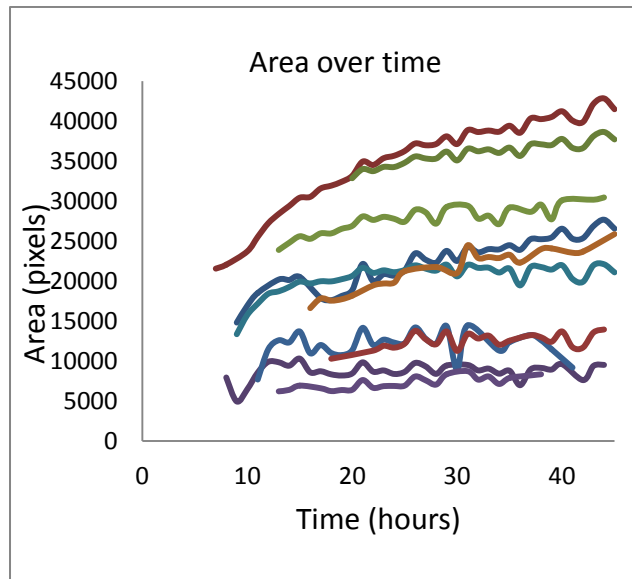
Figure 5. Demonstrating quantitation of colony growth over time. Plate images were compiled and processed to generate colony areas, which were plotted as a function of time. Several representative colonies of different sizes are shown.

4. CONCLUSIONS AND FUTURE WORK

We developed a simple readout for colicin-mediated growth inhibition based on the effects of the presence of colicin production on the area of adjacent colonies. While growth inhibition between strains could occasionally be seen, the inconsistency in the background strains made interpretation of the inhibition data impossible. We conclude from the preliminary data that a synthetic approach to generate truly isogenic strains (without confounding genes and potential regulatory elements introduced by the heterogeneous plasmid backbones) is necessary to evaluate the relative efficacy of the colicin operons. However, the heterogeneous colony growth phenotypes allowed us to develop a robust technique for measuring the growth of colonies over time by using computerized image processing. We will employ the latter in combination with the generation of synthetic colicin producing constructs in the upcoming project period.

During the next year of this effort, we will begin the design and construction of synthetic colicin constructs, beginning with a series of constructs that will allow the monitoring of colicin operon expression using a fluorescent protein reporter (Figure 6). These operons will encode the colicin functions along with reporters for expression and will be placed under the control of a tetracycline-inducible promoter to allow for titration of expression levels. Addition of low levels of anhydrotetracycline to the medium will induce the colicin operons and prevent the non-specific expression of the colicins typically observed.
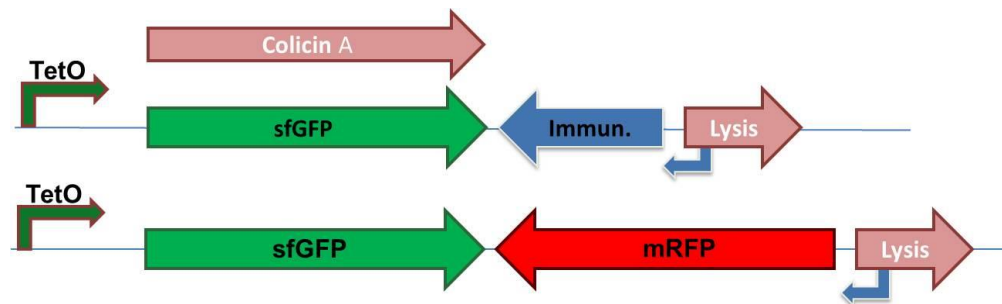
Figure 6. Synthetic colicin-like operons containing fluorescent reporters.

REFERENCES

[1] Wintermute, E.H. and Silver, P.A., *Molecular Systems Biology*, **2010**, 6(407).
[2] Hosoda, K. et al., *PLoS One*, **2011**, 6(2).
[3] Tan, C., Marguet, P., and You, L.C., *Nature Chemical Biology*, **2009**, 5(11), p842-848.
[4] Xavier, J.B., *Molecular Systems Biology*, **2011**, 7(483).
[5] Fiegna, F. and Velicer, G.J., *Proceedings of the Royal Society B:Biological Sciences,* **2003**, 270(1523), p1527-1534.
[6] Sandoz, K.M., Mitzimberg, S.M., and Schuster, M., *Proceedings of the National Academy of Sciences USA*, **2007**, 104(40), p15876-15881.
[7] Maharjan, R.P., Seeto, S., and Ferenci, T., *Journal of Bacteriology*, **2007**, 189(6), p2350-2358.
[8] Manhes, P. and Velicer, G.J., *Proceedings of the National Academy of Sciences, USA*, **2011**, 108(20), p8357-8362.
[9] Majeed, H. et al., *ISME Journal*, **2011**, 5(1), pp71-81.
[10] Li, C.H., Wang, E., and Wang, J., *PLoS One*, **2011**, 6(3), e17888:1-9.
[11] Prindle, A. et al., *Nature*, **2012**, 481(7379), p39-44.
[12] Prost, L.R. and Miller, S.I. *Cell Microbiology*, **2008**, 10(3), p576-582.
[13] Chao, L. and Levin, B.R., *Proceedings of the National Academy of Sciences USA*, **1981**, 78(10), p6324-6328 .
[14] Aoki, S.K. et al., *Science*, **2005**, 309(5738), p1245-1248.
[15] Cascales, E. et al., *Microbiology and Molecular Biology Reviews*, **2007**, 71(1), p158-229.
[16] Pugsley, A.P., *Journal of General Microbiology*, **1985**, 131(2), p369-376.

Role of acetylcholinesterase in the regulation of mesenchymal stem cell proliferation and differentiation

Amber M. Prugh[a], James D. Wright[a], Daniel J. Angelini[b]

[a]U.S. Army Edgewood Chemical Biological Center, Research and Technology Directorate,
5183 Blackhawk Rd, Aberdeen Proving Ground, MD 21010
[b]Excet, Inc., 8001 Braddock Road, Suite 303, Springfield, VA, USA 22151

ABSTRACT

Mesenchymal stem cells (MSC) are multipotent cells located in various adult tissues including bone marrow. These cells play a significant role in tissue maintenance and repair. Recently, it has been reported that bone marrow-derived MSCs express active acetylcholinesterase (AChE) and that disruption of this activity by organophosphate (OP) chemicals affects the ability of MSCs to differentiate into osteoblasts. It is currently unknown what role AChE plays in MSCs proliferation and differentiation. In this study, we tested the hypothesis that OPs affect AChE activity in MSCs and this modification reduces the proliferation and/or differentiation potential of these cells. We established MSC toxicity profiles of the organophosphate chemicals parathion and paraoxon. Also, we determined the optimal parathion/paraoxon doses for AChE inhibition. Once the optimal doses were established, we determined if parathion/paraoxon affected MSC proliferation and MSC differentiation into osteoblasts, adipocytes, chondrocytes, and neurons. Finally, to prove a role for AChE in these processes, we will knockdown AChE expression through the introduction of AChE-directed small interfering (si)RNAs. Understanding the pathways associated with MSC proliferation and differentiation could lead to the development of future MSC-based tissue repair therapies.

Keywords: acetylcholinesterase, differentiation, mesenchymal stem cells, organophosphates, paraoxon, parathion, tissue repair, siRNA

1. INTRODUCTION

Mesenchymal stem cells (MSC) can be isolated from various adult tissues and play a significant role in tissue maintenance and repair. *In vitro*, these cells are capable of self-renewal, and under the appropriate culture conditions, can be differentiated into bone, cartilage, and fat.[1,2] More recent studies have demonstrated that MSCs are capable of differentiating into other cell types such as alveolar epithelium, hepatocytes, myocytes, and neurons.[2] The mechanisms of MSC differentiation are poorly understood, but recent studies have demonstrated that MSCs derived from bone marrow express acetylcholinesterase (AChE)[3,4] and AChE activity levels affect their ability to differentiate into osteoblasts.[4] Given that OPs block AChE activity, it is possible that OPs could affect the ability of MSCs to differentiate and/or proliferate. This is significant to the Army's mission because service members in the field are exposed to or could be potentially exposed to a host of toxic chemicals, including OPs. Exposure to these chemicals could affect MSCs ability to proliferate and/or differentiate, therefore, reducing the ability to recover from injuries sustained during assignments. Also, tissue repair is essential to the long-term health of individuals exposed to chemical warfare agents (CWA). We hypothesize that OPs affect AChE activity in MSCs, reducing the proliferation and/or differentiation potential of these cells. Our long-term objective is to determine the signaling pathways associated with MSC proliferation and differentiation and how these pathways relate to MSC-mediated tissue repair.

2. BACKGROUND AND SIGNIFICANCE

2.1 Mesenchymal stem cells

MSCs, also known as marrow stromal cells, were initially described in 1968 by Friedenstein and colleagues.[5] In their studies, MSCs were isolated from bone marrow due to their characteristic ability to attach to tissue culture

flasks. Once attached, these cells displayed a fibroblast-like morphology. Since their initial discovery in bone marrow, MSCs have been isolated from several other tissues including umbilical cord, Wharton's jelly of the umbilical cord, placenta, adipose tissue, dental pulp, as well as from the lungs of lung transplant patients.[2] MSCs are capable of self-renewal and can be maintained in a multipotent state *in vitro*.[6] Since no single marker is available to identify MSCs, the International Society for Cell Therapy has published a consensus statement regarding identification requirements.[1] According to this definition, MSCs must display the following properties: 1) adherence to plastic under routine cell culture conditions; 2) expression of the cellular markers CD73, CD90, and CD105; 3) lack of expression of CD11b, CD14, CD19, CD34, CD45, CD79a, and human leukocyte antigen (HLA); and 4) the capacity for *in vitro* differentiation into osteoblasts, adipocytes, and chondroblasts.[1]

2.2 MSC proliferation pathways

It has been reported that MSC growth occurs in three distinct phases; these phases include a lag phase (three to five days in culture), a rapid proliferation phase, and a stationary phase.[2] It has been demonstrated that the Wnt signaling cascade plays a critical role in this process and it is likely that there are many other signaling pathways are associated with MSC proliferation yet to be identified; it is possible that AChE may play a role in this process.

2.3 Current understanding of MSC differentiation

Even though MSCs have been traditionally thought of as multipotent progenitors for bone, cartilage, and adipose tissue, recent investigations have revealed that MSCs have the ability to differentiate into other cell types including astrocytes, neurons, alveolar epithelial cells, and hepatocytes.[2] Currently, only a few genes have been identified that play critical roles in MSC differentiation. These genes include, but are not limited to Wnt, Runt-related transcription factor 2 (Runx2), transforming growth factor-β (TGFβ), peroxisome proliferator-activated receptor γ (PPARγ), osterix, and brain-derived neurotrophic factor (BDNF).[2] For example, Runx2 acts as a master gene for the regulation of osteogenic differentiation. Up-regulation of this gene product promotes both osteogenic and chondrogenic differentiation, while inhibiting adipogenic differentiation.[2] Even though AChE has been shown to be expressed in MSCs, the exact role it plays in MSC differentiation is currently unknown.

3. MATERIALS AND METHODS

3.1 Human MSC culture

Primary human bone marrow-derived MSCs were obtained from Lonza (Walkersville, MD) and cultured in Mesenchymal Stem Cell Growth Medium (MSCGM) supplemented with Mesenchymal Stem Cell Growth Supplement (MSCGS), L-glutamine, gentamicin, and amphotericin-B (all supplements from Lonza) as described.[7,8] Only MSCs from *passages* 4-8 will be examined for the proposed studies.

3.2 Preparation of the organophosphate chemicals

We used the organophosphate pesticide parathion as well as its metabolite, paraoxon, in this study. These chemicals were purchased from Sigma-Aldrich (St. Louis, MO) and stock solutions were prepared in 100% ethanol (EtOH) and stored at 4°C.

3.3 MSC toxicity studies

For the proposed toxicity studies, we plated 1×10^4 MSCs in the wells of 96-well tissue culture plates and then allowed the cells to attach for 24 hours. Once the cells had sufficiently attached, we exposed the MSCs to increasing concentrations (1, 10, 30, 100, 300, 1000, 3000, 10000 μM) of parathion, paraoxon, or equivalent volumes of vehicle control (EtOH) for 24 or 48 hours. We used the MTT assay (Roche Applied Sciences; Indianapolis, IN) to evaluate the toxicity of these agents.

3.4 MSC proliferation studies

MSC proliferation was determined by the BrdU Cell Proliferation Assay (Roche Applied Science). Briefly, MSCs were plated at a density of 5×10^3 cells per well in 96-well plates and then allowed to attach for 24 hours. The MSCs were then exposed to parathion, paraoxon, or equivalent volumes of vehicle controls (EtOH) for 48 hours. At the end of the exposure, BrdU was added to the cells and incubated for an additional 4 h. The culture media was then removed and the cells were fixed and washed. A peroxidase-labeled anti-BrdU antibody was added and developed. The plate was then read on a scanning multiwall spectrophotometer and the absorbance values recorded.

3.5 Determination of AChE expression in MSC

Expression levels of AChE in MSCs were determined and quantified through Western blot analysis. Confluent MSCs were exposed to parathion (30 or 100 µM), paraoxon (30 or 100 µM), or equivalent amounts of vehicle control (EtOH) for 24 hours. The MSCs were then lysed and collected in 1X RIPA buffer (Cell Signaling Technology, Inc.; Danvers, MA), centrifuged, and the supernatants assayed for protein concentration with the Pierce 660 nm Protein Assay (Thermo Fisher Scientific; Rockford, IL). The samples were resolved using the 4-12% gradient Bolt[TM] Bis-Tris Plus Gel according to the manufacturer's instructions (Life Technologies; Grand Island, NY) and transferred onto nitrocellulose membranes (Life Technologies) using the iBlot[®] 7-Minute Blotting System (Life Technologies). The membranes were blocked, incubated with rabbit anti-AChE polyclonal antibodies (Abcam; Cambridge, MA), and incubated with anti-rabbit IgG antibodies conjugated to alkaline phosphatase using the iBlot[®] Western Blot System (Life Technologies) according to the manufacturer's instructions. Finally, the membranes were developed using the iBlot[®] Western Detection, Chromogenic Kit (Life Technologies). To ensure equal loading, equivalent samples were run and blots probed with mouse monoclonal anti-GAPDH antibodies and processed as stated above.

3.6 Determination of AChE activity in MSCs

We measured the activity of AChE within the MSCs by the Acetylcholinesterase Assay Kit (Colorimetric) from Abcam according to the manufacturer's recommended protocol. Prior to the AChE activity assay we treated the MSCs with increasing concentrations of parathion (10, 30, 100, 1000 µM), paraoxon (10, 30, 100, 1000 µM), or media alone. AChE activity was reported as a percentage of control AChE activity.

3.7 Evaluation of MSC marker proteins

We examined the expression levels of the MSC markers CD73, CD90, and CD105 by Western blot analysis as stated above during the course of this study.

3.8 MSC differentiation studies

We examined the role of AChE expression/activity in MSC adipogenic, chondrogenic, osteogenic, and neuronal differentiation. These studies were conducted as follows:

3.8.1 Adipogenic differentiation. For these studies, $2x10^5$ MSCs were initially plated in 6-well tissue culture plates and allowed to grow to confluence in the presence of MSCGM. Once the cells reached confluence, the media was replaced with Human MSC Adipogenic Differentiation Medium (Lonza) and Adipogenic Maintenance Medium (Lonza) in cycles in accordance with the manufacturer's recommended protocol. The cells were cultured for a total of 21 days. We then stained the lipid-containing cells with Oil Red O (Lifeline Cell Technology; Frederick, MD) according to the manufacturer's indicated protocol. With this stain, intracellular lipid droplets will appear red in color. Photomicrographs were then taken and the amount of adipogenic differentiation was quantified using image analysis software.

3.8.2 Chondrogenic differentiation. MSCs were washed in incomplete Chondrogenic Differentiation Medium (Lonza) and centrifuged. The MSC pellet was re-suspended in complete Chondrogenic Differentiation Medium, divided into $2.5x10^5$ MSC aliquots and plated onto 96-well plates in 200 µL medium.[9] The MSCs then formed pellets, which were fed every 2-3 days with complete Chondrogenic Differentiation Medium and harvested at 21 days after initiation of the procedure. For harvesting, the pellets were fixed in 10% neutral buffered saline, processed for histologic analysis, and stained with Alcian blue (Lifeline Cell Technology).

3.8.3 Osteogenic differentiation. For osteogenic differentiation, $3x10^4$ undifferentiated MSCs were plated on 6-well plates in MSCGM. After 24 hours, the media was replaced with Osteogenesis Induction Medium (Lonza). This medium was replaced every 3-4 days for 3 weeks. To quantify ostegenic differentiation, we performed the Alizarin Red Assay (Lifeline Cell Technology) according to the manufacturer's protocol.

3.8.4 Neuronal differentiation. For this procedure, we plated $1x10^5$ MSCs in 6-well tissue culture plates and allowed the cells to attach for 24 hours. Then, the cells were washed twice with pre-warmed dPBS followed by the addition of pre-warmed Complete AdvanceSTEM Neural Differentiation Medium (Thermo Fisher Scientific). The neural differentiation medium was replaced after 48h and the cells were fixed in 4% paraformaldehyde at 72 hours. The differentiated MSCs were then washed and blocked with 10% donkey serum and 0.25% Triton X-100 in PBS. Following blocking, the cells were incubated with either rabbit anti-doublecortin or rabbit anti-α-internexin antibodies. Next, the cells were treated with donkey anti-rabbit IgG antibodies that have been conjugated to

AlexaFluor® 488. Finally, the cells were counterstained with Hoechst nuclear stain. Images were captured using the ArrayScan™ High Content Imager (Thermo Fisher Scientific).

3.9 Inhibition of AChE using si(RNA)

SMARTPool small interfering ribonucleic acid (siRNA) duplex products designed to target human AChE (Thermo Fisher Scientific) as well as the appropriate non-targeting siRNA duplexes will be used to knockdown AChE protein expression. The AChE and control siRNAs were preincubated with Dharmafect Transfection Reagent (Thermo Fisher Scientific) according to the manufacturer's protocol, and the transfection complexes were presented to MSCs for 24 hours in the absence of serum. At 48, 72, 96, and 120 hours after transfection, MSCs were lysed and processed for immunoblotting with anti-AChE antibodies as described above. To confirm equivalent protein loading, simultaneously prepared blots were probed with anti-GAPDH antibodies and developed as described above.

3.10 Statistical analysis

A student's t-test was used to compare mean responses between individual experimental and control groups. ANOVA was used to compare the mean responses among experimental and control groups in experiments with multiple groups. The Dunnett and Scheffe F-test was used to determine between which groups significant differences existed. A p-value < 0.05 was considered significant for all experiments.

4. RESULTS

4.1 Human bone marrow-derived MSC culture

Human bone marrow-derived MSCs were grown on tissue culture-treated plastic in MSCGM. The MSCs have attached to the tissue culture-treated plastic and display a fibroblast-like morphology. Figure 1 is a phase contrast photomicrograph of passage 5 MSCs.

Figure 1. Cultured human MSCs. A representative phase contrast image of undifferentiated human MSCs. Bar = 100 μm.

4.2 Human MSC toxicity studies

Human bone marrow-derived MSCs were plated at a density of $1x10^4$ in the wells of 96-well tissue culture plates and then allowed the cells to attach for 24 h. Once the cells had sufficiently attached, the MSCs were exposed to increasing concentrations (1-10000 μM) of parathion, paraoxon, or equivalent volumes of vehicle control (EtOH) for 48 hours. A MTT assay was performed to assess cellular viability (Figure 2A). Losses in cellular viability were observed with paraoxon-treated cells at concentrations > 1000 μM and with parathion at concentrations > 3000 μM. Treatment with vehicle only (EtOH) had little effect on cellular viability.

4.3 Human MSC proliferation studies

Human bone marrow-derived MSCs were plated in 96-well plates and then allowed to attach for 24 hours. The MSCs were then exposed to increasing concentrations (1-1000 μM) of parathion, paraoxon, or equivalent volumes of vehicle control (EtOH) that did not induce any cellular death for 48 hours. A BrdU incorporation assay was performed to assess cellular proliferation (Figure 2B). Parathion treatment altered cellular proliferation rates at concentrations ≥ 100 μM, while paraoxon inhibited cellular growth at concentrations ≥ 300 μM. Treatment of MSCs with vehicle (EtOH) had little effect on the proliferation of these cells at the concentrations tested.
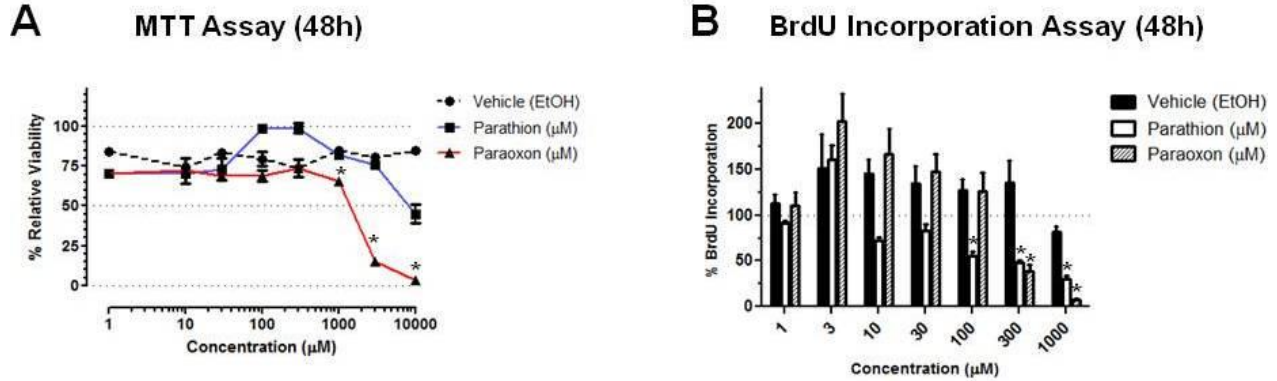
Figure 2. Effects of parathion and paraoxon on the viability and proliferative ability of cultured human MSCs. A) Human MSCs were exposed to increasing concentrations (1, 10, 30, 100, 300, 1000, 3000, or 10000 μM) of parathion (blue, ■), paraoxon (red, ▲), or equivalent amounts of vehicle control (EtOH, dashed, ●) for 48 hours, after which they were assayed for viability using the MTT Cell Viability Assay. The results are reported as mean ± SEM of % Relative Viability; n ≥ 4 for each condition tested. *p ≤ 0.05 versus vehicle control. B) Human MSCs were exposed to increasing concentrations 1, 3, 10, 30, 100, 300, or 1000 μM) of parathion (open), paraoxon (cross-hatched), or equivalent amounts of vehicle control (EtOH, filled) for 48 hours. The cells were then assayed for cellular growth using the BrdU Cell Proliferation Assay. The results are reported as mean ± SEM of % BrdU Incorporation; n ≥ 4 for each condition tested. *p ≤ 0.05 versus vehicle control.

4.4 AChE activity in human MSCs

Cultured human bone marrow-derived MSCs were treated with parathion (10, 30, 100, 1000 μM), paraoxon (10, 30, 100, 1000 μM), or media alone for 24 hours and then assayed for AChE activity (Figure 3A). We observed a dose of 10 μM with either parathion or paraoxon caused an approximate 50% reduction in baseline AChE activity. The maximum concentrations tested of both paraoxon and parathion (1000 μM) reduced AChE activity to approximately 35% of baseline.

4.5 AChE protein expression in human MSCs

Cultured human bone marrow-derived MSCs were treated with parathion (30 or 100 μM), paraoxon (30 or 100 μM), or equivalent amounts of vehicle control (EtOH) for 24 hours and then examined for AChE protein expression by Western blot (Figure 3B). Treatment of the MSCs with either paraoxon or parathion reduced the protein expression levels of AChE in a dose-dependent manner. Vehicle (EtOH) treatment did not affect AChE expression in MSCs.
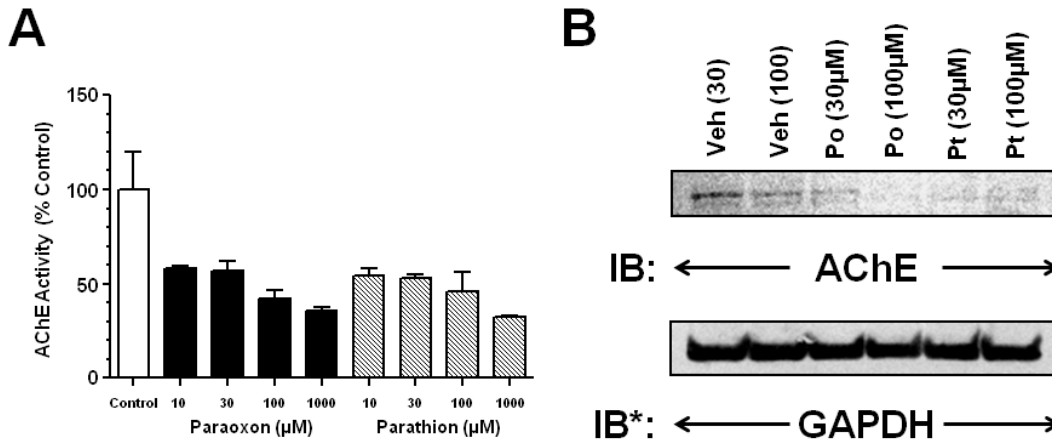
Figure 3. Effects of parathion and paraoxon on the activity and expression of AChE in human MSCs. A) MSCs were exposed in increasing concentrations (10, 30, 100, 1000 μM) of paraoxon (filled), parathion (cross-hatched), or media alone (open) for 24 hours. The cells were then assayed for AChE activity using the Acetylcholinesterase Assay Kit (Colorimetric). The results are reported as mean ± SEM of AChE Activity (% Control); n ≥ 2 for each condition tested. B) Human MSCs were exposed to paraoxon (30, 100 μM), parathion (30, 100 μM), or equivalent amounts of vehicle control (EtOH) for 24 hours. The cells were then lysed and resolved by the gradient Bolt[TM] Bis-Tris Plus Gel and

transferred onto nitrocellulose membranes using the iBlot® 7-Minute Blotting System. The blots were probed with rabbit anti-AChE antibodies followed by alkaline phosphatase-conjugated anti-rabbit IgG antibodies and developed with chromogen. To ensure equal loading, the equivalent samples will be run and blots with probed with anti-GAPDH antibodies. IB: immunoblot. IB*: immunoblot of housekeeping gene product. The blot is representative of three independent experiments.

4.6 Human MSC osteogenic differentiation

Human bone marrow-derived MSCs were plated at a density of $3x10^4$ cells on 6-well plates in MSCGM. After 24 hours, the media was replaced with Osteogenesis Induction Medium and replaced every 3-4 days for a total of 21 days. Figure 4 displays 21-day osteogenic differentiation. The cells have taken an osteoblast-like morphology and have begun to show areas of calcium deposits (red).
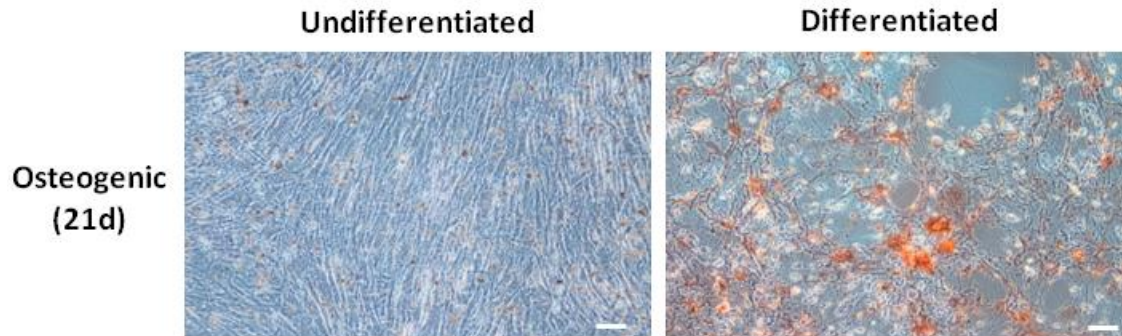

Figure 4: Representative phase contrast image of human MSC osteogenic differentiation. Undifferentiated MSCs ($3x10^4$) were plated on 6-well plates in MSCGM. After 24 hours, the media was replaced with Osteogenesis Induction Medium. This medium was changed every three to four days for three weeks. The Alizarin Red Assay was used to stain calcium deposits within the differentiated MSCs. Bar = 100 μm.

4.7 Human MSC neuronal differentiation

MSCs were plated at a density of $1x10^5$ in a 6-well plate and allowed to attach for 24 h. The cells were then washed and the media was replaced with Complete AdvanceSTEM Neural Differentiation Medium. The MSCs began to show neuron-like morphology as soon as 24 hours after treatment with differentiation medium. Figure 5 is an image of MSCs that have been differentiated for 72 hours. These differentiated MSCs also displayed the neural markers doublecortin and α-internexin (Figure 6).
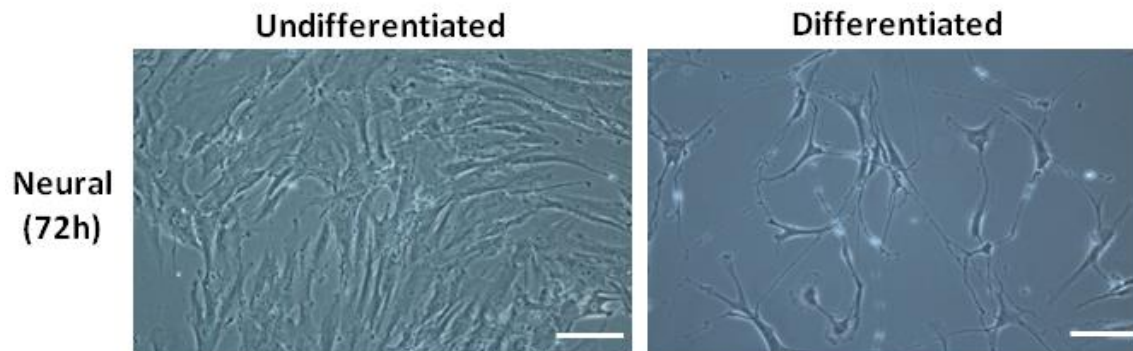
Figure 5. Representative phase contrast image of human MSC neural differentiation. Undifferentiated MSCs ($1x10^5$) were plated in 6-well tissue culture plates and allowed the cells to attach for 24 hours. The cells were then washed twice with pre-warmed dPBS followed by the addition of pre-warmed Complete AdvanceSTEM Neural Differentiation Medium. The neural differentiation medium was replaced after 48 hours and images were taken at 72 hours. Bar = 100 μm.

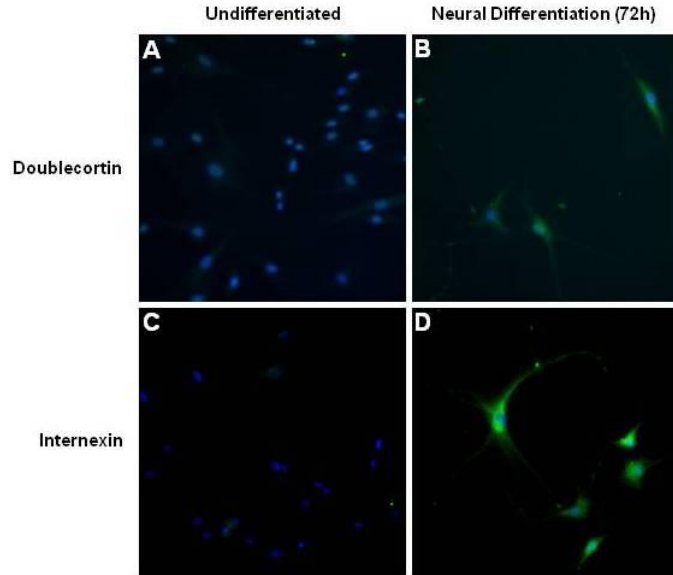**Figure 6. Markers of human MSC neural differentiation. Undifferentiated MSCs (1x10^5) were plated in 6-well tissue culture plates and allowed to attach for 24 hours. The cells were washed twice with pre-warmed dPBS, followed by the addition of pre-warmed Complete AdvanceSTEM Neural Differentiation Medium. The neural differentiation medium was replaced every 24 hours and cells were fixed with 4% paraformaldehyde at 72 hhours. Differentiated cells were stained with either rabbit anti-doublecortin antibodies (A, B) or rabbit anti-α-internexin antibodies (C, D) and visualized by Alexa Fluor® 488-conjugated donkey anti-rabbit IgG antibodies (green). The nuclei were visualized by Hoechst nuclear counterstain (blue). Stains were visualized using the ArrayScan^{TM} High Content Imager.**

4.8 Human MSC adipogenic differentiation

Human bone marrow-derived MSCs were plated and allowed to grow to confluence in a 6-well cell culture dish. Once the cells reached confluence, the media was replaced with MSC Adipogenic Differentiation Medium (MSCADM) in the presence of parathion (100 µM), paraoxon (100 µM), equivalent amounts of vehicle control (EtOH), or differentiation medium alone for 21 days. One well contained MSCGM only to serve as a negative control. The cells were then stained with Oil Red O and analyzed for differentiation (Figure 7). MSCs treated with adipogenic differentiation medium alone or adipogenic differentiation medium in the presence of vehicle (EtOH) displayed clear adipogenic differentiation (Figure 7A); there are very organized lipid droplets within the differentiated cells. Approximately 30-40% of the positive control or vehicle control cells displayed this adipogenic-like morphology (Figure 7B). Treatment with parathion and to a greater extent paraoxon reduced this organization and morphology (Figure 7A). Parathion treatment reduced the adipogenic differentiation by approximately 50% and paraoxon treatment reduced this by about 75% on control levels (Figure 7B).
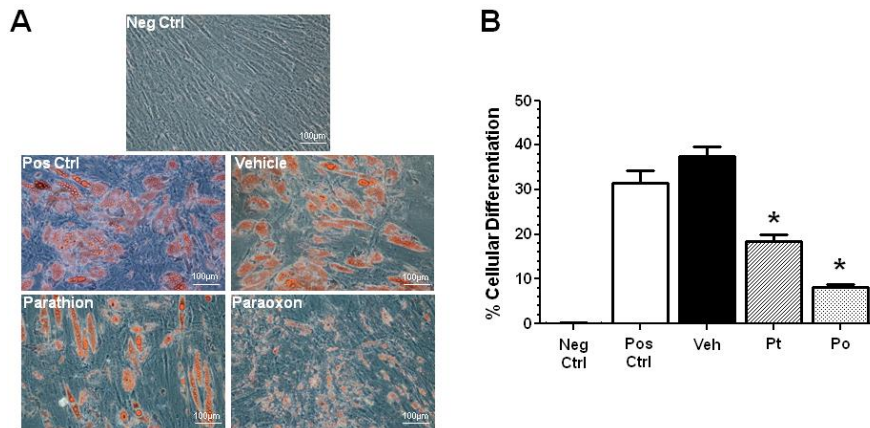

Figure 7. Human MSC adipogenic differentiation. A) Representative phase contrast images of Oil Red O stained adipogenic differentiated MSCs. MSCs (2x10^5) were plated in 6-well tissue culture plates and allowed to grow to

23

confluence in the presence of MSCGM. Once the cells reached confluence, the media was replaced with human MSCADM and cultured for an additional 21 days. During the differentiation process, MSCs were exposed to MSCGM, MSCADM, MSCADM + parathion (100 µM), MSCADM + paraoxon (100 µM), or MSCADM + equivalent amounts of vehicle control (EtOH). The cells were then stained with Oil Red O. Bar = 100 µm. B) Analysis of photomicrographs of adipogenic differentiation using Image J software. The results are reported as mean ± SEM of % Cellular Differentiation. *p ≤ 0.05 versus positive control.

4.9 Human MSC siRNA studies

MSCs ($1x10^4$) were plated in 6-well plates and allowed to attach for 72 hours. The cells were then transfected with increasing concentrations of GAPDH-directed siRNA (25, 33, 42, 50, and 100 nM) or equivalent concentrations of scrambled siRNA in the presence of Dharmafect transfection reagent. At 48, 72, 96, and 120 hours after transfection, MSCs were lysed and processed for immunoblotting with anti-GAPDH antibodies as described above. Transfection of the scrambled siRNA sequence had no effect on the protein expression levels of GAPDH (data not shown), which would suggest the lack of off-target effects. There was an observable reduction in GAPDH expression following the transfection of GAPDH-directed siRNA (data not shown), but this reduction was not complete.

5. CONCLUSIONS

Our results indicate that the OP chemicals, parathion and paraoxon, affect the proliferative ability and differentiation potential of human bone marrow-derived MSCs. In the current study, we demonstrated that parathion and paraoxon reduced the cellular viability of human MSCs in a dose-dependent manner (Figure 2A). The minimum effective concentration was 1000 µM for paraoxon and 10000 µM for parathion following a 48-hour treatment. The estimated IC_{50} for OP-induced cell death was ~1500 µM for paraoxon and ~10000 µM for parathion. Lower concentrations of these chemicals reduced the proliferative potential of MSCs at doses of ≥ 100 µM (parathion) and ≥ 300 µM (paraoxon) following 48-hour treatments (Figure 2B); the concentrations that reduced MSC proliferation were not associated with increased cellular death. We also demonstrated that treatment with parathion and paraoxon reduce both AChE protein expression levels (Figure 3B) as well as activity (Figure 3A) in these cells in a dose-dependent manner. These results suggest that parathion and paraoxon disrupt the normal pathways associated with AChE in human MSCs; these altered pathways are inducing cellular death as well as the normal proliferative function of MSCs. In this study, we have also demonstrated the ability to differentiate human MSCs into several different cell types in our laboratory including adipocytes (Figure 7A), osteoblasts (Figure 4), and neurons (Figures 5 and 6). Prior treatment with either parathion or paraoxon significantly reduces the MSCs' ability to differentiate into adipocytes (Figure 7B); this suggests a possible role of AChE in this process. Studies using AChE-directed siRNA are currently in progress to knock down AChE expression in differentiating MSCs to determine the exact role of AChE in these differentiation pathways.

ACKNOWLEDGEMENTS

REFERENCES

[1]   Dominici, M., et al., *Cytotherapy* **2006**, 8(4), p315-317.
[2]   Rastegar, F., et al., *World Jounral of Stem Cells,* **2010**, 2(4), p67-80.
[3]   Hoogduijn, M.J., et al., *Stem Cells and Development,* **2009**, 18(1), p103-112.
[4]   Hoogduijn, M.J., et al., *Toxicological Sciences,* **2006**, 94(2), p342-350.
[5]   Friedenstein, A.J., et al., *Transplantation,* **1968**, 6(2), p230-247.
[6]   Pittenger, M.F., et al., *Science,* **1999**, 284(5411), p143-147.
[7]   Angelini, D.J., et al., *PloS One,* **2010**, 5(6):e11251.
[8]   Kolosova, I.A., et al., *Stem Cells and Development,* **2013**, 22(2), p239-247.
[9]   Solchaga, L.A.; et al., *Methods in Molecular Biology,* **2011**, 698, p253-278.

A platform approach to produce polymer nanoparticles with modular functionality from block copolymer surfactants

Kato L. Killops[a], Christina Rodriguez[b], Nathaniel A. Lynd[b]

[a]U.S. Army Edgewood Chemical Biological Center, Research and Technology Directorate, 5183 Blackhawk Rd, Aberdeen Proving Ground, MD 21010

[b]Materials Research Laboratory, University of California, Santa Barbara, CA 93106

ABSTRACT

Polymer nanoparticles with peripheral functionality were synthesized via emulsion polymerization using an amphiphilic block copolymer surfactant. The polystyrene-*block*-poly(ethylene oxide-*co*-allyl glycidyl ether) block copolymers with various lengths and functional monomer incorporation were synthesized by anionic polymerization. Modification of the allyl groups was achieved by thiol-ene chemistry using commercially-available mercaptans. Particles ranged in size from sub-100 nm to just over 200 nm. Functionalized particles exhibited pH modulation, as monitored by electrophoretic mobility measurements.

Keywords: nanoparticles, block copolymers, thiol-ene, zeta potential

1. INTRODUCTION

The ability to synthesize colloidal polymer particles in the nanoscale size regime with tunable peripheral functionality has attracted much attention in recent years. Often, emulsion or dispersion polymerization techniques are employed to achieve spherical particles. Emulsion polymerization techniques are highly amenable to industrial processes due to ease of scalability and the use of water as the solvent. The possibility to tailor the particles' functionality lies at the nexus of advanced purification strategies[1,2], as well as expanding opportunities for phonic materials[3], smart coatings[4,5], and abiotic-biological interfaces.[6,7]

Currently, there are many strategies for achieving functional polymer colloids. Mixing a range of monomers in desired proportions can lead to particles with diverse functionality via precipitation polymerization.[7,8] Statistically, these monomers should present themselves on the particle surface, especially if charged or hydrophilic monomers are used.[9] However, it is difficult to control how many of each group is available at the particle interface beyond a statistical distribution. Within the realm of emulsion polymerization, common approaches include incorporation of reactive surfactants or surfmers[10] (surfactant monomers) to achieve peripheral functionality. An alternative approach is to use amphiphilic block copolymers (BCP) as surfactants to stabilize emulsion particles[11], resulting in hairy latexes. Although a number of different BCPs have been used, polystyrene-*b*-poly(ethylene oxide) has been widely studied in emulsion polymerizations.[12]

The use of BCP surfactants confers a number of advantages over their small molecule counterparts, including low critical micelle concentrations and low diffusion coefficients, which aid in anchoring the macromolecules to the particle interface.[13] Our approach capitalizes on the opportunity for macromolecules to provide *multiple* modular functional groups on a single surfactant molecule. Furthermore, the advantage of using a BCP *platform* is that a single precursor polymer can be modified with a variety of moieties in order to create a *library* of functional particles.

Starting from a polystyrene-*b*-poly(ethylene oxide-*co*-allyl glycidyl ether) [PS-*b*-P(EO-*co*-AGE)] amphiphilic diblock copolymer[14,15], we demonstrate the synthesis of hairy polystyrene latexes with tunable functionality. The incorporation of an allyl-functional monomer into the hydrophilic portion of the BCP enables the use of thiol-ene "click" chemistry[16] to decorate the polymer backbone with a diverse range of commercially available thiol-functional groups (examples are shown in Figure 1). This strategy enables modification of allyl groups with a variety of moieties that are charged or neutral, pH sensitive, zwitterionic, etc. We set out to determine how various parameters affect particle formation and stabilization including: BCP molecular weight, BCP composition, incorporation of BCP in emulsion polymerization, and type and charge of functional groups within the BCP.
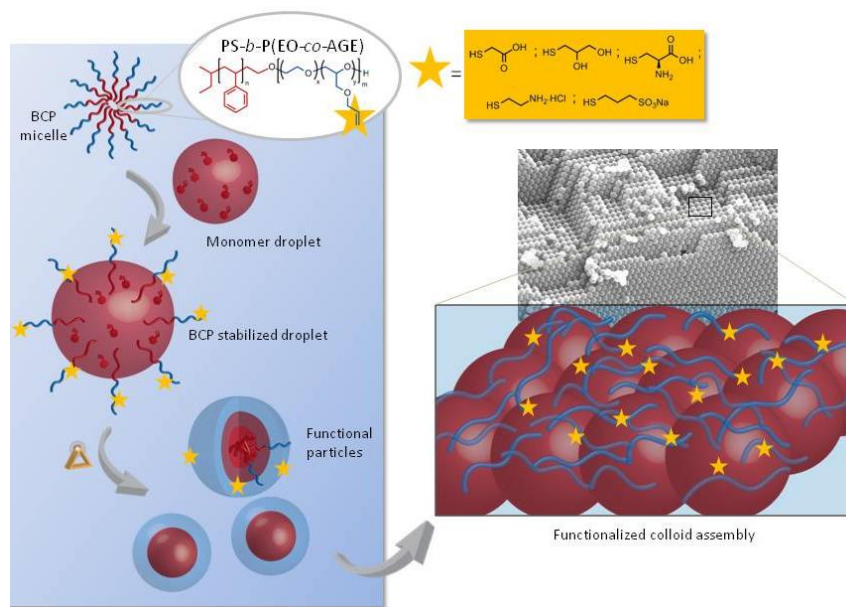
Figure 1. Schematic representation of using emulsion polymerization with modular BCP surfactants to produce latexes with functional corona, and their colloidal assembly structures.

2. EXPERIMENTAL

2.1 Chemicals

All chemicals were purchased from Sigma Aldrich and used without further purification, unless otherwise stated. Allyl glycidyl ether was purchased from TCI America. Styrene was degassed by three freeze-pump-thaw cycles and purified by stirring over dibutylmagnesium at 0°C and distilling into receiving flasks. Ethylene oxide and allyl glycidyl ether were degassed by three freeze-pump-thaw cycles and purified by stirring over butylmagnesium chloride at 0°C and distilling into receiving flasks. Deuterated solvents for nuclear magnetic resonance (NMR) were purchased from Cambridge Isotope Laboratories.

2.2 Instrumentation

NMR (^{1}H, ^{13}C) spectra were recorded on a Bruker DMX-300 MHz spectrometer at room temperature. Chemical shifts are reported in parts per million (δ) relative to CHCl$_3$ (7.24 ppm for ^{1}H), dimethyl sulfoxide (DMSO) (2.50 ppm for 1H), or N,N-dimethylformamide (DMF) (8.03 ppm for 1H) as internal reference. Gel permeation chromatography was performed in DMF on a Waters 2695 Separation Module equipped with a Waters 2414 Refractive Index Detector and a Waters 2996 Photodiode Array Detector. X-ray photoelectron spectroscopy (XPS) measurements were performed using a Kratos Axis Ultra Spectrometer (Kratos Analytical, Manchester, UK) with a monochromatic Al Kα X-ray source (1486.6 eV) operating at 225 W under a vacuum of 1.0×10^{-8} Torr. Charge compensation was carried out by injection of low-energy electrons into the magnetic lens of the electron spectrometer. The pass energy of the analyzer was set at 80 eV for survey scans with an energy resolution of 0.5 eV. The spectra were analyzed using CasaXPS v.2.3.14 software. The C–C peak at 285 eV was used as the reference for binding energy calibration. Scanning electron microscopy was performed on a FEI XL30 Sirion FEG Digital Electron Scanning Microscope at 3.0 to 5.0 keV. Dynamic light scattering and zeta potential measurements were performed on a Wyatt Mobius instrument at ambient temperature.

2.3 Synthesis

2.3.1 Polystyrene-b-poly(ethylene oxide-co-allyl glycidyl ether) (PS-b-P(EO-co-AGE)). The synthesis was performed according to procedures found in Killops, et al.[17]

2.3.2 Functionalization of PS-b-P(EO-co-AGE) via thiol-ene chemistry. Generally, polymer was dissolved in a minimal amount of solvent (typically DMF or tetrahydrofuran (THF)) in a vial fitted with a septum, and ca. 10 eq.

26

(relative to ene) of thiol, and 0.2 eq. (relative to ene) 2,2-dimethoxy-2-phenylacetophenone (DMPA) were added. The mixture was sparged with nitrogen for 5 minutes before the vial was irradiated with 365 nm light for 30 minutes. Conversion of the ene groups was verified by ^{1}H NMR. Functionalized polymers were typically purified by dialysis against Milli-Q water for 24 hours to remove unreacted thiol, and lyophilized to dry.

2.3.3 Particle synthesis. A general recipe was used and scaled accordingly: 10 wt.% styrene in water, 5-20 wt.% BCP (relative to styrene), and 0.8 wt.% (relative to styrene) potassium persulfate. Reactions were typically conducted in 25 to 100 mL of water. First, styrene was suspended with vigorous stirring in half of the total volume of water in a three-neck flask fitted with a condenser; the BCP was dissolved in the other half. The BCP micelle solution was added dropwise to the stirring styrene suspension. The mixture was sparged with N_2 for 30 minutes at room temperature, and then heated to 80°C under N_2 flow. In a separate vial fitted with a septum, potassium persulfate was dissolved in a small amount of water and sparged with N_2 for 10 minutes. The solution was transferred via cannula to the reaction mixture. The emulsion polymerization was stirred at 80°C for 6-16 hours.

3. RESULTS AND DISCUSSION

In order to create a platform to synthesize polymer nanoparticles with diverse peripheral functionality, an amphiphilic BCP scaffold was devised to serve as an emulsion polymerization stabilizer. The PS-*b*-P(EO-*co*-AGE) BCP contains a PS block to anchor the BCP to the particle, as well as a hydrophilic EO-based block to stabilize the styrene droplets. Within the EO block, allyl groups are dispersed along the backbone via copolymerization with allyl glycidyl ether, which permits pre- or post-polymerization functionalization with a diverse range of thiol groups. The PS-*b*-P(EO-*co*-AGE) BCPs were synthesized via standard anionic polymerization in large (>10 g) quantities. A range of PS-*b*-P(EO-*co*-AGE) BCPs were synthesized in order to ascertain the effect of molecular weight and AGE incorporation on particle formation (Table 1).

Table 1. Molecular weight and composition of BCP surfactants.

Polymer Group	Naming Convention	M_n PS[a]	M_n PEO[a]	M_n PAGE[b]	Mol % AGE	Total M_n
PS$_5$-P(EO-*co*-AGE)$_{15}$	**S3**	5000	14100	900	3	20000
PS$_{11}$-P(EO-*co*-AGE)$_{50}$	**M1**	11000	49100	1100	1	61200
	M3	11000	42400	3200	3	56600
	M5	11000	44200	6600	5	61800
PS$_{16}$-P(EO-*co*-AGE)$_{90}$	**L3**	16000	82000	6000	3	104000

[a] Determined by GPC. [b] Determined by NMR.

Emulsion polymerizations were carried out in large batches with water as the solvent, styrene monomer, K_2SO_4 initiator, and PS-*b*-P(EO-*co*-AGE) as the only stabilizer. Initially, alkene functional particles were prepared using BCP **M3**. It was observed that the amount of BCP stabilizer has a dramatic effect on the final diameter of the particles. A substantial decrease in diameter was observed upon increasing the **M3** content from 5 wt. % to 15 wt.% (Table 2).

Table 2. Average diameters of particles with varying BCP content.

BCP Used	Wt. % BCP	Size (DLS) (nm)	Size (SEM) (nm)
None	0	201 ± 1	204 ± 5
S3	10	88 ± 2	55 ± 2
S3	15	96 ± 3	62 ± 3
S3	20	--	86 ± 4
M1	10	230 ± 0	100 ± 4
M1	15	111 ± 0	80 ± 2
M1	20	--	77 ± 1

BCP Used	Wt. % BCP	Size (DLS) (nm)	Size (SEM) (nm)
M3	5	166 ± 12	185 ± 71
M3	10	127 ± 4	71 ± 4
M3	15	102 ± 1	75 ± 1
M3	15	112 ± 3	--
M3	20	125 ± 3	78 ± 6
M5	10	--	Too polydisperse
L3	10	139 ± 0	88 ± 13
L3	15	128 ± 7	110 ± 3
L3	20	134 ± 8	80 ± 13

However, upon increasing the BCP content further, from 15 to 20 wt.%, a saturation point is reached, where steric crowding of the chains prevents additional stabilization of smaller particles. The particles have low polydispersity, and a propensity to form iridescent colloidal crystal arrays (Figure 2). This result prompted us to expand our BCP library in order to determine the effect of molecular weight on particle formation. BCPs consisting of smaller (**S3**) and larger (**L3**) molecular weights relative to **M3** were synthesized, keeping the wt.% of styrene near 20%.

Figure 2 illustrates the effect of BCP molecular weight on latex formation. Particles formed from **M3** are relatively monodisperse, and show a decrease in particle size with increasing BCP incorporation. This trend is not repeated in the case of **S3** and **L3** where the polydispersity increases, and particle diameter is not correlated to BCP incorporation. For **S3**, the size of the particles actually increases with increasing BCP content. Perhaps this is due to the availability of more chains so larger monomer droplets can be stabilized against coalescence without the steric effects in play that hinder the packing of larger BCPs into droplets. In the case of **L3**, there number of chains available for stabilization is lower, so the coalescence of droplets is not well controlled, leading to increasing polydispersity. Furthermore, steric repulsion prevents larger BCPs from packing as densely into a droplet, further decreasing stability. We are currently investigating and confirming the former hypothesis.
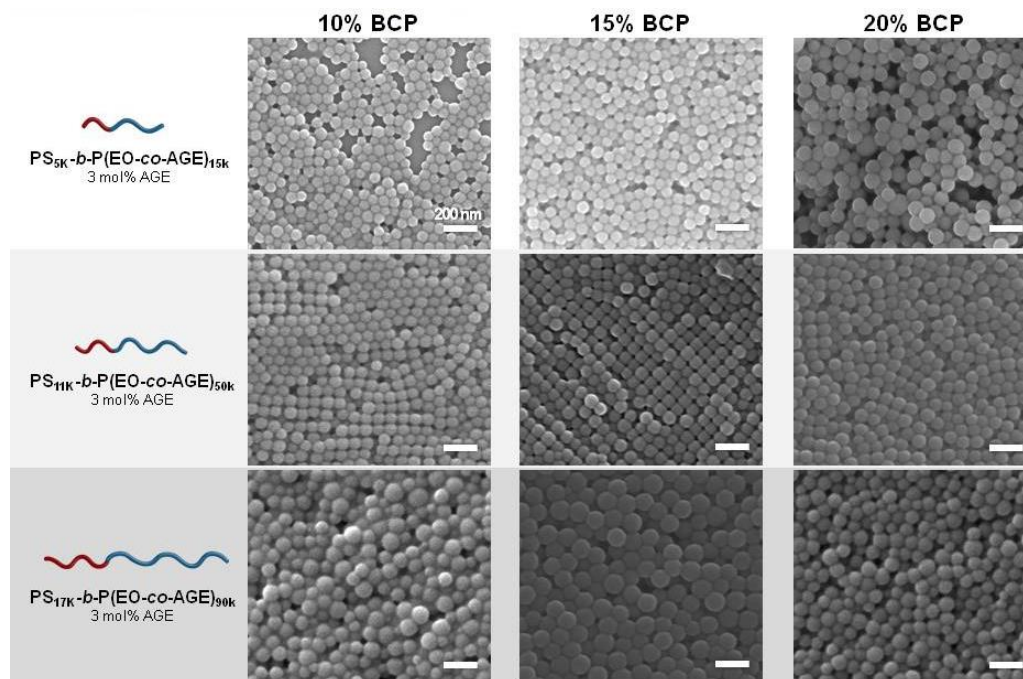

Figure 2. Scanning electron microscope (SEM) images of particles synthesized with different BCP surfactants and varying incorporations of BCP stabilizer. All scale bars are 200nm.

In order to maximize reactive functionality while maintaining control over particle formation, we proceeded to synthesize BCPs with varying levels of AGE in the hydrophilic block. Since **M3** exerted the greatest synthetic control, **M1** and **M5** were synthesized to contain 1 and 5 mol % AGE to investigate these effects. Figure 3 shows representative SEM areas of particles using 10 wt.% **M1**, **M3**, and **M5**, respectively. Although **M1** produced larger particles than **M3**, both syntheses were well-controlled and led to relatively monodisperse latices that crystallized into colloidal arrays. Particles synthesized with **M5** coagulated or were quite polydisperse. It is likely that the increased concentration of alkene groups on **M5** caused additional interparticle coupling that is not observed with lower AGE incorporations.
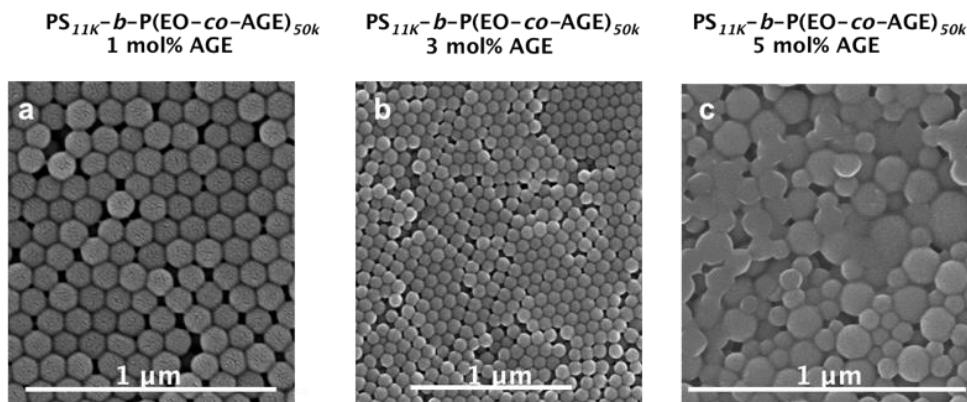

Figure 3. SEM images of particles synthesized with 10 wt% of BCP surfactants with varying incorporations of AGE comonomer.

In order to capitalize on the potentially beneficial aspects of particles with a functional corona, verification of the presence of BCP on the periphery of the particles was required. Initially, particles with and without BCP were analyzed by XPS, which elucidates the presence of elements as well as information about their bonding order within 1-10 nm of the surface. XPS analysis (Figure 4) indicates the presence of BCP within the first 10 nm of the surface, as evidenced by the C-O bond peak at 287 eV, which is absent in the bare PS latex. Angle-resolved XPS allows for probing different depths within the material, and higher angle indicates shallower penetration of the x-ray beam. It is clear that there is no enrichment of ether-containing material within the first few nanometers (75° angle) over the larger depth profiled at 0°. Therefore, from XPS, we can conclude that the BCP is present within the particles, and most likely resides on the surface. FT-IR was also used to monitor the incorporation of the BCP into the particles. Evidence from increased absorbance by ether groups is consistent with particles having increasing BCP weight percentage added to the emulsion polymerization.
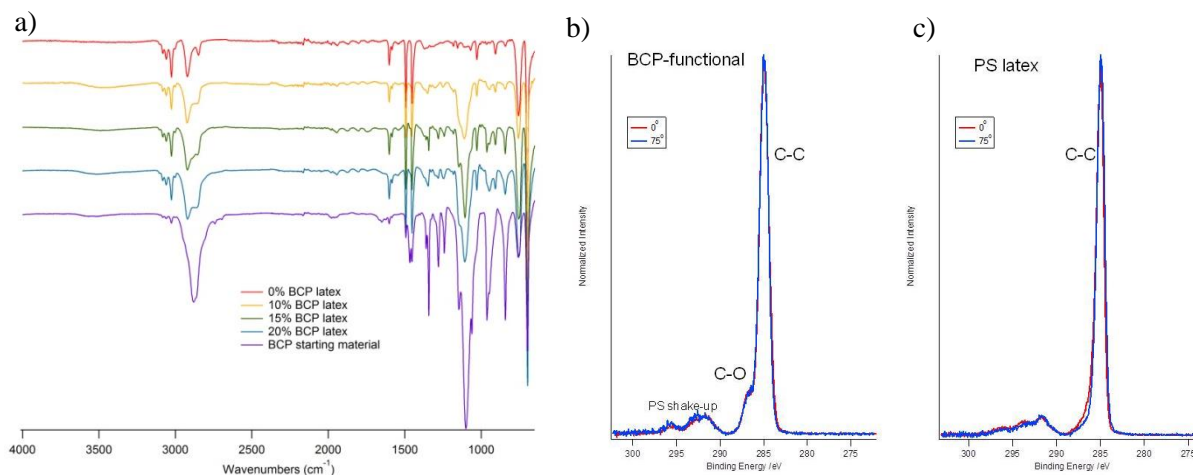

Figure 4. (a) FT-IR spectra of particles with varying incorporation of BCP surfactant. XPS spectra of particles (b) containing BCP and (c) bare PS latex

Functionalization of the BCPs was achieved using thiol-ene chemistry[18] to transform the allyl groups. Commercially available thiols including thioglycolic acid, cysteamine hydrochloride, and sodium 3-mercapto-1-propanesulfonate

were appended to the BCP using the photochemically-initiated thiol-ene reaction, and full conversion of the allyl groups was confirmed by ^{1}H NMR. These groups impart a pH switchability to the particles (*vide infra*).

For further confirmation of BCP anchoring to the surface of the particles, their electrophoretic mobility and zeta potential (ζ) were determined. Particles having a surface charge will migrate in solution according to the direction of an applied voltage potential. Particles having sulfonate, amine, or carboxylic acid functional groups within their corona are well-suited for electrophoretic mobility measurements, as they can become charged depending on pH. As shown in Figure 5, zeta potential and diameter were measured for ammonium particles at range of pH values.
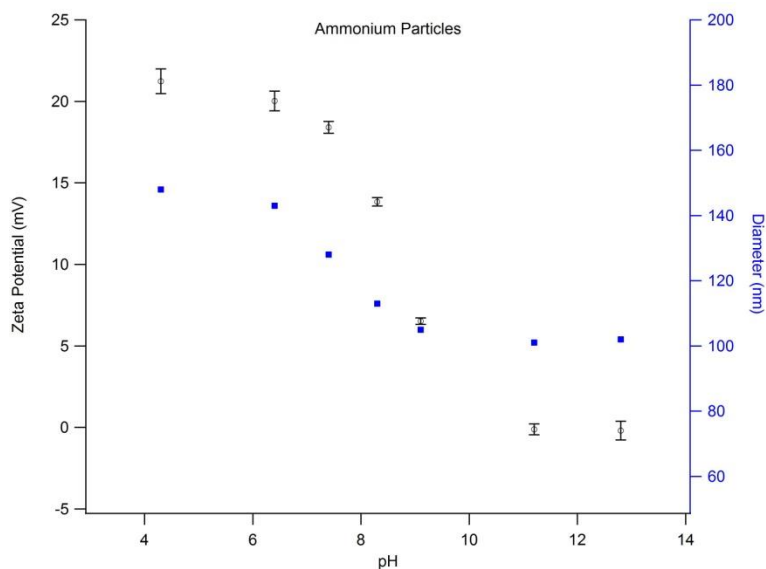

Figure 5. Zeta potential and hydrodynamic diameter dependence on pH for ammonium-functional particles.

The particles are highly charged, with a large positive zeta potential at pH values below the pK_a of ammonium. As the pH is increased, particles become less charged, and zeta potential values approach zero at and above the pK_a of 8.3. Interestingly, the particle diameter exhibits a similar trend, with a decrease in size as the particles become more neutrally charged. This is explained by static repulsion of the chains at low pH where they are highly charged, and a collapsing of more neutral chains in the corona. Particles functionalized with sulfonates and carbonates show a similar, but an opposite trend, as they are neutral at low pH, and become more negatively charged at higher pH values. Clearly, the electrophoretic mobility of the particles supports our hypothesis that that polymer chains indeed extend into solution to stabilize the particles.

4. CONCLUSION

A functional amphiphilic BCP, PS-*b*-P(EO-*co*-AGE), was successfully employed as a stabilizer in emulsion polymerization. We demonstrated control over the size of the particles by varying the amount of BCP incorporated into the particles, to give particles with low polydispersity. However, this control is primarily exerted at a narrow molecular weight value. Smaller and larger BCPs demonstrate a loss of control, primarily due to steric stabilization factors. The inclusion of allyl groups within the hydrophilic portion of the BCP allows for modification of a single polymer scaffold to create a library of particles with functional corona. Analysis from XPS and zeta potential measurements indicates that that the functional corona does reside at the periphery of the particles, extending into solution. We predict that the type of functionality at the corona will have important implications for the self-assembly of the particles into colloidal crystal assemblies, and for advanced applications, which will be explored in the third year of the project.

ACKNOWLEDGEMENTS

REFERENCES

[1] Wei, B.C., Rogers, B.J., and Wirth, M.J., *Journal of the American Chemical Society,* **2012**, 134(26), p10780-10782.

[2] Daniele, M.A., et al., *Small,* **2012**, 8(13), p2083-2090.

[3] Kim, S.H., et al., *NPG Asia Materials,* **2011**, 3(1), 25-33.

[4] Munoz-Bonilla, A., van Herk, A.M., and Heuts, J P.A., *Macromolecules,* **2010**, 43(6), p2721-2731.

[5] Munoz-Bonilla, A., van Herk, A.M., and Heuts, J.P.A., *Polymer Chemistry.,* **2010**, 1(5), p624-627.

[6] Fakhrullin, R.F., and Lvov, Y.M., *ACS Nano,* **2012**, 6(6), p4557-4564.

[7] Lee, S.H., et al., *Journal of the American Chemical Society,* **2012**, 134(38), p15765–15772.

[8] Zakrevskyy, Y., et al., *Advanced Functional Materials,* **2012**, 22(13), p5064.

[9] Zhang, Q., et al., *Langmuir,* **2012**, 28(14), p5940-5946.

[10] Pargen, S., et al., *Macromolecules,* **2012**, 45(3), p1230-1240.

[11] Riess, G., *Colloids and Surfaces A,* **1999**, 153(1-3), p99-110.

[12] Mura, J.L., and Riess, G., *Polymers for Advanced Technologies,* **1995**, 6(7), p497-508.

[13] Riess, G., and Labbe, C., *Macromoecular. Rapid Communications,* **2004**, 25(2), p401-435.

[14] Dimitriou, M.D., et al., *Langmuir,* **2011**, 27(22), p13762-13772.

[15] Lee, B. F., et al., *Journal of Polymer Science Part A: Polymer Cheistry,* **2011**, 49(20), p4498-4504.

[16] Killops, K.L., Campos, L.M., and Hawker, C.J., *Journal of the American Chemical Society,* **2008**, 130(15), p5062-5064.

[17] Killops, K.L., et al., *ACS Macro Letters,* **2012**, 1(6), p758-763.

[18] Campos, L.M., et al., *Macromolecules,* **2008**, 41(19), p7063-7070.

On resonant Raman enhancement driven by nano-scale intermolecular interactions

Jerry B. Cabalo*[a], Erik Emmons[b]

[a]U.S. Army Edgewood Chemical Biological Center, Research and Technology Directorate, 5183 Blackhawk Rd, Aberdeen Proving Ground, MD 21010

[b]Science Applications International Corp., P.O. Box 68, Gunpowder Branch, Aberdeen Proving Ground, MD 21010

ABSTRACT

The purpose of this study is to understand how intermolecular interactions can influence the selection of modes for resonance enhancement in Raman spectroscopy. A series of peptides was studied both experimentally and theoretically. The peptide series consists of optically active Tyrosine and thiol containing Cysteine, where the separation between the two is varied. Ultraviolet-visible and resonance Raman measurements show the same response from each of the peptides, indicating the dominance by the optical chromophore. Additional peaks are enhanced in solid Tyrosine but not in the solution phase. A theoretical method of calculating the resonance Raman spectra has been devised to help connect the effect of intermolecular interactions to the Raman response through calculation of the Franck-Condon factors. Spectra calculated by this method predict that the Raman response from Cysteine is negligible, that symmetric hydrogen motion about the amine group is a primary contributor to the Raman signature, and that the aromatic ring stretches and breathing modes are not significant contributors. Model and experimental spectra differ on a number of Raman bands. These differences may be explained by our choice of water model, functional, or molecular conformation.

Keywords: resonance Raman, intermolecular interactions

1. INTRODUCTION

Raman spectroscopy is a very important analytical tool because it has such a high degree of chemical specificity. This spectroscopic approach is highly applicable to Army missions such as the sensing of hazardous materials, including explosives[1], toxic chemicals[2], and pathogenic organisms.[3] However, low sensitivity limits the utility of this powerful technique. In recent years, a number of methods for enhancing the Raman signal involving Surface Enhanced Raman Spectroscopy (SERS) or Resonance Raman Spectroscopy (RRS) have been demonstrated.

SERS typically provides enhancement factors of six orders of magnitude, and it relies on the interaction between an analyte and a metal surface (Cu, Ag, Au, Pd, or Pt). Reproducible results can be difficult to obtain with SERS because it is highly sensitive to the morphology of the metal substrate, chemical interaction between the substrate and analyte, as well as analyte conformation and orientation on the substrate surface. Another challenge with the SERS approach is that direct contact between the analyte and the SERS substrate is a requirement for SERS. In contrast, RRS is suitable for non-contact analytical methods, while enhancement factors comparable to SERS have been reported.

RRS depends on resonance between the excitation laser and electronic states within the analyte molecule. Only normal mode vibrations involving the atoms within the chromophore experience enhancement.[4] While this selectivity towards vibrational modes within a chromophore is an advantage for some applications, it is also desirable to permit vibrational modes outside of the chromophore to experience resonant enhancement in a controlled manner. Electronic coupling between optically active and "dark" vibronic states have been shown to result in the shifting of intensity.[5] It is reasonable to hypothesize intermolecular interactions can influence intensity transfer. An understanding of how vibrational modes that do not directly involve the chromophore interact with the excited electronic states of that chromophore may permit controlled enhancement of these modes.

To understand the impact of intermolecular interactions, the sum-of-states framework[6,7] is convenient for demonstrating a direct link between the resonance Raman cross section and perturbations to the ground and excited

state vibrational potential energy surface. Within the sum-of-states framework, the polarizability tensor elements depend on the electronic transition dipole moments and vibrational wavefunctions. The vibrational wavefunctions are sensitive to changes in the potential energy surface. More specifically, the symmetric part of the RRS enhancement depends on the probability of transition to the intermediate excited vibrational state and back down to the final vibrational state. These probabilities are the Franck-Condon (F-C) factors.[8] The non-symmetric vibrations are enhanced by the Herzberg-Teller (H-T) terms[9], which are the overlap integrals of the nuclear wavefunctions and the normal mode coordinate. If the vibrational wavefunctions are affected by intermolecular interaction, then it should follow that the resonance Raman cross section should be affected. Furthermore, it is reasonable to expect that intermolecular perturbations to an excited state molecule could result in coupling between the excited vibronic states, thus permitting enhancement of normally dark vibrational modes.[10] The time-dependent correlator approach is not convenient for drawing the link between perturbation to the vibrational potential energy surfaces (PES) and the resonance Raman enhancement.[11]

Coupling between vibrational modes of a molecule means that enhancement may be influenced by the chromophore. We thus expect anharmonicity-induced coupling to permit greater enhancement of vibrational modes that are not directly connected to the chromophore interacting with the excitation laser. An understanding of this process may lead to new approaches for enhancing the Raman signal. We hypothesize that intermolecular interaction-induced anharmonicity will delocalize resonance enhancement from the absorbing chromophore due to greater than expected mixing between vibrational modes. We expect a wider portion of a molecule to experience resonance enhancement when the molecule is in contact with a surface. To understand the relationship between induced anharmonicity and the RRS signal, we probe the RRS response of molecules in solution, and the solid crystal phase. For ongoing work, we intend to probe interactions between the peptides of interest and a nano-scale surface.

2. METHODS

2.1 Overview

To test the above hypothesis we use a set of molecules with a chromophore and a distinctive vibrational mode that can be easily distinguished from the other vibrations. Figure 1 shows the three peptides used for this study, namely TyrCys, TyrGlyCys, and TyrGlyGlyCys. This series of peptides has Tyrosine as a chromophore, a distinctive vibrational mode (the S-H stretch around 2600 cm^{-1}), and Glycine spacers to increase the separation between the thiol functional group and the Tyrosine chromophore. Peptides containing Serine as a spacer instead of Glycine are also investigated. Much work is also done with Tyrosine alone. The resonance Raman spectrum is measured at 229 nm, 244 nm, and 785 nm excitation for the peptides including Tyrosine alone. The measurements are done for both solid and solution phase.
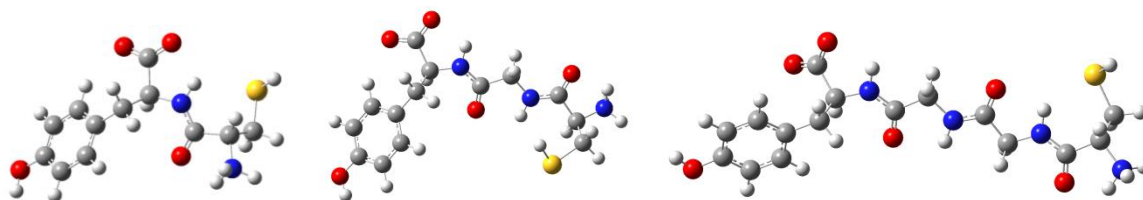

Figure 1. Structures of the peptides used in this study, with Tyrosine as the optical chromophore and Cysteine as the group containing the unique vibrational mode (S-H stretch). The peptides are TyrGlyGlyCys (right), TyrGlyCys (center), and TyrCys (left). The Glycine residue is used as a spacer to increase the distance between the chromophore and the distinctive vibrational mode.

To understand the impact of the separation between the thiol group and the Tyrosine chromophore, the resonance Raman spectra are modeled using the sum of states framework for each of the series of Tyrosine containing compounds. This permits determination of how the F-C factors for the vibrational mode of interest (the S-H stretch) are affected by the Glycine spacers.

2.2 Theoretical methods

We use the theoretical formulation of the dynamic polarizability found in Albrecht[6], which applies first order perturbation theory to simplify the Kramers-Heisenberg-Dirac (KHD) expression for quantum dispersion.[12,13] Using the Born-Oppenheimer approximation, the electronic and nuclear components of the wavefunctions are separable,

33

and the transition moments between vibronic states can be treated as a summation over nuclear wavefunction overlap integrals (F-C factors) and dipole transition moments (H-T terms). Albrecht collects the pure F-C factors into a single expression denoted as the A term, and the H-T containing terms into the B term. For a resonance condition where the excitation laser is in resonance with a single state, the $\rho\sigma^{th}$ element of the polarizability tensor α for an initial vibronic state gi ending in state gj, where g stands for the ground electronic state, i is the initial vibrational state, and j is the final vibrational state, can be expressed as $(\alpha_{\rho\sigma})_{gi,gj} = A + B$. The A term can be expressed as:

$$A = \frac{1}{h}\sum_{\upsilon}\left(\frac{(\mu_\rho)_{g,e}{}^0(\mu_\sigma)_{g,e}{}^0\langle gi|e\upsilon\rangle\langle e\upsilon|gj\rangle}{\nu_{e\upsilon,gi}-\nu_0+i\gamma}\right) \tag{1}$$

where h is Planck's constant, the sum is performed over vibrational quantum number υ of the excited electronic state, $(\mu_\rho)_{g,e}{}^0$ is the ρth component of the electronic transition dipole moment from the ground state g to state e, $(\mu_\sigma)_{g,e}{}^0$ is the σth component of the transition dipole moment, $\nu_{e\upsilon,gi}$ is the frequency difference between the initial vibronic state gi and the intermediate excited vibronic state $e\upsilon$, ν_0 is the frequency of the excitation laser, γ is damping constant related to the lifetime of the excited vibronic state, $<gi|e\upsilon>$ is the F-C factor between the initial vibrational state on the ground electronic state and the vibrational state υ on the intermediate excited electronic state e, and $<e\upsilon|gj>$ is F-C factor between the intermediate vibronic state and the final vibrational state j in the ground electronic state. The B term is similar except it includes H-T terms such as $<gi|Q_a|e\upsilon>$ where Q_a is the normal coordinate of mode a, and sums over all electronic states and all normal modes. The contribution from the B term in the present study is negligible compared to the A term and is not shown here. Vibrational modes involving symmetric motions contribute to the A term, and asymmetric modes contribute to the B term.

For the work to date, the assumption is made that normal mode coordinates determined in the ground electronic state can be projected onto the excited electronic state PES. To date, we neglect coupling that can occur between ground state normal coordinates in the excited state. Using Gaussian 2009, Rev. C1[14], we optimize the geometry in the ground electronic state, and then determine the normal mode coordinates for that optimized geometry. We then calculate the PES along the ground state normal mode coordinates for the ground and ten of the lowest excited electronic states using time-dependent density functional theory (TD-DFT) calculations of single point energies, and the B3LYP/6-311+G(d,p) theoretical method. For validation of the TD-DFT calculations, the electronic spectrum at the equilibrium ground state geometry is calculated for 200 states using TD-DFT. The resulting absorptions are fitted with Gaussian lineshapes of 20 nm of full width at half maximum (FWHM), and compared to results.

Because the zwitterionic form of the peptides is biologically important, a polarizable solvent model is necessary to achieve a stable geometry. The polarizable continuum model (PCM) family of solvent models is used to achieve a stable structure in both the ground and excited electronic states. The Onsager model, integral equation model (IEF-PCM), the static isodensity surface model (IPCM), the self-consistent isodensity model (SCI-PCM), and the conductor screening model (C-PCM) are used for all calculations. Calculations assuming vacuum do not result in stable zwitterionic forms. The electronic transition dipole moment components are also extracted for use in the sum-of-states calculation.

Thirteen single point energies are determined along a grid spacing of 0.05 along the un-mass-weighted normal coordinates. The normal mode coordinates are mass weighted for the determination of force constants. The PESs are treated as a Taylor series expansion to the third order, where the coefficients are determined by fitting a third order polynomial to the grid of single point energies. Unlike the ground electronic state, some of the ground electronic state vibrational modes have first order force constants, indicating that the equilibrium geometry shifts in the excited state. First order force constants and third order force constants (responsible for anharmonicity) are treated as a perturbation to a Harmonic Oscillator (HO) Hamiltonian. Using 16 HO wavefunctions as a basis set, it is possible to determine wavefunctions that account for anharmonicity as well as a change in the equilibrium geometry in the excited electronic state, from first order perturbation theory. Although fewer Morse Oscillator (MO) wavefunctions may fit the true vibrational wavefunctions, the HO wavefunctions are mathematically more convenient. These wavefunctions are then used to calculate the F-C factors and H-T terms used in the polarizability tensor calculation.

The calculation of the Raman intensity I averages over all orientations according to Wilson, Decius, and Cross.[15] The isotropic α_{iso} and anisotropic α_{aniso} invariants are calculated as equations (2-4):

34

$$\alpha_{iso} = \frac{1}{9}\left(\alpha_{xx} + \alpha_{yy} + \alpha_{zz}\right)^2 \tag{2}$$

$$\alpha_{aniso} = \frac{1}{4}\left[\left(\alpha_{xx} - \alpha_{yy}\right)^2 + \left(\alpha_{yy} - \alpha_{zz}\right)^2 + \left(\alpha_{xx} - \alpha_{zz}\right)^2 + 6\left(\alpha_{xy}^2 + \alpha_{xz}^2 + \alpha_{yz}^2\right)\right] \tag{3}$$

$$I \propto 45\alpha_{iso} + 13\alpha_{aniso} \tag{4}$$

where $\alpha_{\rho\sigma}$ is the $\rho\sigma^{\text{th}}$ element of the polarizability tensor, and ρ and σ stand for the Cartesian coordinates. All spectra presented use the vibrational frequencies determined by Gaussian, the intensities calculated using equations (1-4), and the Lorentzian lineshape with a FWHM of 10 cm^{-1}. Vibrational frequencies are scaled with a correction factor of 0.967 that is appropriate for the B3LYP/6-311+G(d,p) method.

Some alternative approaches are also attempted, but do not show results that could aid in the analysis of the experimental data. First, for more accurate determination of anharmonicity and coupling between normal modes, the vibrational self-consistent field (VSCF) method as implemented in the code NWCHEM 6.1 is attempted. To calculate couplings, all possible pairwise combinations of vibrational modes are scanned. While calculations on the individual Tyrosine molecule in vacuum successfully complete, calculations including a polarizable continuum model fail with the VSCF method.

For ongoing work necessary to treat surface interaction induced coupling between modes, coupling between normal coordinates will be handled by treating the PES as two-dimensional rather than one-dimensional. Mixed derivatives describing the two-dimensional PES will be used as a perturbation that effectively mixes the vibrational wavefunctions determined from the one-dimensional case.

2.3 Experimental methods

The solution phase samples for the cross section measurements are prepared by dissolving the material of interest in ultrapure water. High performance liquid chromatography (HPLC)-grade acetonitrile (Sigma-Aldrich) is added to the solutions as a cross section internal standard. The monomer amino acids are obtained from Sigma-Aldrich, while the peptide oligomers are obtained from RS Synthesis. The peptides are sensitive to photodegradation due to ultraviolet (UV) absorption during the measurements. To mitigate this effect, the solution samples are magnetically stirred in small glass cups during the measurements, so that the laser beam is continuously exposed to fresh sample. The cups are covered with UV-transparent quartz cover slips to prevent evaporation of the acetonitrile internal standard. Measurements are also performed with material in the solid state. In these cases, the sample is simultaneously spun and linearly translated under the laser beam to minimize photodegradation.

The UV resonance Raman spectroscopy measurements are carried out with an in-house built spectrometer system. The UV laser light is generated with two different laser systems. A Coherent Sabre FreD frequency-doubled argon-ion laser is used to generate 229 nm and 244 nm continuous wave (CW) excitation light. A Crystalaser frequency-quadrupled pulsed Nd:YLF laser is used to generate 262 nm radiation with a high-repetition rate (~3 kHz) and low pulse energies. In all cases the incident laser power on the sample averages ~10-50 mW. The excitation radiation is weakly focused on the sample with a 150 mm focal length lens. A 15X reflecting objective (Edmund Optics ReflX, N.A. = 0.28, working distance 24.5 mm) is used to collect the Raman scattered light. A backscattering configuration is used in which the laser beam is directed onto the sample by a right angle mirror attached to the central obscuration of the reflecting objective. An additional 150 mm lens focuses the Raman scattered light on the spectrometer entrance slit. The spectrometer slit width is set to 100 μm. UV-grade quartz lenses and aluminum mirrors are used in all cases to steer and focus the laser beam and collect the Raman scattered light. The Rayleigh scattered excitation light is filtered by long-pass filters (Barr Associates) designed for each excitation wavelength. A Princeton Instruments SP2500 triple grating spectrometer (0.5 m focal length, f/6.2) is used to disperse the Raman scattered light. For the measurements described here, a 2400 grooves/mm grating blazed at 300 nm is used. The light is detected using a PI/Acton Pixis 2K thermoelectrically-cooled UV-enhanced charge-coupled device (CCD) camera (2048 × 512 pixels). The Raman shift is calibrated for each excitation wavelength by measuring known bands of acetonitrile and cyclohexane.

UV-visible (UV-Vis) absorption measurements are performed using a Thermo Evolution 60 UV-Vis spectrometer to obtain the absorbance in the wavelength range from 190-800 nm. The samples are measured in a 1 cm path length quartz cell, with concentrations varying depending on the properties of the materials. The absorbance values obtained are then converted to molar absorptivities. In addition to providing general guidance for the resonance Raman spectroscopy measurements, the absorption measurements provide parameters necessary to correct for

absorption effects on the Raman cross section values. As previously mentioned, the cross section standard used in this work is acetonitrile. The cross section values for acetonitrile are obtained from the work of Asher *et al*.[16]

3. RESULTS AND DISCUSSION

3.1 Electronic absorption spectra (UV-Vis) and peptide UV-resonant Raman

The first task is to verify that the Tyrosine chromophore dominates the electronic structure at lower energies of the compounds tested. To satisfactorily test the hypothesis, the effect of the resonance enhancement must arise from the Tyrosine chromophore, and not some other part of the molecule. Figure 2 shows the results of both result of theoretical modeling using the IEF-PCM model of water and experimental UV-Vis measurement. Measurements show little difference in the absorption spectra between Tyrosine, and the Tyrosine containing peptides. We can conclude that experimentally at least, the electronic structure for optical wavelengths greater than 200 nm is dominated by Tyrosine. For the theoretical measurements, the predicted spectra have the general shape as the experimental data, but they underestimate the absorption wavelengths by 20 nm. For Tyrosine, the theoretical model predicts the lowest energy absorption feature would be centered around ~240 nm. A multi-reference *ab initio* method may be necessary to improve accuracy. Theoretical calculations are also performed for a series of peptides containing Serine (TyrSerCys and TyrSerSerCys, these are examined because they are expected to be more water soluble), but the results predicted addition of Serine residues would significantly alter the electronic structure of the peptide. As a result, the Serine containing peptides are not used.
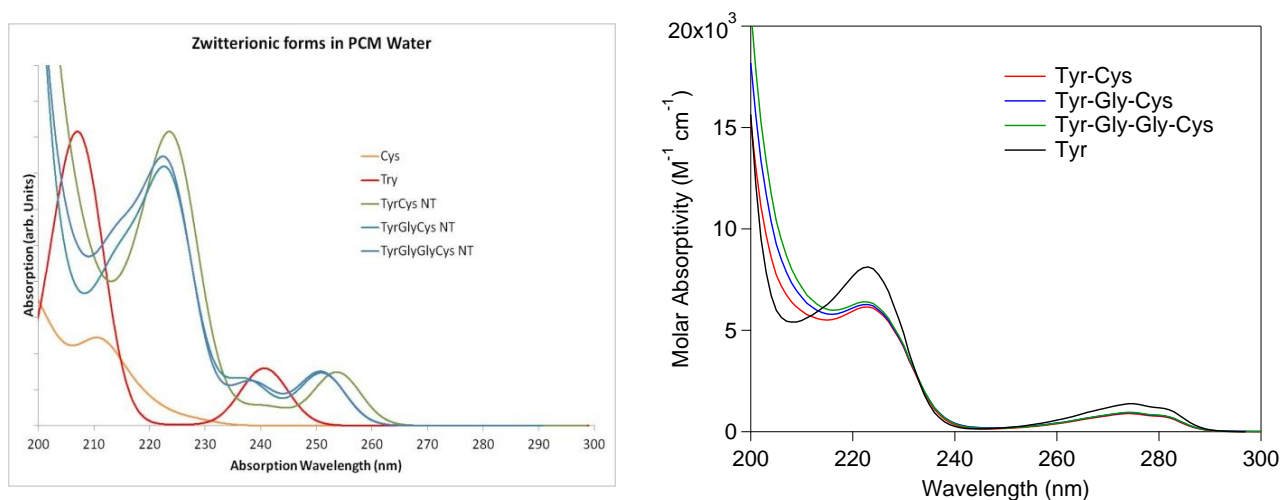

Figure 2. Comparison of the theoretical modeling of the peptide series compared to the experimental UV-Vis measurement. The modeling shows some difference between Tyrosine and the peptide series, but the measurement shows these are almost identical.

Figure 3 shows the RRS spectra of the three peptides of interest at both 229 nm and 244 nm in wavelength. For each of the peptides, the resonance Raman spectrum is nearly identical. This observation is consistent with the UV-Vis measurements, that the Tyrosine chromophore dominates the electronic structure at the lower electronic states.
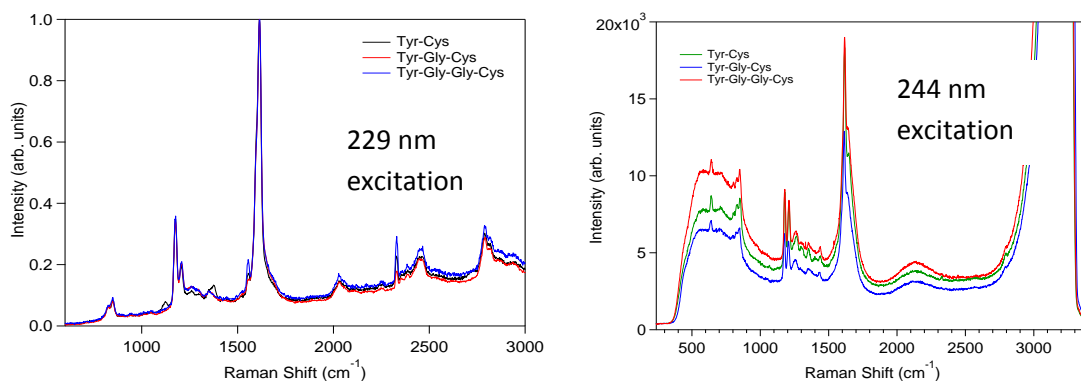
Figure 3. Resonant Raman measurements at 229 nm, and 244 nm of TyrCys, TyrGlyCys, and TyrGlyGlyCys. The spectra are nearly identical to each other and to pure Tyrosine.

3.2 Sum of states modeling of the Tyrosine resonant Raman spectrum

In order to properly benchmark the sum-of-states approach used here, initial modeling efforts focus on Tyrosine rather than the full length peptides. Figure 4 shows the Albrecht A and B terms that contribute to the enhanced Raman spectrum. The first observation that can be made is that according to this sum-of-states model, the A term contribution is up to nine orders of magnitude greater intensity than the B term. Another observation is that in contrast to the A term that only enhance a few vibrational modes, most of the vibrational modes contribute to the B term. Selectivity for the symmetry of the vibrational mode accounts for the few peaks visible in the A term contribution.
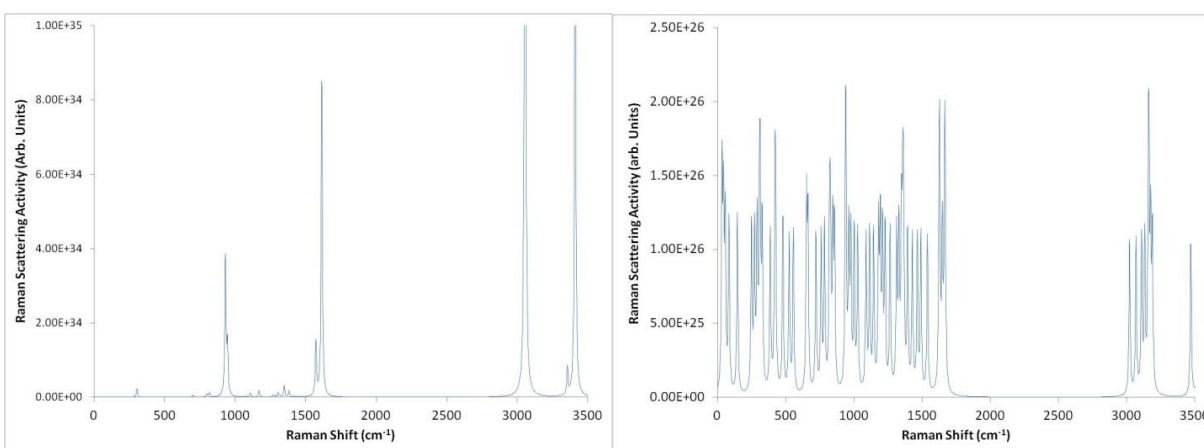

Figure 4. Resulting Spectra from the Albrecht A (left) and B (right) terms. Note the A term contribution is ~nine orders of magnitude more intense than the B term contribution.

The modes that contribute to the most prominent peaks in the A term spectrum appear at 315 cm^{-1}, 800 cm^{-1}, 931 cm^{-1}, 1139 cm^{-1}, 1396 cm^{-1}, 1593 cm^{-1}, 1610 cm^{-1}, and 1613 cm^{-1}. The strongest peak in the predicted Tyrosine spectrum appears at around ~1610 cm^{-1}. A number of vibrational modes at 1613 cm^{-1}, 1610 cm^{-1}, 1593 cm^{-1}, 1575 cm^{-1}, and 1571 cm^{-1} contribute to this feature. Although the feature at 1593 cm^{-1} arises from a mode involving ring stretching (Figure 5), the model predicts its contribution is nearly two orders of magnitude less than the vibrational mode at 1610 cm^{-1}. An examination of the normal mode representations in Figure 5 and their corresponding intensities in the predicted spectrum (arrows indicate the direction of atomic motion along the normal coordinate) show that symmetry filters most of the modes from the resonance Raman. The peak at 1610 cm^{-1} involves very symmetric motions about the protonated amine site. Although the motion vectors of the vibrational aromatic ring stretching mode at 1593 cm^{-1} are also highly symmetric, the motion of the hydrogen on the hydroxyl group breaks this symmetry. The normal mode at 1613 cm^{-1} supports this interpretation as well. Although two of the hydrogen motions around the amine are symmetric, the motion of the third hydrogen breaks this symmetry, and the contribution of this mode to the A term is orders of magnitude less. Perhaps the reduction in symmetry correspondingly reduces the contribution to the A term. It should be noted that the peak at 931 cm^{-1} is nearly as

prominent as the one at 1610 cm^{-1}, yet as can be seen in Figure 5, the out of plane hydrogen bends are not highly symmetric. Although hydrogens that are on opposite sides of the ring move in the same direction (two mirror planes of symmetry for this mode), the magnitudes are not similar. Surprisingly, the model spectrum does not predict any strong Raman features for ring-breathing or ring stretching modes.
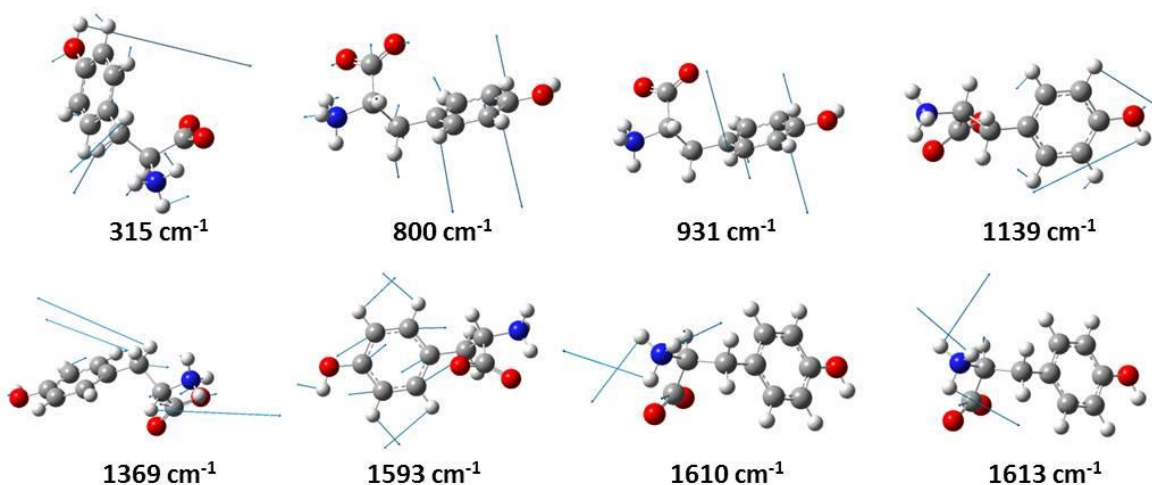

315 cm^{-1} 800 cm^{-1} 931 cm^{-1} 1139 cm^{-1}

1369 cm^{-1} 1593 cm^{-1} 1610 cm^{-1} 1613 cm^{-1}

Figure 5. Pictures of vibrational modes at 315 cm^{-1}, 800 cm^{-1}, 931 cm^{-1}, 1139 cm^{-1}, 1396 cm-1, 1593 cm^{-1}, 1610 cm^{-1}, and 1613 cm^{-1}, respectively. Surprisingly, the sum-of-states implementation used here predicts the strongest peak in the UV-resonance Raman spectrum arises from amine hydrogen motions at rather than stretches around the aromatic ring.

It is instructive to compare the model spectrum and the experimental spectrum of Tyrosine, as shown in Figure 6. The experimental spectrum has peaks at 845 cm^{-1}, 1176 cm^{-1}, 1206 cm^{-1}, 1267 cm^{-1}, 1352 cm^{-1}, and 1616 cm^{-1}. Of these peaks, only the ones at 1176 cm^{-1}, 1267 cm^{-1}, 1352 cm^{-1}, and 1616 cm^{-1} are somewhat in agreement with the model spectrum. Most notably, a number peaks that appear strong in the model spectrum, do not appear at all in the experimental spectrum. The peaks at 931 cm^{-1} and 945 cm^{-1} are nearly the same intensity as the most intense peak. These two modes involve out of plane bends by the aromatic hydrogens, where the motion of hydrogens on opposite sides of the ring points in the same direction. Within the model system, both modes have two mirror planes of symmetry. Based on symmetry selection, these two modes should have significant intensity in the experimental spectrum. A possibility is that the Tyrosine molecules in solution have different conformations. The dihedral angle of the aromatic hydroxyl group on Tyrosine has a dramatic impact on the symmetry of the vibrations, yet the energy barrier to rotation of that angle is not high. It is quite possible that in solution, the dihedral angle is such that the hydrogen points out of the plane of the ring. If so, many of the ring stretching and ring breathing modes become symmetric, and may contribute significantly to the spectrum. Clearly, more minima on the conformational potential energy surface must be explored to determine the effect of conformation on the model spectrum. Certainly, UV-RRS has been used in the literature to measure the α and ψ angles within proteins[17,18], and discrepancies between the model and experimental molecular geometries could account for the differences in the spectra.
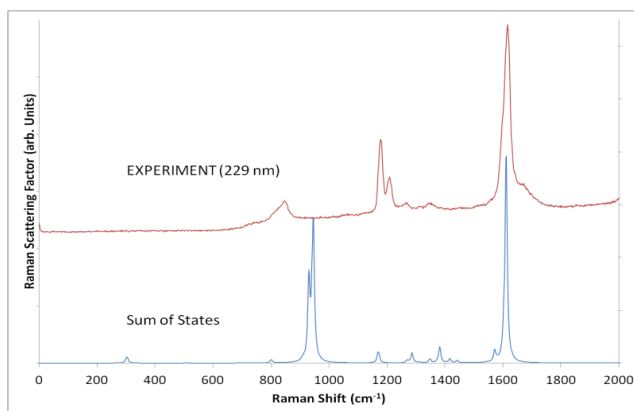
Figure 6. Comparison of the Sum-of-States model to experimental measurement at 229 nm. The experimental spectrum has peaks at 845 cm^{-1}, 1176 cm^{-1}, 1206 cm^{-1}, 1267 cm^{-1}, 1352 cm^{-1}, and 1616 cm^{-1}. Of these peaks, only the ones at 1176 cm^{-1}, 1267 cm^{-1}, 1352 cm^{-1}, and 1616 cm^{-1} are somewhat in agreement with the model spectrum. The model spectrum also emphasizes the large peak at 945 cm^{-1}, which does not have a corresponding peak in the experimental spectrum.

The model results from Tyrosine alone predict that motions of hydrogen on the amine terminus make the greatest contribution to the large peak around 1610 cm^{-1}. If this is so, then we should expect the location of the amine terminus to affect that Raman feature. Figure 7 compares the model spectra predicted for CysGlyGlyTyr (amine terminus on Cysteine) and for TyrGlyGlyCys (amine terminus on the Tyrosine). Figure 7 (left) shows that the peak at 1593 cm^{-1}, where we would expect the amine features to appear, is reduced in intensity relative to the other peaks. Many of the other peaks, especially the modes involving ring breathing and stretching are relatively much stronger. In contrast, for TyrGlyGlyCys, the peak at 1708 cm^{-1} that involves amine hydrogen motion is one of the dominant peaks. However, other modes contribute to the intensity of this feature, including a ring stretching mode at 1628 cm^{-1}, in plane aromatic hydrogen bends, and even some C=O stretching from the acid terminus. Based on this observation, the protonated amine functional group could not serve as a distinctive peak to observe the effect of resonance Raman die-off as a function of distance from the Tyrosine chromophore.
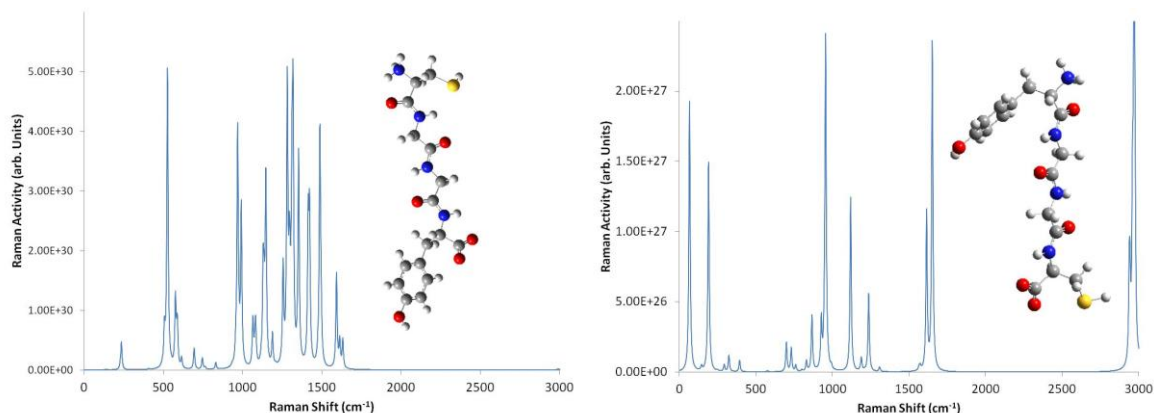
Figure 7: CysGlyGlyTyr (left) and TyrGlyGlyCys (right). Note the lowest energy conformation of the peptides determined by Gaussian is different for the amine terminus on the Tyrosine vs. on the Cysteine.

It should be noted that RRS via the sum-of-states approach could not be calculated for Cysteine alone. Cysteine can photodegrade, and when calculating the excited state potential energy surfaces, a repulsive surface was found (i.e., no local minimum could be determined within the calculation grid). As a result, real force constants, HO wavefunctions, and F-C factors could not be determined. As a result, inclusion of Cysteine as an indicator for Raman enhancement is not helpful.

4. CONCLUSIONS

Peptides containing Tyrosine, Cysteine, and Glycine are used to study RRS and how RRS is affected by the intermolecular environment. Tyrosine serves as the optical chromophore, Cysteine contains the S-H stretch which has a distinctive frequency, and Glycine serves as a spacer to increase distance between the S-H and the Tyrosine chromophore. A means of calculating the RRS response from the ground and excited electronic state vibrational potential energy surfaces has been devised, for both the Albrecht A and B terms. Experimental UV Raman, standard Raman, and UV-Vis absorption measurements are performed on the set of peptides, as well as the free Tyrosine and Cysteine. For the UV-Vis absorption and RRS measurements of the peptides, the response from the series of peptides is nearly identical for both the Raman and the UV-Vis absorption.

A number of difficulties are encountered with the current approach. First, due to the asymmetry of the S-H stretch mode, this mode contributes to the much weaker B term, and we conclude that the S-H stretch is unsuitable for tracking the effect of resonance enhancement. Second, there is significant disagreement between the predicted and measured RRS of Tyrosine. Peaks that appear in the experiment, especially those that would be assigned to aromatic ring stretching or breathing, do not appear in the model spectra, or the model predicts features that do not appear in the experimental measurement. Third, although the model correctly predicts one of the intense features in the experimental spectrum, it is not clear which normal mode at this frequency is the true contributor. The model predicts the protonated amine functional group is the prime contributor, but a ring stretching mode is also close in frequency and is predicted to have two orders of magnitude less intensity. This result is not consistent with previously reported work.

Three aspects of the model need to be explored further to answer the unresolved difficulties above, such as the effect of water model used, the effect of molecular conformation, and the effect of functional choice on the accuracy of the time dependent-density functional theory (TD-DFT) calculations. First, the resonance Raman is known to be sensitive to inter and intra molecular interactions near the optical chromophore, and both the solvent model and conformation have an impact on the Raman. With respect to conformation, it is likely several minima exist on the potential energy surface, and the Raman response as a function of position on that surface would need to be explored to validate (or invalidate) the sum-of-states model used. Second, comparison UV-Vis absorption spectra show disagreement between the UV-Vis measurements and the TD-DFT calculations. Other functionals should be attempted to more accurately model the excited state surfaces, since these are critical to the calculation of the resonance Raman response.

The results of the model used here have been compared to preliminary results calculated by Dr. Semion Saikin at Harvard University. While their results also have significant differences with the experimental measurements, the major bands in their spectra are assigned to the motions of the aromatic ring, which is the more expected result. Validation of our sum-of-states approach may require a different molecule. As risk mitigation, it may be necessary to adopt the approach of Dr. Saikin in the calculation of resonance Raman response as a function of intermolecular interaction.

The primary purpose of this study is to understand the impact of intermolecular interactions on the resonance Raman process. While much effort is devoted to implementing a theoretical method that helps explain that connection, work is ongoing to address the effect of intermolecular interactions.

REFERENCES

[1]   Farrell, M.E., Holthoff, E.L., and Pellegrino, P.M., "Next generation Surface Enhanced Raman Scattering (SERS) substrates for Hazard Detection," in *Chemical, Biological, Radiological, Nuclear, and Explosives*. vol. 8358, A. W. Fountain, Ed., ed, **2012**.

[2]   Christesen, S.D. et al., *Applied Spectroscopy,* **2008**, 62, p1078-1083.

[3]   Guicheteau, J. et al., *Applied Spectroscopy,* **2008**, 62, p267-272.

[4]   Rava, R.P. and Spiro, T.G., *Journal of the Americal Chemical Society,* **1984**, 106, 3.

[5]   Langkilde, F.W. et al. *Journal of Chemical Physics,* **1994**, 100, p3503-3513.

[6]   Albrecht, A.C., *Journal of Chemical Physics,* **1961**, 34, p1476-1484.

[7]   Lombardi, J.R. and Birke, R.L., *Journal of Physical Chemistry C,* **2008**, 112, p5605-5617.

[8]   He, R. et al., *Physical Review B,* 2011, 83.

[9] Birke, R.L., Znamenskiy, V. and Lombardi, J.R., *Journal of Chemical Physics,* **2010**, 132, 214707.

[10] Lathrop, E.J.P. and Friesner, R.A., *Journal of Physical Chemistry,* **1994**, 98, p3050-3055.

[11] Jensen, L. et al., *Journal of Chemical Physics,* **2005**, 123.

[12] Dirac, P.A.M., *Proceedings of the Royal Society of London,* **1927**, 114, p710-728.

[13] Kramers, H.A. and Heisenberg, W., *Zeitschrift fur Physik,* **1925**, 31, p681-708.

[14] Frisch, M.J. et al., "Gaussian 2009, Revision C.01, ed. Wallingford CT: Gaussian, Inc., **2009**.

[15] Wilson, E.B., Decius, J.C., and Cross, P.C., *Molecular Vibrations*. New York: McGraw-Hill, **1955**.

[16] Dudik, J.M., Johnson, C.R., and Asher, S.A. *Journal of Chemical Physics,* **1985**, 82, p1732-1740.

[17] Ma, L. et al., *Journal of Physical Chemistry B,* **2007**, 111, p7675-7680.

[18] Mikhonin, A.V. and Asher, S.A., *Journal of the American Chemical Society,* **2006***, 128, p13789-13795.

SSI PROJECTS
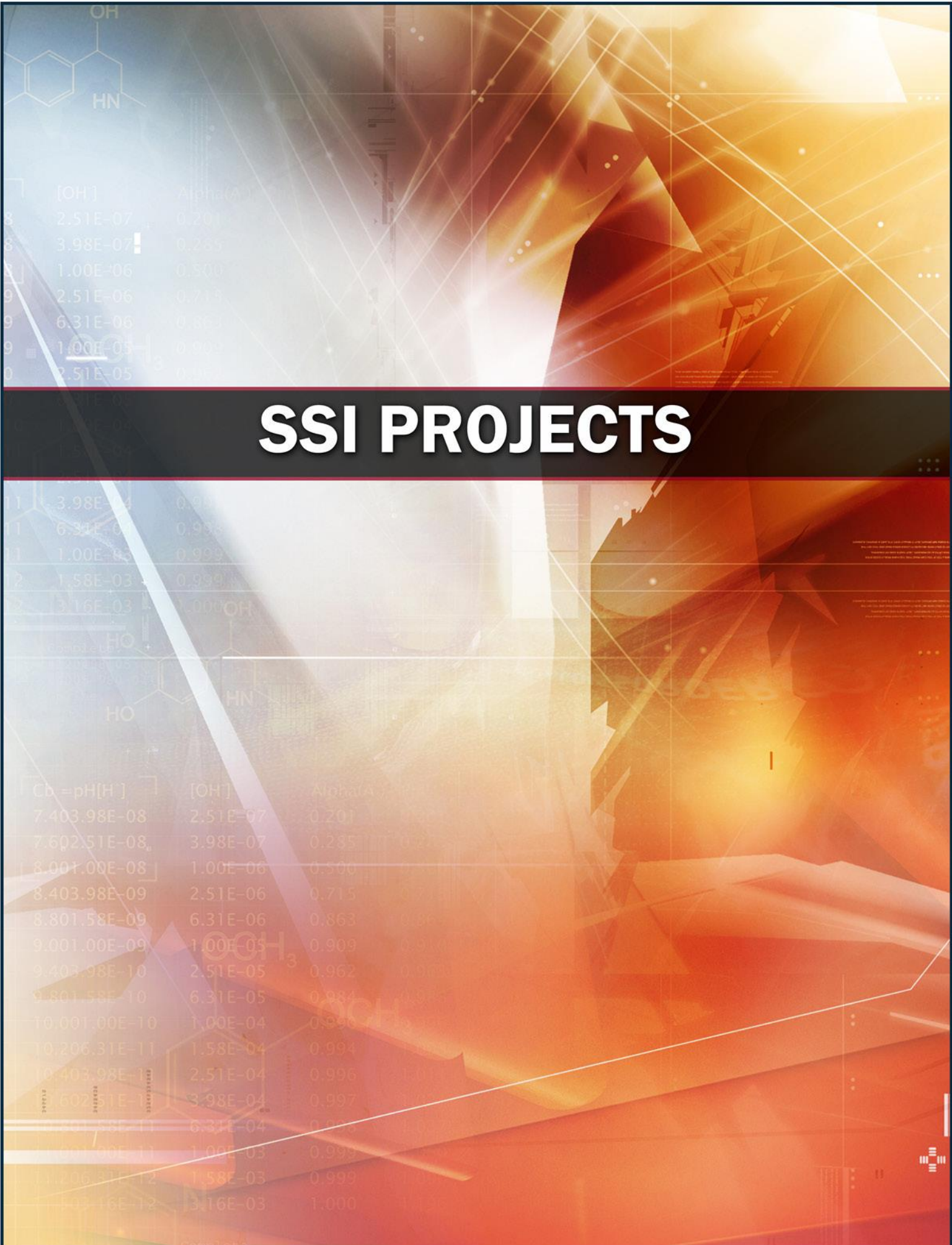
Layer-by-layer self-assembly of plexcitonic nanoparticles

Brendan G. DeLacy[a,*], Wenjun Qiu[b], Marin Soljačić[b], Chia Wei Hsu[b], Owen D. Miller[c],
Steven G. Johnson[c], and John D. Joannopoulos[b]
[a]U.S. Army Edgewood Chemical Biological Center, Research and Technology Directorate,
5183 Blackhawk Rd, Aberdeen Proving Ground, MD 21010
[b]Department of Physics, Massachusetts Institute of Technology
77 Massachusetts Ave, Cambridge, MA 02139
[c]Department of Mathematics, Massachusetts Institute of Technology
77 Massachusetts Ave, Cambridge, MA 02139

ABSTRACT

Colloidal suspensions of multilayer nanoparticles composed of a silver core, a polyelectrolyte spacer layer (inner shell), and a J-aggregate cyanine dye (outer shell) have been prepared for the first time. Absorption properties of the colloid were measured in the visible region. This multilayer architecture served as a framework for examining the coupling of the localized surface plasmon resonance exhibited by the silver core with the molecular exciton exhibited by the J-aggregate outer shell. The polyelectrolyte spacer layer promotes the formation of an excitonic J-aggregate while serving as a means of controlling the plasmon-exciton (i.e., plexciton) coupling strength through changing the distance between the core and the shell. An analytical expression based on Mie Theory and the Transfer Matrix Method was obtained for describing the optical response of these multilayered nanostructures. Computational and experimental results indicate that the absorption wavelength of the J-aggregate form of the dye is dependent on both the distance of the dye layer from the silver core and the degree of dye aggregation.

Keywords: nanomaterials, scattering theory, extinction.

1. INTRODUCTION

Silver and gold nanoparticles (NP) have been studied extensively for their unique optical properties in the ultraviolet (UV), visible (Vis), and infrared (IR) regions of the electromagnetic spectrum.[1-4] These properties arise from the collective oscillation of conduction band electrons throughout the particle in response to optical excitation, a process commonly termed as localized surface plasmon resonance. Resonance occurs when the frequency of incident radiation is at or near the frequency of the electronic oscillation. This resonance results in a strong enhancement of the local electric field, useful for surface-enhanced Raman scattering (SERS), surface-enhanced fluorescence, and the study of nonlinear optical response.[5-7] Additionally, the size and morphology of the silver and gold NPs have a significant impact on surface plasmon resonance frequency and, therefore, have a great significance in such fields as sensors and photonic devices.

Cyanine dyes are commonly used in spectral sensitization, and have potential application in novel optoelectronic materials.[8] Structurally, these dyes consist of two heterocyclic units that are connected by an odd number of methine groups $(CH)_n$ (n = 1,3,5, etc.). The color of the dye is mainly determined by the length of the polymethine chain.[9] A particularly intriguing property of cyanine dyes is their tendency to aggregate under certain conditions in solution. These so called J-aggregates exhibit a narrow absorption band that is red-shifted with respect to the monomer absorption band.[9] The shift in absorption of the aggregate has been described by a Frenkel exciton model, in which excited states are formed by the coherent coupling of molecular transition dipoles.[10,11]

Multi-layered NPs, composed of both a noble metal and a J-aggregate dye, provide a unique framework for studying plexciton interactions. Numerous structures exhibiting these plexciton interactions have been fabricated and studied in recent years. Some nanostructures have involved the direct adsorption of J-aggregate dyes onto the surface of silver NPs with varying geometries.[12-14] Other efforts have focused on the aggregation of cyanine dyes onto complex geometries. For example, cyanine dyes were adsorbed onto silica core/gold shell NPs.[15] In these studies, the absorption spectra of these composite NPs were not the simple sum of the absorption of the metal NP and the J-band of the aggregate. Rather, strong plexciton interactions were observed, resulting in a shift in the absorption bands of

the individual plasmon and exciton resonances. A more recent study by Yoshida *et al.* explored the impact of inserting a spacer layer (inner shell) between a metallic core particle (Au) and an outer J-aggregate dye layer (outer shell).[16] The spacer layer used in the study was a cationic thiol which promoted the J-aggregation of anionic cyanine dyes onto the surface of the nanocomposite. The spectral line shape of these composites was dependent on the strength of the plexciton coupling between the metal core and the J-aggregate shell.

The metallic core composition and size, excitonic shell composition, degree of J-aggregate formation within the excitonic shell, and distance between the plasmonic core and excitonic shell are among the factors that play the most significant roles in controlling optical response. Metallic core particles and excitonic dyes of varying composition are readily available and selection is based on the intrinsic optical properties of the material. In terms of particle shape, a range of metallic core shapes such as spheres, rods, and platelets may be fabricated using well documented solution-based techniques.[17-20] However, spacer layer thickness and its impact on plexciton coupling in these NP systems have not been studied systematically. The spacer layer must serve the two-fold purpose of promoting the formation of a J-aggregate shell while also creating a distance, with specified length, between the metallic core and excitonic shell. To that end, we report the use of a variably thick polyelectrolyte spacer layer as a means of building multilayered plexcitonic NPs and controlling plexciton distance. Specifically, we report the use of alternating cationic poly(diallyldimethyl ammonium chloride) (PDADMAC) and anionic poly(styrene sulfonate) (PSS) as a spacer layer between a silver core and a J-aggregate outer shell. The layer-by-layer self-assembly of oppositely charged polyelectrolytes has been used extensively as a means of coating and functionalizing colloidal particles.[21,22] The thickness of the polyelectrolyte spacer layer was controlled in this study by varying the number of PDADMAC/PSS layers that were adsorbed. The outer J-aggregate shell was formed by adsorbing the cationic form of 1,1'-diethyl-2,2-cyanine iodide (PIC) onto the outermost anionic PSS layer. A schematic of the double-shell structure is provided in Figure 1A. Figure 1B provides a schematic of the electrostatic adsorption of PIC J-aggregates at the surface of a PDADMAC/PSS coated silver NP. The use of a polyelectrolyte spacer layer may be incorporated into a wide range of core-shell systems, regardless of geometry and composition. Therefore, this approach may be used as a means of studying plexciton coupling in a wide range of multilayered plexcitonic structures.
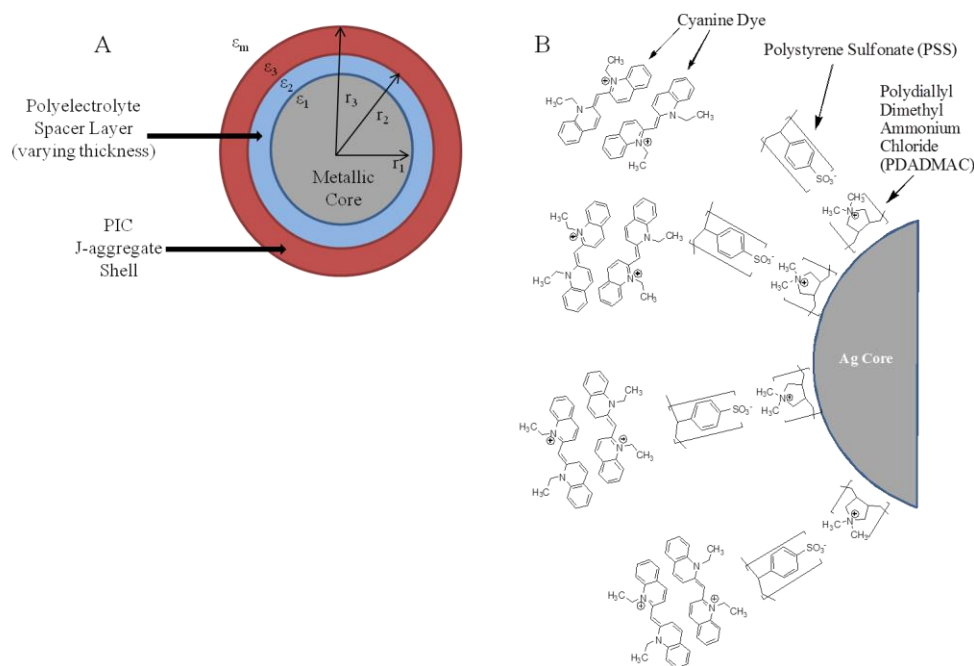

Figure 1. Schematic of (A) a double-shell structure composed of a silver metallic core, a spacer layer consisting of alternating layers PDADMAC/PSS polyelectrolytes, and a PIC exterior shell. The outer radius and dielectric function of individual layers are (R_i, ε_i, i = 1,2,…, n). The dielectric function of the medium is ε_m. (B) The electrostatic adsorption of PIC J-aggregates onto a silver core/polyelectrolyte spacer. Na^+, Cl^-, and I^- ions are not drawn for clarity. Figures are not drawn to scale.

In order to explain the measured absorption features of the silver/polyelectrolyte/PIC composite NPs, Mie Theory and the Transfer Matrix Method were used to calculate the optical response of these multilayered nanospheres.

Numerical simulations yielded good agreement with experimental results. Specifically, the impact of polyelectrolyte spacer layer thickness on the shift of the exciton frequency was elucidated. These results indicate that a polyelectrolyte spacer layer is a plausible means for tuning plexciton coupling in colloidal suspensions of multilayered plexcitonic NPs.

2. EXPERIMENTAL METHODS

Silver nitrate, trisodium citrate tribasic dihydrate, sodium PSS (MW ~70,000), PDADMAC (medium molecular weight 26062-79-3), sodium phosphate monobasic dihydrate, sodium phosphate dibasic dihydrate, and 1,1'-diethyl-2,2'-cyanine iodide were purchased from Sigma Aldrich (St. Louis, MO).

Silver NPs were prepared using a modified procedure by Lee and Meisel in which Ag^+ ions are chemically reduced in aqueous solution.[17] Approximately 110 mg of $AgNO_3$ were dissolved in 400 mL deionized H_2O (18 MΩ) and placed in a 1 L three-neck flask. A condenser tube (250 mm jacket length) was placed on the center neck of the flask to minimize evaporation losses. An addition funnel, containing 10 mL of 1% (wt/wt) trisodium citrate solution, was attached to a second neck of the flask. The solution was magnetically stirred and heated to 100°C using a heating jacket and temperature controller (Glass-Col, Terre Haute, IN) while refluxing. Once the boiling point was reached, the trisodium citrate solution was slowly added drop-wise. The mixture was heated and stirred for an additional hour at 100°C. The solution was then cooled to room temperature and stirring continued for an additional hour. Assuming a 100% yield, the silver colloid had an approximate concentration of 0.3 mg/mL.

A standard solution of PIC was prepared by dissolving 25 mg PIC in 100 mL phosphate buffer (pH = 6.0).

Silver core – polyelectrolyte shell NPs were prepared by exposing the silver solution to supersaturated concentrations of polyelectrolytes. First, 10 mL silver solution was transferred to a 50 mL polypropylene centrifuge tube. The sample was centrifuged at 4000 RPM for 15 minutes and the supernatant containing excess citrate was removed. 5 mL H_2O were then added to the tube followed by sonication. Next, 5 mL PDADMAC (1 mg/mL, 0.01 M NaCl) were added, and the suspension was vigorously mixed for 1 minute. The solution was allowed to stand for 30 minutes. Centrifugation (4000 RPM, 15 minutes) was used to remove the supernatant and excess polymer. Two cycles of a 10 mL water addition, followed by sonication, centrifugation, and supernatant removal were performed to ensure the removal of excess polymer. The same solution concentration and procedures used for the adsorption of PDADMAC were used for adsorption of additional polyelectrolyte layers (i.e., PSS, 1 mg/mL, 0.01 M NaCl). Combinations of 2, 4, and 6 polyelectrolyte layers, (i.e., PDADMAC/PSS$_{1,2,3}$), were adsorbed onto the silver particles. The silver core – polyelectrolyte shell NPs were re-suspended in 5 mL water with sonication.

For the *in situ* generation of a J-aggregate shell on the silver core – polyelectrolyte shell NPs, the concentration of the silver core - polyelectrolyte shell NP suspension was adjusted until absorbance measurements yielded an approximate absorbance of 0.5 to 1.5 absorbance units. This involved diluting 1 mL of the suspension to 25 mL with water, placing 3 mL of the diluted suspension in a 10 mm optical path quartz cuvette, and then adding 100 μL aliquots of PIC standard (0.25 mg/mL) to the cuvette, followed by mixing and immediate absorbance measurement.

Silver/polyelectrolyte/PIC composite NPs were also prepared by exposing silver core - polyelectrolyte shell NPs to PIC for 24 hours. This involved placing 5 mL silver core – polyelectrolyte shell NPs in a 50 mL polypropylene centrifuge tube, follow by the addition of 5 mL of PIC standard. The samples sat for 24 hours to ensure adequate adsorption and aggregation of the dye onto the surface of the particles. The following day, the colloidal suspensions were centrifuged at 4000 RPM for 15 minutes, and the supernatant discarded for removal of excess PIC standard. The solid NPs were washed with 10 mL water followed by sonication, centrifugation, and supernatant removal to ensure the removal of excess PIC. The particles were then re-suspended in 5 mL water and sonicated. Finally, excessively large NPs were removed using a 0.22 μm Millex GP syringe filter. This procedure was repeated for each of the silver/polyelectrolyte/PIC NP combinations.

All UV-Vis absorption spectra were measured in a quartz cuvette (10 mm optical path length) using a V-670 spectrophotometer (JASCO Co.). Spectra were measured from 190 nm to 800 nm. Transmission electron microscopy (TEM) images were observed in a FEI (Hillsboro, OR) Tecnai 12 TWIN TEM operating at 100kV. Samples were prepared by placing 5.0 μL of the particle solution onto a freshly ionized 300 copper mesh carbon coated/formvar grid. The samples were allowed to dry completely. Images were collected using an Olympus Soft Imaging System (Lakeland, CO) Megaview III digital camera. Figures were assembled in Adobe Photoshop using

only linear adjustments in brightness and contrast. For the determination of zeta-potential (ζ-potential), a Zetasizer Nano ZS (Malvern Instruments) was used to measure the electrophoretic mobilities of colloidal particles. The mobility (μ) was converted into a ζ-potential using the Smoluchowski relation ($\zeta = \mu\eta/\varepsilon$, where η is the viscosity of the solvent and ε is the permittivity of the solvent). The hydrodynamic radius was also determined using the Zetasizer Nano ZS instrument. This measurement is a dynamic light scattering technique.

3. THEORETICAL METHODS

In order to calculate the optical response of the silver/polyelectrolyte/PIC nanocomposites, we generalize Mie theory to multilayer nanospheres via the Transfer Matrix Method.[23-25] For multilayer nanospheres, the electric field can be decomposed into orthogonal channels labeled by (σ,l), where σ takes transverse electric (TE) or transverse magnetic (TM) modes, and l = 1, 2, 3, …, n.[26-29] The scattering and absorption cross-sections are the sum of contributions from each channel, and the extinction cross-section is the sum of scattering and absorption cross-sections:

$$\sigma_{sca} = \sum_{\sigma}\sum_{l=1}^{\infty}\frac{\lambda^2}{8\pi}(2l+1)\left|1-r_{\sigma,l}\right|^2 \tag{1}$$

$$\sigma_{sca} = \sum_{\sigma}\sum_{l=1}^{\infty}\frac{\lambda^2}{8\pi}(2l+1)\left|1-r_{\sigma,l}\right|^2 \quad \sigma_{ext} = \sigma_{sca} + \sigma_{abs} \tag{2}$$

In order to determine $r_{\sigma,l}$, we decompose the electric field inside each shell into incoming and outgoing spherical waves with coefficients (A_n, B_n). The coefficients of adjacent shells are connected by the transfer matrix of that interface, whose elements are determined by the boundary condition of TE or TM modes:

$$\begin{bmatrix} A_{i+1} \\ B_{i+1} \end{bmatrix} = M_{i+1,i}\begin{bmatrix} A_i \\ B_i \end{bmatrix} \tag{3}$$

The transfer matrix of the whole system can be calculated by combining the transfer matrices of individual interfaces:

$$\begin{bmatrix} A_{n+1} \\ B_{n+1} \end{bmatrix} = M_{n+1}, M_{n,n-1}...M_{3,2}, M_{2,1}\begin{bmatrix} A_1 \\ B_1 \end{bmatrix} = M\begin{bmatrix} A_1 \\ B_1 \end{bmatrix} \tag{4}$$

Since the second kind of spherical Bessel function is singular at the origin, we can set $A_1 = B_1 = 1$. Therefore,

$$r_1 = \frac{B_{n+1}}{A_{n+1}} = \frac{M_{21} + M_{22}}{M_{11} + M_{12}} \tag{5}$$

Incorporation of the appropriate dielectric constant for the aggregated form of PIC is required for the total cross-section calculations. We use a model that describes the red-shifted energy of aggregate forms of cyanine dyes, in which[30]:

$$\varepsilon = \varepsilon_0 - 2V\cos\left(\frac{\pi}{N_c+1}\right) \tag{6}$$

Here, V is the nearest neighbor coupling energy, N_c is the number of coherently coupled molecules that make up the aggregate, and ε_0 is the frequency dependent dielectric constant of the monomer. Using this model for PIC, a red-shifted J-aggregate absorption peak at 575 nm is expected for aggregates composed of 14 or more dye molecules. This prediction is consistent with numerous experimental observations in which aggregated forms of PIC, both in solution and adsorbed onto surfaces, exhibit absorption at 575 nm.[16,31] Hence, 575 nm was taken as the excitation wavelength of the J-aggregate for the complex frequency-dependent dielectric function of the PIC J-aggregate, which was approximated using:

$$\varepsilon(\omega) = \varepsilon_0 + \frac{f\omega_0^2}{\omega_0^2 - \omega^2 - i\omega_0\gamma\omega} \tag{7}$$

Here, $\varepsilon_0 = \varepsilon_{medium} = 1.85$, ω_0 corresponds to the excitation frequency of the J-aggregate (corresponding to 575 nm), γ is the relaxation rate, and f represents the oscillator strength. Literature values for γ range from 0.01 to 0.02, and for f range from 0.01 to 1.[32]

4. RESULTS AND DISCUSSION

The citrate reduction method used in this study yielded silver core NPs with an average particle size of 54.5 nm and a standard deviation of 9.8 nm. Figure 2A displays a TEM image of the silver NPs. Most of the particles have a spherical shape with a relatively narrow size distribution, although a small amount of non-spherical particles are observed. Figure 2B displays the absorbance spectra of the silver colloid (blue curve) and the PIC standard (red curve). The silver colloid and PIC standard solutions are characterized by an absorption λ_{max} at 442 nm and 523 nm, respectively. Of particular note is the absence of the PIC J-aggregate peak, which is commonly observed at or near 575 nm. This observation is consistent with published data, as the concentration of the PIC standard in this solution is too low for the formation of the J-aggregate.[16,31]
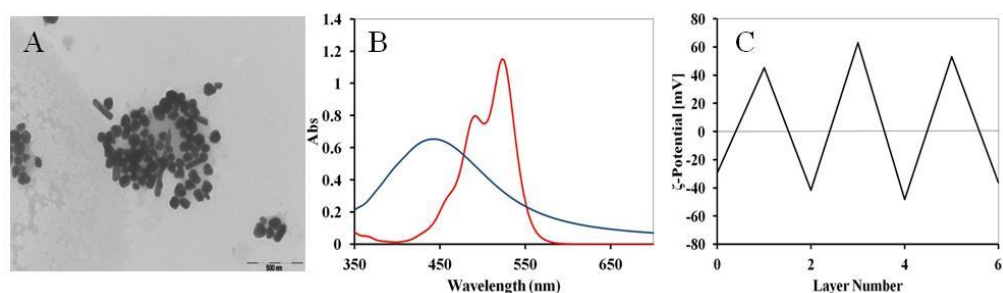

Figure 2. (A) TEM image of silver NPs fabricated using the citrate reduction method. (B) Experimental absorbance spectra of solutions containing 0.022 mg/mL silver solution (blue curve) and 0.023 mg/mL PIC (red curve). λ_{max} = 442 nm for the silver solution. λ_{max} = 523 nm for the PIC solution. (C) Zeta-potential as a function of layer number for silver particles coated with alternating layers of PDADMAC and PSS. Polyelectrolyte deposition of PDADMAC and PSS was performed in 0.01 M NaCl.

Insertion of a polyelectrolyte layer between the silver core and the cyanine dye outer shell was a central theme in this study. Specifically, our goal was to demonstrate the formation of the PIC J-aggregate on a silver core – polyelectrolyte shell composite NP. The layer-by-layer self-assembly of polyelectrolytes on colloidal particles is an established technique for building stable and functionalized multilayers on NPs. The irreversible electrostatic interaction between cationic and anionic polyelectrolyte layers aid in stabilizing these films. In our study, the sequential addition of PDADMAC and PSS, with PSS forming the outermost polyelectrolyte layer, was used to control the thickness of the polyelectrolyte layer and to render the outer surface of the particles with a negative charge. The negative surface charge promotes the adsorption and J-aggregation of the cationic PIC dye onto the surface of the particles. Figure 2C provides a summary of the ζ-potential measurements of silver particles coated with sequential layers of PDADMAC and PSS. The ζ-potential alternates between positive and negative values for the sequential additions of PDADMAC and PSS, respectively.

Silver core – polyelectrolyte shell NPs were exposed to PIC in a series of experiments. First, UV-Vis absorbance measurements of silver core – polyelectrolyte shell colloids (0.013 mg/mL) were taken immediately after the addition of 100 μL increments of PIC standard, in order to determine if the PIC J-aggregate would form *in situ*. All *in situ* experiments were performed on silver particles coated with one PDADMAC/PSS bi-layer. Figure 3 displays the absorbance spectra of these particles. As a control, the absorbance spectrum of silver/PDADMAC/PSS was determined prior to the addition of PIC. The absorbance spectrum of silver/PDADMAC/PSS is characterized by a λ_{max} at 435 nm; compared to the absorbance spectra of the silver solution displayed in Figure 2, it has a somewhat broader absorbance from 600 nm to 700 nm, possibly due to the slight agglomeration of silver core-polyelectrolyte shell NPs. As PIC standard was incrementally added, a sharp peak near 570 nm is observed, indicative of J-aggregate formation. We note that the concentration of the PIC standard is too low to form J-aggregates in solution; therefore, the observed J-aggregation of PIC must be promoted by the presence of the polyelectrolyte shell. After the sequential addition of 100 μL, 200 μL, and 300 μL of PIC standard, J-aggregate peaks were observed at 570 nm, 571 nm, and 571 nm, respectively. Typically, when fully aggregated, the J-aggregate of PIC is characterized by an

absorbance at 575 nm. Based on the theoretical model of the J-aggregate absorbance wavelength, we conclude that the PIC shell in this experiment is not in a fully aggregated form.
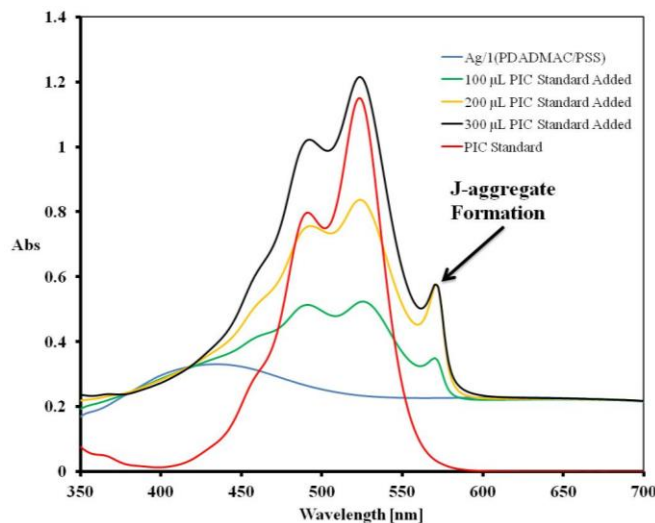

Figure 3. Experimental absorbance spectra immediately following the sequential addition of PIC standard to a colloidal suspension containing silver core-PDADMAC/PSS NPs (0.013 mg/mL), and 100 μL portions of a 0.23 mg/mL PIC standard to 3 mL of the suspension. The formation of the red-shifted J-aggregate peak was observed at 570 nm, 571 nm, and 571 nm upon addition of 100 μL, 200 μL, and 300 μL quantities of the PIC standard, respectively. For comparison, the absorbance spectra of the silver core/polyectrolyte NPs and PIC standard (0.023 mg/mL) are provided.

Next, we studied the impact of spacer layer thickness. This was achieved by adsorbing PIC to silver/polyelectrolyte composite NPs composed of one PDADMAC/PSS bi-layer, two PDADMAC/PSS bi-layers, and three PDADMAC/PSS bi-layers. In this set of experiments, formation of a fully aggregated PIC shell was promoted by exposing silver/polyelectrolyte composite NP suspensions to PIC dye for 24 hours. A TEM image of the silver/polyelectrolyte/PIC NPs is provided in Figure 4A. Figure 4C also displays the absorbance spectra of these experiments. The spectra is characterized by the formation of a red-shifted J-aggregate peak at 581 nm, 581 nm, and 579 nm for silver particles coated with one (PDADMAC/PSS), two (PDADMAC/PSS), and three (PDADMAC/PSS) shells, respectively.
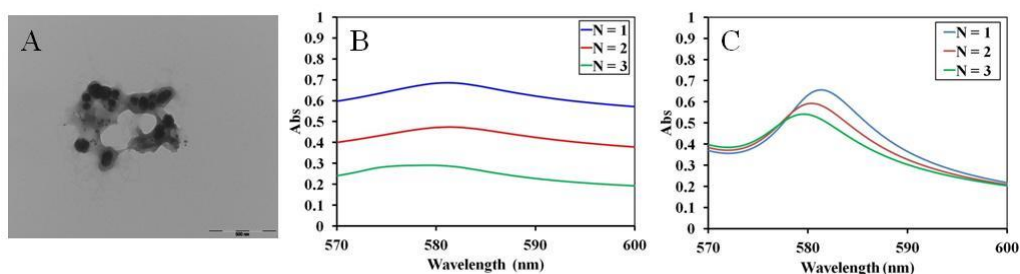

Figure 4. (A) TEM image of silver/polyelectrolyte soaked in PIC for 24 hours. (B) Experimental absorbance spectra of PIC coated silver core-polyelectrolyte shell NPs, with varying polyelectrolyte layer thickness. 1 (PDADMAC/PSS) (blue curve), 2 (PDADMAC/PSS) (red curve), and 3 (PDADMAC/PSS) (green curve) correspond to 2, 4, and 6 alternating layers of PDADMAC and PSS, respectively. Formation of the red-shifted J-aggregate peak was observed for the silver/1(PDADMAC/PSS)/PIC, silver/2(PDADMAC/PSS)/PIC, and silver/3(PDADMAC/PSS)/PIC NPs at 581 nm, 581 nm, and 579 nm, respectively. (C) Simulated absorbance spectra for the impact of spacer layer thickness on the absorption wavelength of the J-aggregate peak. An oscillator strength (f) of 0.35 and a relaxation rate (γ) of 0.015 were assumed in the calculations.

The J-aggregate peaks were observed at wavelengths that were comparatively longer than what is commonly reported in the literature for PIC (i.e., 575 nm). Additionally, the J-aggregate peak wavelength was found to increase with decreasing spacer thickness. These results suggest that the PIC was fully, or close to fully aggregated, and that the plexciton interaction further red-shifted the J-aggregate peak. This observation is consistent with the fact that

47

plexciton interactions are enhanced as the distance between the J-aggregate shell and the silver core particles is diminished.

Simulated absorbance spectra of silver/(PDADMAC/PSS)/PIC NP composites were calculated in Figure 4C in order to explain the main absorption features of the experimental data. For the dielectric constants, we used experimental frequency-dependent complex dielectric constant for the silver[33], literature values of 2.25 for PDADMAC and 2.56 for PSS[34], and Equation 8 (with $f = 0.35$ and $\gamma = 0.015$) for the PIC J-aggregate. We assume a silver core of 54.5 nm (with SD = 9.8 nm), a J-aggregate dye outer shell of 5 nm, and a polyelectrolyte spacer of thickness 1 nm per bi-layer. This calculation is consistent for similar structures, in which the thickness of the polyelectrolyte bi-layers was determined to be 1.7 to 3.0 nm.[21,34] The simulation result in Figure 4C was in qualitative agreement with the experimental absorbance spectra in Figure 4B. Namely, the experimental and simulation results demonstrate the dependence of coupling strength and shift of the exciton frequency on spacer layer thickness. The red-shifted energy of the J-aggregate peak increases as the spacer layer thickness is minimized, i.e., the plexciton interaction is maximized. Discrepancies between the experimental and simulated results, in terms of J-aggregate peak shape, may be attributed to the fact that non-spherical and/or aggregated particles were not included in the simulated results.

5. CONCLUSION

Multilayered plexcitonic NPs composed of a silver core, polyelectrolyte spacer layer, and a PIC outer shell have been synthesized. The optical properties of the composite NPs in aqueous solution were measured in the UV-Vis regions. Absorbance spectra of the colloidal NPs indicate that PDADMAC/PSS spacer layers successfully promoted the J-aggregation of PIC. The *in situ* generation of the J-aggregate was observed when PIC standard was added directly to a colloidal suspension containing silver core – polyelectrolyte shell composite NPs. The formation of the fully J-aggregated form was observed when PIC was exposed to a colloidal suspension of silver core – polyelectrolyte shell NPs for 24 hours. The 24-hour study yielded a J-aggregate absorbance at 579-581 nm, indicating the formation of a fully aggregated dye on the surface of the composites. The fully aggregated form of PIC is typically observed at 575 nm. The additional red-shift in energy that was experimentally observed may be explained by the plexciton interaction between the silver core and the J-aggregate exterior. It is concluded that the use of oppositely charged polyelectrolytes is a valid approach for inducing the formation of J-aggregates on silver core-polyelectrolyte shell particles. Furthermore, polyelectrolyte spacer layers are a means of controlling the plexciton distance, which can ultimately be used to control the shift in exciton frequency. Finally, the ease with which polyelectrolyte layers are assembled onto colloidal NPs of varying shape and composition, makes this technique suitable for building a wide range of plexcitonic particles.

ACKNOWLEDGMENTS

REFERENCES

[1]   Kerker, M., *The Scattering of Light and Other Electromagnetic Radiation*, Academic Press, New York, **1969**.
[2]   Maier, S.A., *Plasmonics: Fundamentals and Applications*, Springer, New York, **2010**.
[3]   Noguez, C., *Journal of Physical Chemistry C,* **2007**, 111, p3806-3819.
[4]   Wang, H. et al., *Accounts of Chemical Research,* **2007**, 40, p53-62.
[5]   Kneipp, K. et al., *Chemical Reviews,* **1999**, 99, p2957-2976.
[6]   Lakowicz, J.R., *Analytical Biochemistry,* **2005**, 337, p171-194.
[7]   Chakraborty, P.J. *Journal of Materials Science,* **1998**, 33, p2235-2249.
[8]   Tani, T. [Photographic Sensitivity], Oxford University, New York, **1995**.
[9]   Wurthner, F. et al., *Angewandte Chemie International Edition,* **2011**, 50, p3376-3410.
[10]   Davydov, A.S., *Theory of Molecular Excitons*, Plenum, New York, **1971**.

[11] van Burgel, M. et al., *Journal of Chemical Physics,* **1995**, 102, p20-33.
[12] Hranisavljevic, J., et al., *Journal of the American Chemical Society,* **2002**, 124, p4536-4537.
[13] Wurtz, G. A. et al., *Nano Letters,* **2007**, 7, p1297-1303.
[14] Kometani, N. et al., *Langmuir,* **2001**, 17, p578-580.
[15] Fofang, N. T. et al., *Nano Letters,* **2008**, 8, p3481-3487.
[16] Yoshida, A. et al., *Langmuir,* **2009**, 25, p6683-6689.
[17] Lee, P.C. and Meisel, D., *Journal of Physical Chemistry,* **1982**, 86, p3391-3395.
[18] Busbee, B.D. et al., *Journal of Advanced Materials,* **2003**, 15, p414-416.
[19] Zhang, Q.; et al. *Journal of the American Chemical Society,* **2011**, 133, p18931-18939.
[20] Jana, N. R.; et al. *Chemical Communications,* **2001**, 0(7), p617-618.
[21] Sukhorukov, G.B., et al. *Colloids and Surfaces A: Physicochemical and Engineering Aspects*, **1998**, 137, p253-266.
[22] Sukhorukov, G.B.; et al. *Polymers for Advanced Technologies,* **1998**, 99, p759-766.
[23] Qiu, W. et al., *Optics Express,* **2012**, 20, p18494-18504.
[24] van de Hulst, H.C., *Light Scattering by Small Particles*, Dover, New York, **1981**.
[25] Bohren C. and Huffman, D., *Absorption and Scattering of Light by Small Particles*, John Wiley & Sons, New York, **1983**.
[26] Hamam, R. E. et al., *Physical Review A,* **2007**, 75, p053801.
[27] Ruan, Z. and Fan, S., *Physical Review Letters,* **2010**, 105, p013901.
[28] Ruan, Z. and Fan, S., *Journal of Physical Chemistry* C, **2010**, 114, p7324-7329.
[29] Ruan, Z. and Fan, S. *Applied Physics Letters,* **2011**, 98, p043101.
[30] Kobayashi, T., *J-Aggregates*, World Scientific Publishing Co. Pte. Ltd., Singapore, **1996**.
[31] Dixon, A. et al., *American Journal of Undergraduate Research,* **2005**, 3, p29-34.
[32] Kuhn H.; and Foresterling, H.D., *Principles of Physical Chemistry*, Wiley, New York, **2000**.
[33] Palik, E.D., *Handbook of Optical Constants of Solids*, Academic, New York, **1985**.
[34] Zong, Y. et al., *Analytical Chemistry,* **2008**, 80, p5246-5250.

Highly ordered nanowire arrays based on polydiacetylene for sensing applications

Kato L. Killops[a], Liangliang Zhu[b], Luis M. Campos[b]

[a]U.S. Army Edgewood Chemical Biological Center, Research and Technology Directorate, 5183 Blackhawk Rd, Aberdeen Proving Ground, MD 21010

[b]Department of Chemistry, Columbia University, 3000 Broadway, New York, NY 10027

ABSTRACT

Semiconducting diacetylene polymers have been synthesized by two different strategies. By using a block copolymer as a template to induce phase separation, thin films exhibiting hierarchical structure have been produced. The polydiacetylene films show photoluminescent behavior, as well as colorimetric transitions when exposed to thermal stimulus. The thin films have been evaluated by atomic force microscopy, ultroviolet-visible spectroscopy, and fluorimetry.

Keywords: polydiacetylene, block copolymer, self-assembly, thin films

1. INTRODUCTION

The warfighter is exposed to a diverse range of hazards in the field such as explosives, toxic chemicals, biological pathogens, and fatigue, which can significantly compromise their overall health and cognitive abilities to perform complex operations. This high-risk environment places heavy demand on the development of robust abiotic sensing materials that display the *sensitivity*, required for detecting threats at low concentrations, and *selectivity*, in order to distinguish harmful substances from their less toxic analogues. To address this need, recent advances in nanotechnology and self-assembling materials, specifically in the area of conjugated polymers[1], have led to miniaturization and signal amplification for sensing applications. There has been a wealth of research dedicated to the study of polydiacetylene (PDA) for use as a colorimetric sensing material.[2,3] The conjugated backbone of PDA is responsible for a blue to red shift in light absorption upon exposure to external stimuli such as temperature[4], pH[5], mechanical stress[6], electric current[7], and binding of analytes.[8,9] This colorimetric response can be detected using standard ultraviolet-visible (UV-Vis) absorption spectroscopy techniques. While this stimulus sensitivity is highly desirable in sensing applications, it also precludes the use of PDA for rugged conditions where it is critical to avoid false positives due to environmental exposure. Furthermore, it is known that PDA additionally possesses luminescent and conductive properties; however, these attributes have not been previously combined to further increase the utility of PDA as a sensing platform.
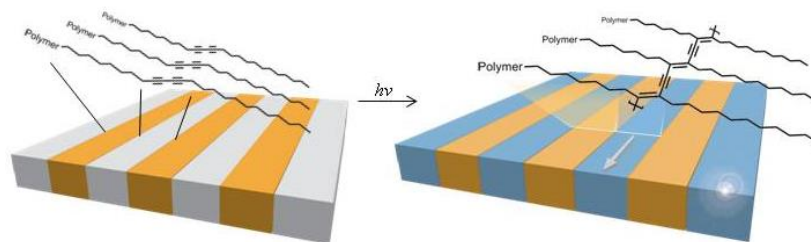

Figure 1. Schematic representation of diacetylene polymer self-assembled in a thin film.

To circumvent these issues and capitalize on the multifaceted response of PDA, we developed a block copolymer (BCP) based approach where diacetylene (DA) units are incorporated in a comb configuration along the backbone. We anticipate that by incorporating DA into a phase separating BCP, we can achieve long-range order coupled with enhanced stability derived from the DA being attached to a polymer backbone. Furthermore, employing a

macromolecule provides the opportunity for adding diverse functionality via a post-polymerization modification strategy. Herein, we present the synthesis, characterization, and preliminary self-assembly results for DA-containing BCPs and random copolymers.

2. EXPERIMENTAL

2.1 Materials

Reagents and solvents were purchased from Sigma-Aldrich and used without further purification, unless otherwise noted: 10,12-pentacosadiynoic acid (PCDA) was purchased from GFS Chemicals, N-hydroxysuccinimide was purchased from Acros Organics, and styrene and methyl methacrylate were purified over a column of neutral alumina.

2.2 Instrumentation

Nuclear magnetic resonance (NMR) spectra (^{1}H, ^{13}C) were recorded on a Bruker DMX-300 MHz spectrometer at room temperature. Chemical shifts are reported in parts per million (ppm) relative to chloroform (CHCl$_3$) (7.24 ppm for ^{1}H), dimethyl sulfoxide (DMSO) (2.50 ppm for ^{1}H), or dimethylformamide (DMF) (8.03 ppm for ^{1}H) as internal reference. Gel permeation chromatography was performed in CHCl$_3$ on a Malvern Viscotek 270max equipped with a refractive index detector, ultraviolet-photodiode (UVP) array, viscometer, and low-angle and right-angle light scattering detectors. Fourier transformed infrared (FT-IR) spectroscopy was performed using a Bruker Tensor 27 FT-IR spectrometer equipped with a Bruker Platinum Attenuated Total Reflectance (ATR) accessory. Spectra are the sum of 16 scans acquired at a resolution of 4 cm^{-1}. Atomic force microscopy (AFM) was conducted on a Bruker Icon system in tapping mode. AFM data was processed using the Nanoscope Analysis software. UV light irradiation of the samples was carried out with a 15 W UVP Black Ray UV bench lamp XX-15 L, fitted with 254 nm bulbs.

2.3 Synthesis

N-methacryloxysuccinamide (NMAOS) was synthesized according to published procedures.[10] The synthesis of 2,2'-(ethylene dioxy)-*bis*-ethylamine-functional PCDA (EDEA-PCDA) and ethylene diamine-functional PCDA (EDA-PCDA) were synthesized according to literature methods.[11] All DA-functional molecules and macromolecules were stored in amber vials away from light to prevent premature polymerization.

2.3.1 15k Polystyrene macroinitiator. To a round bottomed flask were added 8.507 g (81.7 mmol) styrene, 90 mg (0.46 mmol) ethyl 2-bromoisobutyrate, and 189 mg (1.09 mmol) pentamethyldiethylenetriamine (PMDETA). The solution was sealed and degassed by three freeze-pump-thaw cycles, frozen, and CuBr (66 mg, 0.46 mmol) was added under positive N$_2$ pressure. The mixture was heated to 90°C for 4 hours with stirring, after which, the solution was diluted with tetrahydrofuran (THF) and run over a plug of neutral alumina before precipitating twice into methanol. [Dried *in vacuo;* recovered 3.59 g white powder; MW$_{NMR}$=14580.]

2.3.2 5k PS macroinitiator. Synthesized analogously to 15k PS. [MW$_{NMR}$=6950; MW$_{GPC}$=5200, PDI=1.14.]

2.3.3 PS-b-P(MMA-co-NMAOS). To a round bottomed flask were added 5k PS macroinitiator (1.04g, 0.208 mmol), N-methacryloxysuccinamide (NMAOS) (686 mg, 3.74 mmol), methyl methacrylate (MMA) (384 mg, 3.83 mmol), PMDETA (37 mg, 0.21 mmol), and 1 mL of anisole. The mixture was sealed, stirred to dissolve solids, and degassed by three freeze-pump-thaw cycles. The CuBr (44 mg, 0.31 mmol) was added under positive N$_2$ pressure, and the mixture was heated to 90°C for 30 min. The mixture was diluted with dichloromethane and run over an alumina plug, followed by concentration and two precipitations into methanol. [Recovered 1.51 g off-white powder; MW$_{NMR}$=8950; MW$_{GPC}$=8090, PDI=1.27.]

2.3.4 PS-b-P(NMAOS) (large block). To a round bottomed flask were added 15k PS macroinitiator (890 mg, 5.93x10^{-2} mmol), NMAOS (476 mg, 2.60 mmol), PMDETA (39 mg, 0.23 mmol), and 2 mL of anisole. The mixture was sealed, stirred to dissolve solids, and degassed by three freeze-pump-thaw cycles. The CuBr (16 mg, 0.11 mmol) was added under positive N$_2$ pressure, and the mixture was heated to 110°C overnight. The mixture was diluted with dichloromethane and run over an alumina plug, followed by concentration and two precipitations into methanol. [Recovered 970 mg off-white powder; MW$_{NMR}$=17330.]

2.3.5 PS-b-P(NMAOS)(small block). Prepared analogously to large block. [MW$_{NMR}$=15900.]

2.3.6 Functionalization of NMAOS groups with amine-functional DA. The polymer was dissolved in THF and 1 equivalent (to NMAOS) of triethylamine was added. A solution of DA-amine (2-3 equivalents to NMAOS) in THF was added slowly to the polymer solution. N-Hydroxysuccinimide (NHS) precipitated out of solution as the reaction progressed. The solution was heated at 60°C for 3 hours, before cooling, filtering NHS solid, concentrating, and precipitating into methanol. Conversions were approximated from the disappearance of the peak at 2.8 ppm from the methylene protons on NMAOS in ^{1}H NMR.

3. RESULTS AND DISCUSSION

3.1 Covalent polymers

With the goals of enhanced stability and hierarchical, long-range self-assembly in mind, commercially available 10,12-PCDA was appended to a BCP backbone. Initial efforts in fiscal year 2012 (FY12) focused on a chain-end functional BCP system well-known to phase separate polystyrene-*b*-polylactic acid. In this strategy, an alkyne-functional diacetylene[12] was attached to the chain end of the azide-functional BCP[13] using copper-catalyzed alkyne-azide cycloaddition, or click reaction. It was ultimately determined that the volume fraction of DA was too low to promote ordered phase separation at the chain end, and an alternate strategy was employed.

In order to increase the volume fraction of the DA component, and keep the DA molecules in a preferred orientation for topochemical polymerization, a comb-coil architecture was devised. In this strategy, DA units are grafted directly to the backbone of a homopolymer, random copolymer, or block copolymer. A reactive monomer, NMAOS, is easily homo- or copolymerized using standard atom transfer radical polymerization (ATRP) techniques.[10]

ATRP was used to synthesize random copolymers and BCPs containing the reactive NMAOS monomer. Post-polymerization functionalization via nucleophilic substitution of the succinimide by amine-functional DA molecules was carried out to create DA-containing polymers. Since many BCPs that are prone to phase separation do not form ordered structures directly from spin coating, additional treatments are often needed to promote chain mobility to achieve ordered arrays.[14] The self-assembly properties of the DA-containing macromolecules were evaluated by spin-coating thin films from solution. Order was improved by annealing in a solvent-saturated environment.

AFM provides a means to image the microstructure of thin films without the need for additional sample preparation. In the case of the random copolymer, long, fiber-like structures were formed in the as-cast films (Figure 2). These features have a width of 40-50 nm and a height of 5-6 nm, which agrees well with the predicted end-to-end length of two PCDA molecules.[15] More remarkably, these structures span up to several microns in length, which is a promising result for their potential use as resistance-sensing elements. However, these films displayed a disordered morphology overall, and a more predictable microstructure is desirable for precision applications.
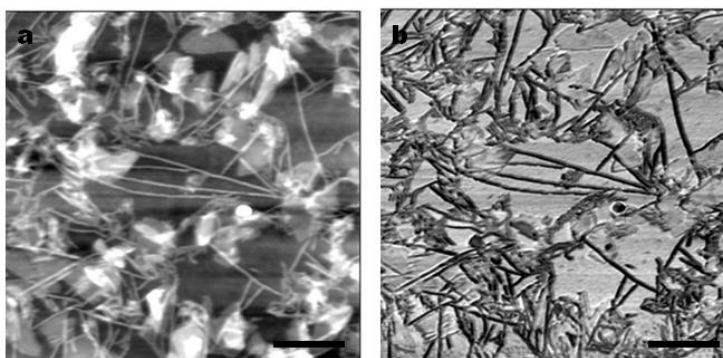

Figure 2. AFM images of (a) height and (b) phase DA polymer thin films. All scale bars 1 μm.

The colorimetric properties of the polymeric materials were tested to ensure that they retain the ability to undergo topochemical polymerization upon exposure to UV light. Films were drop cast from solution onto quartz plates and exposed to 254 nm light in order to induce polymerization of the DA groups that form a blue-colored conjugated polymer. Within 5 seconds, a significant absorbance between 400-700 nm, with a maximum at 622 nm, was observed. Furthermore, DA polymers drop cast on paper exhibit a marked, reversible color change from blue to red upon the application of heat (Figure 3). Further testing regarding temperature-responsive properties, as well as responsiveness to solvent or gas-phase stimuli, is currently being conducted.
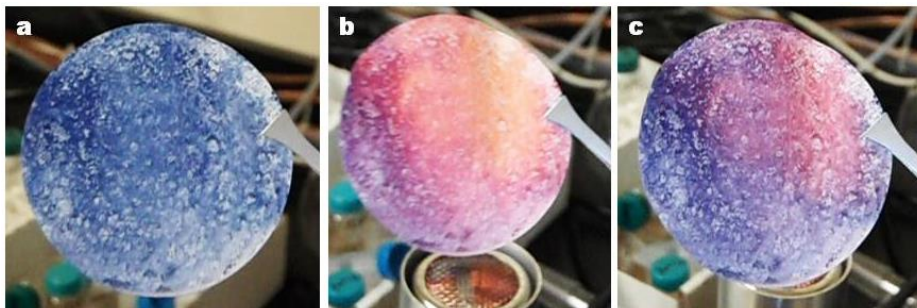
52

Figure 3. Film of DA BCP on filter paper after irradiation: (a) before heating, (b) after heating, and (c) partially cooled.

3.2 Hydrogen-bonded polymers

In a parallel approach, phenyl DA mesogens with a hydrogen-bonding acceptor moiety have been appended to a hydrogen bond-donor BCP in a supramolecular configuration. The mesogenic molecule was synthesized in several steps from commercially available starting materials and characterized by ^{1}H and ^{13}C NMR, mass spectroscopy, and UV-Vis spectroscopy. Three different mesogens have been synthesized: a long-chain alkane tail, short-chain alkane tail, and a mesogen containing bifunctional hydrogen-bond acceptors.

Preliminary investigations into the photoluminescence (PL) behavior of the materials were investigated by UV-Vis and fluorescence spectroscopy. Conversely to the covalent, aliphatic system, the mesogens of the phenyl DA system exhibit blue PL emission without being appended to the polymer. Templating of the mesogen via hydrogen bonding to the polymer backbone provides a significant enhancement over the non-templated mesogen small molecules. There is very little change in the PL spectrum with non-templated mesogen after irradiation with 254 nm light. However, after hydrogen-bonding of the mesogen to the polymer backbone, a significant red shift is observed, both in solution and in thin films (Figure 4).
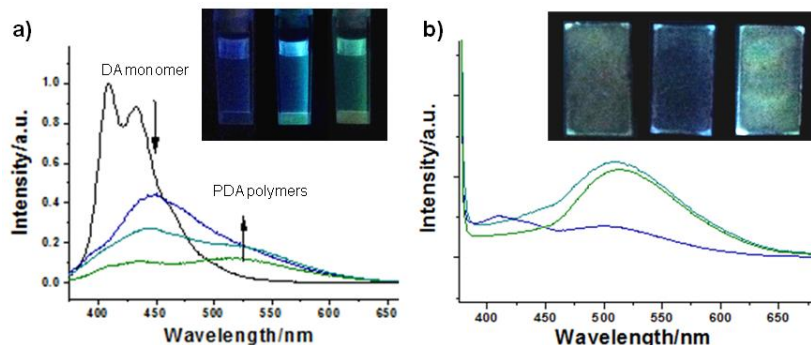

Figure 4. Photoluminescence spectra of phenyl diacetylene mesogen or polymers (a) in solution and (b) thin films.

Self-assembly of the supramolecular polymers was investigated by spin-coating thin films onto Si wafers from dilute solution. AFM was utilized to probe the surface structure. As-cast, the films were flat, but disordered, and solvent annealing was required to promote phase separation. Annealing for up to 36 hours in a saturated solvent environment prompted phase separation of the blocks into what appears to be a cylindrical morphology (Figure 5).
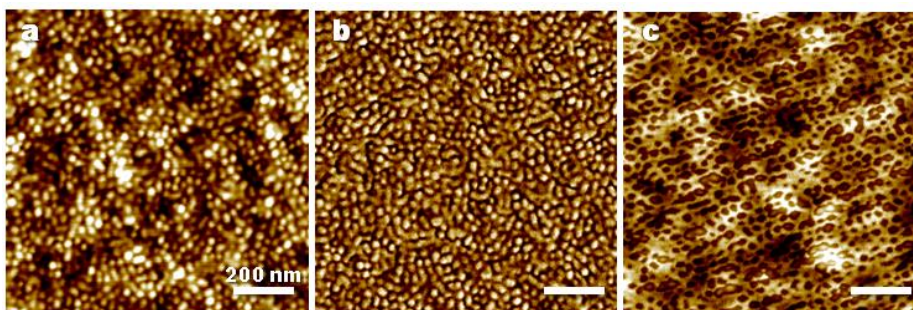

Figure 5. Atomic force microscopy of H-bonded mesogen-block copolymer thin films after annealing in dimethylformamide: (a) height and (b) phase before ultraviolet, and (c) phase after ultraviolet exposure/polymerization.

The films were also exposed to UV light to initiate topochemical polymerization, and a change in morphology is observed on the surface of the film by tapping mode AFM. Examination of the conductive properties of the films will be carried out via conductive AFM (C-AFM) measurements, whereby a bias is applied between the tip and the substrate. If PDA is present throughout the thickness of the film, electrons will be able to flow through the semiconductor material to the tip, which would be reflected in the resulting image in that mode.

4. CONCLUSION

With the aim of producing stable DA structures with hierarchical, long range order, DA-containing molecules were appended to the backbone of homopolymers, random copolymers, and BCPs. Parallel strategies using either a reactive monomer post-modification approach or a supramolecular hydrogen-bonding configuration were employed. The self-assembly properties of the various polymer architectures were evaluated through the formation of thin films by solution spin casting. The films have been evaluated preliminarily by tapping mode AFM, although more detailed studies by small-angle X-ray scattering (SAXS), grazing-incidence small-angle X-ray scattering (GISAXS), C-AFM, and X-ray reflectivity (XRR) are forthcoming. The films were also evaluated with respect to their colorimetric properties by UV-Vis absorbance spectroscopy. It was found that the materials polymerize within several seconds of irradiation and annealing may help to increase susceptibility to polymerization.

ACKNOWLEDGEMENTS

REFERENCES

[1] McQuade, D.T. et al., *Chemical Reviews,* **2000***, 100(7), p2537-2574.
[2] Sun, X. et al., *Chemical Society Reviews,* **2010***, 39(11), p4244.
[3] Reppy, M.A. and Pindzola, B.A., *Chemical Communications,* **2007***, (42), p4317-4338.
[4] Peng, H. et al., *Journal of the American Chemical Society,* **2005***, 127(37), p12782-12783.
[5] Dautel, O.J. et al., *Journal of the American Chemical Society,* **2006***, 128(50), p16213-16223.
[6] Caruso, M.M. et al., *Chemical Reviews,* **2009***, 109(11), p5755-5798.
[7] Peng, H. et al., *Nature Nanotechnology,* **2009***, 4(11), p738-741.
[8] Charych, D.H. et al., *Science,* **1993***, 261(5121), p585-588.
[9] Lee, J. et al., *Advanced Functional Materials,* **2012***, 22(8), p1632-1638.
[10] Shunmugam, R. and Tew, G., *Journal of Polymer Science Part A: Polymer Chemistry,* **2005***, 43(23), p5831-5843.
[11] Jung, Y. et al., *Advanced Functional Materials,* **2008***, 18(5), p701-708.
[12] Leal, M. et al., *Chemistry - A European Journal,* **2011***, 17(6), p1828-1836.
[13] Campos, L. et al., *Macromolecules,* **2008***, 41(19), p7063-7070.
[14] Albert, J.N. et al., *ACS Nano,* **2012***, 6(1), p459-466.
[15] Huggins, K.E. et al., *Macromolecules,* **1997***, 30(18), p5305-5312.

A rational design approach to multifunctional nanostructured materials

Amanda L. Jenkins*[a], Alex Balboa[b], Margaret M. Hurley[c], Christopher J. Karwacki*[b]
[a]ASK Incorporated, 7447 Rockawalkin Rd. Hebron, MD 21830
[b]U.S. Army Edgewood Chemical Biological Center, Research and Technology Directorate,
5183 Blackhawk Rd, Aberdeen Proving Ground, MD 21010
[c]U.S. Army Research Laboratory, Aberdeen Proving Ground, MD 21005

ABSTRACT

Interest in graphene-based materials has been growing over the last decade given the unique mechanical and electronic properties. These properties can be tuned or modified to create novel materials displaying both sensing and catalytic functionalities. In this study, we build rationally-designed architectures based on graphene materials. Using alizarin and titanium isopropoxide, we successfully prepared a hybrid form of nanostructured graphene-titanium oxide using a bottom-up synthetic approach. Its enhanced photocatalytic activity is demonstrated through the degradation of methylene blue under ultraviolet light irradiation and carbon monoxide oxidation. Novel photoluminescent materials were prepared from the reaction of graphene oxide and luminescent lanthanides (europium, terbium, gadolinium, samarium, and dysprosium) in methanol at high pH. The two classes of materials, although studied separately, can be combined to create a multifunctional Janus-type architecture for sensing and decontaminating threats.

Keywords: Graphene, titanium oxide, lanthanides, photocatalysis, sensing, detoxification, multifunctional materials

1. INTRODUCTION

1.1 Integrated graphene-titanium oxide material

Integrated graphene-titanium oxide (Gr-TiO_2) materials show great promise as photocatalysts and catalysts in many reactions.[1-3] The graphene domains in the hybrid structures enhance the intrinsic catalytic and photocatalytic properties of bare-TiO_2 to improve the efficiency of the reactions.[1] The composite structure serves as an example of excellent use of graphene, a material with many unique properties. For example, in photocatalytic reactions, graphene serves as a hole or electron trap, slowing down charge recombination in TiO_2 and allowing the reaction to proceed more efficiently compared to bare-TiO_2.[4] Specifically, under ultraviolet (UV) irradiation induces band-gap excitation in TiO_2 followed by electron injection into the graphene clusters. This increases the excited lifetime of TiO_2, enabling more efficient photocatalytic reactions.[5] The schematic in Figure 1 illustrates this mechanism for graphene clusters.
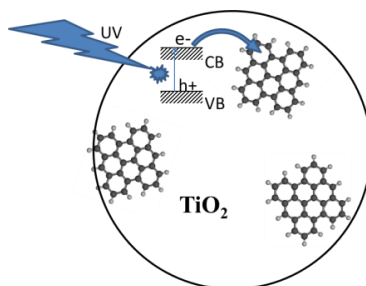

Figure 1. The mechanism in which graphene patches accept the photoexcited electron from TiO_2.

Graphene can also be integrated into TiO_2-supported gold nanoparticles (NP) for carbon monoxide (CO) oxidation. In this non-photo-induced catalytic example, graphene acts as a molecular wire.[6] The molecular wire enhances

charge separation from the gold catalyst to the metal oxide surface and promotes more efficient oxidation of adsorbed CO.

The organic dye alizarin (1,2-dihydroxy-9,10-anthracenedione), an anthracene derivative, acts as a precursor for graphene. The molecule efficiently chemisorbs to the surface of TiO_2 through its hydroxyl functional groups. The molecule has been shown to be an efficient sensitizer of TiO_2 in electron transfer studies.[7] Furthermore, the dye is capable of forming a homogenous solution with the TiO_2 precursor titanium isopropoxide (TIP) in isopropanol, ensuring complete and total homogeneous mixture of the two precursors. Upon calcination, alizarin converts to graphene clusters by thermal cyclodehydrogenation[8,9], which preserves the carbon sp^2 bond character of the anthracene backbone.

In this work, we developed a novel synthetic approach to grow integrated Gr-TiO_2 structures following a bottom-up synthesis and demonstrated their photocatalytic activity. The graphene component was grown from alizarin *in situ* with TiO_2 formation. We also showed that the graphene component of the bottom-up synthesized Gr-TiO_2 composite played an active role in degrading methylene blue (MB) dye. As the graphene loading was increased, introducing more active sites within the hybrid structure, the rate of MB degradation increases as well. Determination of the relationship and mechanism between electron injection into the graphene and kinetics is an ongoing effort. The bottom-up synthesis technique demonstrated in this work leads to the concept of rationally-designed materials whose properties are controlled during the synthesis. This up-front synthesis control of properties results in materials with tailored functionality.

1.2 Lanthanide – graphene oxide materials

The use of lanthanides as probe ions and signal transducers in sensing applications is widely accepted, as they can often provide sensitivity in the parts per trillion range and lower.[10] Lanthanides comprise the largest naturally-occurring group in the periodic table, and their similarities arise from a resemblance in the electronic configurations of the elements which consists of the xenon levels, filled 6s sublevel, and a varying amount of electrons occupying the 4f sublevel. Generally, the optical absorption and emission spectra of the ions formed by the triply-charged free lanthanide ions consist of very narrow lines (0.1-0.01 nm). Quantum mechanical calculations have indicated that the energies and the radial extensions of the 4f eigenfunctions dramatically drop at the beginning of the lanthanide series so that the maxima of the 4f eigenfunctions no longer exceed those of the 5s and 5p eigenfunctions.[11] Thus, the 4f orbitals are not the outermost shell, but are largely shielded from the external environment by the filled 5s and 5p shells. (Since these 4f orbitals are shielded, the electrostatic field in lanthanide complexes, induced by coordinating ligands that cause small perturbations in the 4f electrons energy levels.) As a result, the lanthanides within the complex retain their semi "atomic" nature, which gives the characteristic narrow bands observed in lanthanide emission and excitation spectra.[12,13] These narrow features often result in analyses which are both selective and sensitive.

Europium is the most commonly used lanthanide for sensing applications. The spectral splitting patterns of europium are generally less complex (fewer peaks) and easier to interpret than the other lanthanides. Additionally, europium has the $^5D_0 \rightarrow {}^7F_2$ transition, which is a "hypersensitive transition" reflecting even minor changes in its environment with very intense luminescence.[14] (In this case the term luminescence is preferred over other terms such as fluorescence or phosphorescence because the intra-configurational transitions may or may not involve a change in spin). Europium is also the most reactive of the lanthanides because unlike most lanthanides, which are primarily trivalent, europium also exists in the +2 state (electron configuration $_4F^7$), and the half-filled *f*-shell gives more stability.[15]

Complexation by organic ligands was found to significantly enhance the luminescence intensity of the tripositive lanthanide (Ln(III)) ions.[10,15-18] This enhancement was explained by a ligand-to-metal energy transfer mechanism.[19,20] The proposed mechanism indicates that when an excited triplet state of a coordinating ligand overlaps an excited lanthanide electronic level, the lanthanide luminescence is effectively pumped by the large cross-section molecular absorbance of the ligand rather than by the weak lanthanide absorbance. This process is believed to be much more efficient than direct absorption of light by the lanthanide since the lanthanides themselves exhibit low molar absorptivities. Proper ligand choice is therefore crucial in the preparation of lanthanide complexes.

In this study, europium, terbium, gadolinium, samarium, or dysprosium were selected and combined with graphene oxide (GO) since they have partially filled subshells, which provide them with enhanced sensitivity to the environment and increased luminescence properties. GO was selected as a coordinating ligand for the lanthanides

because of its unique structural, electronic, and optical properties[21], as well as its high mechanical strength.[22] GO was chosen over graphene because the intrinsic oxygen was needed to coordinate with the lanthanide.

Since each lanthanide has luminescence in a different region of the spectra, incorporating several into GO materials luminesced in many colors. The resulting europium, terbium, gadolinium, samarium, and dysprosium complexes with GO, were verified by Raman and laser-induced luminescence. The surface morphology and physical properties of the graphene/lanthanide materials (europium and terbium) were investigated by scanning electron microscopy (SEM) and transmission electron miscroscopy (TEM).

2. METHODOLOGY

2.1 Photocatalytic activity of graphene-titanium oxide

Gr-TiO$_2$ materials were synthesized by autoclaving a high pH, TIP sol-gel in hydrothermal conditions. Different wt.% of alizarin were dissolved into the TIP sol-gel to create an alizarin-TiO2 hybrid structures. To establish the relationship between calcination temperature and resulting structures, the powder was heated to 475°C and 700°C. For photocatalysis experiments, the samples were heated up to 700°C. The temperature of 700°C was chosen to strip selectively any carbonyl and hydroxyl groups off alizarin, leaving behind only the graphene-like anthracene backbone.

Bare-TiO$_2$ and Gr-TiO$_2$ powders were characterized for their structural and morphological properties using X-ray diffraction (XRD; PANalytical X'Pert powder X-ray diffractometer with CuKα radiation),and SEM (JEOL 6300F). Raman spectra were recorded at room temperature using JASCO NRS-3200 Raman microscope with a 532 nm laser. X-ray photoelectron spectroscopy (XPS) spectra were recorded using a Perkin Elmer Phi 570 ESCA/SAM system employing Cu K-alpha X-rays. The photocatalytic activity was tested on a MB dye aqueous solution. A 365 nm UV lamp was used to irradiate the sample. An Agilent Hewlett-Packard 8453A UV-Vis-NIR Spectrophotometer was used to measure the intensity of the supernatant MB solution after UV exposure.

2.2 Lanthanide-graphene oxide materials

GO was prepared by Teresa Bandosz, (City College New York) and used as obtained. The GO was dissolved in alkaline water and mixed with lanthanide nitrates, La(NO$_3$)$_3$·5H$_2$O. The solids were centrifuged and then washed with water and acetone. The lanthanide-graphene oxide (La-GO) solids were air dried on a watch glass overnight.

GO, lanthanide oxide, lanthanide nitrates, and the resulting La-GO samples were evaluated using a laser-induced fluorescence system. Excitation wavelengths of 465.8, 488, 496, and 514 nm were evaluated for all materials. The La-GO compounds with the highest overall luminescence intensity were selected for SEM and TEM.

3. RESULTS AND DISCUSSION

3.1 Characterization and photocatalysis of integrated graphene-titanium oxide

TiO$_2$ was prepared in high pH conditions, using NH$_4$OH as the base. The XRD patterns of the bare-TiO$_2$ synthesized in basic, NH$_4$OH conditions, at temperature treatments of 130°C, 475, and 700°C are shown in Figure 2a. The anatase structure is preserved in this material even at 700°C, with minimal rutile formation, indicated by the small rutile (110) peak at 27.4° (inset in Figure 2a). Figure 2b shows that the Gr-TiO$_2$ samples also retain their anatase structure with increased temperature. Interestingly, no rutile peaks are observed in Gr-TiO$_2$ at 700°C (Inset, Figure 2b). Furthermore, no graphene spectrum is observed in Figure 2b. This is likely because the low (0.24 wt.%) loading of alizarin does not yield any stacked graphene sheets. The proposed graphitization pathway is based on a process of thermal cyclodehydrogenation, which produces small graphene clusters.[8] However, even in the small clusters, the desired charge transport properties of graphene are observed in graphitic structures as small as 1.7 nm.[23] Herein, we incorporate a lower concentration of graphene precursor compared to other studies because the first goal of this work is to study small graphene clusters within the hybrid structure and then test the photocatalytic properties of higher loaded composites.

For the Gr-TiO$_2$ samples used in the photocatalytic experiments, the structure of all three materials was also confirmed as anatase with the use of XRD. Figure 2c shows that the anatase structure is preserved for all three samples, loaded at 1, 2, and 5 wt.% graphene, after 700°C calcination.
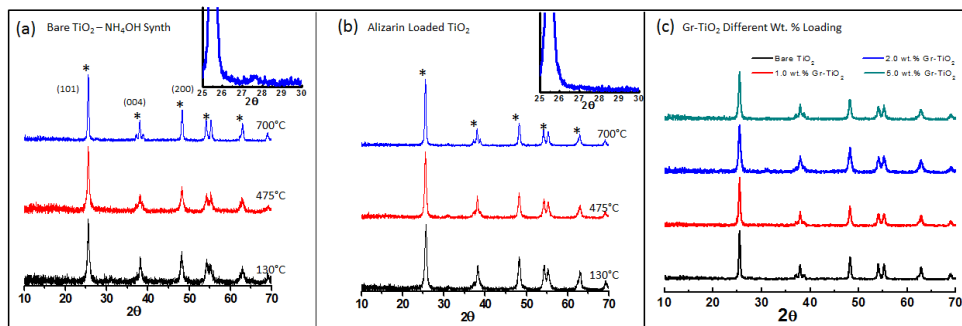

Figure 2. XRD patterns of (a) bare-TiO$_2$ synthesized (130°C) in pH=12, (b) alizarin-TiO$_2$, (c) XRD of higher wt.% loaded Gr-TiO$_2$ samples for photocatalytic studies. * denotes anatase peaks. Insets show zoomed-in XRD of rutile peak region.

The size of the TiO$_2$ crystallites can be approximated by using the Debye-Scherrer equation, which determines the length of a crystalline domain in a specific crystallographic direction. To compare the relative sizes of the crystals calcined at different temperatures we choose the length in the [101] direction, which corresponds to the XRD peak at $2\theta \approx 25°$. The Debye-Scherrer lengths in the [101] direction presented in Table indicates that the individual crystallites grow as the calcination temperature is increased, as expected. The addition of alizarin does not change the crystallographic properties of the TiO$_2$ NPs, such as size and crystal structure. The sizes of the crystalline domains of TiO$_2$ and 0.24 wt.% Gr-TiO$_2$ remain similar at all temperatures. Therefore, presumably, the anatase structure of TiO$_2$ is preserved.

Table 1. TiO$_2$ crystal size following thermal treatment.

Sample	Mean Crystal Size[a] (nm)	Sample	Mean Crystal Size[a] (nm)
TiO$_2$-130	32.6	Gr-TiO$_2$-130	29.9
TiO$_2$-475	34.7	Gr-TiO$_2$-475	34.7
TiO$_2$-700	47.9	Gr-TiO$_2$-700	44.8
a. Referenced to the (101) Surface			

Raman spectroscopy and XPS were used together on all samples (0.24 wt.% - 5 wt.%) to identify and characterize graphitic structures in the composite material. Raman spectra of graphitic materials feature peaks at approximately 1350 cm^{-1} and 1590 cm^{-1}, corresponding to the D and G bands, respectively. The intensity and shift of the D band is indicative of disorder, whereas the intensity and shift of the G band is indicative of sp^2 carbon amount and morphology. Figure 3a shows the Raman spectra for alizarin-TiO$_2$ materials calcined at 130°C, 475°C, and 700°C. The spectrum of 130°C and 475°C 0.24 wt.% Gr-TiO$_2$ features peaks corresponding to anatase and unreacted alizarin, along with a strong fluorescent background, which is typical for such dyes as alizarin. The Raman spectrum alizarin-TiO$_2$ sample calcined at 700°C shows graphene D and G peaks at 1350 cm^{-1} and 1603 cm^{-1}, respectfully, and no fluorescence background. Lack of fluorescence and emergence of the D and G peaks are indicative of total conversion from the dye precursor to graphene. To confirm that alizarin indeed forms graphene structures in absence of TiO$_2$, alizarin was calcined in a ceramic boat under dry N$_2$ flow at 700°C. The spectrum also features the D and G peaks at 1330 cm^{-1} and 1580 cm^{-1}. Figure 3c is a plot of all Raman spectra for the higher loaded samples together. It is clearly seen from the figure that the intensity of the D and G peaks grow with the loadings. Moreover, the D and G graphene bands grow homogeneously as the loading of alizarin is increased (Figure 3d). The corresponding wavenumber values of the D and G peaks remain at 1374±14 cm^{-1} and 1591.9±2 cm^{-1}, respectively at all loadings along with the D/G peak height ratio remaining at 1.01±0.01. The G peak value is blue-shifted from the G peak of calcined alizarin. Comparing these results to work done by Ferrari *et al*, this indicates that nanocrystalline graphene clusters are formed throughout the anatase crystals for all alizarin loadings. Higher loading of alizarin does not increase the size of the graphene sheets; rather, there is an increase of amount of small graphene clusters.
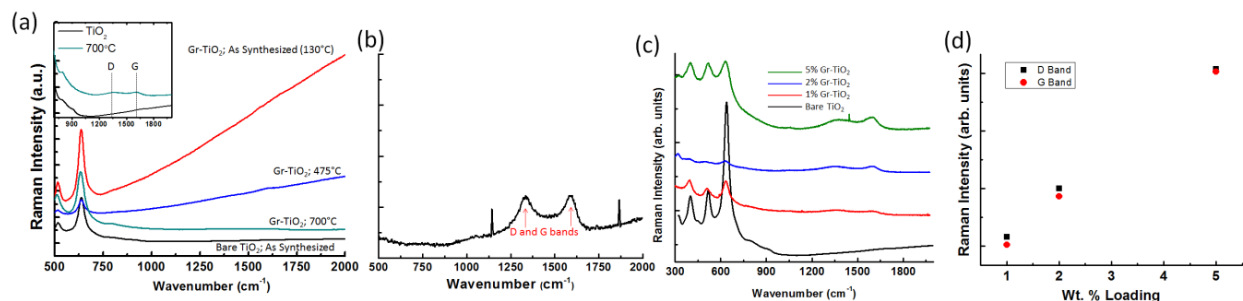
Figure 3. Raman spectra of (a) bare-TiO₂, Gr-TiO₂ (130°C), Gr-TiO₂ (475°C), Gr-TiO₂ (700°C), and (b) 700°C calcined pure alizarin. (c-d) Raman spectra and peak analysis of 1.0 to 5.0 wt.% Gr-TiO₂ samples used in photocatalysis, respectively.

XPS peaks are able to discern between different types of carbon or oxygen bonds in the material and provide a relative amount of species containing those bonds. XPS was collected of all Gr-TiO₂ samples, calcined at different temperatures and compared to bare-TiO₂. The C1s and O1s XPS data indicated that the majority of the carbon in the sample has defect-free, sp^2-hybridized, or graphene-like, bonds. The minority of carbon in the hybrid sample comes from the sp^3-hybridized C-C and C-H bonds. The C1s XPS results combined with the Raman spectroscopy results further confirms that majority of carbon structure on the TiO₂ surface converted to graphene.

3.2 Photocatalytic activity

To demonstrate the photocatalytic activity of the Gr-TiO₂ material, and show its potential as a rationally designed functional material, the hybrid structure was tested against bare-TiO₂ to degrade the organic MB dye. Three loadings of alizarin were tested: 1.0 wt.%, 2.0 wt.%, and 5.0 wt.% (1.0% Gr-TiO₂, 2.0% Gr-TiO₂, 5.0% Gr-TiO₂, respectively). The three loadings are expected to show progressive enhancement of dye degradation kinetics, illustrating how precise tailoring the material's properties leads to change in its performance. Gr-TiO₂ samples and bare-TiO₂ were each suspended in aqueous MB solution and stirred under UV irradiation. UV-Vis spectroscopy was used to monitor the supernatant MB solution after 20, 40, 60, 95, and 155 minutes of 365 nm UV exposure. The individual photocatalysis UV-Vis results at each time step, for all TiO₂ loadings. Figure 4a shows the residual concentration of MB of the Gr-TiO₂ samples with time, compared to bare-TiO₂. The residual C/Co ratios at 150 minutes for each graphene loading are presented in the table in Figure 4b. TiO₂ alone is able to decompose MB to 56% at 150 minutes. As graphene is added to TiO₂ during synthesis, the residual MB concentration lowers after 150 minutes of reaction, implying less residual MB in solution.
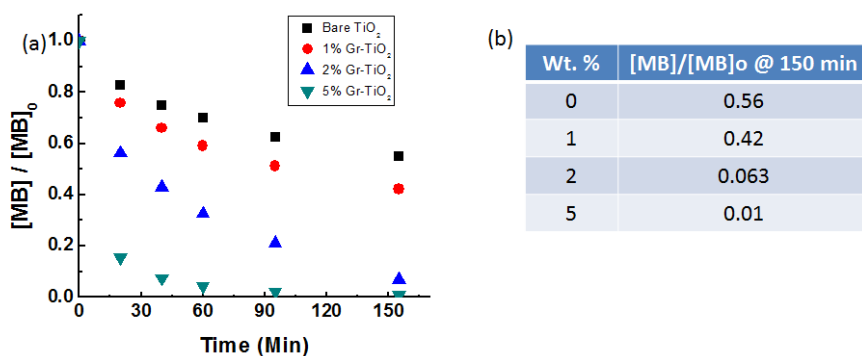

Wt. %	[MB]/[MB]o @ 150 min
0	0.56
1	0.42
2	0.063
5	0.01

Figure 4: Photocatalytic degradation on methylene blue using Gr-TiO₂.

3.3 Lanthanide – graphene oxide materials

As expected, the europium samples exhibited the greatest intensity (visibly red/orange) and interpretation of its spectral line patterns was easiest (based on number of peaks). Europium benefits from being one electron short of a half-full shell, making it easy for it to accept the electron for strong energy transitions. The conversion from europium oxide to europium nitrate was confirmed spectroscopically by a comparison with the spectra published by Buenzli et al.[24] Europium samples were evaluated using excitation wavelengths of 465.8 nm, 472.7 nm, 488.0 nm,

and 514.5 nm. Excitation at 465.8 nm was determined to have the highest luminescence intensity and give the best peak resolution, confirming previously published results. Complexation between the lanthanide and the GO was determined by spectral changes and increased luminescence when compared with the luminescence of the lanthanide and the GO by themselves. The europium-graphene oxide (Eu(GO)) sample with the highest luminescent intensity was that prepared with 1.5 g of europium nitrate (Figure 5). The sample prepared with 0.5 g of europium nitrate showed no spectral difference from the GO sample alone. This trend of highest luminescence for the complexes prepared 1.5 g of lanthanide nitrate was followed for all the lanthanides examined in this study, and it was these samples that were chosen for full characterization.
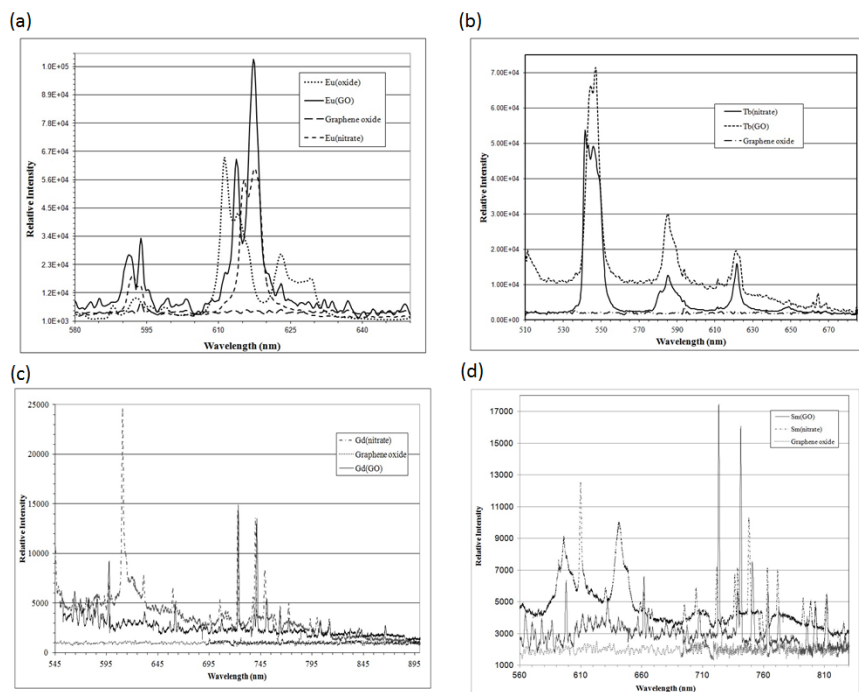

Figure 5. Luminescence spectra of lanthanide compounds: (a) Eu, (b) Tb, (c) Gd, and (d) Sm.

In comparing the luminescence spectra of GO, europium nitrate, and Eu(GO), several transitions were evaluated (Figure 5a). The $^5D_0 \rightarrow {}^7F_1$ transition of the europium (from about 590-595 nm) exhibited a 1 nm shift when converted from the nitrate complex at 592 nm and the Eu(GO) complex at 591 nm. Additionally, the two peaks in the 595 nm region are better resolved in the Eu(GO) complex. The Eu(GO) peak at 595 nm is also higher in intensity; however, this could be due to the fact that the GO itself has a fluorescence peak at that wavelength.

The hypersensitive $^5D_0 \rightarrow {}^7F_2$ europium transition was also evaluated for evidence of Eu(GO) complex formation. The europium nitrate peak at 615 nm was shifted one nanometer to the blue (614 nm) in the Eu(GO) and also reduced in intensity relative to the peak at 617.5 nm. The peak at 617.5 nm was shifted 0.1 nm to the blue in the nitrate complex. Comparing these splitting patterns with the calculations done by Stump *et al.*[16] (and taking into account no peaks were seen in the $^5D_0 \rightarrow {}^7F_1$ transition) the site symmetry for both molecules is likely D_2 or D_2d with either a tetragonal or rhombic crystal system. If only one transition could be analyzed for binding, this would be the one chosen due to its sensitivity and intensity.

The terbium, samarium, gadolinium, and dysprosium samples were evaluated in a similar manner with the results summarized in Table 1. The terbium complexes (excited at 514 nm) exhibited the second strongest luminescence (visibly green) and had the next easiest spectra to evaluate (Figure 5b) Terbium has higher intensity bands than expected because, like europium, it is one electron away from having a half full (stable) f shell. This makes promotion of the extra electron easier and gives rise to stronger luminescence. The first transition evaluated, the $^5D_4 \rightarrow {}^7F_5$ had the strongest luminescence. In this spectral region, three peaks were seen for the terbium nitrate (541.5, 543.3, and 545.8 nm) while only two peaks were noted for the terbium-graphene oxice (Tb(GO)) complex (544.5 and 547.0 nm). The intensity of the largest peak also red shifted from the nitrate to the Tb(GO). In the $^5D_4 \rightarrow {}^7F_4$ transition, the terbium nitrate has two unresolved peaks (581.0 and 585.25 nm) while the Tb(GO) complex has only one (585.0 nm). The $^5D_4 \rightarrow {}^7F_3$ transition has one peak at 621.5 nm for the nitrate and two unresolved peaks at

621.3 and 622.8 nm in the Tb(GO) complex. The GO and Tb(GO) complex both had weak peaks at 536.8 and 593.8 nm, which were not seen in the terbium nitrate spectrum.

The gadolinium, situated on the periodic table between europium and terbium does not have the same intense luminescence characteristics as its neighbors because it has the stability of a half-filled f shell, making it very difficult to promote an electron to the excited state. An excitation wavelength of 488 nm was used for the gadolinium complexes. While 488 nm is not necessarily the optimal excitation wavelength for gadolinium, it was the strongest band output by the laser available and gave the best results. UV excitation using a hand-held type source emitting at 254 nm and 365 nm was also attempted with no success. As seen in the previous complexes, the gadolinium-graphene oxide (Gd(GO)) had an overall luminescence increase over the nitrate and was much more intensely luminescent than the GO alone (Figure 5c). New strong luminescence bands were seen in the 600-620 nm region, as well as peak shifts and splitting changes in the 660-670 nm, 740-755nm, and 785-800 nm regions. These changes were attributed to the complexation of the gadolinium and the GO. There are so many bands associated with gadolinium complexes that assigning the transitions with certainty was not possible, and spectral changes were identified by region of the spectrum.

Samarium, the lanthanide immediately preceding europium has many absorption bands in the region below 500 nm and efficient fluorescence occurs from the $^4G_{5/2}$ level for solid materials. The emission is divided between many terminal levels making spectral interpretation difficult, and many ion-ion self-quenching transitions are possible. The preparation of the samarium complexes was also more difficult. The materials had to be purified by dissolving the materials in equal parts water/methanol and recrystallizing. Excited at 488 nm, the overall luminescence increase from the samarium nitrate to the samarium-graphene oxide (Sm(GO)) complex was not as intense as that seen for europium and terbium. As seen in Figure 5d, wavelengths of 254 nm, 465.8 nm, 472 nm, and 514 nm were also evaluated, but gave no notable luminescence. As expected, the spectrum was much more complicated than that of terbium or europium, making it less useful as a probe ion, but still providing another color region for optical applications. Confirmation of complexation between the samarium and the GO was verified by spectral changes in several regions. In the transitions $^4G_{5/2} \rightarrow {}^6H_{5/2}$ (580-600 nm region), $^4G_{5/2} \rightarrow {}^6H_{7/2}$ (600-620 nm region), and $^4G_{5/2} \rightarrow {}^6H_{9/2}$ (640-660 nm region) peak splitting changes were noted as well as the appearance as new intense luminescence bands. In the $^4G_{5/2} \rightarrow {}^6H_{11/2}$ transition (740-770 nm region) splitting changes and peak shifts were noticed as well as an intensity increase. In the $^4G_{5/2} \rightarrow {}^6F_{7/2}$ transition (790-820 nm region) splitting changes and peak shifts were observed between the nitrate and Sm(GO) complex. All of these indicate successful coordination of the materials.

Dysprosium, the lanthanide immediately following terbium, was also reacted with GO and evaluated. Regardless of the excitation used, no changes were detected between the dysprosium nitrate and the dysprosium-graphene oxide (Dy(GO)) material. The synthesis was attempted many times using many different ratios with little luminescence response from any of them. The energy levels for dysprosium are typically very high, making it hard to excite without complexation with organic ligands to provide intersystem crossing, and it is surmised that the GO does not provide the levels needed. The Raman spectra did exhibit significant changes between the nitrate and the GO complexes, which supports this conclusion.

The SEM analysis was performed on the GO as well as the Eu(GO) and Tb(GO) materials in an effort to better understand what was going on at the surface. The SEM of the GO showed the expected sheet-like structure. In the Eu(GO) as well as the Tb(GO) SEM images, the sheet-like structure can still be identified, and the large lanthanide ions are seen to cover the surface (Figure 6a).

TEM images were also collected for the Eu(GO) and Tb(GO) particles (Figure 6b) High-resolution analysis of the Eu(GO) particles shows limited graphene crystallinity. Energy-dispersive X-ray spectroscopy (EDS) data collected on the sample found the expected europium, oxygen, and carbon. The X-ray mapping illustrated the strong correlation of the europium being bound to the GO particles. The lower magnification TEM images for the Tb(GO) particles sample showed the graphene present as mostly planar flakes. The high magnification TEM indicated that the particles exhibited good crystallinity of the graphene, as the atomic lattice features of the graphene particles were clearly visible. The EDS spectra confirmed the presence of terbium, oxygen, and carbon in the sample while X-ray mapping showed the uniform coverage of the terbium on the GO particles.
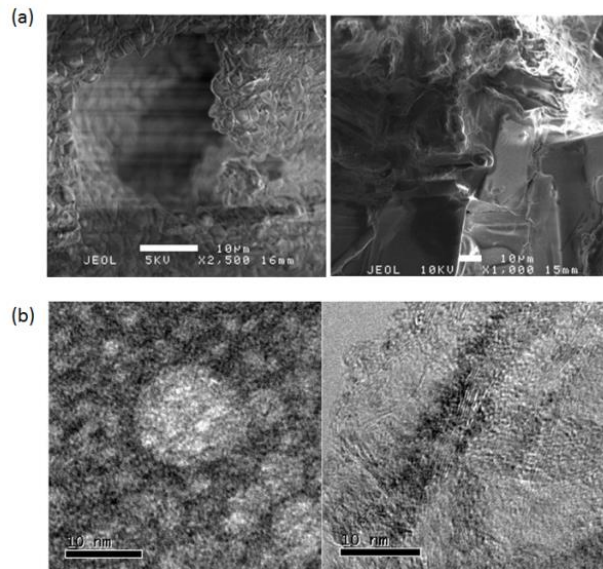
Figure 6. (a) SEM images of (left) terbium-graphene oxide and (right) europium-graphene oxide. (b) TEM images of (left) terbium-graphene oxide and (right) europium-graphene oxide.

4. CONCLUSIONS

Integrated Gr-TiO$_2$ structures were synthesized following a bottom-up route starting with precursor molecules alizarin and TIP. The approach produced a material with TiO$_2$ and graphene in intimate contact since the precursor molecules formed a stable, homogeneous phase. The precursor alizarin was chosen such that it intimately binds to TiO$_2$ through the hydroxyl groups and already possesses the graphene building block through its anthracene backbone. A low concentration of the precursor was chosen to minimize the deposition of alizarin dimers, which would have caused multiple layers of graphene to form. XPS and Raman spectroscopy showed that the material contained majority sp^2-hybridized carbon that formed graphene-like clusters. The XRD study indicated that TiO$_2$ maintained its anatase crystallography in the integrated structure, preserving the material's properties without going through a phase transition to rutile. Furthermore, the method does not induce crystal growth through ripening since XRD and SEM show that the NPs remained the same size throughout the calcination process. The material was shown to be active in photocatalytic decomposition of MB dye under UV irradiation.

Lanthanide-based GOs offer a new series of materials with enhanced optical, electrical, and magnetic properties that can be utilized in a wide array of research areas. Using the majority of the luminescent lanthanides, in addition to the commonly studied europium, expands the capabilities of the materials to provide luminescence in many colors. The lanthanides also have magnetic and electronic properties, which can be used to tune and enhance those features in the GO. These materials were relatively easy to prepare and purify, thus adding to their usefulness. Since lanthanides are relatively non-toxic, they can be applied as sensors and biosensors in addition to the electronic applications of displays and batteries.

The two materials can be combined through an interface on the same substrate, to create a multifunctional system, which can respond by detecting a threat and detoxifying it. The findings from this work inform development of rational designed novel materials.

REFERENCES

[1]   Kamat, P. V., *Journal of Physical Chemistry Letters,* **2010**, 1(2), p520-527.
[2]   Morales-Torres, S. et al., *Environmental Science and Pollution Research,* **2012**, 19(9), p3676-3687.
[3]   Zhong, J. et al., *Journal of Physical Chemistry C,* **2009**, 114, p933-939.

[4]   Zhang, Y. et al., *ACS Nano,* **2010**, 4(12), p7303-7314.

[5]   Štengl, V. et al., *Journal of Physical Chemistry C,* **2011**, 115, p25209-25218.

[6]   Chen, F. and Tao, N.J., *Accounts of Chemical Research,* **2009**, 42(3), p429-438.

[7]   Di Iorio, Y. et al., *ChemPhysChem,* **2009**, 10(7), p1077-1083.

[8]   Diev, V.V. et al., *Journal of Organic Chemistry,* **2012**, 77(1), p143-159.

[9]   Schwab, M.G. et al., *Journal of the American Chemical Society,* **2012**, 134(44), p18169-18172.

[10] Jenkins, A.L. and Murray, G.M., *Analytical Chemistry,* **1996**, 68(17), p2974-2980.

[11] Stump, N.A., *A Study of Lanthanide Fluorescence Shifts caused by Near Neighbor Perturbation*, University of Tennessee: Blount Hall, **1991**.

[12] Cotton, S., *Lanthanides and Actinides*, Oxford University Press, New York, **1991**.

[13] Murray, G.M. et al., *Inorganic Chemistry,* **1989**, 28(10), p1994-1998.

[14] Judd, B. R., *ACS Symposium Series,* **1980**, 131, p267-274.

[15] Greenwood, N. et al., *Chemistry of the Elements*, Elsevier Science, **2013**.

[16] Carlos, L.D. et al., *Advanced Materials,* **2009**, 21(5), p509-534.

[17] Bernardo, P.D. et al., *Coordination Chemistry Reviews,* **2012**, 256(1-2), p328.

[18] Xu, H. et al., *RSC Advances,* **2013**, 3(29), p11367-11384.

[19] Crosby, G.A. and Kasha, M., *Spectrochimica Acta,* **1958**, 10(4), p377.

[20] Crosby, G.A. et al., *Journal of Chemical Physics,* **1961**, 34(3), p743-748.

[21] Novoselov, K.S. et al., *Science,* **2004**, 306(5696), p666-669.

[22] Lee, C. et al., *Science,* **2008**, 321(5887), p385-388.

[23] Langlais, V.J. et al., *Physical Review Letters*, **1999**, 83(14), p2809-2812.

[24] Buenzli, J.C.G. and Yersin, J.R., *Inorganic Chemistry,* **1979**, 18(3), p605-607.

Understanding the role of physical and chemical adsorption on the Raman enhancement from metallic nanoparticles and nanostructured surfaces

Jason Guicheteau[a], Ashish Tripathi[b], Erik Emmons[b], Jerry Cabalo[a], and Steven Christesen[a]

[a]U.S. Army Edgewood Chemical Biological Center, Research and Technology Directorate, 5183 Blackhawk Rd, Aberdeen Proving Ground, MD 21010

[b]Science Applications International Corp., P.O. Box 68, Gunpowder Branch, Aberdeen Proving Ground, MD 21010

ABSTRACT

In this effort, we explore the effects of chemical and physical adsorption on the surface-enhanced Raman intensity. Our goal was to provide an *improved experimental and theoretical understanding of the physical phenomena* that govern the adsorption and interaction of analytes with metallic nanoparticles and nanostructured metallic surfaces. We specifically aimed to understand the effect of molecular polarity and surface electronegativity on the analyte surface binding and the subsequent surface-enhanced Raman scattering (SERS) intensity. A better understanding of these phenomena will lead to the ability to predict SERS activity towards a specific class of chemicals and tailor SERS substrate sensitivity to specific chemical moieties for improved selectivity. This summary consists of results obtained over the past year, identifying the physisorption and chemisorption characteristics of thiophenol adsorbed onto commercial gold substrates. We also developed a theoretical understanding of the sharing of electron density across thiophenol molecules which result in a better match of predictive SERS spectra.

Keywords: surface-enhanced Raman spectroscopy, adsorption kinetics, chemisorption, physisorption, density functional theory.

1. INTRODUCTION

SERS is potentially a very valuable tool for detecting low concentrations of analytes.[1-4] The ability to detect extremely low concentrations and even single molecules is made possible when molecular vibrations strongly couple to the electromagnetic fields near or at the surface of certain nanostructured materials; enhancing the Raman signal as much as 10^6. While the mechanisms governing the SERS response are well understood (i.e., chemical and electromagnetic enhancement), much of the attention has been focused on factors to improve the electromagnetic enhancement. One of the remaining issues with SERS is that many molecules exhibit little or no affinity for the metallic surfaces and, therefore, have no measurable SERS response. Since the electromagnetic field is only enhanced near the surface, it is essential for enhancement that the molecule be either chemisorbed or physisorbed to the substrate surface. Many of the molecules reported in SERS experiments are generally restricted to classes of molecules that tend to strongly bind at the nanostructured substrate surface (e.g., thiols, amines, and aromatic macrocycles). These molecules are invaluable for characterizing the SERS phenomenon, but the results obtained cannot be extrapolated to other molecules. There exists a wide array of molecules, such as ketones and carboxylic acids, that are not SERS active due to weak analyte-metal interactions.

Thiophenol is one of the most studied SERS active molecules due to the strong propensity of thiols to form covalent bonds with noble metal surfaces and the observation that aromatic thiols in particular produce strong SERS spectra.[5,6] This study focuses on the reaction mechanisms of the analyte binding as a function of pH. Thiols are known to chemisorb on noble metals through loss of the sulfhydryl hydrogen and covalent bond formation between the sulfur and metal surface.[7] Although several groups have studied the adsorption of thiophenol on metallic surfaces, there are still aspects of the kinetics, energetics, and reaction mechanisms that are not fully understood.

The adsorption mechanism is expected to depend on the physical state of the thiophenol molecule when interacting at the surface (i.e., in gas phase or solution). In the gas phase, the thiophenol molecules are intact when they impinge upon the surface and must lose the hydrogen atom before chemically binding to the surface. However, in solution, they may be either intact or ionized depending on the pH. The acid dissociation constant (pKa) for the sulfhydryl proton dissociation of thiophenol is approximately 7, which indicates that under acidic conditions, the majority of the molecules will remain intact; however, while under basic conditions, the majority is ionized as the thiophenolate ion. This is particularly important since it affects whether or not the sulfhydryl hydrogen will need to dissociate at the surface in order for chemisorption to occur.

By performing time-, temperature-, and pH-dependent measurements of thiophenol in aqueous solution, we can elucidate the nature of the adsorption mechanisms for thiophenol. From the shape of the kinetic growth profiles and the temperature dependence of the rates, we can infer the mechanism and calculate the activation energy. In addition, measurements at different pH values can be used to determine differences in the mechanism depending on whether the thiophenol molecules are protonated or deprotonated. These types of measurements described here are critical for developing a predictive model of SERS performance.

2. EXPERIMENTAL

Thiophenol was purchased from Sigma-Aldrich (Cat#20249-10G) and used without further purification. Due to the low solubility of thiophenol in water, stock solutions were prepared in ethanol at various concentrations and then diluted to final working concentrations with deionized water (18.2 MΩ·cm). Hydrochloric acid (Sigma-Aldrich Cat#320331-2.5L) was used to obtain acidic conditions and sodium hydroxide (Sigma-Aldrich Cat#221465-25G) was used to obtain alkaline conditions. Aqueous solutions of thiophenol were prepared by diluting 35 μL of thiophenol solution in ethanol at a known concentration with 7 mL of aqueous medium at a particular pH value. This gives an ethanol content of 0.5%. The solution was vigorously shaken and allowed to equilibrate for at least 30 minutes at the measurement temperature before exposing it to the gold substrate.

2.1 Gold SERS substrate

Commercially available gold SERS substrates (Klarite®, KLA-312, Renishaw Diagnostics Ltd., UK) were used for this work. The substrates provide adequately strong and reproducible SERS enhancement when 785 nm excitation is used. Figure 1a shows a scanning-electron microscope (SEM) image and plasmon reflectivity spectrum of a typical Klarite substrate illustrating the inverted pyramid structure and plasmon absorption. The SEM image was acquired with a Phenom Pro-X desktop SEM (Phenom World).
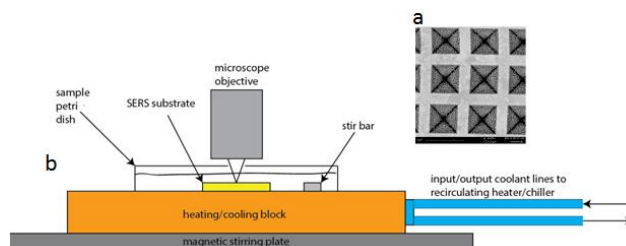

Figure 1. a) SEM image of commercial Klarite and b) schematic of temperature control unit.

2.2 Raman microscopy

The Raman measurements were performed with a JASCO NRS-3200 dispersive Raman microscope system operating at 785 nm excitation with approximately 4 mW power incident on the sample. A 10× microscope objective was used both to focus the laser on the substrate and to collect the Raman return light. The relatively modest laser power and magnification were used to minimize any laser-induced heating of the substrate. Stirring the temperature-controlled reaction bath also helped to minimize any local heating effects.

2.3 Temperature control and sample handling

A temperature control system was designed to maintain isothermal conditions for the 7 mL of thiophenol solution and Klarite® substrate. Figure 1b shows the schematic setup of the temperature control module in conjunction with the sample holder. The analyte sample chamber was composed of a Klarite® substrate mounted in a 50 mm diameter

polystyrene Petri dish (Model 351006, BD Biosciences) and a magnetic stir bar (Catalogue # 1451363, Fisher Scientific) to continuously stir the thiophenol solution. A 3 mm diameter hole was drilled into the lid of the Petri dish to allow the laser to pass through and illuminate the substrate without interference from the polystyrene cover. The sample holder was placed on top of a liquid cooled copper block for thermal management. A silicone-based heat sink compound (Radio Shack, part number 2760255) was applied between the bottom of the Petri dish and the copper thermal block to ensure proper thermal contact. A digitally-controlled, refrigerated, circulating water bath (Polyscience model MX 07R-20A11B) was used to continuously flow liquid coolant (50% ethylene glycol aqueous solution) through the thermal block. The thermal block was placed on top of a magnetic stir plate (Model Labdisc S1, Fisher scientific); set at maximum speed. Measurements were initiated upon the addition of thermally equilibrated solution on top of the Klarite substrate. New Klarite® substrates and sample holders were used for each experiment since they cannot be cleaned and reused.

2.4 Quantum calculations

Quantum mechanical calculations were performed using Gaussian 2009, revision C.01 on neat thiophenol chemically-bound to silver clusters with one, three, five, and seven atoms. The hydrogen attached to the thiol group in the free molecule was not included in the calculation and was considered already detached. Two geometries were explored for the three-silver-atom cluster calculations. Where the three-silver cluster formed an equilateral triangle, one geometry attached the sulfur of the thiophenol to the apex of the cluster, and the other geometry attached it to a side of the triangle. For the five and seven atom metal clusters, the atoms were laid out in a plane to approximate a surface, although these sheet-like clusters were allowed to relax without constraints during geometry optimization. All calculations involving the silver metal clusters were performed with the hybrid B3LYP functional with the LANL2DZ double ζ basis set with relativity corrected effective core potentials. To explore basis set effects, additional calculations were performed on molecular thiophenol and the B3LYP functional with the triple ζ 6-311+G(d,p) and correlation corrected aug-cc-pVTZ basis sets. Excitation frequency dependent spectra were calculated using the coupled perturbed Hartree-Fock equations at 785 nm for all calculated Raman spectra. The vibrational wavenumbers have been scaled by a factor of 0.961 for the B3LYP/LANL2DZ method.[8] Time-dependent density functional theory (TD-DFT) calculations for the lowest 200 electronic states were performed to investigate the influence of the metal-molecule interaction on the electronic structure for the thiophenol and 4-mercaptophenol. To examine different molecular orientations, the Raman spectrum was calculated from a model containing two thiophenol molecules and a seven-silver-atom cluster where the open shell, unrestricted calculation was performed. The presence of a second molecule during geometry optimization forced one molecule into an upright position and brought the ring of the other molecule into contact with the metal cluster. Raman signal was attributed to a particular molecule in the model by weighting the Raman scattering factor by the Cartesian atomic displacements of the atoms in that molecule. Generally, the normal modes separated cleanly between the two analyte molecules. The interaction between analyte molecules mediated by the metal surface was modeled with one to three analyte molecules, where each molecule was associated with a single silver metal atom. The clusters of three analyte molecules and three metal atoms, and two analyte molecules with two metal atoms, were permitted to relax without constraints during the geometry optimization.

3.   RESULTS AND DISCUSSION I

In the experimental part of this study, our focus was on gaining insight into the adsorption characteristic profile and self-assembled monolayer (SAM) formation of thiophenol. The mechanisms governing the kinetics of SAM formation of thiols in a liquid media on a stationary gold substrate can be separated into two steps: solution phase transport of the thiolated molecule to the gold surface followed by the adsorption of the thiol to that surface. In order to explore these mechanisms further, several experimental factors needed to be understood. These include mass transport mitigation, proper thiol/Klarite® analyte ratio, and controlling the ionized and non-ionized form of thiophenol via pH.

3.1 Mass transport mitigation

In order to study the chemical kinetics adsoprtion profile of thiophenol on a planar gold substrate in an aqueous media, it is crucial that the kinetic rates observed are not limited by mass transport. To ensure this, the mass transport rates of the thiophenol molecules in the aqueous phase should be considerably faster than the kinetic rates of chemical binding of thiophenol with gold. To mitigate the effects of diffusion limited mass transport, two initial

experiments were performed. Both were conducted at a concentration of 5×10^{-7} M thiophenol, at a temperature of 1.7°C and a pH of 2.0. The rationale for using low temperatures for this study was that the diffusion rate is much slower at low temperature and established a "worst-case" scenario in terms of diffusion-limited rates. The only difference in the two experiments was the use of active stirring with a stir bar. As can be seen in Figure 2(a), the temporal responses are quite different. By monitoring the 1076 cm^{-1} thiophenol band it can be seen that the intensity reaches a maximum value within three hours with stirring (red curve, inset). However, when unstirred there is a remarkable reduction in the rate (blue curve). It is estimated that relying on mass transport by diffusion alone reduced the binding rates by 30 times; demonstrating that stirring efficiently overcomes mass transport limitations.

3.2 Thiolphenol/Klarite analyte ratio

Another experimental parameter is the selection of the optimal thiophenol concentration. A key consideration is that the rate of formation of the thiophenol SAM should be slow enough that it can be measured with a high level of confidence. On the other hand, it is also important that the number of thiophenol molecules present in the aqueous phase be more than sufficient for the SAM formation to be completed. With these two constraints in mind, thiophenol solutions in varying concentrations of 10^{-8}, 10^{-7}, 5×10^{-7}, 5×10^{-6} and 5×10^{-5} M in pH 10 aqueous media were prepared. A temporal study was conducted with each of the prepared solutions at 30°C. At this temperature, the rates of binding are expected to be fast enough to conduct the study in a reasonable time frame. Figure 2(b) shows the effect of concentration on the rate of binding along with an estimation of the sufficiency of the number of thiophenol molecules for the reaction to produce a complete monolayer. Following the temporal response curves for the 1076 cm^{-1} band at each concentration, it is clear from the figure that the 7 mL volume of 10^{-8} M thiophenol solution does not contain enough thiophenol molecules for a SERS response to be observed on Klarite®. A 7 mL volume of 10^{-7} M thiophenol solution contains enough molecules to sufficiently observe a SERS response; while using higher concentrations does not seem to improve on the plateau value of the peak area of 1076 cm^{-1} feature. Based on this evidence, we chose 7 mL of 5×10^{-7} M thiophenol solution for our further experiments, since it contains a sufficient number of thiophenol molecules to form a SAM on the Klarite® substrate.

3.3 Ionization considerations

The study of the chemical interaction of thiophenol with gold in aqueous media can be a complex problem due to the possibility of ionization of the thiol group by detachment of the sulfhydryl proton resulting in the formation of the thiphenolate ion. The reported pKa for thiophenol at room temperature (25°C) is in the range of 6.5 to 8.0.[9] For our calculations, we assume the pKa value to be 7.0. It can be interpreted that at a pH of 7.0, a solution of thiophenol will contain 50% non-ionized thiophenol molecules in equilibrium with 50% ionized thiophenolate. With the use of an acidic solution, it can be ensured that most of the thiophenol molecules are not ionized. Figure 2c graphically shows the relationship between thiol and thiophenolate ion as it relates to pH and concentration. At pH 2, only 0.001% of the thiophenol molecules will ionize to thiophenolate ions. At this pH, the expected concentration of thiophenolate ions is 5×10^{-12} M, which contains about four orders of magnitude less than the number of thiophenolate ions required to form a SAM on Klarite® as discussed in the previous section. By maintaining pH 2, the chemical interaction of intact thiophenol molecules with gold can be studied. Conversely, with the use of alkaline solution the equilibrium shifts towards more complete ionization of thiophenol to thiophenolate. Based on equilibrium at pH 10, about 99.9% of the thiophenol molecules ionize to thiophenolate ions. The expected concentration of thiophenol molecules is 5×10^{-10} M, which contains about one hundred times fewer molecules than the number of thiophenol molecules required to form a SAM on Klarite®. By setting the pH, control over the level of ionization becomes much simpler and the experimental probe becomes thiophenol in either its non-ionized or ionized form.
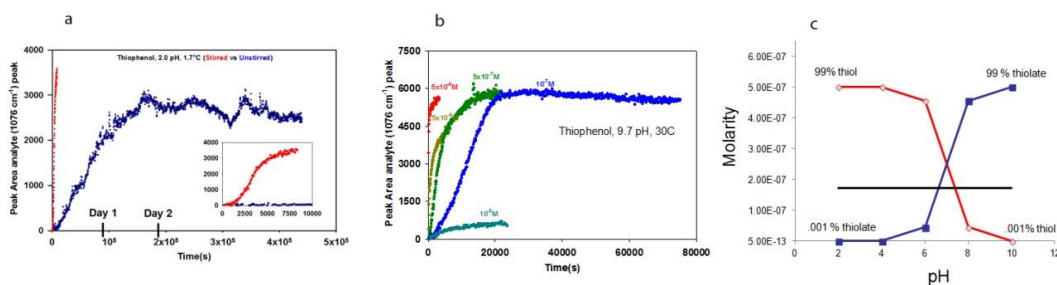

Figure 2. (a) Effect of stirring and mass transport on rate of SAM formation, b) effect of thiophenol concentration on rate of binding, and c) graphical representation showing thiol/thiolate availability versus pH.

An example of a time-resolved SERS response of thiophenol interacting with Klarite® at various pH values is shown in Figure 3. In each case, 7 mL of 5×10^{-7} M thiophenol solution was added to the sample chamber, and the Raman spectral response was recorded as a function of time. The process was repeated at pH 2, 4, 6, 8 and 10. Figure 4 shows the results for pH 2, 6 and 10. These experiments were performed at constant temperatures just above 0°C. It is observed that for acidic solutions (pH 2 and 6) there is a delay in time before the Raman spectral features for thiophenol begin to increase. This delay is not observed in alkaline solutions (pH 10). Scaled temporal responses of a few selected Raman active vibrations of the thiophenol molecule at 422 cm^{-1}, 695 cm^{-1}, 1003 cm^{-1}, 1027 cm^{-1}, and 1076 cm^{-1} are shown in the top panels of Figure 3. The scaling was obtained by dividing the peak area value at a given time by the saturation value of the peak area. It is observed that the temporal response shows a logistic growth curve[9] for all the selected features in acidic media (pH 2 and 6); with the maximum response being reached within 2 hours after the start of the experiment. However, as the pH is increased, the growth curve shows a Langmuir or exponential rise-to-maximum response.[10] The time to reach the saturation point at the higher pH of 10 is nearly twice as long (about 4 hours). This indicates that the mechanism of thiol binding changes with pH.
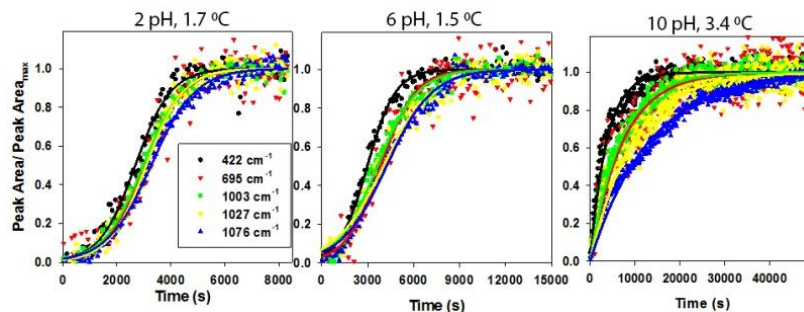

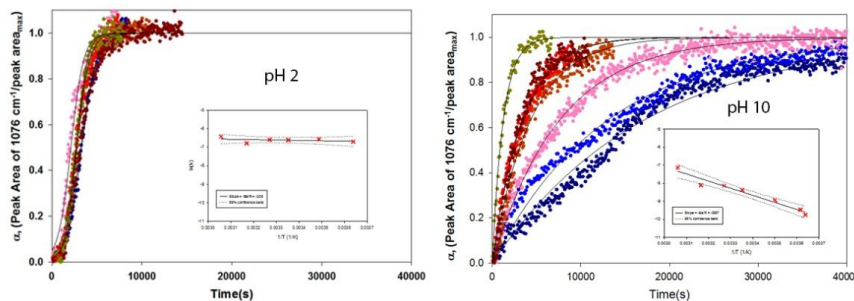**Figure 3. Time resolved SERS responses of thiophenol at various pH values.**

Figure 4. Normalized temperature profiles of the 1076 cm^{-1} thiophenol band at pH 2 and 10. Insets are resulting Arrhenius plots.

From Figure 3, it is clear that the temporal curve for the 422 cm^{-1} band (black curve) reaches the saturation point faster than the temporal curves for the rest of the vibrational bands followed. A similar phenomenon was observed by Van Duyne *et al*. and was attributed to a change in the angle of the C-S stretch.[10-11] The phenyl ring mode at 1076 cm^{-1} shows the strongest band intensity when compared with the remaining Raman features and is primarily used to evaluate chemical kinetic parameters for the formation of SAMs on the gold substrates. It is believed that the SERS intensity of this ring breathing mode is less sensitive to orientation than the C-S stretching mode and would give a more accurate indication of the surface coverage. Murray and Bodoff have also shown that the SERS intensity per molecule can decrease as a function of coverage due to depolarizing effects from adjacent adsorbed molecules. This may affect different bands of the same molecule in different amounts.

An examination of the temporal response of the spectral feature at 1076 cm^{-1} at pH 2, as shown in the top left of Figure 3 (blue curve), reveals a logistic type growth curve. Several studies have shown that thiols interacting with planar gold surfaces tend to form "islands" or two-dimensional arrays. This is a strong indication of a nucleation site build-up model where an earlier deposited thiol site on gold acts as a catalyst for deposition of subsequent thiol molecules. As will be shown later, it is believed this is also related to physisorption at low pH values as physisorbed thiophenol molecules are more likely to dissociate and chemisorb at island edges. This will be elucidated further in a later section on temperature-dependent measurements. The island formation exhibited by thiophenol interaction with

gold is an autocatalytic process. Autocatalytic reactions follow the Prout-Tompkins model (P-T).[30] The rate equation for a first-order auto-catalyzed reaction is shown below.

$$\frac{d\theta}{dt} = k_b(1 - \theta) \tag{1}$$

Here θ is the conversion fraction, t is the time of reaction, and k_b is the conversion-fraction-dependent rate constant. In auto-catalyzed reactions, k_b is assumed to be a linear function of θ; therefore, $k_b = k\theta$ where k is the conversion-fraction-independent rate constant. The rate equation (1) can be rewritten as:

$$\frac{d\theta}{dt} = k\theta(1 - \theta) \tag{2}$$

Integrating the above equation (2) and rearranging:

$$\theta = \left(1 + e^{-k(t-t_0)}\right)^{-1} \tag{3}$$

where t_0 is an integration constant. By fitting the temporal intensity curve of the Raman feature at 1076 cm^{-1} to the above equation (3), the rate constant, k, is obtained.

A similar examination of the temporal response of the spectral feature at 1076 cm^{-1} at pH 10, as shown later in the top right of the Figure 4 (blue curve), reveals a Langmuir isotherm type curve (exponential rise-to-maximum curve) indicating first order chemical kinetics. In this case, the rate equation (1) is simplified by substituting k_b with k.

$$\frac{d\theta}{dt} = k(1 - \theta) \tag{4}$$

Integrating equation (4) and rearranging,

$$\theta = 1 - e^{-kt} \tag{5}$$

Therefore, by fitting the temporal curve of the Raman feature at 1076 cm^{-1} to the equation (5), the rate constant, k, is obtained. In this case we believe there is no physisorbed precursor, as will be examined in more detail in the next section.

3.4 Effect of temperature

To broadly understand the nature of the binding process of thiophenol with gold, including whether the process is rate limited by physisorption or chemisorption, estimation of the activation energy of binding is important. If the activation energy of the binding is near zero (or very low), it is highly likely that the binding process is rate limited by physisorption.[31] Conversely, if the activation energy is high, the process is considered to be chemisorption rate limited.[31] To investigate the nature of the rate limiting step, a temperature-dependent study for each of the five pH values (2, 4, 6, 8 and 10) was conducted. As discussed in the previous section, the temporal response of the Raman spectral feature at 1076 cm^{-1} was selected to estimate the chemical kinetic rate constant, k. Figure 4 shows the scaled temporal response curves of the 1076 cm^{-1} band at pH 2 and 10. At pH 2, 99.999% of thiophenol is in the non-ionized form thiophenolate (Figure 2c) and the liquid phase interaction of thiol mimics the gas-phase absorption where the thiophenol molecules are presented to the gold sites in non-ionized form. Clearly, the change in temperature at pH 2 does not seem to significantly influence the rate at which the peak builds over time or the shape of the temporal profile. This lack of temperature dependence further validates our contention that stirring has eliminated the effect of mass transport on the physisorption rate. If the rate were diffusion-limited, it would increase with increased temperature. Because the shape of the profile matches a logistic growth curve, the temporal profiles for pH 2 in Figure 4(a) were fit to the P-T model as described by equation (3); with the black lines showing the fit curves. Through curve fitting the data, the rate-constant, k, can be estimated.

Ionization of 99.9% of thiol to thiophenolate is expected to occur at pH 10 (Figure 2c). Clearly, the temporal profiles observed at pH 10 show remarkable differences from those obtained at a lower pH with a strong dependence on temperature. As the temperature increases the reaction rate also increases. The shape of the temporal profile shifts from logistic at a pH 2 to Langmuir at pH 10. At high pH, the time-dependent Langmuir isotherm, described by equation 5, was used to fit the temporal profiles and determine the rate constant, k.

Using the estimated rate constants at each temperature and pH, the Arrhenius equation can be used to calculate the activation energy of binding, E_a. According to the Arrhenius equation, k is a function of absolute temperature, T, as shown below:

APPROVED FOR PUBLIC RELEASE

$$k = Ae^{-E_a/_{RT}} \tag{6}$$

where, A is the pre-exponential or frequency factor and R is the gas constant.[10] Equation 6 in logarithmic form is shown below:

$$\ln(k) = \ln(A) - \frac{E_a}{RT}. \tag{7}$$

According to the equation (7), a plot of the natural logarithm of k verses the inverse of the absolute temperature is expected to be a straight line with a slope of $-E_a/R$. The inset of Figure 4 show the Arrhenius plots of each of the pH values. For pH 2, the Arrhenius plot shows little or no dependence of the rate constant on temperature. The activation energy values are also close to zero, which implies that the rate limiting step in the attachment of non-ionized thiophenol is not a chemical binding step; since that would require crossing a measurable activation energy barrier.[10] Therefore, we reason that the rate limiting step is physisorption. When examining the case where greater than 99% thiophenolate is available for attachment to gold at pH 10, a different behavior is observed. The Arrhenius plot at pH 10 shows a strong dependence on temperature, and the activation energy value is calculated to be 32.7 kJ/mol. Since the activation energy for pH 10 is significantly greater than zero, it implies that the rate limiting step in the attachment of thiophenolate is a chemical binding step (chemisorption).[31]

A plot of activation energies at various pH values is shown in Figure 5a. As discussed earlier, at pH 2 and 4 (>99% non-ionized thiophenol) the activation energies are near zero and at pH 10 (>99% thiophenolate) the activation energy is significantly greater than zero. Not surprisingly, the data for pH 6 and 8 show a transitional region in activation energies. At low pH, where non-ionized thiophenol molecules are in abundance, a negligible activation energy of binding is observed. At high pH, where thiophenolate ions are in abundance, a measureable activation energy (between 25-32 kJ/mol) is observed. This implies a change in the rate-limiting mechanism from physisorption (for non-ionized thiophenol) to chemisorption (thiophenolate).

In summary, Figure 5b illustrates the proposed reaction mechanisms. At low pH (left panel), the thiophenol molecule approaches the surface intact. After island nucleation on the surface has occurred, it is more likely that additional molecules will physisorb on the islands and then bind at their edges. When the final binding step occurs, the sulfur-bound hydrogen detaches and a sulfur-gold covalent bond is formed. Since this appears to be a nucleation and growth process, the sigmoid-shaped (autocatalytic) curve is reasonable for describing the kinetics. Also, since physisorption can be the rate limiting step, the negligible activation energy observed is reasonable. At high pH (right panel), the molecule interacts with the surface in the thiophenolate ion form. It can then directly chemisorb to the surface without having to first undergo hydrogen detachment. The binding then tends to occur at random sites on the surface without nucleation and growth, resulting in a typical Langmuir kinetic profile. Since chemisorption is the rate-limiting step, significant activation energy is observed.
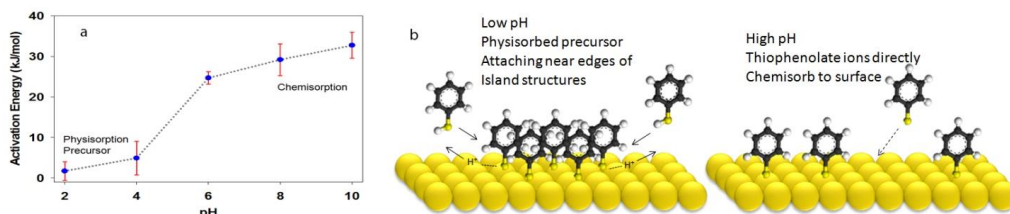

Figure 5. a) Summary of activation energies showing a physisorption phase transitioning to a chemisorption phase for the binding of thiophenol on gold surfaces. b) Proposed binding mechanisms.

4. RESULTS AND DISCUSSION II

In the theoretical-based part of this study, our focus was on gaining insight into the predictive SERS responses of analytes on surfaces. This year's work culminated with a publication in the Journal of Physical Chemistry A, detailing the inclusion of interaction between multiple thiophenol analyte molecules as being essential to account for the relative enhancements observed experimentally. An examination of the molecular orbitals showed sharing of electron density across the entire model of multiple thiophenol molecules mediated by the metal atoms.

Figure 6 compares the experimental thiophenol on silver SERS spectrum to spectra calculated from a single thiophenol and silver atom to three thiophenol molecules and three silver atoms. The experimental spectrum has

peaks at 416 cm^{-1}, 689 cm^{-1}, 986 cm^{-1}, 996 cm^{-1}, 1020 cm^{-1}, 1069 cm^{-1}, 1155 cm^{-1}, 1181 cm^{-1}, 1470 cm^{-1}, and 1571 cm^{-1}. These peaks appear in the theoretical spectra below the experimental one. The three theoretical spectra were calculated from the models shown, where the number of thiophenol plus silver units are increased from one to three. The most striking observation that can be made is that as thiophenol plus silver units are added to the model, the relative intensities between the peaks at 970 cm^{-1}, 996 cm^{-1}, 1052 cm^{-1}, and 1560 cm^{-1}, begin to resemble the relative intensities of the experimental peaks at 996 cm^{-1}, 1020 cm^{-1}, 1069 cm^{-1}, and 1571 cm^{-1}, respectively.

SERS Frequencies and Relative Intensities

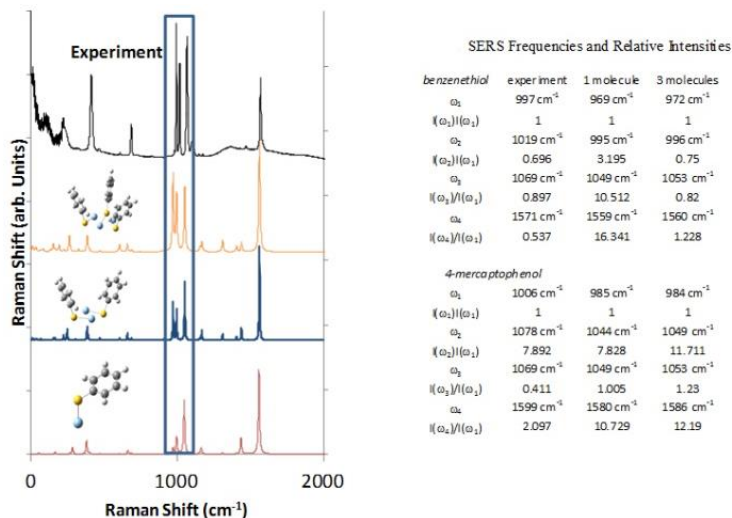| benzenethiol	experiment	1 molecule	3 molecules
ω_1	997 cm^{-1}	969 cm^{-1}	972 cm^{-1}
$I(\omega_1)/I(\omega_1)$	1	1	1
ω_2	1019 cm^{-1}	995 cm^{-1}	996 cm^{-1}
$I(\omega_2)/I(\omega_1)$	0.696	3.195	0.75
ω_3	1069 cm^{-1}	1049 cm^{-1}	1053 cm^{-1}
$I(\omega_3)/I(\omega_1)$	0.897	10.512	0.82
ω_4	1571 cm^{-1}	1559 cm^{-1}	1560 cm^{-1}
$I(\omega_4)/I(\omega_1)$	0.537	16.341	1.228
4-mercaptophenol			
ω_1	1006 cm^{-1}	985 cm^{-1}	984 cm^{-1}
$I(\omega_1)/I(\omega_1)$	1	1	1
ω_2	1078 cm^{-1}	1044 cm^{-1}	1049 cm^{-1}
$I(\omega_2)/I(\omega_1)$	7.892	7.828	11.711
ω_3	1069 cm^{-1}	1049 cm^{-1}	1053 cm^{-1}
$I(\omega_3)/I(\omega_1)$	0.411	1.005	1.23
ω_4	1599 cm^{-1}	1580 cm^{-1}	1586 cm^{-1}
$I(\omega_4)/I(\omega_1)$	2.097	10.729	12.19

Figure 6. Effect of analyte-molecule interaction with comparison of experimental and theoretical benzenethiol on silver SERS spectra. As intermolecular interaction between analyte molecules is increased, ring breathing and stretching modes become more pronounced. Table shows frequency agreement between theoretical and experimental.

The numbers in the adjoining table of Figure 6 show the degree of agreement between experiment and models for both the single analyte and metal atom system and for the three analyte molecule and three metal atom systems that appear in Figure 7. The frequencies listed in the table of Figure 6 correspond to similar vibrational modes in both thiophenol and 4-mercaptophenol. Interestingly, ω_1 through ω_3 correspond to ring breathing modes, and ω_4 corresponds to a ring stretching mode with stretching along the two C-C bonds parallel to the C-S bond. The intensities have been normalized using the intensity of ω_1. For the ω_2, ω_3, and ω_4 frequencies of thiophenol with a single analyte molecule, the predicted relative intensities are up to 30 times greater than what is seen experimentally. However, when three analyte molecules are considered together, the theoretical relative enhancements are much closer to the experimental values.
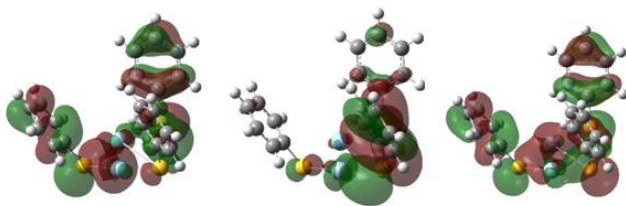

Figure 7. Three highest energy occupied molecular orbitals distributed over the three-membered cluster of thiophenol/sliver.

The results point toward a key assumption in the previous simulations that the benzenethiol surface densities are low, so that there is no interaction between these molecules. X-ray studies have shown that in fact, self-assembled monolayers from aromatic thiols form densely packed, highly ordered structures on noble metal surfaces such as silver.[12] Furthermore, the 24.5° cant angle between the molecule and the vector normal to the substrate shows the molecules are tightly packed, where isolated molecules tend to come into contact with the substrate. Since the packing of the benzenethiol molecules forces them to be in the upright position, they must be close enough to influence the electronic structure of each other and, thus, the degree of Raman enhancement as well. Figure 7 shows the highest occupied molecular orbital (HOMO) and the two molecular orbitals (MOs) immediately below the HOMO in energy for benzenethiol. It can be seen that sharing of electron density occurs across all three model

71

molecules for both analyte compounds. This result demonstrates that interaction between analyte molecules on the SERS substrate surface should be included, and that charge transfer states can be considered to involve groups of molecules and the metal substrate. In the sum of states framework, these charge transfer states contribute to the sum over the ground and excited electronic and nuclear states.

5. CONCLUSIONS

The mechanism of thiophenol binding on a stationary gold substrate in an aqueous media has been shown to exhibit pH dependence. Although many studies have recognized the importance of pH in SERS response, to our knowledge, this is the first study to quantitatively show the difference between physisorption and chemisorptions based on pH. The estimated near-zero activation energy of binding of non-ionized thiophenol strongly suggests that the binding process with gold is physisorption rate-limited. The binding mechanism transitions to Langmuir or first order kinetics at high pH (e.g., pH 10) where 99.9% of the thiophenol is ionized to thiophenolate. In this case, the activation energy was calculated to be 32.7 kJ/mol, indicating that the rate-limiting step is chemisorption through the attachment of thiophenolate to gold. While molecules covalently bound to a noble metal surface, such as thiols, have appreciable surface-enhanced Raman signatures, they are not representative of many molecules the broader community is interested in detecting. Since all molecules do not produce a measureable SERS response, it is important to understand the mechanisms that facilitate or inhibit binding at the substrate.

The most important finding for the thiophenol on silver system is that interaction between analyte molecules must be included to account for relative enhancements of the identified vibrational modes. Also, the effect of molecular orientation relative to the SERS surface is a strong contributor to the observed response and an upright orientation of the thiophenol molecule was found to be most prevalent.

This year's work collimated in two peer-reviewed publications. The experimental work described above was recently accepted in the Journal of Physical Chemistry C, while the theoretical work was captured in the Journal of Physical Chemistry A.

ACKNOWLEDGEMENTS

REFERENCES

[1]   Guicheteau, J. et al., *Applied Spectroscopy,* **2011**, 65(2), p144-151.
[2]   Guicheteau, J. et al., *Applied Spectroscopy,* **2013**, 67(4), p396-403.
[3]   Kneipp, K. et al., *Physical Review Letters,* **1997**, 78(9), p1667-1670.
[4]   Pearman, W.F., *Applied Spectroscopy,* **2006**, 60(4), p356-365.
[5]   Biggs, K.B. et al., *Journal of Physical Chemistry A,* **2009**, 113(16), p4581-4586.
[6]   Carron, K.T. and Hurley, L.G., *Journal of Physical Chemistry,* **1991**, 95(24), p9979-9984.
[7]   Kang, H. et al., *Ultramicroscopy,* **2009**, 109(8), p1011-1014.
[8]   In *NIST Standard Reference Database Number 101*; Release 15b ed.; III, R. D. J., Ed.; NIST:
        http://cccbdb.nist.gov/, **2011**.
[9]   Candlin, J.P. and Wilkins, R.G., *Journal of the Chemical Society,* **1960**, 0(0), p4236-4241.
[10] Brown, M.E., *Thermochimica Acta,* **1997**, 300(1-2), p93-106.
[11] Atkins, P.W., *Physical Chemisty*. W.H. Freeman and Company: New York, **1999**.
[12] Frey, S. et al., *Langmuir,* **2001**, 17, p8
.

APPROVED FOR PUBLIC RELEASE

SEEDLING PROJECTS
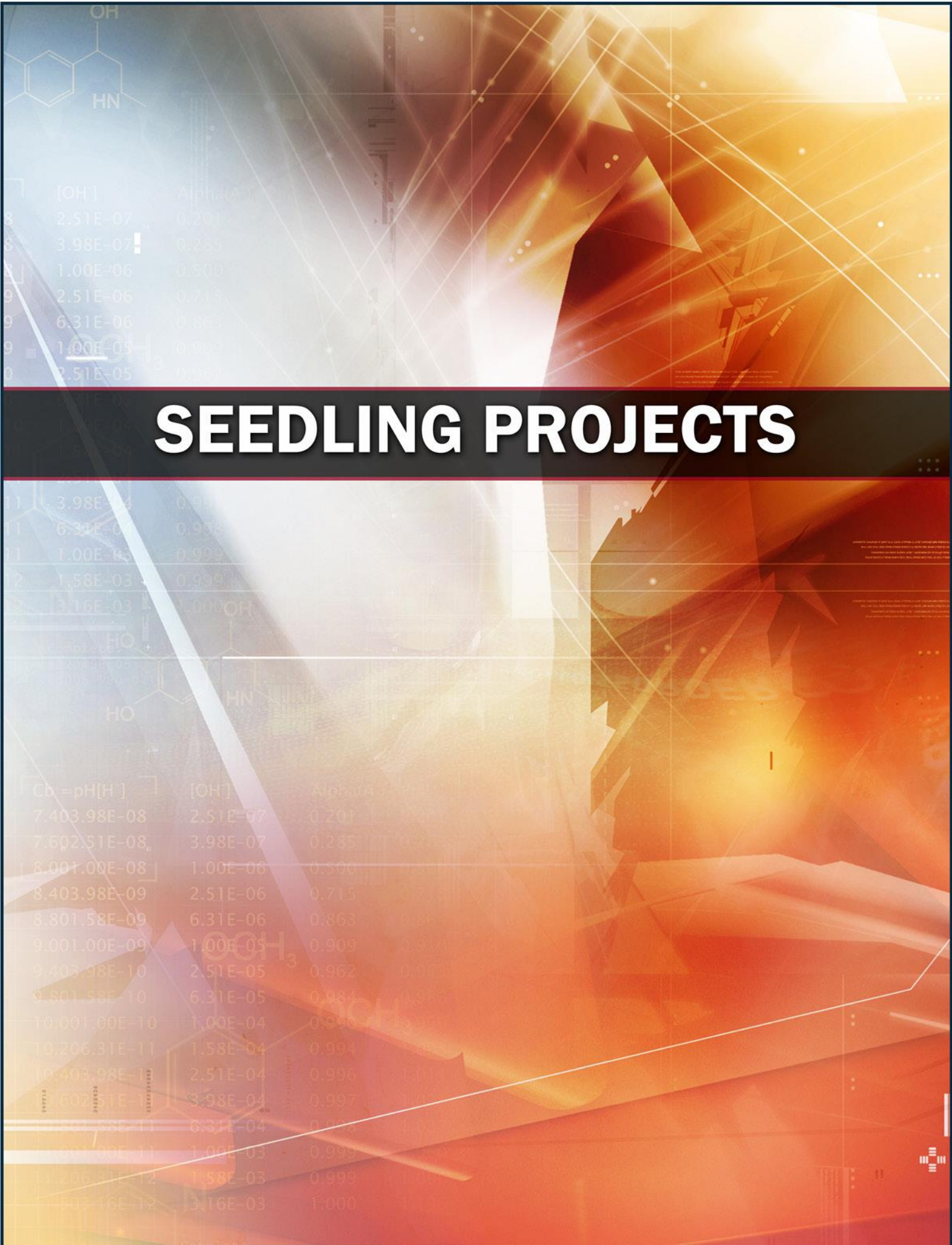
Decontamination of sulfur mustard by polymerization

Patrick C. Riley*[a], Matthew P. Willis[b], Amanda M. Schenning[a]
[a] Leidos, Gunpowder Branch, P.O. Box 68, Aberdeen Proving Ground, MD 21010-5424;
[b] U.S. Army Edgewood Chemical Biological Center, Research and Technology Directorate, 5183 Blackhawk Rd, Aberdeen Proving Ground, MD 21010

ABSTRACT

A polymerization reaction was performed between sulfur mustard (HD) and bisphenol A. This report demonstrates through several experiments that a condensation reaction occurs between HD and phenols, which allows for polymerization. The work highlights the importance of HD forming a more reactive intermediate in order for step-wise polymerization to proceed. This method of polymerization presents a pathway for bulk decontamination.

Keywords: Chemical warfare agent, polymer, synthesis

1. INTRODUCTION

The improvement of decontaminant technology requires an understanding of material-contaminant interactions to produce decontaminants that can mitigate hazards and reduce material damage. Dynamic contact angle (DCA) experiments have demonstrated an incompatibility between polycarbonate (Lexan) and certain contaminants (sulfur mustard (HD) and emerging threats) that resulted in a "thickening" of the applied contaminant. One possible explanation for this behavior is the occurrence of a polymerization reaction between the polycarbonate and applied contaminants.

Polycarbonate can be synthesized by a condensation reaction between bisphenol A (BPA) and phosgene, a potential electron acceptor whose structure is similar to HD. In the traditional synthesis of polycarbonate, BPA is treated with sodium hydroxide (NaOH) to deprotonate the phenol moieties on both sides of the molecule. The resulting diphenoxide[1,2] can subsequently allow for step-wise polymerization between phosgene and additional phenoxides. Analogous to the polycarbonate synthesis described, previous research has demonstrated that phenol can be reacted with HD in a similar condensation reaction.[3]

The current study aimed to react BPA with HD to yield a novel polymeric product that may explain the noted "thickening" of contaminants observed in DCA experiments. In the proposed reaction, we predicted that HD could behave as a Lewis acid and accept electrons from each of two deprotonated BPA molecules, resulting in a desired copolymer. Optimally, the generation of a solid non-hazardous by-product could present a pathway for bulk decontamination efforts. At a minimum, the generation of a solid by-product with residual characteristic toxicity may provide a decreased risk and expense for the transport and destruction of the neat (pure) material.

The experimental design utilized a small-scale vial reactor in order to rapidly test several configurations and minimize the amount of hazardous chemical agent required for testing. The research utilized three experiments designed to optimize reaction conditions, determine the need for the formation of the HD cyclic sulfonium ion intermediate, and to elucidate the types of pathways that could be used to synthesize the resulting polymer. The first experiment centered on reacting two less hazardous simulants, phenol in place of BPA and 2-chloro ethyl ethyl sulfide (CEES) in place of HD, to narrow down the experimental design and techniques to be employed. The second experiment reacted phenol and HD to examine the mechanism of the reaction, and the final experiment reacted BPA with HD to demonstrate polymerization and to analyze the final reactant product.

The information gained through the polymerization reaction involving HD could lead to the elucidation of a novel decontamination solution for not only HD, but also for emerging threat contaminants. Polymerization studies could provide a powerful tool in developing bulk decontamination methods. Additionally, insight into this chemical mechanism provides essential knowledge to the decontamination community when approaching new material-contaminant-decontaminant challenges.

2. METHODS

2.1 Small scale vial reactor

The experimental effort utilized a small-scale vial reactor method to duplicate earlier results[3] and provide an appropriate experimental design synthesizing the desired condensation reaction product. The execution of each experiment utilized similar testing equipment, reagents, and designs. Vial reactions were carried out in borosilicate glass vials and/or 7.5 mL Pyrex disposable culture tubes. For a typical vial reactor, 1.0 mL of the non-contaminant reactant solution was charged to the reactor and equilibrated to the desired temperature in a Torrey Pines Temperature-Controlled Orbital Shaker. Following equilibration, the vial reactor was dosed with contaminant in a single droplet, mixed for 10 seconds on a VWR Digital Vortex Mixer, returned to the temperature-controlled environment, and shaken during the reaction period.

The small scale vial reactor study employed both dilute and neat contaminant dosing. Traditional reactor testing uses neat chemical contaminant dosed into an excess amount of liquid decontaminant, and reaction products are sampled from the reactor reagent volume. However, due to low solubility and/or slow rates of dissolution of some organic chemical contaminants (e.g., HD in water), the contaminant may not distribute uniformly within the reactor, and may present a heterogeneous solution of contaminant droplets within the synthesis solution. If the contaminant droplets do not readily or rapidly dissolve, the synthesis reaction occurs primarily on the surface of the liquid droplet, and may become encapsulated by the polymerization reaction. The delivery of dilute contaminant to the vial reactor ensured an even dispersion of the contaminant throughout the reactor, which enabled an assessment of the reaction uninhibited by mass transport limitations. Delivery of neat contaminant ensured that reaction rates and products obtained would more accurately reflect bulk decontamination conditions.

The chemical agent used in this study was Chemical Agent Standard Analytical Reference Material (CASARM) grade HD. Chemical agents were used only in properly certified surety facilities capable of handling such chemicals safely. The personnel handling the chemical agents for this study were fully trained and certified for such operations. Dilute HD contaminant spiking solutions were prepared by transferring a known volume of contaminant to a glass vial and diluting with a known volume of methanol. Concentration of the spiking solution was determined using an established gas chromatographic-triple quadripole (GC-QQQ) analytical method.

All non-surety chemicals utilized in the preparation of solutions for this study were of American Chemical Society (ACS) reagent grade or better and were used as received from the manufacturer. CEES (CAS no. 693-07-2, 98%), NaOH (CAS no. 1310-73-2, ≥97% powder), phenol (CAS no. 108-95-2, ≥99.9%, crystalline, loose), methanol (CAS no. 64-56-1, Chromasolv, for HPLC, ≥99.9%), and BPA (CAS no. 80-05-7, ≥99%) were purchased from Sigma-Aldrich (Milwaukee, WI). Non-agent solutions were prepared on a weight/volume basis using Class A volumetric glassware and were mixed by inversion.

2.2 Experiment 1: phenol and CEES synthesis

In the first experiment, equal volumes of methanolic solutions of 1 M phenol and 1 M NaOH were mixed at ambient temperature in an attempt to produce the desired sodium phenoxide reactant. A 0.5 mL aliquot of the reactant was dosed with 0.025 mL of neat CEES, mixed well, and set to react overnight. Observations of the reaction mixture immediately following CEES addition showed no evidence of precipitation; however, after ~18 hours, a clear, flaky precipitate was observed in the bottom of the reaction vessel. The solution was heated in a water bath to >40°C with no observed dissolution of the precipitate. Upon the addition of 3 mL of cold deionized (DI) water, the precipitate was observed to dissolve resulting in a cloudy white solution. Following overnight refrigeration, the solution appeared clear, and an immiscible droplet was observed in the bottom of the vial. The droplet was extracted from the solution with a Pastuer pipet and examined on a Thermo-Nicolet 670 Fourier transform infrared spectroscopy (FTIR) spectrometer equipped with a GoldenGate diamond single bounce attenuated total reflection (ATR) accessory.

2.3 Experiment 2: phenol and HD synthesis

A single reactant solution of 0.48 M NaOH and 0.48 M phenol was prepared in methanol and distributed in 0.5 mL aliquots to each of six reactor tubes. The tubes were equilibrated to 40°C for 30 min. Following equilibration, the tubes were contaminated with 0.5 mL of dilute HD (0.240 M in methanol), vortexed, and shaken at 40°C for one hour. At the end of the reaction period, no salt formation was noted in the tubes. An aliquot from each tube was removed, diluted in chloroform, and analyzed for remaining HD on an Agilent 7890A gas chromatograph (GC) equipped with a 5975C Mass Selective Detector (MSD). An unspecified amount of ice water was added to the

remaining contents of each reactor tube, resulting in the immediate formation of a cloudy white precipitate, similar to that observed in Experiment 1. The reactor tubes were stored at ambient temperature overnight to allow collection of the observed product. Observations of the tubes made the following morning revealed a white needle precipitate and an immiscible clear fluid. Samples of each product were collected and analyzed by the GC/MSD.

2.4 Experiment 3: BPA and HD polymerization reaction

A reactant solution of 0.64 M NaOH with 0.48 M BPA was prepared in methanol. Six reactor tubes were filled with 0.750 mL of the NaOH/BPA reactant and six tubes were filled with 1.0 mL of the same solution. All tubes were equilibrated to 40°C for 30 min. Following equilibration, the reactors containing 0.750 mL of reactant were contaminated with 0.250 mL of dilute HD (1.2 M in methanol), and the reactors containing 1.0 mL of reactant were contaminated with 0.030 mL of neat HD. All 12 tubes were vortexed and shaken at 40°C for 3 hours. Following the reaction period, each tube was sampled and analyzed by GC/MSD for remaining HD. Ice water was added to the remaining contents of each tube, again resulting in the immediate formation of a cloudy white precipitate.

A subset of the reaction vials, three each of the dilute and neat contaminant conditions were returned to the 40°C shaker and reacted for an additional 3 hours, to determine if additional reaction time would affect product yield or composition.

In a separate experimental condition, 0.25 mL of 1.44 M BPA in methanol was added to 1.0 mL of 0.958 M NaOH in water in a scintillation vial. The contents of the vial was spiked with 0.50 mL of the dilute HD (1.2 M in methanol), resulting in the formation of a cloudy white precipitate upon the addition of HD. The scintillation vial contents remained at ambient and static conditions for several days to allow for formation and observation of additional reaction products.

At the conclusion of the BPA and HD reaction experiments, the formation of three separate reaction products was observed, based upon the treatment of the reactors in the three sets of experimental conditions described above. Each of the three products was sampled and screened by ^{1}H nuclear magnetic resonance (NMR) and ^{13}C NMR on a 400 MHz JEOL ECS-400 NMR.

3. RESULTS AND DISCUSSION

3.1 Experiment 1 results: synthesis of 2-phenoxyethyl ethyl sulfide

Following the reaction of CEES and phenol a product was confirmed by visual inspection and is shown in Figure 1.
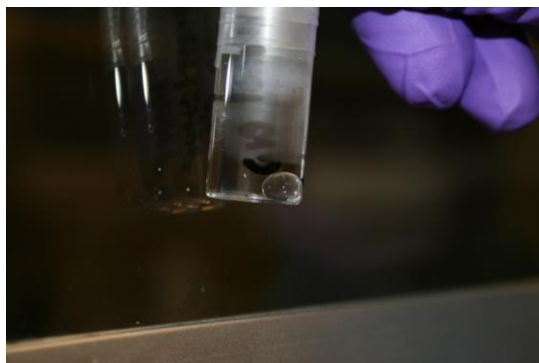

Figure 1. Immiscible product obtained in the reaction of CEES and phenol.

The product was analyzed by FTIR-ATR and the following spectra in Figure 2 and corresponding peak analysis in Table 1 were obtained.
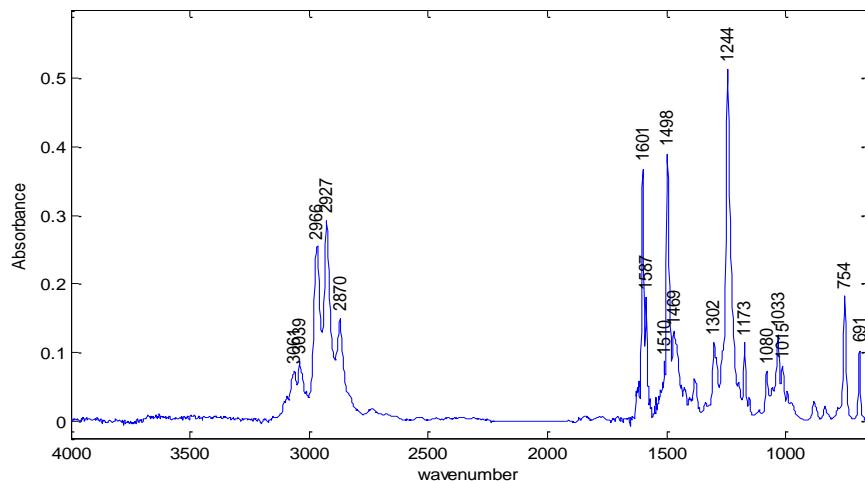
Figure 2. FTIR-ATR spectra of 2-phenoxyethyl ethyl sulfide.

Table 1. Peak analysis of IR Spectra shown in Figure 1. This analysis confirms the synthesis product obtained in Experiment 1.

Position(cm^{-1})	Origin
691	Aromatic ring bend (mono-substituted)
754	Aromatic out of plane C-H bend (mono-substituted)
1033	Aromatic in plane C-H bend
1015	C-O-C stretch
1244	C-O-C stretch, S-CH$_2$ deformation
1498, 1601	Aromatic ring modes
2870	CH$_3$ symmetric stretch
2927	CH$_2$ asymmetric stretch
2966	CH$_3$ asymmetric stretch
3039, 3061	Aromatic C-H stretch

The analysis demonstrates that the chlorine in CEES was removed during the reaction and replaced with a phenoxy, forming 2-phenyoxyethyl ethyl sulfide. Figure 3 illustrates the crystalline sold that formed during the experiment. The solid can be attributed to the formation of NaCl, because the melting point was above 40°C, indicating it was not phenol, and because the salt dissolved readily in water. Additionally, the predicted reaction mechanism allows for the formation of NaCl when the phenoxy oxidizes the sulfide, removing the chlorine and leaving a free Na$^+$.
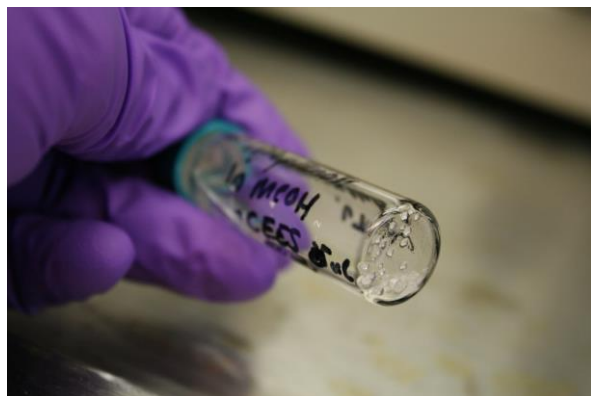
Figure 3. Salt precipitate formed during experiment.

3.2 Experiment 2 results: synthesis of bis(2-phenoxyethyl) sulfide

In the second experiment, the objective was to examine the reaction mechanism. In the previous experiment, the formation of NaCl during the reaction period was used to indicate reaction completion. In the second experiment, no salt formation was visually confirmed to indicate the reaction had occurred. Therefore, aliquots of solutions were analyzed by GC/MSD to determine if HD was present in the solution. The sampling was qualitative; if HD was present the reaction was either occurring very slowly or not at all. The GC/MSD spectra indicated that HD was not readily reacting. Ice water was then added to the samples and immediately a cloudy white precipitate formed. The formation of the precipitate indicated that water was needed for HD to react with itself and previous work[4] has shown that this was most likely due to the increased polarity of the environment, which allows HD to readily form the reactive intermediate cyclic sulfonium ion.

Figure 4 presents the two products that displayed different physical states. The solid needles in Product 1 and the "oily" droplet in Product 2 were analyzed by GC/MSD. Figure 5 is the spectra resulting from GC/MSD analysis of the two products. The figure contains the identified fragments for each peak. These spectra demonstrate that the white needles were the product confirmed by previous work[3] that reacted HD and phenol, bis(2-phenoxyethyl) sulfide. The spectrum also displays a "half-product" where only one chlorine ion is removed during the reaction and replaced with a phenoxy.

Figure 4. White needles on left, Product 1 and immiscible liquid on right, Product 2.
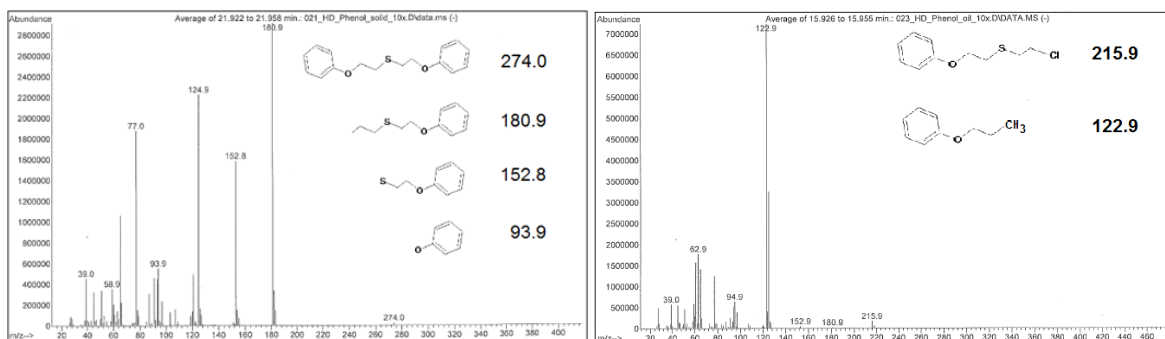

Figure 5. Product 1, left, bis(2-phenoxy ethyl) sulfide and Product 2, right.

3.3 Experiment 3 results: polymerization reaction

The main objective of the third experiment was to demonstrate the proof of concept of the polymerization reaction between HD and BPA. Secondary to the actual product formation, the experiment aimed to discern the effects of variation in reactor treatment to suggest areas for optimization in the experimental design to benefit product formation. Four reactor treatment conditions were considered: neat verses dilute HD delivery, temperature, agitation and length of reaction period, and the introduction of water to the reaction system.

The results indicate that no difference in product formation occurred using both neat and dilute HD. However, three distinct product forms were observed for three distinct reactor conditions. Figure 6 illustrates the three products formed. Product A resulted from a 3 hour reaction period, followed by the addition of ice water to the reaction vessel. Product B was formed similar to A, but reacted an additional 3 hours after ice water was added. Finally,

Product C resulted from the introduction of HD to an aqueous based BPA reaction solution, with no additional heat or mixing. Differences in the physical properties of the three products were encountered while attempting to separate the product layer from the solution. Product A was characterized as a "stringy" cloudy solid, Product B was found to be a viscous, "sticky", white solid, while Product C was flaky and free floating in solution.

Figure 6. Products obtained by different processing methods. Product A reacted and received ice water to precipitate product; Product B reacted, received water to precipitate product, and reacted for three additional hours; and Product C formed product immediately, used NaOH prepared in water and received no additional heat or mixing.

The polymerization reaction suggested that in all three conditions, the addition of water was crucial to the formation of a reaction product. The presence of water in the reaction may create the necessary degree of polarity to allow formation of an HD cyclic sulfonium intermediate, which in turn reacts with the deprotonated BPA ions in solution, forming the polymeric product. The precipitate seen in Figure 7 suggests the formation of a long chain polymer, as indicated by the viscosity and stretching nature of the product.
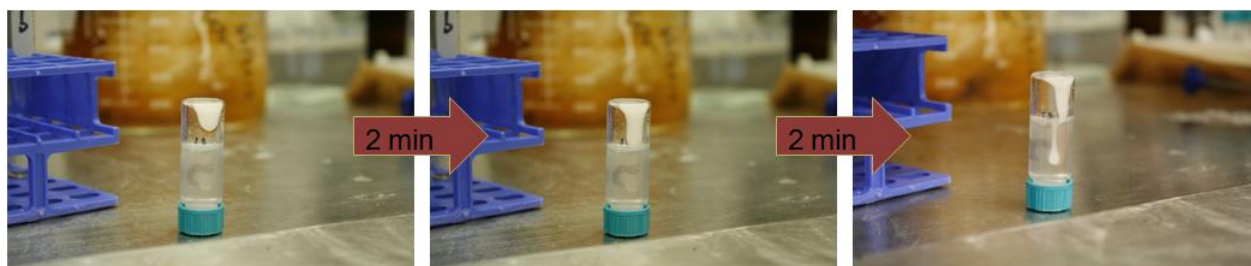
Figure 7. Demonstration of Product B viscous nature, polymers with long chains tend to exhibit this behavior.

The products were analyzed by ^{13}C NMR to discern whether the distinct physical characteristics were attributed to differences in chemical composition, or could be attributed to properties such as chain length. Figure 8 demonstrates a predicted spectrum for the polymer with terminating hydroxyl groups and Figure 9 demonstrates the resulting NMR spectra for the three products.
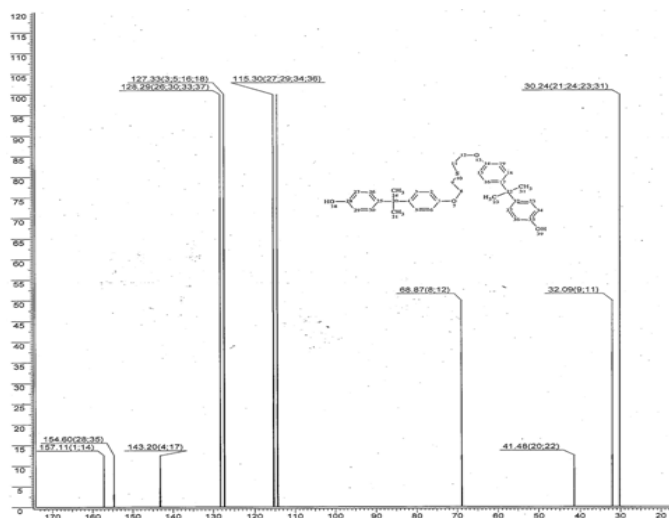

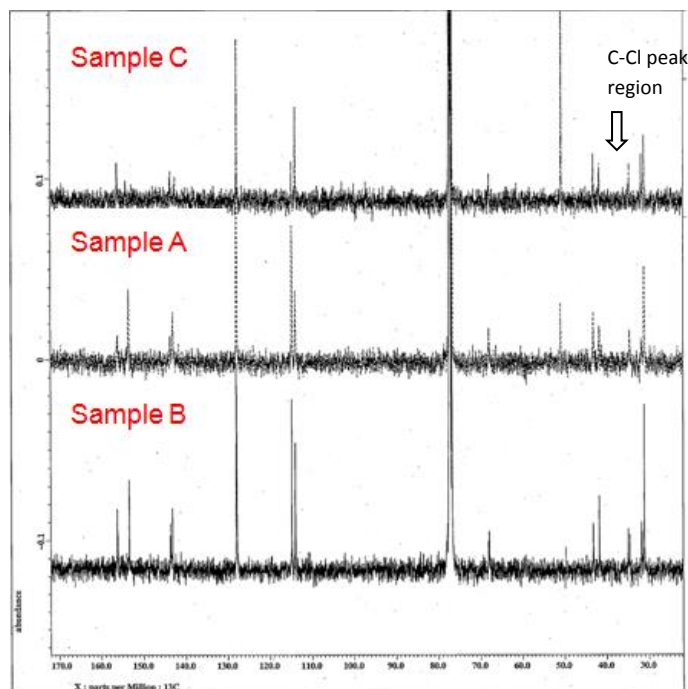**Figure 8. Predicted spectrum of ^{13}C NMR.**

78

Figure 9. ^{13}C NMR spectra of HD + BPA reaction products showing the A (middle), B (bottom), and C (top) products. The CH$_2$Cl group of HD is still observed, indicating that either some HD is unreacted or else that some molecules are only half reacted on terminating polymer ends.

The NMR results show that the product shared many features with the predicted spectra. Highlighted are the peaks between 30 and 50 ppm that are not present in the predicted spectra and are characteristic of the chloro ethyls in HD. This is similar to results from the synthesis between phenol and HD, which demonstrated a half-reacted product, Product 2. While additional testing would be required to determine the exact composition or presence of unreacted HD, it is suggested that the carbon chlorine bond is present due to none hydroxyl terminating polymer chains.

3.4 Final mechanism

The mechanism predicted for the polymerization between BPA and HD is shown in Figure 10.
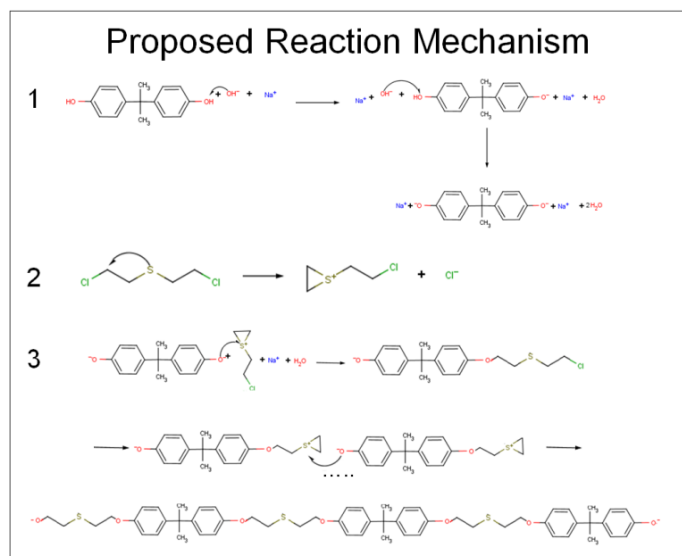
Figure 10. Proposed reaction mechanism between BPA and HD. Step 1 demonstrates the salting of the phenol group on BPA. Step 2 shows the formation of the cyclic sulfonium ion. Finally, step 3 demonstrates the condensation reaction between HD and BPA.

79

The mechanism is consistent with a condensation reaction and stepwise polymerization reaction. The mechanism does not balance the Na^+ or Cl^- ions with salt formation because the salt was not visually detected in the final reaction. While the mechanism demonstrates that water is formed and auto catalyzes, results indicate that additional water is required to precipitate product.

The addition of water formed a white cloudy mixture in every stage of the experimental analysis. This demonstrates water is a key component for the reaction to proceed. Water increases the polarity of the solution, which allows for the sulfonium ion to more readily form. Therefore, step 2 may only take place in the presence of water. The exact experimental conditions with which the sulfonium will form are unknown.

Step 3 shows a step-growth polymerization of BPA and HD. Results indicate that terminating polymer ends may contain carbon chlorine bonds. Limiting the number of chlorine terminating ends may prove challenging and weaken this mechanism as a method for decontamination. The exact toxicity of the resulting polymer is currently unknown, but by lowering the formation of a reactive sulfonium ion the hazard risk associated with HD contamination may be reduced.

For use as bulk decontamination method further testing is required to determine the lowest molar ratios to completely react HD. The polymerization reaction may release excess heat or water vapor that makes use of this reaction in tonne containers unfavorable. The reaction which took place forming product C demonstrates that without heat or mixing the reaction will proceed naturally and immediately. This attribute would be practical in situations where other methods of decontamination are not available.

4. CONCLUSIONS

In previous work, reactions between polycarbonate, phenol, and HD indicated that a condensation reaction could be used to polymerize HD. Initial experiments confirmed that a visible condensation product could be synthesized utilizing relatively low molar concentrations of reactants. An HD polymerization reaction, using phenol as a BPA analog confirmed that the addition of water was crucial to the reactivity of HD. Using a step growth process, HD was polymerized with BPA, producing a white, adhesive product. The reaction occurred readily, independent of the presence of mixing or heat.

Challenges remain with determining the exact composition of the final product. The separation of the product is difficult due to its adhesive properties. Toxicological testing is required to determine if the new product is less toxic than HD. Further work can be done to improve the experimental effort, increase yield, and refine the overall synthesis method. Other contaminants demonstrate similar material incompatibilities with Lexan. Similar investigations may identify potential bulk decontamination methods for these contaminants. The method presents a viable path forward in bulk decontamination and future challenges can utilize an array of collaborative efforts.

ACKNOWLEDGEMENTS

REFERENCES

[1] Moyer, W.W. "Polycarbonate Process" U.S. Patent 2,970,131, Jan. 31, 1961.
[2] Heuer, H.W. et al., "Inhibition of Catalytically Active Impurities in Polycarbonate by the Melt Transesterification Process" U.S. Patent No. 7,250,483, Jul. 31, 2007.
[3] Helfrich, O.B and Reid, E.E., *Journal of the American Chemical Society*, **1920**, 42(6), p1208-1232.
[4] Bae, S.Y. and Winemiller, M.D., *Journal of Organic Chemistry*, **2013**, 78(13), p6457–6470.

Raman spectroscopic analysis of whole blood acetylcholinesterase

Phillip G. Wilcox

U.S. Army Edgewood Chemical Biological Center, Research and Technology Directorate,
5183 Blackhawk Rd, Aberdeen Proving Ground, MD 21010

ABSTRACT

Raman spectra were taken of whole sheep's blood with varying levels of acetylcholinesterase (AChE) inhibition using 229 and 532 nm laser excitation wavelengths. AChE levels were inhibited using the organophosphates malathion, paraoxon-ethyl, and octamethyldiphosphoramide and confirmed using the Ellman method. This AChE activity level was combined with the Raman spectra and analyzed using a partial least squares calibration and cross validation to determine if the AChE activity could be predicted from the Raman spectrum. Correlation scores of 0.78 and 0.26 between the measured and predicted AChE activity were observed using 229 and 532 nm excitation, respectively. A estimate limit of detection was found to be approximately 0.01 ΔA/min.

Keywords: Raman spectroscopy, acetylcholinesterase, whole blood, partial least squares calibration

1. INTRODUCTION

Acetylcholinesterase (AChE) is an enzyme used to break down the neurotransmitter acetylcholine. Exposure to organophosphate (OP) nerve agents and insecticides can inhibit AChE levels which can lead to a range of physiological responses, including restlessness and agitation to seizures, coma, and eventually death.[1] There are currently two main methods used to measure AChE activity – the Ellman assay and the Michel assay. Both methods involve drawing a blood sample from a patient, adding reagents observing a chemical reaction over several minutes. The Ellman assay (or modified versions of it) measures the change in optical absorbance at a fixed wavelength and the Michel method measures the change in pH.[2,3]

A drop in AChE activity levels can indicate OP exposure even before symptoms are present. A quick test without any consumables would allow for more frequent monitoring which of AChE activity and could reduce the time between exposure and beginning treatment. In this effort, we examined the ability to use ultraviolet (UV) and visible Raman spectroscopy as a rapid and reagentless method to measure AChE activity in whole blood. Raman scattering has been used to measure other constituents of whole blood such as glucose, cholesterol, and hemoglobin[4,5], but to our knowledge, no one has tried to determine AChE activity levels. Raman spectroscopy can be scaled to interrogate very small volumes of liquid which would reduce amount of blood needed down to a finger prick instead of a full blood draw.

2. EXPERIMENTAL SETUP

To determine whether Raman spectroscopy can be used to measure AChE activity, Raman spectra were taken on heperinized whole sheep's blood (Hemostat Laboratories, Dixon, CA) using various excitation wavelengths. All blood samples arrived the day after it was drawn from the animal. Blood was stored a 5°C between arrival and used less than 11 days later. AChE levels were inhibited using the OPs paraoxon-ethyl (CAS# 311-45-5), malathion (CAS# 121-65-5), and octamethyldiphosphoramide (OMPA – CAS# 152-16-9). The paraoxon-ethyl and malathion were commercially available from Sigma-Aldrich (St. Louis, MO) and the OMPA was acquired through a custom synthesis from Hestia Laboratories (New Berlin, WI). An Ellman assay (described in section 2.3) was run simultaneously with the UV and visible Raman measurements to correlate the spectra to a known AChE activity level.

2.1 Blood sample preparation and measurements

At the beginning of each sequence of measurements, the heparinized whole sheep's blood was added to three containers; 4 mL was placed in a glass vial for the 532 nm Raman measurements and OP contamination, 0.5 mL was

APPROVED FOR PUBLIC RELEASE

placed in a small 25 mm wide open air dish for 229 nm Raman measurements, and 5 μL was added to a 10 mm square polystyrene UV-Vis cuvette for Ellman measurements. These measurements were run simultaneously. After these measurements were completed, 0.2 μL of one of the OP compounds was added to the 4 mL glass vial and slowly inverted 10 times to ensure thorough mixing and placed in an ice bath for 5 minutes. After 5 minutes, 0.5 mL of the mixture was taken for 229 nm Raman measurements, 0.5 μL was taken for the Ellman assay, and the remaining ~3.5 mL was taken for 532 nm Raman measurements, which were run simultaneously. Afterwards, another 0.2 μL of OP compound was added to the remaining ~3.5 mL vial and the sequence was repeated until the AChE level was fully inhibited.

2.2 Raman instrumentation

The 229 nm measurements were collected using a Princeton Instruments Acton SP2500 Spectrometer and Pixas 2K camera with approximately 8 cm^{-1} resolution. The 229 nm excitation came from a Coherent Sabre FreD continuous wave (CW) frequency doubled argon ion laser which delivered approximately 5 mW at the sample. All samples were measured in an open air plastic dish approximately 25 mm in diameter. A magnetic stir bar was used to minimize damage to the sample caused by the UV laser. The 532 nm measurements were collected using high resolution echelle spectrographs from EIC Laboratories with Andor iDus 420A-OE CCD camera with approximately 1 cm^{-1} resolution. The 532 nm excitation came from an Oxxius 532-300-COL-PP CW frequency doubled single longitudinal mode Nd:YAG laser. The 532 nm excitation and collection was performed through an EIC RamanProbe fiber optic probe which delivered approximately 150 mW to the sample. All blood samples were measured through a 4 mL glass vial.

2.3 Ellman assay

AChE levels were measured using the Ellman assay.[2] Prior to the measurements two reagents were made. The first was a 10.6 mM solution of 5,5'-dithiobis(2-nitrobenzoic acid) (DTNB – CAS# 69-78-3) in phosphate buffer solution (PBS). This DTNB solution is also known as Ellman's reagent. The second reagent was a 76.3 mM solution of acetylthiocholine iodide (ATCI – CAS# 1866-15-5). The PBS used for these measurements was at 1.0 M and 7.4 pH (25°C). All reagents were stored at 5°C and were used within 30 days.

To perform these measurements, 3 mL of PBS was placed in a 10x10 mm polystyrene cuvette. The cuvette was placed into a Thermo Evolution 60 UV-Visible spectrometer to take a reference background spectrum. Then 5 μL of whole blood, 25 μL of DTNB solution, and 20 μL of ATCI solution were added to the PBS. The cuvette was then inverted approximately 10 times and returned to the spectrometer. The optical absorbance at 410 nm was monitored for 5 minutes. A linear fit was used to determine the change in optical absorbance over time (ΔA/min). This change in absorbance directly corresponds to enzyme activity. Throughout the remainder of the paper all AChE activity values are given in ΔA/min. For reference, uninhibited blood ΔA/min varied from 0.17-0.26 ΔA/min with fully inhibited blood getting as low as 0.00087 ΔA/min.

3. EXPERIMENTAL DATA

Raman spectra of the uninhibited blood were taken at four different excitation wavelengths ranging from the visible to near-infrared at the beginning of this effort. Figure 1 shows a representative spectrum from each wavelength along with the integration time. The 785 nm excitation resulted in a large fluorescence signal, which overwhelmed the Raman signal. Raman scattering has a relationship proportional to λ^{-4}, which can be observed as the required integration time greatly reduced from 300 to 10 seconds as the excitation wavelength shortened from 785 nm to 229 nm.
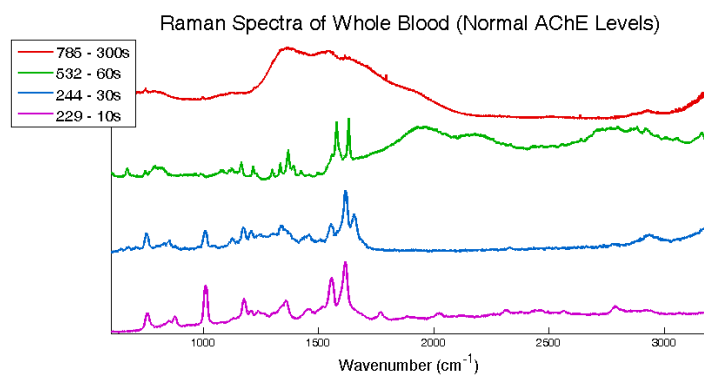
Figure 1. Raman spectra for uninhibited whole blood using 785, 532, 244, and 229 nm excitation with integration times ranging from 10 to 300 seconds.

Based on our test configuration, only one UV wavelength could be selected for further AChE measurements; therefore, 229 nm was selected along with 532 nm for further analysis. The integration time of 60 seconds for 532 nm and 10 seconds for 229 nm were kept constant throughout the study. Five spectra were collected at 532 nm, and ten spectra were collected at 229 nm for each AChE concentration. Figure 2 shows the average spectrum for each AChE concentration for 532 nm (left) and 229 nm (right).
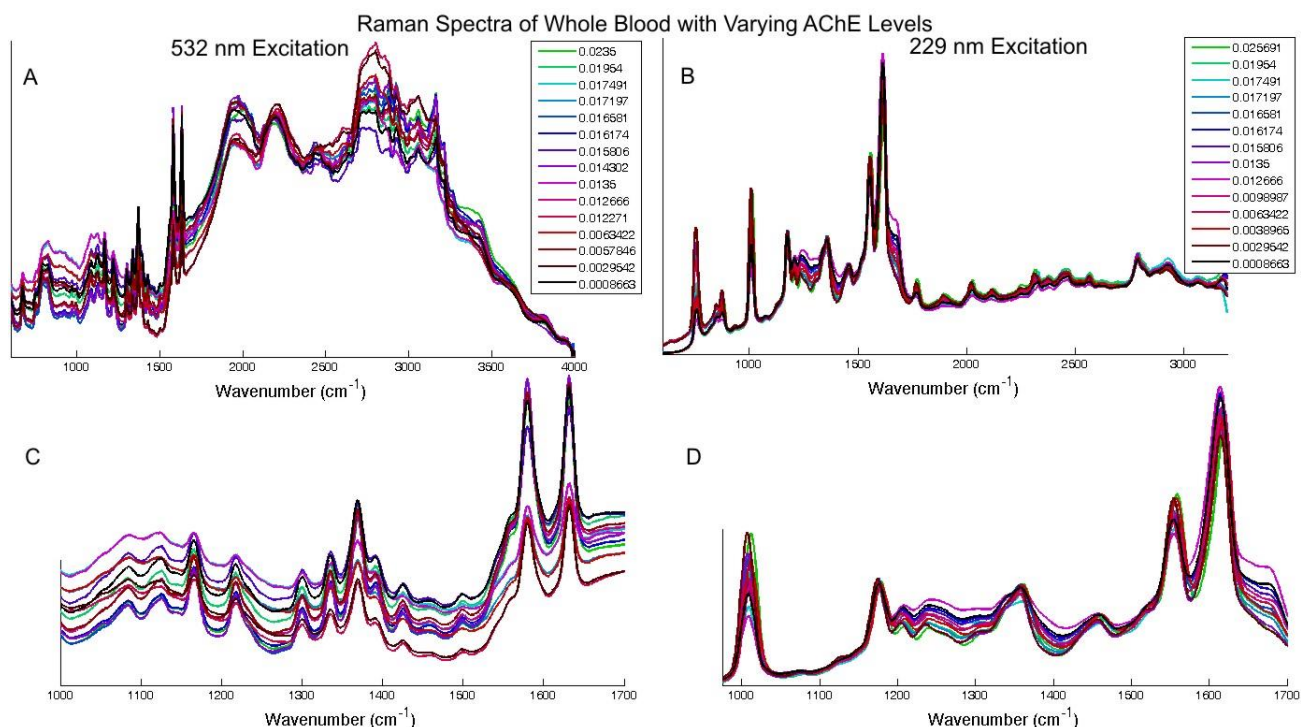
Figure 2. Average Raman spectrum for each measured AChE concentration using excitation wavelengths of (A) 532 nm and (B) 229 nm. Expanded views from ~1000-1700 cm^{-1} are shown for (C) 532 nm excitation and (D) 229 cm^{-1} excitation. Concentration values are expressed in ΔA/min acquired using the Ellman assay.

4. ANALYSIS

4.1 Data pretreatment

Some of the 229 nm spectra had cosmic rays that were removed using a five-point median filter. A seven-point mean filter was then used to smooth the data. The 532 nm did not have cosmic rays and was not mean filtered.

APPROVED FOR PUBLIC RELEASE

Because the 532 nm spectra were taken on a higher resolution instrument a wider mean filter of 23 points was used to smooth the data. All spectra were normalized to a common area.

4.2 Partial least squares calibration

All spectra were individually analyzed using partial least squares (PLS) calibration. This technique is detailed by Haaland and Thomas.[6] The PLS calibration algorithm combines the Raman spectra and the measured Ellman values to generate two outputs – the PLS loading vectors and a relating score vector. The PLS loading vectors are a series of i component spectra that can be linearly combined to create each of the Raman spectra, S, using a series of scalars, a_i, and some residual R as shown in Equation 1.

$$S = a_1 V_1 + a_2 V_2 + \cdots a_i V_i + R \tag{1}$$

The relating score vector relates the a_i scalars to the measured Ellman concentration, c^m. The loading vectors and relating score vector can then be applied to an unknown spectrum and predict the concentration, c^p. The data was analyzed using a cross validation in which all replicate spectra taken at a given AChE data were removed and the loading and relating score vectors were created using the remaining dataset. The removed spectra were then analyzed one at a time using these vectors to predict the concentration of the removed spectra. These results were then compared against the measured values. This was repeated until the concentrations had been predicted for all spectra. The 229 nm data used six to eight loading vectors and the 532 nm data used four to eight loading vectors. These numbers were selected to minimize the root mean squared error of prediction (RMSEP) defined in Equation 2, where n is the total number of spectra collected.

$$RMSEP = \sqrt{\frac{\sum_{k=1}^{n}(c_k^m - c_k^p)}{n}} \tag{2}$$

In addition to full spectrum analysis, the spectra were truncated so that only certain areas of the spectrum were used in the analysis. Spectral windows around the Raman fingerprint region of 700-1700 cm^{-1} were isolated for analysis, but did not significantly change the results as shown in Table 1.

Table 1. Correlation and RMSEP value for PLS prediction values by isolating different spectral regions for 532 nm and 229 nm excitation data.

532 nm Excitation					229 nm Excitation			
Spectral Range	**Correlation**	**RMSEP**	**# of PLS Vectors**		**Spectral Range**	**Correlation**	**RMSEP**	**# of PLS Vectors**
537-3991 cm^{-1} (Whole Spectrum)	0.031	0.01524	5		460-3200 cm^{-1} (Whole Spectrum)	0.115	0.02886	8
537-1656 cm^{-1}	0.326	0.01394	5		708-1746 cm^{-1}	0.203	0.02538	8
1011- 1447 cm^{-1}	0.351	0.01457	8		708-1056 cm^{-1}	0.239	0.02255	6
1257-1656 cm^{-1}	0.492	0.01247	7		1104-1810 cm^{-1}	0.1502	0.02581	8
1479-1656 cm^{-1}	0.358	0.01375	6		1486-1810 cm^{-1}	0.1172	0.2566	7

Figure 3 shows the prediction plot for analysis of the 708-1056 cm^{-1} region for 229 nm excitation and 1257-1656 cm^{-1} for 532 nm excitation. The measured Ellman concentrations are along the x-axis and the PLS prediction concentration is along the y-axis. The prediction for the 532 nm data was slightly better than the 229 nm data with a lower RMSEP (0.01247 compared to 0.02255) and a higher Pearson correlation (0.492 compared to 0.238); however, the error for both is too large to provide any useful prediction information.
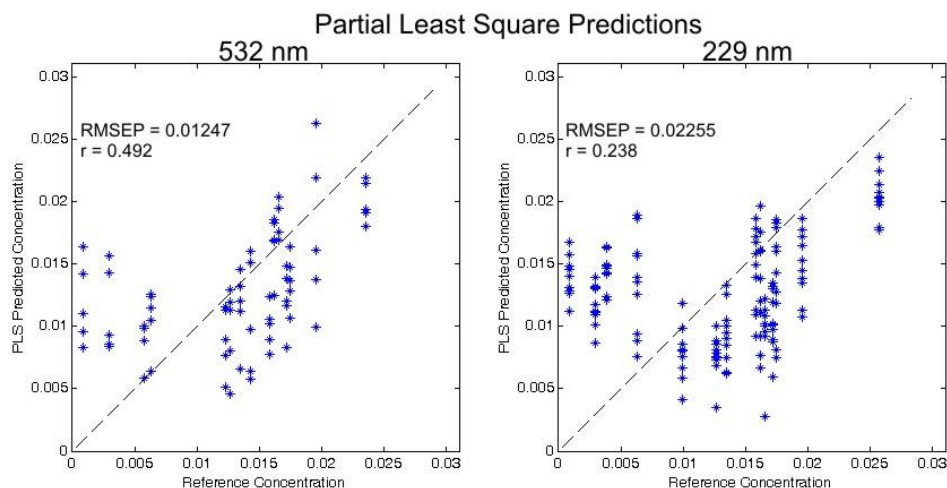
Partial Least Square Predictions

Figure 3. Analysis of PLS predicted concentrations to Ellman measured values for 532 nm (left) and 229 nm (right) data sets using a cross validation technique. Plots list the RMSEP and Pearson correlation score, r.

During analysis, the data points with low AChE activity had worse correlation than the data points with higher AChE activity, as shown in the 229 nm data in Figure 3. If you average the prediction concentrations at the concentrations above 0.01 ΔA/min, it follows a trend in the correct direction; however, the average of the prediction values less than 0.01 ΔA/min remains fairly constant. The data was reanalyzed to include only the concentrations above 0.01 ΔA/min with the results shown in Figure 4.

Partial Least Square Predictions
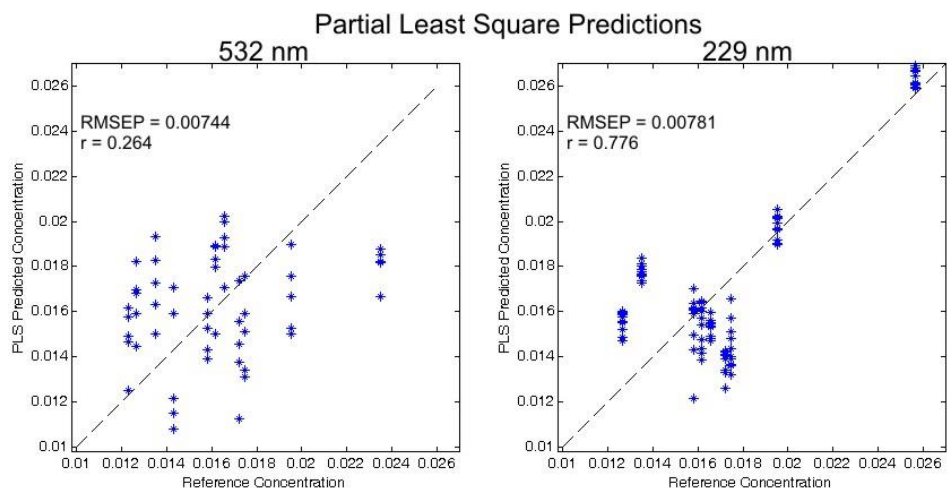
Figure 4. PLS Prediction plots using data points where AChE activity was measured at greater than 0.01 ΔA/min.

The analysis performed in Figure 4 covers the same the spectral regions as the Figure 3 analysis (708-1056 cm^{-1} for 229 nm and 1257-1656 cm^{-1} for 532 nm). The RMSEP for both excitation wavelengths decreased and the correlation greatly increased for the 229 nm data. The 229 nm data used four loading vectors and the 532 nm used seven. This indicates a limit of detection of approximately 0.01 ΔA/min. For comparison, uninhibited blood varied from 0.17-0.26 ΔA/min in this study.

5.   CONCLUSION

There was no main spectral feature that could be correlated to AChE activity; however, using a multivariate PLS calibration technique focused from 708-1056 cm^{-1}, it was possible to predict a trend in AChE activity using Raman spectra using 229 nm excitation. This spectral region includes four peaks at 754, 848, 875, and 1007 cm^{-1} which changed in intensity and shifted frequency as the AChE levels changed. This does not show the same quality of results as a laboratory technique, but could potentially be used as a trigger for a blood draw and more precise

APPROVED FOR PUBLIC RELEASE

measurement using the current methodology. After analyzing the Raman data, a limit of detection corresponding to approximately 0.01 ΔA/min was noticed. Removing this data from the training algorithm significantly improved the prediction results. The technique is rapid and reagentless and could be performed on very small blood samples (i.e., finger prick) which could be performed with greater frequency. More frequent measurements would lead to earlier diagnosis and treatment of OP exposure.

From this study, it is unclear whether the spectral changes directly relate to AChE activity or a different chemical reaction related to the introduction of OP compounds to the blood, but ultimately may not matter as long as it is a consistent effect of OP poisoning. This was mitigated in our experiment by using three different OP compounds of varying toxicities.

Future work will perform a similar study using infrared absorption spectroscopy.

ACKNOWLEDGEMENTS

REFERENCES

[1]   Burtis, C.A. and Ashwood, E.R., *Tietz Fundamentals of Clinical Chemistry Fifth Ed.*, W.B. Saunders Company, Philadelphia, p651-652, **2001**.
[2]   Ellman, G.L., et al. *Biochemical Pharmacology,* **1961**, 7, p88-95.
[3]   Haigh, J.R., et al. *Chemico-Biological. Interactions*, **2008**, 75, p417-420.
[4]   Enejder, A.M.K., et al, *Optics Letters*, **2002**, 27(22), p2004-2006.
[5]   Berger, A.J., et al, *Applied Optics*, **1999**, 38(13), p2916-2926.
[6]   Haaland, D.M. and Thomas, E.V., *Analytical Chemistry*, **1988**, 60(11), p1193-1202.

Magnetic measurement of particle adhesion forces

Jerry B. Cabalo*, Erin D. Davis, Paul De Luca

U.S. Army Edgewood Chemical Biological Center, Research and Technology Directorate,
5183 Blackhawk Rd, Aberdeen Proving Ground, MD 21010

ABSTRACT

The understanding of the processes governing the resuspension of hazardous particulates is critical to protection of the warfighter. A key component of this understanding is the force of adhesion between a particle and a surface in air. The purpose of this study is to examine the contribution of chemical interactions to the adhesion force using the interaction between carboxylic acid functionalized polystyrene latex (PSL) beads and substrates coated with functionalized self-assembled monolayers. Force measurements are performed using magnetic PSL beads and a well characterized magnet. Two technical barriers are encountered during this study of adhesion. First, the magnetic force on the beads (6.5×10^{-12} N for the 2.85 µm beads used in this study) is two to three orders of magnitude less than atomic-force microscopy measurements of the chemical contribution to adhesion force. Second, difficulties are encountered in producing a distribution of single PSL particles on the substrate without any liquid or solid material between the particles and the substrate. Use of larger particles with higher magnetic material content should result in sufficient magnetic force to detach particles from the surface. Larger particles should facilitate more efficient deposition onto the test substrates.

Keywords: aerosols, adhesion, resuspension.

1. INTRODUCTION

The understanding of the processes governing the resuspension of radiological, toxic, or pathogenic aerosols is critical to human health and protection of the warfighter. This understanding can lead to a better knowledge of the fate of these materials and better capabilities for predicting the behavior of these materials. Aerosol resuspension is an important area of research because it is a factor in diverse fields, such as indoor air quality[1], nuclear energy[2,3], pollution control[4], as well as chemical-biological (CB) defense.[4,5] The adhesion force between a particle and a surface and the factors governing it are critical to the understanding of aerosol resuspension. The adhesion force has several components, including chemical forces, electrostatic forces, van der Waals or dispersion forces, and capillary forces. Because chemical interactions are the most selective, these forces are the focus of this effort. We hypothesize that the binding force depends on chemical reaction between functional groups embedded on both the particle and substrate surface. We expect the adhesion will be linearly proportional to density of chemical binding sites.

Adhesion forces are a very challenging problem because of the wide variety of hazardous particle materials, an even wider variety of different surfaces that can harbor and release particles, as well as the influence of particle size and surface roughness.[6-8] Additionally, particulates can change over time by aggregating with other particles or accumulating moisture. As a result, there is a kinetic component to the problem as well.

A number of studies have been performed to address this problem[9], but there are still knowledge gaps. Studies focusing on operationally relevant surfaces such as grass or concrete poorly characterize these substrates. As a result, it is difficult to relate those results to a different environment. For several laboratory studies, although the substrate and particle interactions could be well characterized, the substrates were idealized laboratory substrates such as smooth silica or silicon.[10] Again, it can be difficult to generalize the laboratory results and predict particle suspension rates in relevant settings.

A number of atomic-force microscopy (AFM) studies have been performed to obtain precise measurements of particle-surface adhesion[10-13], and it is helpful to review some of those studies here. In a typical experiment, a particle, such as a polystyrene latex (PSL) bead is epoxied to the tip of an atomic force microscope. The detachment force is then measured. In one study, the detachment force between a particle composed of an energetic material and a functionalized self-assembled monolayer (SAM) surface was performed. It was found that certain functional

APPROVED FOR PUBLIC RELEASE

groups on the SAM promoted chemical adhesion between the particle and the surface. Adhesion forces on the order of 30-140 nN were reported between particles of explosive materials and a SAM on the surface. This study demonstrated measureable increase in adhesion due to chemically specific interactions. In another study by Rabinovich[14], the capillary adhesion force between a ~3 μm particle and a flat surface was found to be about ~2 μN, where an annulus of water had condensed between the particle and the surface. But, as demonstrated in this study, only a few measurements could be made.

In order to test our hypothesis and quantitatively measure adhesion forces between particles and a large variety of substrate materials, it is desirable to have a means of measurement that is both quantitative and has high throughput (i.e., a rapid method that permits a large number of measurements). As a result, we propose to make measurements with a new technique capable of measuring the adhesion force of a large sample set of particles to a surface as a function of chemical composition of that surface. The availability of commercially available uniform, magnetic PSL particles with acid or amine functionalized surfaces at known surface densities provides an opportunity perform adhesion measurements on a large ensemble of particles while having a measurement of the adhesion force. If the magnetic moment of a particle can be determined as well as the gradient of the magnetic field from a magnet, then the amount of force exerted on that particle can be determined as well.[15] SAMs enable precise control of the surface composition, permitting "tuning" of the surface concentration of different functional groups.[16,17] Thus, it is possible to measure the interaction force between particles coated with a known concentration of acid or basic functional groups and a corresponding surface.

2. METHODS

2.1 Overview

We intend to use uniform magnetic beads (COMPEL™ UMC3N Glacial Blue Dyed 2.85 μm diameter, 1.23 g/cm^3 density, 2.20 x 10^8 –COOH groups/μm^2 surface density, Bangs Laboratories, Inc.) and a well characterized magnet to perform measurements of the adhesion of particles to a surface as a function of the chemical composition of that surface. The magnetic beads are functionalized with a known surface concentration of carboxylic acid groups. Chemical interactions between this surface and a SAM consisting of different concentrations of amine terminated or acid terminated molecules are targeted for measurement. The detachment force for removing particles from the surface is to be accomplished by measuring the distance between surface of the characterized magnet and a SAM coated slide with a coating of the functionalized beads. Since the beads are fluorescent dyed, they are illuminated with 365 nm UV light, and removal from the surface is observed by recording the change in fluorescence. Detachment force is measured by reduction in fluorescence on the SAM surface as a function of distance between that surface and the surface of the magnet. For early measurements of detachment force of the PSL beads, particles were deposited without washing, where tween surfactant and NaN$_3$ was used as a preservative. Subsequent measurements were performed with beads washed six times with nano-pure plasma grade water (beads removed from suspension with the magnet, the supernatant liquid removed and replaced with nano-pure water).

2.2 Theory

For calculation of the force acting on a particle, we follow the method of Shevkoplyas[15], where the force on a superparamagnetic PSL bead was calculated for the small magnetic fields (~mT) generated by current passing through a wire. In this study, the magnetic field strengths were far below the limit where the PSL bead induced magnetization became saturated. In the present study, we maximize the force on the beads with a strong magnetic field (~0.5 T) where saturation of the bead magnetization is to be expected. We thus adapt the approach of Shevkoplyas to the saturation limit regime. The force on a magnetic dipole (PSL) bead can be described as:

$$\vec{F} = (\vec{m} \cdot \nabla)\vec{B} \tag{1}$$

where $\vec{F}$ is the force in Newtons, $\vec{m}$ is the magnetic moment in (J/T), and $\vec{B}$ is the magnetic field strength in units of T. Because experiments are performed so that particle motion is directed normal to the magnet surface and there is no variation of the magnetic field along the other direction, equation (1) is simplified to only the z direction in equation (2):

$$F_z = m_z \frac{\partial B_z}{\partial z} \tag{2}$$

Due to the difficulty of calculating the magnetic moment of the beads from first principles, measurements of the induced magnetization by mass as a function of magnetic field intensity curves provided by the bead manufacturer (Bangs Laboratories, Inc.) can be used to derive empirical expressions for the induced magnetization on a bead. Figure 1 shows an example curve for ~3 μm COMPEL™ beads.
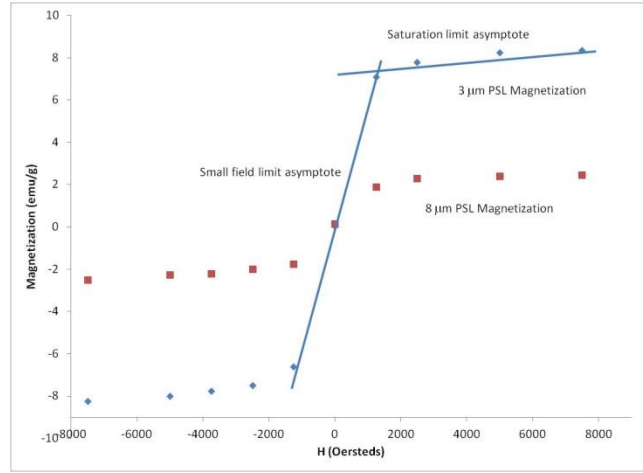

Figure 1. COMPEL™ PSL bead induced magnetization as a function of magnetic field intensity. Small field limit and saturation limit behavior shown as solid lines.

As is evident in Figure 1, for small fields (B<<0.1 T or 1000 Oe), the induced magnetization can be empirically treated as linear as is done by Shevkoplyas. However, measurements in the present study are performed at field strengths in the range of 0.1 T (1000 Oe) to 0.5 T (5000 Oe), where the magnetization dependence approaches a different linear asymptote. As a result, we use a similar functional form to Shevkoplyas for magnetization of a bead, but the empirical fit is done on a different part of the curve for equation (3):

$$m_{BEAD} = \rho V \left(m_0 + \frac{\chi_{BEAD}}{\mu_0 \rho} B_z \right) \tag{3}$$

where m_{BEAD} is the average magnetization per bead, ρ is the density of the bead, V is the volume of a bead, m_0 is the y intercept of the saturation limit asymptote, μ_0 is the magnetic permeability of vacuum, and χ_{BEAD} is the slope of the saturation limit asymptote. Substitution of equation (3) into equation (1) results in equation (4) for force on a bead as a function of the magnetic field gradient:

$$F_z = \rho V \left(m_0 + \frac{\chi_{BEAD}}{\mu_0 \rho} B_z \right) \frac{\partial B_z}{\partial z} \tag{4}$$

In order to compare predicted magnetic force on the PSL beads to easily perform experimental measurements of the bead terminal velocities in liquid, we use the balance of forces between drag in water and the magnetic force F_z and the force of gravity. Using the standard expression for Stokes drag, we can use equation (5) to calcualte particle velocity as a function of distance from the magnet for particles suspended in water:

$$v(z) = \frac{1}{6\pi\mu r} \left[\rho V g + \rho V \left(m_0 + \frac{\chi_{BEAD}}{\mu_0 \rho} B_z \right) \frac{\partial B_z}{\partial z} \right] \tag{5}$$

where μ is the viscosity of the liquid in Pa s, g is 9.8 m/s², and r is the radius of the PSL bead. Using the definition of velocity ($v=dz/dt$), and rearranging the differentials and integrating, we get an expression for time t_0 to traverse a distance z_0 in equation (6). Equation (6) can be solved numerically with the summation:

$$t_0 = \int_0^{t_0} dt = \int_0^{z_0} \frac{dz}{v(z)} \approx \sum_{i=1}^{N} \frac{\Delta z}{v(i \cdot \Delta z)} \tag{6}$$

where N is the number of numerical integration steps, and Δz is the integration step. Equation (6) allows a relationship to be drawn between the magnetization on a PSL bead and measurement of the time required for the magnet to remove the beads from measured depth of solution.

2.3 SAM preparation

SAMs are prepared on 1" x 1" gold coated glass slides with a Cr sublayer by EMF Corp. Organic contaminants on the gold are removed with Piranha solution (30:70 v/v solution of 30% H_2O_2 and concentrated H_2SO_4). Glassware is cleaned in a base bath (KOH in isopropanol). SAMs are made by allowing 1-undecanethiol, a long-chain alkane with a sulfur head group, to react with the gold surface in pure ethanol. Acid and base functional groups are added by mixing in either 11-mercaptoundecanoic acid or 11-amino-1-undecanethiol. The order in the SAM is characterized with reflection-absorption IR spectroscopy (RAIRS).

2.4 Particle detection by UV-fluorescence microscopy and scanning electron microscopy

Since the detachment force of the particles is to be measured by the distance between the magnet and the SAM surfaces required to remove particles, UV-induced fluorescence is used to measure the depletion of particles on the SAM surface. The magnetic beads are dyed with a fluorescent dye with maximum response at 360 nm. For excitation, we use a 365 nm semi-collimated light from a Nichia LED that delivers ~10 mW of UV to the sample area. The output of this system is filtered with a Schott-UG-11 glass filter that removes any emission with wavelengths longer than 400 nm. Figure 2 shows the fluorescence microscope with UV light source to the left in the photo.
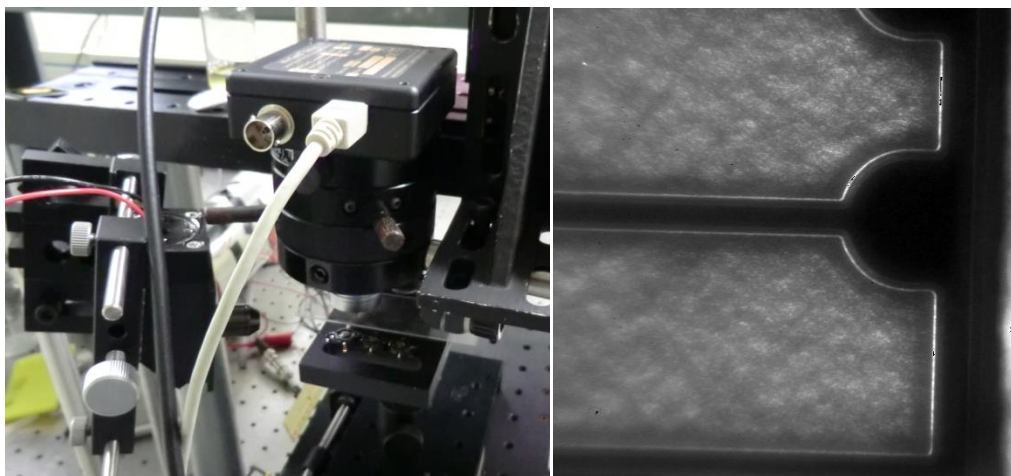

Figure 2. Photograph of the UV-fluorescence microscopy set-up and an image of part of a 1 mm x 1 mm LED. The notched features in the LED image are 250 μm wide.

The optical motion stage of the microscope is assembled from micrometer actuated optical components. The microscope body is mounted on an XYZ micrometer actuated motion stage for focusing. A Leica 50× UV microscope objective is used to collect fluorescence light because of its large numerical aperture (NA=0.25) and its long working distance (~6 mm). Because the objective is to measure fluorescence, not image individual particles, a longer working distance of 8 mm is used to increase the field of view, although the effective magnification is reduced. A DataRay WinCam-D UCD-12 1024 x 1024 pixel CCD scientific camera collects the fluorescence image of particles on the motion stage. The pixel dimensions are 4.65 μm x 4.65 μm. Exposure times of 500 ms or more are necessary to collect fluorescence images of the 2.85 μm diameter magnetic beads. To remove UV light scattering, an Asahi multi-layer dielectric long pass filter with a cutoff at 405 nm is placed between the camera and the microscope objective. The effective magnification of the system is measured by using a Lumileds LED emitting at 450 nm of known size (1 mm x 1 mm), and moving it known distances across the field of view. A magnification of 10× was determined so that the field of view within an image is 500 μm x 500 μm. For SEM images, a JEOL Ltd. JCM-5700 instrument is used with an acceleration voltage in the range of 3-6 kV.

2.5 Characterization of the magnet

An axially magnetized, NdFeB Grade N52 purchased from K and J Magnetics, with a countersunk hole is used for the force measurements. A Bell Labs Bell 5170 Gaussmeter with an axial probe is used to precisely measure the magnetic field around the magnet. Since we neglect components of the magnetic field normal to the magnet axis, measurements are only made for the magnetic field normal to the magnet surface. The Gaussmeter probe was mounted on a micrometer actuated XYZ stage. Because of the cylindrical symmetry of the magnet, measurements

are performed from the magnet axis to the edge of the magnet at varying distances. Figure 3 (left) shows the result of these measurements, where the origin is the edge and the magnet axis is at 0.5". Figure 3 (right) shows a finer grid measurement with 0.25 mm spacing between measurements. A third order polynomial fits this curve with an R^2 value of 0.9998, and is used to analytically calculate the magnetization of the beads at a given distance from the surface of the magnet as well as the gradient of the field. For the initial measurements, the magnet surface is placed 1 mm in height away from the sample surface. Because it is not possible to simultaneously place the magnet and view the region underneath it with the microscope, a motion stage with a large range micrometer is used. It is possible to move the sample underneath the magnet, and return to the same field of view under the microscope.
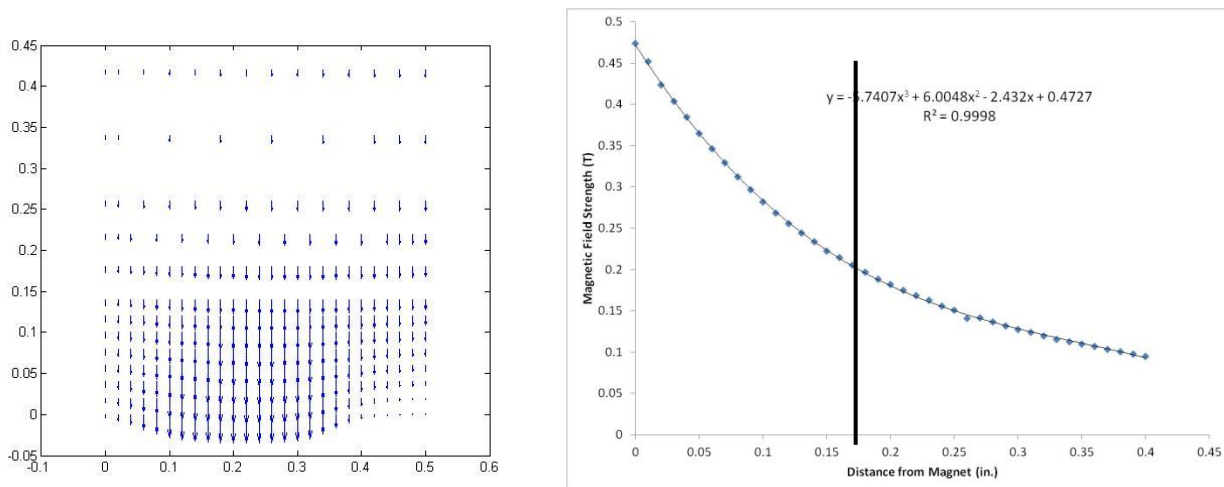
Figure 3. Magnet Characterization. Left: Vector field picture above the magnet in the plane containing the magnet axis and an edge. Note that the field does not change much as distance normal to the magnet axis is changed between 0.1" and 0.3". Right: The panel shows data point measured every 0.010" (~0.25 mm) along the path denoted by a black line on the left. A third order polynomial is used to fit that data. The gradient of the magnetic field is determined by analytically differentiating the polynomial.

2.6 Characterization of the beads

As an independent means of determining the average magnetic moment of the beads, magnet induced settling velocity is used. A cuvette measuring 4.14 mm wide, with the fluid level 10.0 mm from the surface of the magnet, is used to hold a water suspension of the magnetic beads. The cuvette is positioned so that the magnetic field is nearly constant as a function of distance from the magnet axis. The magnet is mounted within a Varian Spectrophotometer. Using a wavelength of 500 nm, the percent transmission is measured as a function of time after the cuvette is placed on top of the magnet. The force of gravity and the magnet are in the same direction. Three measurements were made and averaged together, where at time 0, there was minimum transmission through the cuvette due to light scattering of the beads, and maximum transmission was obtained when the beads were removed from the suspension. Since an identical cuvette could not be used in the reference beam of the spectrophotometer, the transmission data is scaled so that ~0% transmission occurs at time 0 and 100% transmission occurs at long times (5 minutes). The scaled transmittances are converted to absorbance ($-\log(I_o/I_{max})$), which is proportional to the concentration of beads in solution by the Beer-Lambert Law. Experimental settling times are determined when the absorbance decreases to ~5% of that at time 0. Figure 4 shows the absorbance as a function of time. Although the particles are technically scatterers and not absorbers, the effect of particle light scattering is the same. A settling time of 22.4 seconds indicates it requires that time for a particle to transverse the distance of the depth of the liquid under the influence of the magnet.
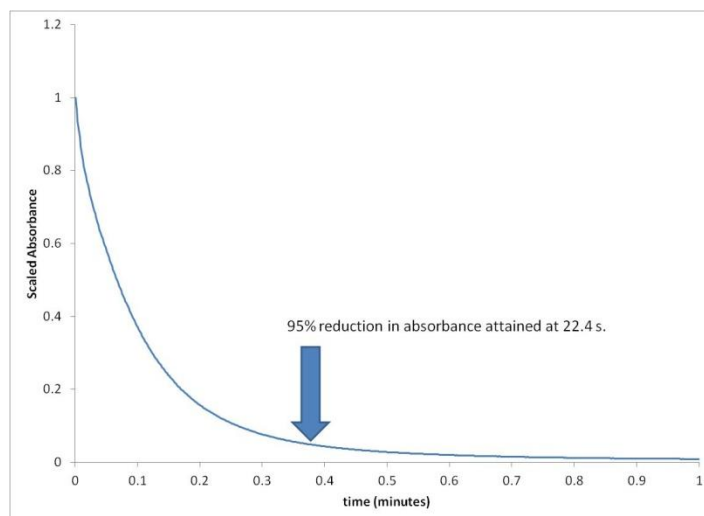
Figure 4. Absorbance as a function of time as beads are removed from the liquid suspension that is ~9 mm deep. The result shows rapid removal of particles from the suspension by the magnet.

2.7 Magnetic Bead Application Methods

Two basic methods are used to deposit magnetic beads on the surface with the goal of producing single particles. The goal is for the dominant interaction for the beads to be between the beads and the substrate surface. The first method relies on deposition of a liquid suspension of particles followed by evaporation of the solvent. First water, then ethanol is attempted. Dilution of the suspensions are also attempted to reach the goal of single particles. Both UV-fluorescence microscopy and SEM microscopy are used to examine the deposited beads. The second approach involves aerosolization of dilute particle suspensions, drying the resulting aerosol down to individual particles, and then dry deposition on a substrate. Two aerosol generation techniques are used, an ECBC inkjet aerosol generator (IJAG) and a medical nebulizer. The IJAG is capable of producing single drops on demand up to 2000 Hz. Several particle concentrations are attempted to produce single particles on the substrate surface. In order to boost the amount of droplets formed so that enough single magnetic PSL particles could be deposited, a medical nebulizer is also used, and a fan is used to increase particle velocity to enhance impaction of the particles. For these tests, particles are impacted on transparent glass slides, and imaged with an Oxford Lasers Ltd. particle sizer.

3. RESULTS

3.1 Calculation of the magnetic force on a bead

Using equation (4) and the approach of Shevkoplyas, we calculate the force on a bead. Of course, this value will depend on the gradient of the magnetic field which in turn depends on the distance from the magnet. For consistency with the experiments, the force is calculated at a distance of 1 mm. At 1 mm distance, the magnetic field strength is determined to be 0.386 with a gradient of -78.2 T/m. The total average magnetization per 2.85 μm bead is determined to be 6.5 x 10^{-15} J/T. This results in 6.48 x 10^{-13} N per bead at that distance. Using manufacturer data to calculate the force on the larger 8 μm bead, we determine a total average magnetization per bead of 4.97 x 10^{-14} J/T, and the corresponding force on that bead to be 3.53 x 10^{-12} N per bead.

To check the estimate of average force on a bead we compare the estimate of settling time from the force calculations to measurements performed in the spectrophotometer. Using equations (5) and (6) to calculate the settling time we determine a settling time of 943 seconds, based on the manufacturer-supplied data. If we supply a correction factor of 12.5 to the equation for the magnetic moment of the beads, a settling time of 22.4 seconds, which is consistent with experiment, is calculated. Clearly, the estimate of magnetic moment from the manufacturer-supplied data underestimates the magnetic moment of the beads, as well as the magnetic force. Using the correction factor to the magnetic moment, values of force obtained for the 2.85 μm and 8 μm beads are 6.50 x 10^{-12} N and 4.73 x 10^{-11} N, respectively. For the sake of comparison, values in the literature for adhesion forces in the range of 10^{-9} to 10^{-6} N, especially of capillary forces between a particle and a surface where there is liquid, are reported. Based on

APPROVED FOR PUBLIC RELEASE

the calculated applied force, at least two orders of magnitude more force is required to detach particles from a substrate, especially if there is a film of liquid between the particles and the substrate.

3.2 Application of single beads to the substrate

The first technical challenge encountered involved the proper application of magnetic PSL beads to the test substrate. Single, unagglomerated particles interacting directly with the substrate surface was desired. For beads obtained from the stock solution without washing, single beads were easily obtained by evaporating solvent (both water and ethanol) after a particle suspension was applied to the substrate. A comparison of the fluorescence image microscopy and SEM microscopy on the same slide demonstrate fluorescence from single magnetic fluorescent PSL beads can be detected (Figure 5). Both images measure 250 μm wide to show multiple beads within the same field of view. Figure 6 compares the SEM image of a single bead (left) to the fluorescence image of a single bead (right). Both images show individual magnetic PSL beads. We conclude the UV-fluorescence microscope is suitable for detecting the presence of individual particles as well as their removal.
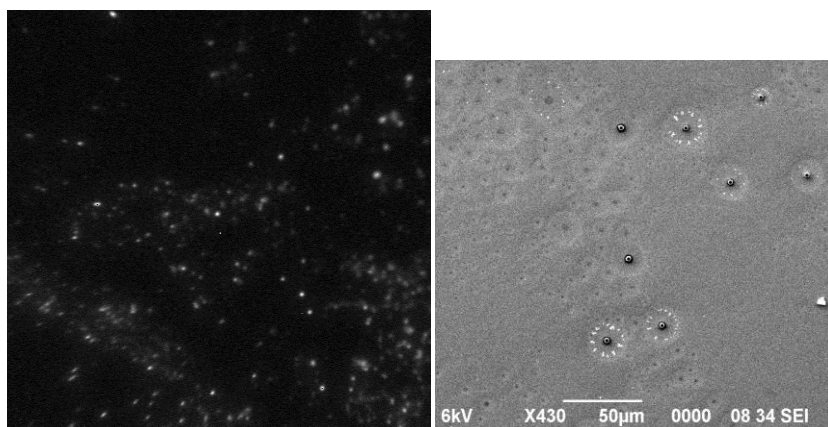

Figure 5. Comparison of the UV-fluorescence microscope and the SEM of PSL beads on an uncoated slide. Both panels are 250 μm wide.
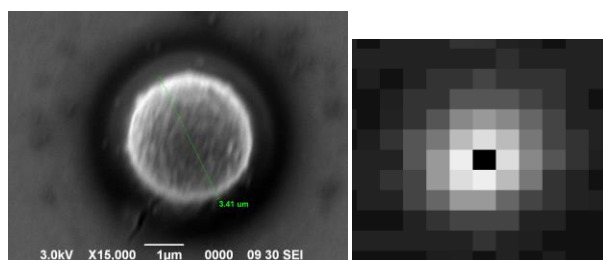

Figure 6. Comparison of an SEM image and a UV-fluorescence image of a single particle. The UV microscope image measures ~0.5 μm per pixel, which a visible in this blown up image.

Panels 1 and 2 of Figure 7 show a comparison of the same region of a slide before and after exposure to the magnet at a distance of 1 mm. As can be seen, no significant reduction in the fluorescent beads in the image can be seen. Panels 3 and 4 show the individual particles embedded in dried surfactant and the NaN_3 antibacterial salt. Clearly, this material behaves as an adhesive and increases the binding force between the particle and the surface. To overcome this issue, the particles are washed 10× with rapidly evaporating High-performance liquid chromatography (HPLC) grade ethanol. While the surfactant and NaN3 salt are eliminated, both fluorescence microscopy and SEM images show that although a dilute suspension of the particles are spread over the gold slide, capillary forces gather the particles into a compact "cake", as shown in Figure 8. An examination of panel (4) in Figure 8 shows the particles appear cemented together. Clearly, interaction between individual particles and the surface are dominated by interactions between the particles themselves. We concluded that particles could not be dispersed to surfaces by direct application of a suspension of particles. Furthermore, although the surface had been coated with a non-polar SAM (undecanethiol on gold), the magnet was unable to remove the particles stuck to the surface.
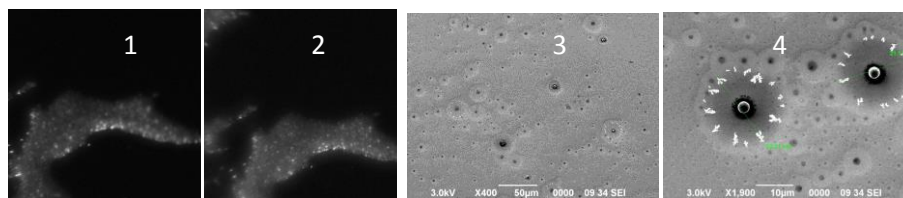
Figure 7. Fluorescence microscopy image of the same region of a gold slide (showing an agglomeration of particles on the surface) before exposure to the magnet (1) and after exposure to the magnet (2). No significant difference can be seen between the two images. SEMs of the same slide (3) with a similar field of view and (4) a closeup of individual particles. SEMs show the particles are embedded in surfactant and the NaN$_3$ anti-bacterial salt.
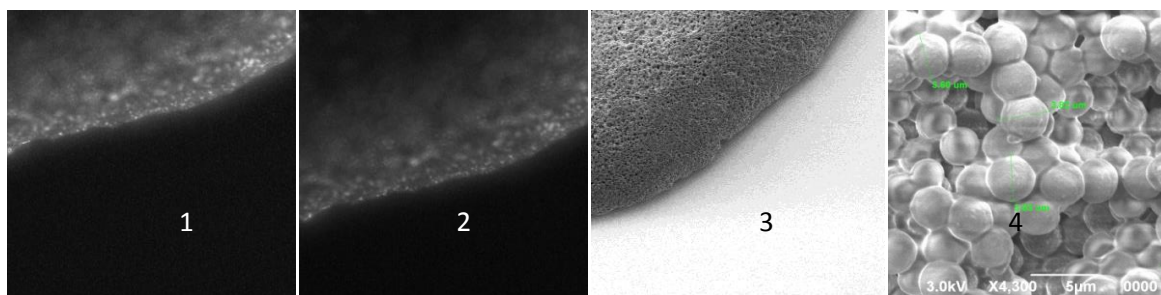

Figure 8. Fluorescence and SEM microscopy of the PSL particle "cake" formed after evaporation of the solvent after washing. (1) Edge of the "cake" before exposure to the magnet. (2) Same region after exposure to the magnet. (3) Same region at same field of view as (1-2). (4) Individual particles embedded within the "cake". Capillary forces have gathered the particles into a single agglomerate.

The next approach attempted to impact particles onto the surface in the dry state. The purpose is to eliminate the embedding of articles in dried surfactant/Sodium azide or the interference of residual solvent between the particles and the substrate. For the IJAG, the droplet production frequency is an issue. As shown in Figure 9, left, many particles appear as agglomerates. Although the particles are washed several times in plasma grade nanopure water, a solid contaminant is evident that embeds particles. When the particle suspension is diluted so that no more than single magnetic PSL beads could be in a single droplet in the IJAG, the IJAG particle production rate became a problem. For sufficiently dilute suspensions, most drops from the IJAG have no particles in them, and thus a great throughput of particles is necessary to produce a measureable quantity of particles on a substrate surface. The IJAG maximum frequency is not sufficient to produce measureable quantities of particles. For the medical nebulizer, another issue is encountered. The medical nebulizer produces much smaller droplets. It thus becomes very difficult to impact the particles on the substrate surface. Previous measurements with the fluorescence microscopy demonstrate detection of single particles on the surface. Surfaces investigated with UV-fluorescence microscopy that had particle dry deposition by dilute IJAG or nebulizer show little or no fluorescence from the dyed microspheres. We concluded that the particle deposition methods attempted have not succeeded in leaving an even distribution of particles on the surface of the slides. Most likely, use of the larger 8 μm particles would facilitate dry deposition of the magnetic PSL particles on the test surfaces.
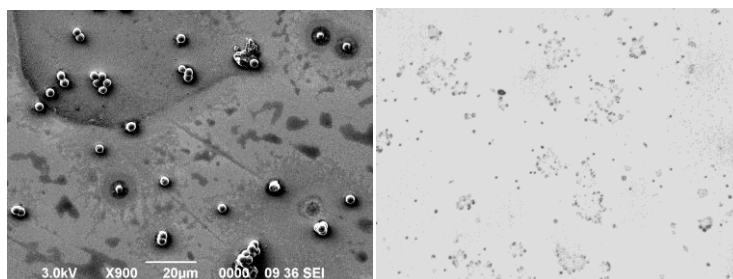

Figure 9. Results of dry deposition with the IJAG (left) and the medical nebulizer (right). The IJAG SEM image shows particle agglomeration. The medical nebulizer shadowgraph shows what appear to be individual particles. These particles do not appear under UV-fluorescence microscopy.

4. CONCLUSIONS

There is a need, in not only the CB Defense community but also the environmental science and nuclear energy communities, for understanding aerosol particle resuspension. The forces governing particle adhesion to substrates are key to understanding this phenomenon. We attempt to use the force of a well characterized magnet on uniform PSL beads containing magnetite particles to study the influence of chemical interactions on particle adhesion. We encountered two technical barriers to this approach. First, our measurements of magnetic force on the particles (10^{-12} to 10^{-11} N) are at least two to three orders of magnitude less than the measurements of chemical sticking forces reported in the literature using atomic force microscopy. A comparison to capillary forces arising from the presence of an annulus of liquid between a particle and the substrate (10^{-6} N) is even less favorable. We conclude that the magnetic PSL beads used in this study do not produce sufficient induced magnetic dipole moment to fall into the dynamic range of the adhesion forces of interest. Larger PSL coated particles of nearly pure magnetite would be necessary to probe adhesion forces between particles and substrate.

The second technical barrier is application of single beads to the substrate without solid contaminants. Simple solvent evaporation from suspensions of particles either results in particles embedded in an unwanted solid or agglomerates of particles. Application of dried aerosols from an IJAG and nebulizer is complicated by the presence of multiple PSL particles in droplets before drying, which result in agglomerated particles. When the particle suspension is diluted so that a maximum of one particle could be present in the original droplets, then most of the droplets would be empty, resulting in too few aerosolized particles to coat the substrate. The 2.85 μm size of the particles used is also problematic since smaller particles are more difficult to deposit on a surface. Use of the 8 μm could be expected to surmount this technical challenge. In conclusion, larger particles containing more magnetic material could be expected to circumvent the two technical challenges and achieve the goal of performing particle adhesion measurements on large ensembles of particles and substrates.

REFERENCES

[1]   Qian, J. et al. *Indoor Air,* **2012***, 22, p339-351.
[2]   Merrill, B.J., Humrickhouse, P.W., and Sharpe, J.P., *Fusion Engineering and Design,* **2011**, 86, p2686-2689.
[3]   Leifer, R.Z. et al., *Health Physics,* **2002**, 83, p892-900.
[4]   Colbeck I. and Lazaridis M., *Naturwissenschaften,* **2010**, 97, p117-131.
[5]   Birenzvige, A. CRDEC, CRDEC-TR-413, **1992**.
[6]   Cheng, K.C., Goebes, M.D., and Hildemann, L.M., *Atmospheric Environment,* **2010**, 44, p2062-2066.
[7]   Ziskind, G., *Reviews in Chemical Engineering,* **2006**, 22, p1-123.
[8]   Kumar, A., Staedler, T., and Jiang, X., *Journal of Colloid and Interface Science,* **2013**, 409, p211-218.
[9]   Layshock, J.A. et al., *Biosecurity and bioterrorism: biodefense strategy, practice, and science,* **2012**, 10, p299-303.
[10] Guleryuz, H. et al., *Journal of Sol-Gel Science and Technology,* **2012**, 62, p460-469.
[11] Guo, D. et al, *Langmuir,* **2013**, 29, p6920-6925.
[12] Chaffee-Cipich, M.N., Sturtevant, B.D., and Beaudoin, S.P., *Analytical Chemistry,* 2013, 85, p5358-5366.
[13] Fischer, H.R., Gelinck, E.R.M., and Asme, *Determination of Adhesion Forces Between Smoother and Structured Solids*, **2013**.
[14] Rabinovich, Y.I. et al., *Langmuir,* **2011**, 27, p13514-13523.
[15] Shevkoplyas, S.S. et al., *Lab on a Chip,* **2007**, 7, p1294-1302.
[16] Love, J.C. et al., *Chemical Reviews,* **2005**, 105, p1103-1169.
[17] Zakon, Y. et al., *Journal of Physical Chemistry C,* **2012**, 116, p22815-22822.

APPROVED FOR PUBLIC RELEASE

Raman interrogation of viable and non-viable spores for determination of biomolecular information activity

Jason A. Guicheteau[a], Ashish Tripathi[b], Jana Kesavan[a], Deborah Schepers[c], Phillip Wilcox[a]

[a]U.S. Army Edgewood Chemical Biological Center, Research and Technology Directorate,
5183 Blackhawk Rd, Aberdeen Proving Ground, MD 21010
[b]Science Applications International Corp., P.O. Box 68, Gunpowder Branch,
Aberdeen Proving Ground, MD 21010
[c]Excet Inc., 8001 Braddock Road, Suite 303, Springfield, VA 22151

ABSTRACT

Raman microspectroscopy analysis is used to decipher unique biomolecular information by monitoring the effect of residence time of Bacillus spores suspended in deionized water. Suspensions of viable and non-viable spores of *Bacillus atrophaeus* were prepared and spectrally monitored from initial deposition (time zero) and intermittently for fourteen days. Questions addressed include if spectral variations are significant with residence time under non-germination conditions, and are there markers indicating pre-germination activity. Clear spectral distinction between the viable and non-viable spores was observed along with slight variations with respect to residence time for the viable spores. Temporal spectral analyses shows that select wavenumbers suggest an increase in pre-germination activity that was otherwise thought not to occur.

Keywords: Raman microscopy, *Bacillus atrophaeus,* principal components analysis, germination activity.

1. INTRODUCTION

Bacterial spores are known to remain viable, yet dormant, for decades in the outdoor environment, and are believed to be biomolecularly inactive during this time. It is expected that essentially no metabolic activity exists unless appropriate physical, chemical, or biological triggers are manifested on the spore (typically associated with a food source).[1-5] However, Edgewood Chemical Biological Center (ECBC) scientists in a very limited study using Raman microspectroscopy observed spectral changes in supposed dormant spores. This activity defeats the known or believed dormant physical property of spores and may provide insight into pre-germination, protein-metabolite activity, as well as an enhanced proteome understanding of bacterial spores.

The purpose of the initial study was to characterize and determine what, if any, effect does the suspension time have on the Raman signature of the spores. From this, we observed that the spectral signatures were in fact changing over time, in non-nutrient rich environment. These temporal changes were most prominent between one and two days from initial suspension and after two days tended to subside and we believe that this suggests a pre-germination activity phase. This phenomenon may be explained by the organism expending energy for seeking the presence of growth media substances and/or conditions in the non-nutrient environment. Figure 1a summarizes these initial results from a viable *Bacillus anthracis sterne* sample and shows that from the Raman spectra alone (which accounts for vibrational modes associated with both surface proteins and internal molecules) obvious changes were occurring over time from a supposed dormant spore. The three peaks highlighted at 1013, 1450, and 1575 cm^{-1}, when plotted as spectral intensity versus time (Figure 1b), show an increase in intensity at 20 hours following a decrease and eventually leveling off at seven days.
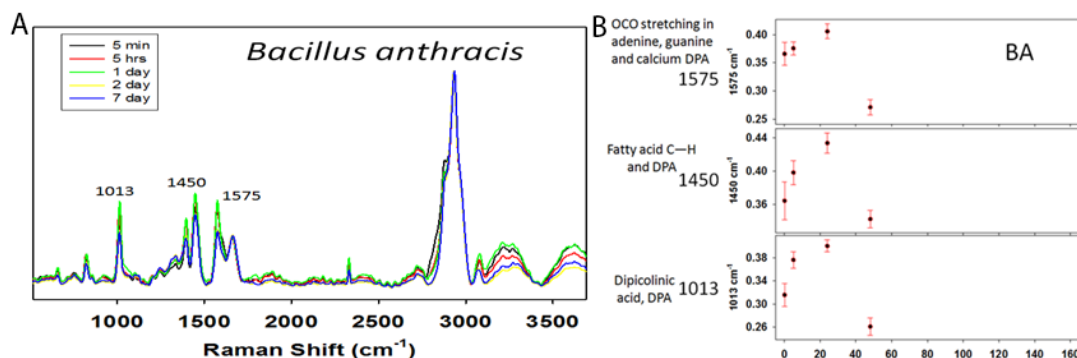
Figure 1A. Data from *B. anthracis* ames highlighting temporal changes in the Raman spectra. 1B, temporal display of wavenumber intensities showing variability over seven days.

While this data was promising, additional information needed to be gathered. This work shows the next phase in our effort to build a larger program to decipher this supposed pre-germination bimolecular activity. Additional experiments were design to incorporate repeat measurements from the original data collection as well monitoring non-viable (inactivated spores). The key component of this study is in fact the response of the non-viable spores. If no spectral changes are observed over time in a non-nutrient environment than our initial study begins to hold merit. Below are the results from this expanded study.

2. EXPERIMENTAL SECTION

2.1 Bacterial spore preparations

Lyophilized viable *Bacillus globigii* (BG) spores were received from Dugway Proving grounds and stored in freezer at -22°C until needed. The stock was separated with one half undergoing heat inactivation at 122°C for 15 minutes via autoclave and the other remaining viable. Upon initiation of study, each set was rehydrated in 18.3 MΩ H_2O (in 0.05% tween). The samples were then washed two times with 18.3 MΩ H_2O via centrifugation at 7000 RPM for 5 minutes with the water/tween mixture followed by three times washings with only DIW. Final concentration was brought to 1.5 mg/mL in 18.3 MΩ H_2O for each sample. The samples were then again split in half with one half for Raman interrogation measurements and the other half for growth data use.

2.2 Raman instrumentation

A modified FALCON II Raman Chemical Imaging (RCI) System (ChemImage, Pittsburgh, PA) fitted with a Fiber Assisted Spectral Translator (FAST) was used for spectral analysis. The FAST system utilizes a 13x14 fiber bundle array (182 total) allowing rapid scans of entire wavelength ranges as opposed to the step process of conventional RCI systems that use a liquid crystal tunable filter. Briefly, a 532 nm laser is defocused through the fibers and bathes the entire field of view (known as wide-field imaging). Spatially resolved Raman spectral information is collected and reimaged into a charge-coupled device (CCD) detector. Software is then used to reconstruct both the spatial and spectral information into a Raman hyper spectral cube (RHSC) in which each pixel of the reconstructed image contains an associated, full Raman spectrum. Figure 2 shows a representative schematic of this process and the resulting RHSC enabling isolation of pixel groups for spectral extraction. Spectral data was acquired 150× objective allowing interrogation of individual spores. Each acquisition was photobleached (field of view containing spores bathed in excitation light continuously) for minimally 5 minutes before a 60-second spectral interrogation acquired with repeat measurements.
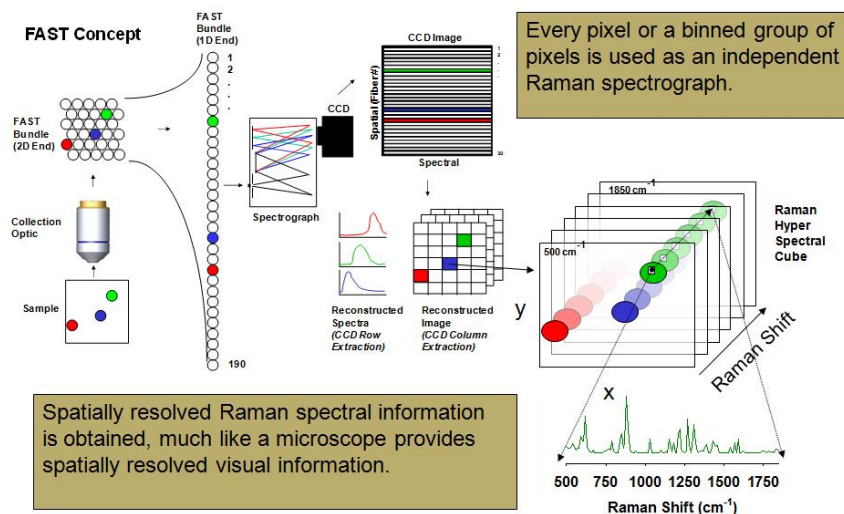
Figure 2. Schematic of FAST Raman Chemical Imaging

2.3 Slide preparation

Each slide was prepared in a similar fashion. As described above, upon final washing of DIW a 4 µL aliquot of the 1.5 mg/mL bacterial sample was deposited onto an aluminum coated microscope slide. The initial spot was recorded at "5 minutes" and was deemed the start or time equal to zero moment. After which, a 5 hour sample was prepared following the same procedure. After the first day and from then on, prior to deposition of the sample, 7 mL were extracted from the stock solution of the bacterial sample, washed twice in DIW water and volume brought back up to 7 mL. From the washed sample, again a 4 µL aliquot was deposited onto an aluminum microscope slide and the time recorded. This procedure was repeated for the 2nd, 3rd, 4th, 7th, 8th, 9th, 10th, 11th, 14th, 15th, and 17th day from zero.

2.4 Growth curve

From the original stock solution (time = zero) of the viable BG, 100 mL was used to monitor growth data simultaneously along with the Raman data collection. Growth curve data was acquired on a Beckman Du7400 UV-Vis Spectrometer. Starting with the original time = zero sample, 0.5 mL of the BG DIW sample was pipttetted into 50 mL of tryptic soy broth (TSB) and a timer started immediately. Immediately, 1 mL was extracted, and the UV-Vis was acquired. The flask was then covered and placed in a shaker/incubator at 100 rpm, at 37°C. The absorption response was monitored every 30 minutes until the readings started to spike (more than 0.5 between previous and current readings). After which samples were collected every 15 minutes over the next several hours. Finally, the sample was allowed to incubate over night with a final reading taken which was the resulting maximum growth of the BG. This procedure was repeated daily throughout the 17-day period.

3. RESULTS AND DISCUSSION

Data was collected from viable and non-viable BG spores suspended in DIW over a two-week period. As described above, concurrently being analyzed along with the Raman data was spore growth of the viable BG. Figure 3 shows adsorption response (converted to minutes until % growth) versus time. Immediately noticeable is that there is a significant difference in growth time between the days. Day 8 exhibits the fastest growth trend from day one and that after that day it appears to be trending back towards an initial growth response. Again, it's it typically believed that a dormant spores in a non-nutrient rich environment should not and are not changing meaning the spores should grow at a similar rate regardless of how long they have been suspended. That is clearly not necessarily the case.
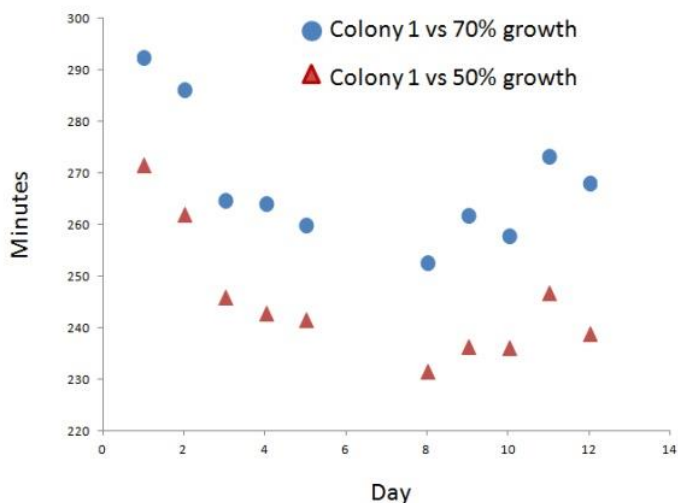
APPROVED FOR PUBLIC RELEASE

Figure 3. growth curve data showing change in growth as a function of suspension time.

Supporting the growth rate changes, the Raman spectral data also exhibited significant differences in spectral features between the viable and non-viable. Figure 4 shows a side by side comparison of the average daily spectra obtained from both bacterial forms. The spectra from the viable BG shows several peaks that appear to change over time including 1393 cm^{-1}, 1660 cm^{-1}, 1663 cm^{-1} which are associated with amide I & amide III vibrational modes. The bands associated with phenylanline (1000 cm^{-1} and 1030cm^{-1}) also are exhibiting variations. In stark contrast, the non-viable spectra are strikingly different with several modes being complexly absent including the aforementioned amide III vibration along with the mono-substituted phenyl stretch at 1030 cm^{-1}. From the visual indicators alone, it is obvious that spectrally viable and non-viable bacteria are quite different. However, this is only for one case of inactivation (heat-killed), and other types of inactivation methods (gamma irradiation) still need to be examined.
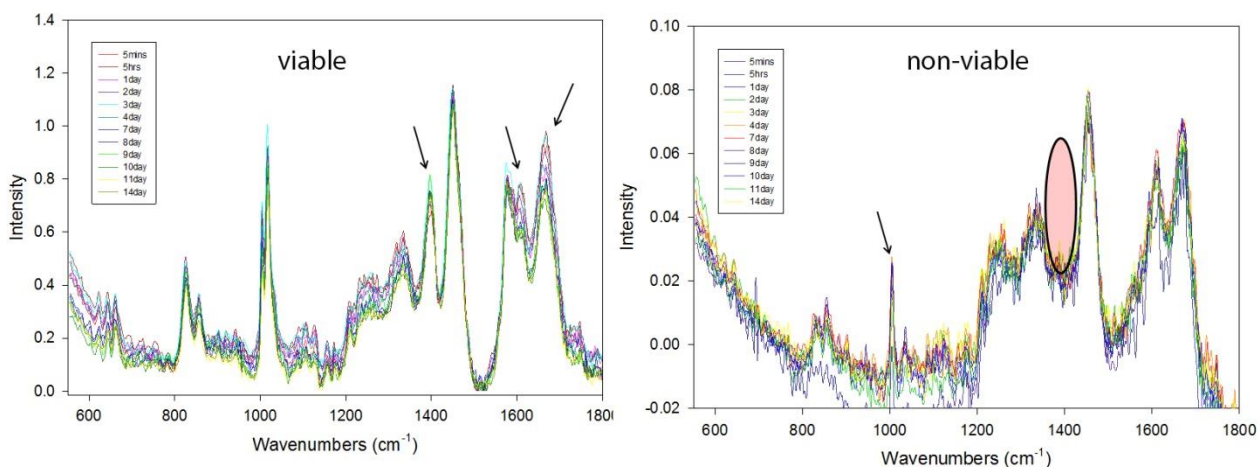

Figure 4. Average daily spectra from both the viable and non-viable BG highlighting differences between the two as well as peak variations in the viable data.

To explore these differences further, Principal Component Analysis (PCA) was used to evaluate the effect of suspension residence time and the temporal spectral intensity changes. Prior to PCA analysis (performed in Matlab), spectra were baseline corrected (2nd order), smoothed (Savitsky-Golay), energy normalized and truncated to 800 cm^{-1} 1060 cm^{-1}, 1140 cm^{-1} to 1714cm^{-1}.

Figure 4 shows the resulting analysis plot of PC 1 versus PC 2. Figure 5a, shows all the days individually colored. While it is somewhat difficult to discern it appears that Days 1-4 tend to separate from the days 7-14. In order to show this clearer the same data was plotted but the color coding was changed to red for all the data encompassing

99

days 1-3 and blue for all the remaining days (Figure 5b). This variation is not more distinct but does show that over time the relative spectral response from a viable spore is in fact changing.
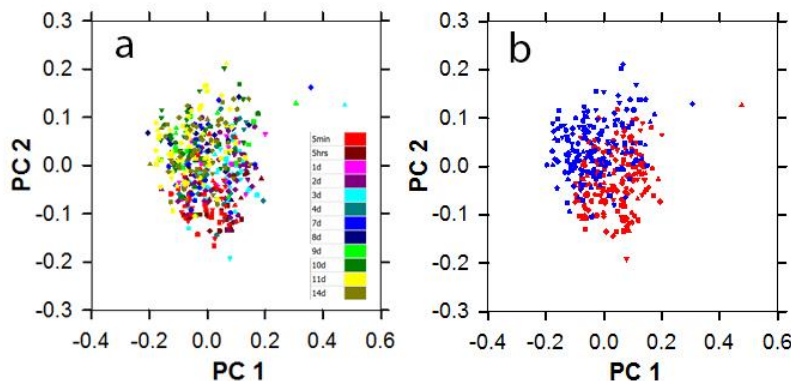

Figure 5. a) PCA analysis of PC 1 versus PC 2 for live (viable) BG spores over 14-day period. b) same data was color coded to show distinction between days 1-3 (red) and 4-14 (blue).

Figure 6 shows the resulting PCA analysis of the inactivated (non-viable) BG spores. Even though there is a clear separation between the two groups there is no distinction between days. Again, the data was color coded similar to the viable data (days 1-4 & 7-14) and the resulting PCA shows no discernible distinction over time. The source of the separation was tracked to the several peaks (including the 1030 cm⁻¹ and 1600 cm⁻¹) that appeared to be present in some of the spectra but actually absent others. We attribute this to the process of inactivation (heat) and that some spores (even though were certified inactive) were thermally degraded more so than others. Again, visually referencing Figure 3 the average vibrational modes in the non-viable spectra do not appear to change throughout time. However, by performing a peak ratio analysis of the data, the worry that the non-viable bacteria was changing was alleviated.
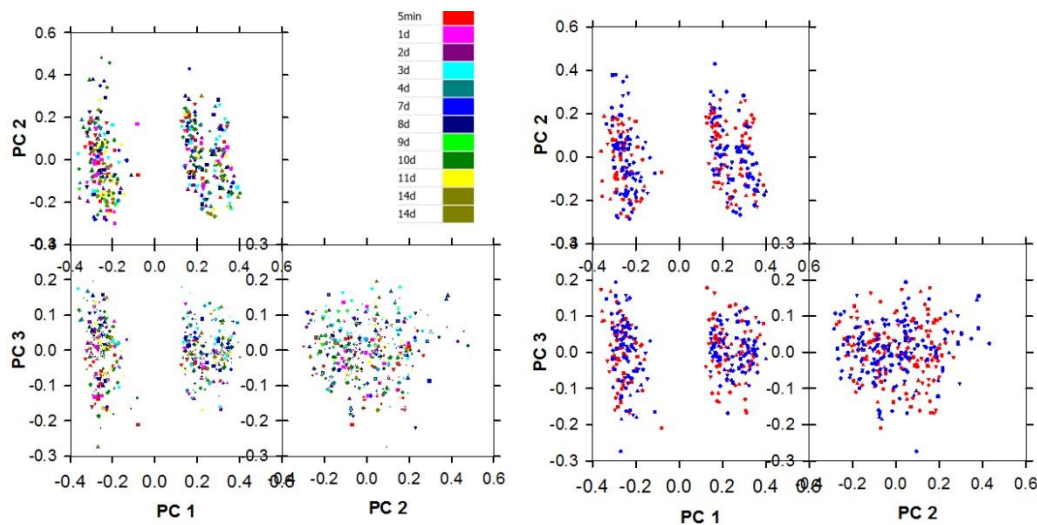

Figure 6. PCA analysis of the inactivated (non-viable) BG spores.

Figure 7 shows the relative Raman spectral intensity vs. the suspension time of a DIW sample of BG spores. The area under to the curve for the region of 1593 cm⁻¹ to 1741 cm⁻¹ was ratioed to the 1451 cm⁻¹ band for both states of the bacteria. As can be seen in Figure 7a, there is a downward trend of the daily response of the viable spores as opposed to almost a flat line for the non-viable spores (Figure 7b). Even though the error bars are quite significant (due to spectral variability of an individual spore) we believe this does show that the killed bacteria are not changing.
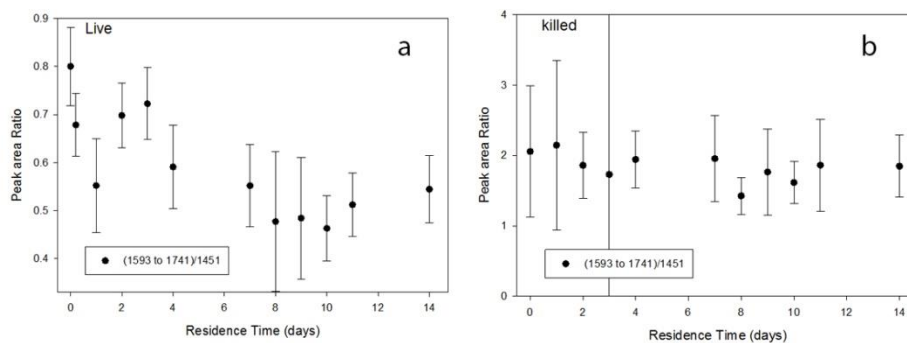
Figure 7. Plots of Raman intensity of selected wavenumbers vs. suspension time for (a) viable and (b) non-viable BG.

4.   CONCLUSIONS

It appears that the residence time of *Bacillus* spores suspended in a nutrient free suspension yields sufficient Raman spectral variance while inactivated spores do not. While the nature of the variance is not understood these results do successfully add weight to our previous study with solely live bacteria. Following this work, we plan to lengthen and augment this study to ascertain the source of the pre-germination activity, which we believe is occurring. The potential pre-germination protein and/or metabolite activity discovery may be fundamental to understand the processes that initiate the biological transition from dormant spores to replicating bacterial cells. We will look to transition this seedling into either an In-house Laboratory Independent Research effort or approach outside agencies (DTRA, NIH) to broaden the scope and to incorporate liquid chromatography-electrospray tandem mass spectrometry (LC-ESI-MS/MS) and proteomics to analyze the suspended spore samples by their extracted proteins at various suspension times in DIW. This will be much larger effort in which we endeavor to ascertain qualitative changes to the spores and provide structural information about the proteins and/or metabolites involved in the presumed pre-germination activity. If successful, to our knowledge, we will be the first to understand the biochemical components that are expressed in spores that trigger the germination process.

ACKNOWLEDGEMENT

REFERENCES

[1]   E. W. Davidson, et al., *Applied and Environmental Microbiology,* **1984**, 47, p125-129.
[2]   D. V. Lim, et al., *Clinical Microbiology Reviews,* **2005**, 18, p583-607.
[3]   S. Eichler, et al., *Applied and Environmental Microbiology,* **2006**, 72, p1858-1872.
[4]   R. Hoffman, et al., *Environmental Science and Technology,* **2009**, 43, p5165-5170.
[5]   A. Tripathi, et al., "Biomolecule Raman Spectral Temporal Flux From Resting *Bacillus* Spores in Deionized Water Matrix". *SPIT-International Optical Engineering*, 8358, 83580D, **2012.**

APPROVED FOR PUBLIC RELEASE